Stress Corrosion Cracking and Internal Oxidation of Alloy 600 in High Temperature Hydrogenated Steam and Water

A thesis submitted to the University of Manchester for the degree of Doctor of Philosophy in the Faculty of Engineering and Physical Sciences

2014

JOHN LINDSAY

SCHOOL OF MATERIALS
Materials Performance Centre

CONTENTS

Table of Contents 3

List of Figures 9

List of Tables 17

Abstract 19

Declaration 21

Copyright 23

Acknowledgements 25

Introduction 27

I Literature Review 31

1 Material 33
- 1.1 Composition . . . 34
- 1.2 Microstructure . . . 36
- 1.3 Production . . . 38
  - 1.3.1 Annealing . . . 38
  - 1.3.2 Thermal Treatments . . . 39

2 Oxidation 41
- 2.1 PWR Oxidation . . . 42
  - 2.1.1 Oxide Structure . . . 42
  - 2.1.2 Chromium Effect . . . 43
  - 2.1.3 Environment . . . 44
  - 2.1.4 Surface Finish . . . 45
- 2.2 Internal Oxidation . . . 45
- 2.3 Considerations for Steam Oxidation . . . 48

    2.3.1 Oxygen Partial Pressure . . . 49
    2.3.2 Volatile Species . . . 49
    2.3.3 Pressure . . . 50

3 Stress Corrosion Cracking 53
  3.1 The SCC Problem . . . 54
  3.2 Influencing Factors . . . 55
    3.2.1 Nickel and Chromium . . . 55
    3.2.2 Carbon Content and Carbide Distribution . . . 57
    3.2.3 Grain Size and Orientation . . . 59
    3.2.4 Stress, Strain and Creep . . . 60
    3.2.5 Cold Work and Strain Path . . . 62
    3.2.6 Temperature . . . 65
    3.2.7 Environment . . . 66
  3.3 Stress Corrosion Cracking Mechanisms . . . 69
    3.3.1 CEPM . . . 69
    3.3.2 Film Rupture . . . 71
    3.3.3 Internal Oxidation . . . 72

II Experimental and Analytical Techniques 77

4 Material Preparation 79
  4.1 Surface Finish . . . 79
    4.1.1 Grinding and Polishing . . . 79
    4.1.2 Electrochemical Polishing . . . 80
    4.1.3 Cleaning - Plasma Cleaning . . . 80
    4.1.4 Etching . . . 81
      4.1.4.1 Grain Boundary Etching . . . 81
      4.1.4.2 Carbide Etching . . . 81
  4.2 Introducing Cold Work . . . 81
  4.3 Samples . . . 82

5 Environmental Exposures 85
  5.1 Hydrogenated Steam Testing Systems . . . 85
    5.1.1 Calculations . . . 85
    5.1.2 Calibration . . . 88
      5.1.2.1 Flow Rates . . . 88
      5.1.2.2 Environment . . . 89
    5.1.3 Oxidation Rig (Rig 1) - Samples . . . 89
    5.1.4 SCC Test Rig (Rig 2) - Samples . . . 90
  5.2 Autoclave Testing - Samples . . . 91

6 Microscopy and Analysis Techniques 95
6.1 SEM . . . 95
6.1.1 Overview . . . 95
6.1.2 Imaging Modes . . . 96
6.1.3 Utilised SEM's . . . 97
6.2 FIB . . . 98
6.2.1 Overview . . . 98
6.2.2 Cross-Sectioning . . . 98
6.2.3 Serial Sectioning . . . 99
6.2.4 TEM Sample Preparation . . . 100
6.3 TEM . . . 101
6.3.1 Overview . . . 101
6.3.2 Sample Preparation . . . 102
6.3.2.1 PIPS . . . 103
6.3.2.2 Electrochemical Polishing . . . 103
6.3.2.3 Focused Ion Beam . . . 103

III Results and Discussion 105

7 Material Characterisation 107
7.1 WF675 . . . 108
7.1.1 Grain Size . . . 108
7.1.2 Grain Boundary Statistics . . . 112
7.1.3 Grain Structure . . . 112
7.1.3.1 As Received . . . 113
7.1.3.2 Cold Worked . . . 113
7.1.4 Precipitates and Inclusions . . . 114
7.1.4.1 Carbides . . . 115
7.1.4.2 Titanium Nitrides . . . 117
7.1.5 Surface Preparation . . . 119
7.2 Solution Annealed Alloy 600 . . . 120
7.2.1 Grain Size . . . 120
7.2.2 Precipitates and Intermetalics . . . 121

8 Steam Oxidation 123
8.1 Calibration of the Environment using Nickel 200 . . . 123
8.2 Observations of the Oxides Formed on the Surface . . . 125
8.2.1 Oxidising Environments (R<1) at 400°C . . . 125
8.2.2 Reducing Environments (R>1) at 400°C . . . 127
8.2.2.1 Oxidation at Grain Boundaries . . . 130
8.2.3 Reducing Environments (R>1) at 500°C . . . 131

8.2.3.1 Oxidation at Grain Boundaries 135
8.2.4 Cold Worked vs As-Received 136
8.3 Internal Oxidation 136
8.3.1 Temperature Dependency 137
8.3.2 Effect of Exposure Time 138
8.3.3 Observations of Slip Bands 139
8.3.4 Cold Worked vs As-Received 140
8.4 Cross-Sectional Views of the Preferential Oxides 141
8.4.1 Effect of Temperature on Oxidation Kinetics 141
8.4.2 Dependency on Surface Oxide Morphology 144
8.4.3 The Effect of Carbides 148
8.4.4 Elemental Analysis of Preferential Oxides 153
8.4.4.1 AR-WF675, 500°C, 66 h 153
8.4.4.2 15%CW-WF675, 500°C, 66 h 159
8.4.4.3 15%CW-WF675, 400°C, 500 h 162
8.4.5 Discussion of the Mobility of Chromium During Oxidation . 166
8.5 The Effect of Surface Finish 170
8.5.1 Surface Oxidation 170
8.5.2 Preferential and Internal Oxidation 171
8.6 Solution Annealed Alloy 600 171
8.6.1 Morphologies of Grain Boundary Oxides 172
8.6.2 Preferential Oxidation 174
8.6.3 Metalic Nickel Nodules 176
8.6.4 Surface Finish 177

9 Autoclave Oxidation 181
9.1 Observations of the Oxides Formed on the Surface 181
9.1.1 The Effect of Surface Finish 181
9.1.2 Oxidation at Grain Boundaries 183
9.2 Cross-Sectional Views of the Preferential Oxides 184
9.2.1 Cold Worked vs As-Received 185
9.2.2 The Effect of a Deformed Layer 186
9.2.3 Cross-Sections of Twins 187
9.2.4 The Role of Carbides on Oxidation 188

10 Stress Corrosion Cracking Tests 191
10.1 Stress Corrosion Cracking in Steam 191
10.1.1 Fractography 191
10.1.2 Environment and Susceptibility 192
10.1.3 Surface Finish and Susceptibility 194
10.1.4 Summary of Steam SCC Tests 197
10.2 Reference PWSCC Samples 199

10.2.1 Carbides on the Crack Path 200
10.2.2 Surface Finish 201

IV Further Discussion **203**

11 Oxidation of Alloy 600 **205**
11.1 Internal Oxidation 207
11.1.1 Oxygen Diffusivity 207
11.1.2 Formation of Nickel Nodules 209
11.2 Grain Boundary Preferential Oxides 210
11.3 Oxidation of Carbides 213
11.4 The Effect of Surface Finish 214

12 Comments on the Implications for SCC Studies **217**
12.1 The Validity of Steam as an Environment for PWSCC Studies . . 217
12.2 The Effect of Surface Finish 218

V Conclusion **221**

13 Conclusions **223**

14 Future Work **227**

VI Appendix **229**

A Converting R to cc/kg of Hydrogen **231**

B Hydrogenated Steam Flow Calibration Curves **233**

C Rig 1 Operating Procedure **235**

D Rig 2 Operating Procedure **237**

E 500 h, 500°C, As-Received WF675 3D Image **239**

F 500 h, 500°C, Cold Worked WF675 3D Image **241**

G Calculations of the Volume Change Associated with Internal Oxidation **243**

Bibliography **245**

Final Word Count: 50,241

LIST OF FIGURES

1 Influence of alloying additions to nickel 200 (99% pure Ni) on the corrosion properties . . . 28
2 Ni-Fe-Cr ternary phase diagram at 400°C with alloys of interest to the nuclear industry marked . . . 29

1.1 Locations of Alloy 600 and its associated weld metals in the PWR's primary circuit . . . 34
1.2 Ternary phase diagrams for Ni-Fe-Cr and the predicted liquidus . . . 36
1.3 Examples of the different carbide distributions . . . 37
1.4 Typical Thermo-Mechanical-Process used for the production of Ni-Fe billets . . . 38
1.5 Carbide precipitation curve for Alloy 690 with a typical thermal treatment overlaid . . . 40

2.1 Schematic representation of the oxide formed on Alloy 600 under PWR conditions . . . 42
2.2 Early stages of oxide formation on Alloy 600 . . . 43
2.3 Oxide structure of Alloy 600 as a function of the dissolved hydrogen at 320°C . . . 44
2.4 Internal oxidation morphologies as a function of oxygen partial pressure and reactive solute concentration in Fe-Si binary system . . . 46
2.5 Types of IO observed in high temperature testing on Ni-Cr alloys . . . 47
2.6 Mechanism of grain boundary sliding to accommodate plastic deformation . . . 48
2.7 Partial pressure of SiO at 1000°C as a function of the oxygen partial pressure . . . 50
2.8 Oxidation rate of steels at 650°C and 700°C as a function of steam pressure . . . 51

3.1 Influencing factors for SCC . . . 53
3.2 Time line showing incidents of SCC detection in Alloy 600 . . . 54

3.3 Effect of nickel content on the alloy susceptibility to transgranular and intergranular SCC in pure or chlorinated water 56
3.4 Effect of chromium content on nickel alloys susceptibility to PWSCC 56
3.5 Effect of carbide distribution on PWSCC in Alloy 600 58
3.6 Effect of grain size on PWSCC susceptibility 59
3.7 PWSCC as a function of grain boundary orientation and effect of orientation on carbide precipitation 60
3.8 Data showing stress threshold for SCC and initiation dependence as a function of stress 61
3.9 Work by Morton et al. showing the relationship between stress and initiation time and strain and initiation time 62
3.10 Results showing the observed localisation of strain at the grain boundaries and the subsequent crack growth rates 62
3.11 Oxide formed on annealed (a) and cold worked (b) 316L stainless steel when exposed to simulated PWR conditions at 300 °C 63
3.12 CGR as a function of orientation 64
3.13 Initiation time and propagation rate of PWSCC cracks as a function of temperature 65
3.14 PWSCC susceptibility measured as a function of pH 66
3.15 Relationship between the hydrogen partial pressure and the crack propagation and initiation time 68
3.16 Graphic illustration of the CEPM process 70
3.17 Graphic illustration of the film rupture process 72
3.18 Graphic illustration of the internal oxidation process at grain boundaries 73
3.19 Comparison of experimental diffusion rates for oxygen in nickel with the rate required for IO included 74

4.1 The orientations used by Leonard when analysing SCC susceptibility in WF 675 and cold worked WF 675 82
4.2 (a) $2 \times 19 \times 20$ mm^3 corrosion coupons used in oxidation exposures. (b) 1 mm thick dog bone samples used for SCC tests 82

5.1 Calibration set up used for calibrating the water pump and hydrogen flow rates 89
5.2 Schematic of the steam oxidation rig used to test samples 90
5.3 Schematic of the steam oxidation rig built to conduct SCC tests . 91
5.4 Cormet supplied schematic of the used autoclave 92
5.5 Photo of the samples suspended in the autoclave prior to exposure 93

6.1 Schematic showing the location and geometry of possible electron beam interactions within a sample 95

6.2 Schematic representation of the geometries present in the operation of the FIB . . . 98
6.3 Outline of stages in the preparation of a FIB cross-section . . . 99
6.4 Ion beam (a) and electron beam (b) images showing a sample prepared for serial sectioning . . . 100
6.5 Outline of stages in the preparation of a FIB TEM sample . . . 101
6.6 Schematic representation of the electron optics associated with TEM and example instrument . . . 102

7.1 Representative EBSD maps obtained from the AR (a), 15%CW (b) and 19%CW (c) materials used in this study . . . 110
7.2 Typical EBSD maps taken from the AR and 19%CW forms of WF675 showing abnormal grains . . . 111
7.3 TEM images showing the microstructural features observed in WF675 in the AR condition . . . 113
7.4 TEM images showing the microstructure of WF675 in the CW condition . . . 114
7.5 Mixed ghost/ intragranular structure of the observed precipitates (a) and the corresponding binary image used for analysis (b) . . . 115
7.6 Bright field image of a chromium carbide with diffraction pattern and solution confirming it as a M_7C_3 . . . 116
7.7 $M_{23}C_6$ carbides observed in WF675 . . . 117
7.8 Cracked carbide observed in the 19%CW material . . . 117
7.9 Titanium nitride's observed in the matrix with magnesium rich inclusion at the centre . . . 118
7.10 Titanium nitride observed to act as a initiation site for carbides in the alloy . . . 118
7.11 EDM surface on the coupons as they were received and FIB cross-section . . . 119
7.12 Optical image of the OPS surface finish and SEM SE image of the electrochemically polished surface finish . . . 120
7.13 FIB Cross-section of the P600 surface finish showing the deformed layer produced via this surface finish . . . 120
7.14 Optical image of the SA alloy etched to reveal its grain structure . 121
7.15 Precipitates observed in the solution annealed alloy . . . 122

8.1 Grazing angle XRD spectra from Ni 200 samples exposed to different R values for 24 h at 400°C . . . 124
8.2 Photos taken of the Ni 200 samples used for calibration tests at 400°C for 24 h . . . 124
8.3 Inlens (a) and SE (b) images taken from tests with a oxidising environment (R=0.1) at 400°C for 100 h (a) and 500 h (b) . . . 125

8.4 Grazing angle XRD taken from AR-WF675 exposed to 400°C steam for 500 h with an R of 0.1 126
8.5 TEM EDX line scan and corresponding HAADF image form 15%CW WF675 oxidised at 500°C for 500 h with an R of 0.5 127
8.6 SE (a) and ESB (b) images of AR-WF675 surface after being tested at 400°C with an R of 20 for 66 h 127
8.7 HAADF image of the oxide formed in the vicinity of a grain boundary in 15%CW-WF675 after 500 h in a reducing environment (R=20) at 400°C and the corresponding EDX Elemental maps (b-f) 129
8.8 SE and ESB images respectively of oxidised grain boundaries and carbides observed on the surface of the 66 h, 400°C R = 20 test . . 130
8.9 SE images of the surface after exposure to 500°C hydrogenated steam with a R of 20 for 66 h (a,b) and 500 h (c,d) 131
8.10 Grazing angle XRD results from the 500 h test at 500°C with an R of 20 132
8.11 HAADF Image of the nickel nodules present in the TEM sample and the corresponding EDX elemental maps 133
8.12 HAADF Image of the sharp edged oxide present at the sample surface and the corresponding EDX elemental maps 134
8.13 Selection of SE images taken for the 500°C, 500 h test illustrating the observed grain boundary types 135
8.14 SE images illustrating the effect of cold work on the oxidation of the alloy for both R>1 and R<1 136
8.15 TEM images from the surface of the 350°C, 400°C and 500°C tests showing the presence of internal oxidation 137
8.16 EDX line scan and corresponding HAADF image of the internal oxide formed at 500°C after 66 h 138
8.17 EDX line scan and corresponding HAADF image of an internal feature observed to be oxidised after 500 h exposure in 400 °C steam 138
8.18 FIB SEM and bright field images of the maximum IO penetration 139
8.19 FIB SEM image of what has been interpreted to be an internally oxidised slip bands after 500°C exposures 140
8.20 FIB SEM images of the internally oxidised layer in AR (a) and 15%CW (b). It can be seen that in the AR condition the depth of penetration varies whilst the 15%CW remains relatively constant . 140
8.21 FIB SEM images of the internally oxidised layer in AR (a) and 15%CW (b) where a surface film has formed, thus preventing the inward diffusion of oxygen and hence internal oxidation 141
8.22 Preferential oxidation observed by FIB SEM from the 350°C 500 h (a), 400°C 500 h (b) and the 500°C 66 h (c) tests 142

8.23 Bright field, FIB SEM and HADDF images showing the maximum observed preferential oxidation in steam (R=20 143
8.24 Calculated preferential oxidation rates as a function of temperature in hydrogenated steam 144
8.25 SE surface image of a NFZ boundary and the corresponding FIB SEM cross-section of the boundary 145
8.26 SE surface image of a NNFZ boundary and the corresponding FIB SEM cross-section of the boundary 146
8.27 SE surface image of a HH boundary and the corresponding FIB SEM cross-section of the boundary 147
8.28 FIB SEM cross-sectional images of the preferential oxidation observed in a sample exposed for 500 h and 500°C, (a) is a NFZ (and a HH), (b) is a HH, (c) is a NNFZ and (d) is an example of a nodule free zone having slight internal oxidation. Cross sections (b) - (d) are taken from the serial sectioning of a single boundary, thus showing the GB Morphology can change without a clear change in grain boundary character 147
8.29 Carbide observed by FIB SEM which appears to be below the internal oxidation zone, but still oxidised 148
8.30 HAADF image and EDX line scan obtained from an oxidised carbide (a-b), the oxygen peak obtained in the spectrum at 190nm (c) on the line A-B is given with a comparison to that obtained in the spectrum located at 0nm (d) on the line A-B 150
8.31 A sequence of images from FIB SEM serial sectioning showing an oxidised carbide which proceeds beyond the internally oxidised layer 151
8.32 Carbide observed to be oxidised as a result of proximity to the grain boundary 152
8.33 HAADF Image of a oxidised carbide (a) and the corresponding EDX elemental maps obtained from this region (b-f) 152
8.34 Oxygen peak obtained in the EDX spectrum from the preferential oxide (a) and a reference point in the matrix (b). Spectrum (a) is taken from the 200 nm position of the line A-B in figure 8.35(b) whilst spectrum (b) is taken from 0 nm position of the line C-D in figure 8.35(c) 153
8.35 HAADF image and EDX line scans of the preferential oxidation on a HH boundary and surrounding regions 156
8.36 Chromium and oxygen maps obtained by EDX from the sample in Figure 8.35 157
8.37 Bright Field image of preferential oxidation on a NNFZ boundary (a) and the corresponding EDX elemental maps obtained from this region (b-f) 157

8.38 Bright field image of the preferential oxide tip with EDX point analysis and spectra indicating a enrichment of titanium and oxygen in the chromium depleted zone 158
8.39 HAADF image and EDX line scans of the preferential oxidation observed on a HH boundary 160
8.40 HAADF image and EDX line scans of the preferential oxidation observed at a higher magnification to identify any small depletion in the none depleted grain 161
8.41 HAADF image annotated with locations of EDX point analysis locations from a preferential oxide formed at 400°C and spectra confirming the presence of oxygen 162
8.42 HAADF image of preferential oxidation formed at 400 °C (a) and the corresponding EDX elemental maps obtained from this region (b-h) 164
8.43 HAADF image of the preferential oxidation and the grain boundary in advance with EDX line scans indicating chromium depletion. Lines 1, 2 and 3 are shown in (b), (c) and (d) respectively 165
8.44 Dark field image (a) and EDX maps showing nickel enrichment (b) and chromium depletion (c) along the trace of the original grain boundary, a lower magnification image of the boundary can be found in Figure 8.35 167
8.45 Dark field image (a) with location of EDX point scans and annotated version showing the interpitation 168
8.46 Dark field image with layered EDX map indicating the presence of a carbide 169
8.47 FIB SEM images with the preferential oxide appearing to deviate from the grain boundary 169
8.48 SE and ESB images of the oxide formed on the OPS and P600 surfaces at 500°C in hydrogenated steam after 500 h 170
8.49 FIB SEM cross-sections of the OPS (a) and P600 (b-d) surface, after a 500°C exposure for 500 h 171
8.50 Low magnification SE images of the surface oxidation of SA-HT93510 after 66 h at 480°C with a R of 20 172
8.51 EBSD map showing that the grain boundary oxide changes morphology's when the grain boundary character changes 172
8.52 NFZ grain boundaries observed on SA-HT93510 after 66 h at 480°C with a R of 20 173
8.53 NNFZ grain boundaries observed on SA-HT93510 after 66 h at 480°C with a R of 20 174
8.54 HH grain boundary observed on SA-HT93510 after 66 h at 480°C with a R of 20 174

8.55 FIB SEM cross-section of a NNFZ grain boundary in the SA-HT935 10175
8.56 FIB SEM cross-section of a NFZ grain boundary in the SA-HT935 10175
8.57 FIB SEM cross-section of a twin grain boundary in the SA-HT935 10176
8.58 EBSD map showing nodules on the grains appear to be mapped as $\Sigma3$ boundaries 177
8.59 SE images of the oxides formed on the OPS, 1 µm and a P600 surface after oxidation 178
8.60 FIB SEM images taken in a attempt to locate a grain boundary on the P600 surface of the SA alloy after oxidation 179

9.1 SE images of the oxide formed on AR-WF675 after autoclave exposure on the OPS (a) and P600 (b) surface 182
9.2 SE Image of a oxide spinel formed on the P600 (a) and a corresponding FIB SEM cross-section (b) 182
9.3 SE images showing low visibility grain boundaries with backscattered image giving an indication that the grain boundary has been oxidised 183
9.4 FIB SEM images of the maximum preferential grain boundary oxidations observed in AR-WF675 (a) and 15%CW-WF675 (b) as a result of autoclave exposure to 350°C water with a hydrogen overpressure of 30 cc/kg. 184
9.5 FIB SEM images of the typical grain boundary preferential oxidation observed in the AR (a) and 15%CW (b) state 186
9.6 FIB SEM cross-sectional images of the P600 surface after autoclave oxidation, showing no grain boundary preferential oxidation, but preferential oxidation of the deformed layer 187
9.7 FIB SEM cross-sectional images of twin boundaries from the OPS (a) and P600 (b) surface 188
9.8 SE image showing visibly oxidised carbides from the surface (a) and FIB SEM cross-section produced from the carbides (b) 188
9.9 FIB SEM cross-section showing two adjacent grain boundaries in 15%CW-WF675 after a 500 h in 350°C water with a hydrogen overpressure of 30 cc/kg. The grain boundary with a carbide is seen to have a deeper preferential oxide 189
9.10 FIB SEM cross-section showing carbides in the deformed layer after oxidation 189

10.1 Fractography of the fracture surface produced in hydrogenated steam with R = 8 192
10.2 SE images of the largest observed cracks from SCC tests with R values of 0.1, 8, 20 and 66 193

10.3 Plot of SCC susceptibility vs Log (R), this can be seen as a comparable to the plots in the literature relating PWSCC susceptibility to potential 193
10.4 Low magnification SE image showing that all initiation sites on a failed 19%CW-WF675 SCC sample (R=8) originate from the OPS surface 194
10.5 Sequence of SE images taken from the same failed SCC sample but on opposite side at a range of magnifications, (a), (c) and (e) are from the P600 surface whilst (b), (d) and (f) are from the OPS surface 195
10.6 Cumulative probability crack distribution for the OPS and P600 surface as a function of crack length 196
10.7 SE images of test 4 from the P600 (a) and OPS (b) surfaces 199
10.8 SE image of a PWSCC crack propagating beyond a carbide, with no visible PWSCC crack path around the carbide (a) and a backscatter image showing a PWSCC crack partially cracking the boundary just beyond a carbide (b) 200
10.9 PWSCC crack propagating around a carbide 201
10.10 AsB image of a mechanically cross-sectioned PWSCC sample of AR-WF675, the deformed layer present can be observed at the surface 202

11.1 Schematic of the NFZ, NNFZ and HH boundary types, including the internal oxidation associated with the grain boundary surface oxide 206
11.2 The calculated preferential oxidation rates as a function of temperature 211

B.1 Calibration curve obtain for Rig 1 using pure hydrogen 233
B.2 Calibration curve obtain for Rig 1 using 5%hydrogen bal. nitrogen 233
B.3 Calibration curve obtain for Rig 2 using 5%hydrogen bal. nitrogen 234

LIST OF TABLES

1.1 Chemical composition of Alloy 600 and Alloy 690 35

5.1 Book values for the Gibbs free energy 88

7.1 Chemical composition of WF675 and HT93510 compared to the specification 108
7.2 Grain boundary statistics of WF675 and its cold worked form, in terms of the percentage of HAGB, LAGB and $\Sigma 3$ present 112

8.1 The maximum observed internal oxidation in WF675 and 15%CW-WF675 139
8.2 The maximum observed grain boundary preferential oxidation depths in WF675 and 15%CW-WF675 after exposure to hydrogenated steam with R=20 142
8.3 Results of the EDX point scans shown in Figure 8.41 163
8.4 Results of the EDX point scans shown in 8.45(a) 168

9.1 Summary of the preferential oxidation observed in AR-WF675 and 15%CW-WF675 185

10.1 Summary of results from the crack counting 197
10.2 Summary of all relevant hydrogenated steam tests conducted in the SCC rig 197

11.1 Oxygen Diffusion rates in WF675 at 400°C and 500°C 208
11.2 The calculated preferential oxidation rates as a function of temperature for AR-WF675 and 15%CW-WF675 211

A.1 Table converting steam test parameter R to equivalent cc/kg of hydrogen at 325°C 232

ABSTRACT

"Stress Corrosion Cracking and Internal Oxidation of Alloy 600 in High Temperature Hydrogenated Steam and Water"

John Lindsay, The University of Manchester, 2014.

In this study, the possibility of using low pressure hydrogenated steam to simulate primary water reactor conditions is examined. The oxides formed on alloy 600 (WF675) between 350°C and 500°C in low pressure hydrogenated steam (with a ratio of oxygen at the Ni/NiO to oxygen in the system of 20) have been characterised using analytical electron microscopy (AEM) and compared to oxide that formed in a high pressure water in a autoclave at 350°C with 30 cc/kg of hydrogen.

Preferential oxidation of grain boundaries and bulk internal oxidation were observed on samples prepared by oxide polishing suspension (OPS). Conversely, samples mechanically ground to 600 grit produced a continuous, protective oxide film which suppressed the preferential and internal oxidation. The surface preparation changed the form of the oxides in both steam and autoclave tests.

The preferential oxidation rate has been determined to be

$$K_{oxide} = A \exp^{\frac{-Q}{RT}}$$

with $A = 2.27 \times 10^{-3}\ m^2 s^{-1}$ and $Q = 221$ kJ.mol^{-1} (activation energy) for WF675 and $A = 5.04 \times 10^{-7}\ m^2 s^{-1}$ and $Q = 171$ kJ.mol^{-1} for 15% cold worked WF675. These values are consistent with the activation energy of primary water stress corrosion cracking (PWSCC) initiation.

Bulk oxygen diffusivities were calculated from the internal oxidation after 500 h exposures. At 500°C the oxygen diffusivity was determined to be $1.79 \times 10^{-20}\ m^2 s^{-1}$ for WF675 and $1.21 \times 10^{-20}\ m^2 s^{-1}$ for 15% cold worked WF675, the oxygen diffusivity at 400°C in 15% cold worked WF675 was calculated to be $1.49 \times 10^{-22}\ m^2 s^{-1}$.

The Cr-depletion associated with preferential oxidation has been assessed by AEM. The Cr-depletion was asymmetric and it could not be accounted for by local variations in the diffusion rate. Chemically induced grain boundary migration is suggested as a possible explanation.

Constant load SCC tests conducted in hydrogenated steam at 400°C have shown a similar trend to the classical dependency of PWSCC as a function of potential. The SCC samples were also prepared with two surface finishes, OPS and 600 grit. In all SCC tests, significantly more cracking was observed on the OPS surface and all failures initiated from this surface.

DECLARATION

I declare that no portion of the work referred to in the thesis has been submitted in support of an application for another degree or qualification of this or any other university or other institute of learning.

COPYRIGHT

i. The author of this thesis (including any appendices and/or schedules to this thesis) owns certain copyright or related rights in it (the "Copyright") and he has given The University of Manchester certain rights to use such Copyright, including for administrative purposes.

ii. Copies of this thesis, either in full or in extracts and whether in hard or electronic copy, may be made **only** in accordance with the Copyright, Designs and Patents Act 1988 (as amended) and regulations issued under it or, where appropriate, in accordance with licensing agreements which the University has from time to time. This page must form part of any such copies made.

iii. The ownership of certain Copyright, patents, designs, trade marks and other intellectual property (the "Intellectual Property") and any reproductions of copyright works in the thesis, for example graphs and tables ("Reproductions"), which may be described in this thesis, may not be owned by the author and may be owned by third parties. Such Intellectual Property and Reproductions cannot and must not be made available for use without the prior written permission of the owner(s) of the relevant Intellectual Property and/or Reproductions.

iv. Further information on the conditions under which disclosure, publication and commercialisation of this thesis, the Copyright and any Intellectual Property and/or Reproductions described in it may take place is available in the University IP Policy (see `http://www.campus.manchester.ac.uk/medialibrary/policies/intellectual-property.pdf`), in any relevant Thesis restriction declarations deposited in the University Library, The University Library's regulations (see `http://www.manchester.ac.uk/library/aboutus/regulations`) and in The University's policy on presentation of Theses.

ACKNOWLEDGEMENTS

I would like to thank all the people whom helped me in the completion of this thesis, first and foremost my former supervisor and the project initiator, Prof. Robert Cottis, with whom this project would not have been possible. My project supervisors Xiaorong Zhou and Fabio Scenini who managed to keep me from diverting too much from the original plan. From EDF I would like to thank my industrial supervisors Florence Carrette and Francois Vaillant for the support and technical expertise provided.

I was fortunate enough to form part of the first year of the advanced metallic systems centre for doctoral training. I would like to thank Brad Wynn and Philip Prangnell whose work made the CDT possible and Claire Hinchliffe, the CDT manager who managed to bring organisation to the chaos.

Throughout my PhD I have had to use a wide range of equipment, as such I would like to thank all those who have trained me in there use, Kenneth Gyves (sample preparation), Michael Faulkner (SEM), Xiang li Zhong (SEM), Ali Gholinia (FIB), Judith Shackleton (XRD), Gary Harrison (XRD) and Jonathan Duff (autoclaves).

I would like to acknowledge all the students who made my time in Manchester enjoyable, especial Fabien Léonard who showed me what to do when I first started and Giacomo Bertali who's support work as part of a masters project proved invaluable.

I am grateful to Freyja Peters for helping with the administrative tasks associated with the PhD and Paul Jordan for all the assistance he provided in the setting up of laboratories and being the first person to contact when anything went wrong.

Finally a special mention goes to Teruo Hashimoto and Grace Burke, both of whom provided a significant (almost all of it) amount of technical expertise in the acquiring and analysis of the TEM data presented.

INTRODUCTION

Nuclear reactors provide a significant proportion of the world's electricity, of these reactors over 60% (by number, 70% by power output) are classified as Pressurised Water Reactors (PWR's) [1]. PWR's can be seen as the future of nuclear with 53 of the 65 reactors under construction being PWR and significantly more in the planning and consulting stages [2].

These reactors use H_2O as a primary coolant, this is held at a sufficient pressure to maintain it in a liquid state (hence PWR), reactors without the pressuriser which allow the water to boil are referred to as boiling water reactors (BWR's). There are many technical challenges in the design, construction and maintenance of these reactors, one such challenge is material selection. The material chosen for a specific component depends on a number of factors; the major materials of construction in PWR's are [3]:

- Low alloy steels ≈ 1900 *tons*
- Stainless steels ≈ 900 *tons*
- Nickel based alloys ≈ 280 *tons*

Zirconium alloys, Ag-In-Cd alloys and ceramics (UO_2-PuO_2) are also significant in PWR construction, Cobalt alloys are also present.

Low alloy steels provide a relatively cheap structural material, but suffer from significant corrosion issues. Stainless steels (SS's) form a passive oxide layer giving them better general corrosion resistance, relative to that of low alloy steels. The passive nature of SS's made them a logical material of choice for piping and containers of a corrosive medium. SS's good general corrosion resistance cannot however be used to imply overall corrosion resistance as SS's can suffer significantly from stress corrosion cracking (SCC) when exposed to specific environments. A number of the environments present in PWR's were known, or have been discovered to induce SCC in SS.

To alleviate the problem of SCC, nickel based alloys were used as an alternative. Nickel based alloys were chosen as they have good generic corrosion properties, a low corrosion product release rate, similar thermal expansion coefficient to low alloy steels (16MND5) and the high nickel content provides excellent resistance to chloride ion induced cracking [4]. The corrosion properties of the alloys can be tailored by the addition of alloying elements, as summarised in Figure 1.

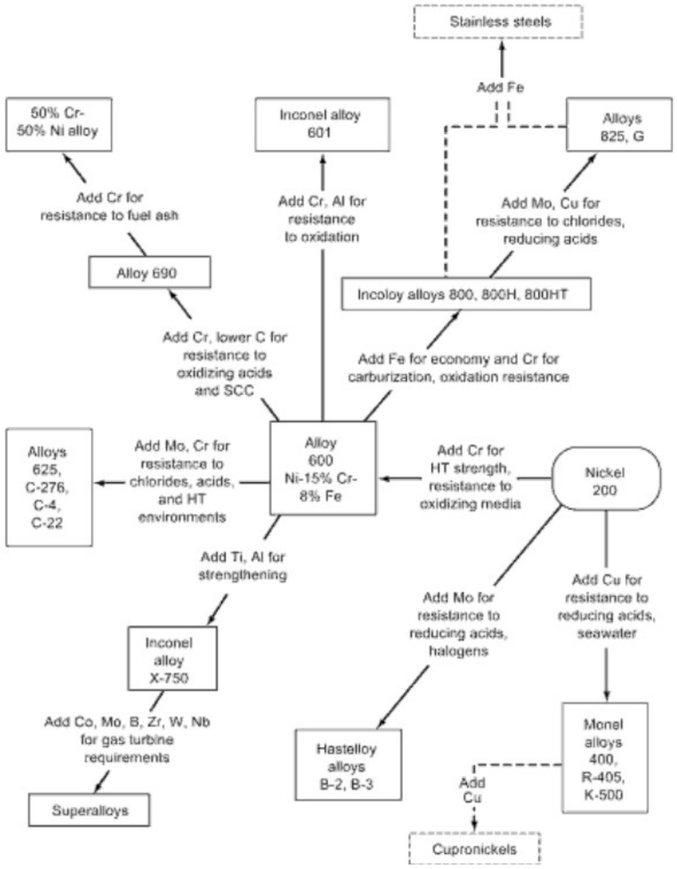
Stainless steels
Add Fe
50% Cr-
50% Ni alloy
Inconel alloy
601
Alloys
825, G
Add Cr for
resistance to fuel ash
Add Cr, Al for
resistance
to oxidation
Add Mo, Cu for
resistance to chlorides,
reducing acids
Alloy 690
Incoloy alloys 800, 800H, 800HT
Add Cr, lower C for
resistance to
oxidizing acids
and SCC
Add Fe for economy and Cr for
carburization, oxidation resistance
Alloys
625,
C-276,
C-4,
C-22
Add Mo, Cr for
resistance to
chlorides, acids,
and HT
environments
Alloy
600
Ni-15% Cr-
8% Fe
Add Cr for
HT strength,
resistance to
oxidizing media
Nickel
200
Add Ti, Al for
strengthening
Add Cu for
resistance to
reducing acids,
seawater
Add Mo for
resistance to
reducing acids,
halogens
Inconel
alloy
X-750
Add Co, Mo, B, Zr, W, Nb
for gas turbine
requirements
Hastelloy
alloys
B-2, B-3
Monel
alloys
400,
R-405,
K-500
Add
Cu
Superalloys
Cupronickels

Figure 1 – Influence of alloying additions to nickel 200 (99% pure Ni) on the corrosion properties of the resulting alloys (HT = high temperature) [5].

Of the available nickel based alloys, Alloy 600 and 690 are the most common. Both these alloys are Ni-Fe-Cr alloys, the same as SS but with nickel being the bulk element (Figure 2 lists the main Ni-Fe-Cr alloys of interest in nuclear systems). They are used because they are more resistant to the cracking experienced in SS's, they have a similar thermal expansion coefficient to that of low alloy steels and they have excellent general corrosion properties with a low corrosion product release rate [6].

Alloy 600 was used extensively in the PWR primary circuit (the circuit used in heating the water directly from the fuel). Alloy 600 is more resistant to chloride ion induced cracking relative to SS; however in 1959, Coriou et al. [8] iden-

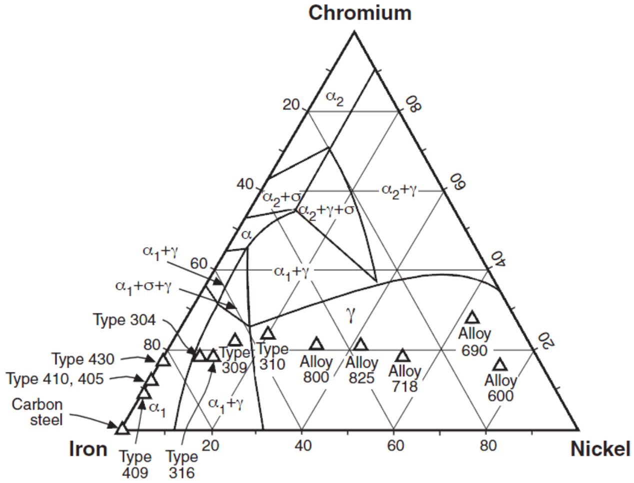
Chromium
α_2
20
80
40
$\alpha_2+\sigma$
$\alpha_2+\gamma$
60
$\alpha_2+\gamma+\sigma$
α
$\alpha_1+\gamma$
60
40
$\alpha_1+\sigma+\gamma$
$\alpha_1+\gamma$
γ
Type 304
80
20
Type 430
Type 410, 405
Carbon steel
Type 309
Type 310
Alloy 800
Alloy 825
Alloy 718
Alloy 690
Alloy 600
α_1
$\alpha_1+\gamma$
Iron
Type 409
Type 316
20
40
60
80
Nickel

Figure 2 – Ni-Fe-Cr ternary phase diagram at 400°C with alloys of interest to the nuclear industry marked. Samples entitled "Alloy" are considered nickel based alloys, while "‘Type" implies a stainless steel [7].

tified the alloy as being susceptible to primary water stress corrosion cracking (PWSCC). Primary water is pure, deaerated water with boron, lithium and hydrogen additives. Coriou et al. results were disputed as other experiments were unable to replicate the results [9], however using different testing methods, other laboratories began to replicate the results. Any remaining doubt on the issue was removed, when in 1971, SCC cracks were detected in Alloy 600 steam generator tubes at the Obrigheim plant (Germany) [10].

The mechanism by which PWSCC occurs is disputed, though a number of models have been proposed. The leading proposed mechanisms of PWSCC are film rupture, internal oxidation (IO) and the corrosion enhanced plasticity model (CEPM). The uncertainty in the mechanism of PWSCC is a significant problem as it hinders the ability to predict the susceptibility of other alloys to PWSCC. Alloy 690 and 800 have been used for replacements in France and Germany respectively. Theses alloys are more resistant to PWSCC and initially were considered to be immune to SCC, however the uncertainty in the mechanism means that the components constructed of alloys 690 and 800 true susceptibility to PWSCC cannot be predicted without extensive testing.

The project presented in this thesis aims to expand the understanding of the mechanism of PWSCC by exploring the inward transport of oxygen (and associated changes in local chemistry), determining the diffusivity values and explaining the effect surface finish has on the transport. The results of which will allow the viability of the IO model to be assessed in terms of reactive elements availability and advice given on the sample preparation which should be used for future PWSCC experiments.

The materials used for this project are WF675 and HT93510. The WF675 is in three conditions, as-received, 15% cold worked by tension and 19% cold rolled, the HT93510 is solution annealed. The majority of experiments conducted are based on low pressure hydrogenated steam exposures. It should be noted that the PWSCC properties of as-received and 15%CW WF675 has been extensively studied in previous projects, but the work primarily focused on the role of microstructure on PWSCC, not the oxidation of the alloy [11,12]. Scenini et al. [13,14] used low pressure hydrogenated steam to oxidise Alloy 600 (solution annealed HT93510) and Alloy 690. High pressure hydrogenated steam was used for oxidation and PWSCC tests The surface oxides produced were characterised and high pressure hydrogenated steam PWSCC tests indicated that the surface finish may be significant for PWSCC.

Part I

Literature Review

CHAPTER

ONE

MATERIAL

The material examined in this study is Alloy 600 (UNS N06600), trademarked by the Special Metals Corporation as Inconel® 600. Alloy 600 is a nickel-iron-chromium alloy that was developed in 1932 by O.B.J. Fraser [15]. The alloy is desirable as it is a moderate strength, workable alloy with excellent mechanical properties and corrosion resistance [4, 16]. In addition the alloy is weldable by conventional fusion welding and friction stir welding [17]. The alloy can be operated at temperatures ranging from cryogenic to in excess of 1000°C [18].

The alloy's versatility is reflected in the wide range of applications it is used for, these include [4, 19]:

- Thermocouple sheathing for aggressive atmospheres.
- Components for heat treatment furnaces with a carburising or nitriding atmosphere.
- Exhaust liners and turbine seals for jet engines.
- Processing equipment used in the production of chlorinated and fluorinated hydrocarbons.

In addition to these uses, the alloy was also the material of choice for specific uses in pressurised water reactors (PWR). The alloy was first used due to its excellent resistance to chloride induced cracking, relative to stainless steels [20]. The alloy also benefits from a thermal expansion coefficient similar to that of the low alloy steels (16MND5) used in the fabrication of the reactor pressurizer and pressure vessels [21]. These features, combined with its good generic corrosion properties and a low corrosion product release rate, have resulted in its extensive use in PWRs. The main components of the primary circuit in a PWR that are constructed of Alloy 600 are shown in Figure 1.1. Alloys 82 and 182 labelled in Figure 1.1 are the weld metals used for Alloy 600.

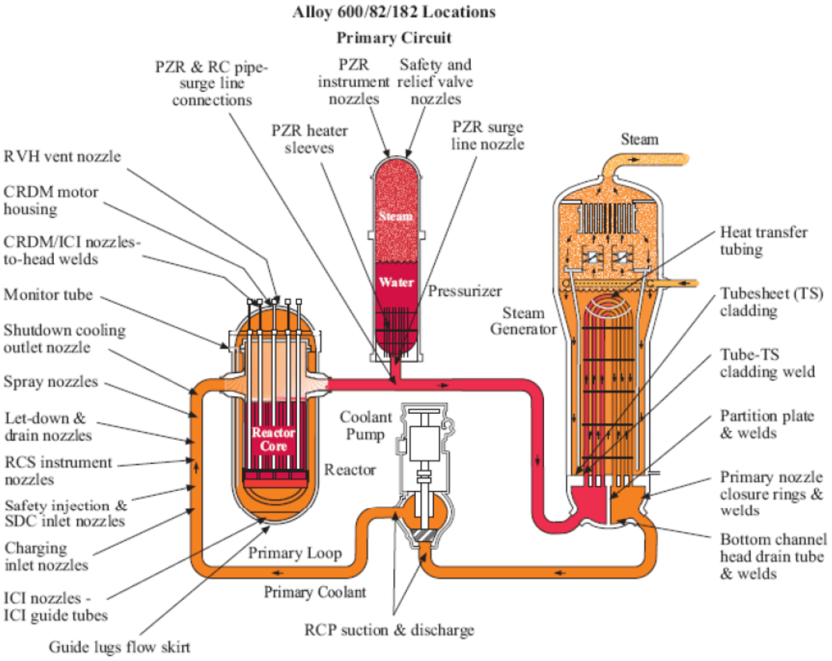
Alloy 600/82/182 Locations
Primary Circuit
PZR & RC pipe-surge line connections
PZR instrument nozzles
Safety and relief valve nozzles
PZR heater sleeves
PZR surge line nozzle
Steam
RVH vent nozzle
CRDM motor housing
CRDM/ICI nozzles-to-head welds
Monitor tube
Shutdown cooling outlet nozzle
Spray nozzles
Let-down & drain nozzles
RCS instrument nozzles
Safety injection & SDC inlet nozzles
Charging inlet nozzles
ICI nozzles - ICI guide tubes
Guide lugs flow skirt
Steam
Water
Pressurizer
Steam Generator
Reactor Core
Coolant Pump
Reactor
Primary Loop
Primary Coolant
RCP suction & discharge
Heat transfer tubing
Tubesheet (TS) cladding
Tube-TS cladding weld
Partition plate & welds
Primary nozzle closure rings & welds
Bottom channel head drain tube & welds

Figure 1.1 – Locations of Alloy 600 and its associated weld metals in the PWR's primary circuit [11].

Despite the extensive use of Alloy 600, it has been shown to be susceptible to primary water stress corrosion cracking (PWSCC), as a result Alloy 690 (Inconel® 690) was developed by H.R. Copson and G. Economy [15]. Alloy 690 has a higher chromium content and low carbon solubility, this is believed to give it an increased resistance to PWSCC [22]. The increased chromium content does however increase the cost of the alloy. Alloys 52, 52M and 152 are the weld metals used for Alloy 690. However, when the alloy was first developed, alloys 82 and 182 were used as the ASM code did not specify a specific weld metal for the alloy [23].

1.1 Composition

The major components of Alloy 600 and 690, with respect to weight are Ni-15%Cr-10%Fe and Ni-30%Cr-9%Fe respectively. In addition to the base elements, there are a number of minor alloying elements present, the full specification for Alloy 600 and 690 are shown in Table 1.1 (Note: different countries have different regulations, the given table is intended as an overview).

The high nickel content of the alloys results in generally good corrosion properties when they are exposed to alkaline or reducing environments. In addition, it provides the alloy with a resistance to chloride-ion induced stress corrosion cracking [24]. The chromium content provides solid solution strengthening and improves the alloys corrosion properties in oxidizing environments by the formation of a passive oxide on the surface [5]. Iron in the matrix acts as a solid solution strengthener. The iron also acts to reduce the formation of Ni_2Cr intermetallics, a hard brittle phase which could compromise the integrity of the alloy. This was initially raised as a concern for Alloy 690 as its Ni-Cr ratio is close to the 2:1 ratio of the intermetallic phase [13].

Table 1.1 – Chemical composition of Alloy 600 and Alloy 690 (wt. %). Al, Ti and P can also be specified, but is consumer dependant [4, 25, 26].

Element	**Alloy 600** (wt. %)	**Alloy 690** (wt. %)
Nickel	72.0 min.	58.0 min.
Chromium	14.0 – 17.0	27.0-31.0
Iron	6.00 – 10.00	7.0-11.0
Carbon	0.15 max.	0.05 max.
Manganese	1.00 max.	0.50 max.
Sulphur	0.015 max.	0.015 max.
Silicon	0.50 max.	0.50 max.
Copper	0.50 max.	0.50 max.
Cobalt	0.10 max.	0.10 max.

In addition to the major alloying elements, there are a number of minor alloying elements, the most significant of which is carbon. Both alloys have a low carbon solubility (equations (1.1) and (1.2)), resulting in carbide precipitation. The carbide location and forms are dependent upon the post processing of the material. Typically in Alloy 690, the carbides are almost all of the form $M_{23}C_6$ (where M dictates a metal, this is >90% chromium) and are predominantly intergranular (when mill annealed above 1050°C). Alloy 600 has both intergranular and intragranular carbides and they can be in the form of $M_{23}C_6$ or M_7C_3 [27, 28]. Some nuclear specifications can also include a minimum carbon content, in addition to a maximum; this is to ensure the desired carbide distribution is attainable.

In the manufacturing process, manganese, silicon, aluminium and titanium are added for the deoxidation, desulfurisation and decarburisation of the alloys. These elements affect the recovery, recrystallization, grain growth and deformation processes of the alloys in what is generally considered a beneficial way [13].

Boron, cobalt, copper, molybdenum, niobium, nitrogen, phosphorus and sulphur are present in the alloys as impurities with no specified application, as such the quantity should be kept to a minimum to reduce possibility of them affecting the material [5, 13]. Boron has been used to increase the workability, but it is recommended that its use is kept to a minimum as it affects the carbide precipitation kinetics [29]. The ASM standard states that the nickel content of Alloy 600 is the sum of the nickel and cobalt present, however, for nuclear applications the cobalt content is limited (Table 1.1) as it can form ^{60}Co when irradiated by neutrons [30]. The presence of molybdenum and niobium has been seen to have a detrimental effect on the corrosion properties of the alloys when in concentrations up to a few percent [5].

1.2 Microstructure

Alloy 600 and 690 are pure austenitic alloys (γ phase), with the nickel atoms forming the base of a face centred cubic (FCC) structure. Solid solution strengthening occurs in the alloys as a result of the chromium and iron atoms substituting the nickel. The γ phase is stable in both alloys up to the liquidus, as illustrated in Figure 1.2. Titanium, aluminium, silicon and niobium act as α' stabilises. However, to the best of the authors knowledge, there have been no reported cases of the α' phase being observed in both Alloy 600 and 690, even with the presence of α' stabilising alloying elements.

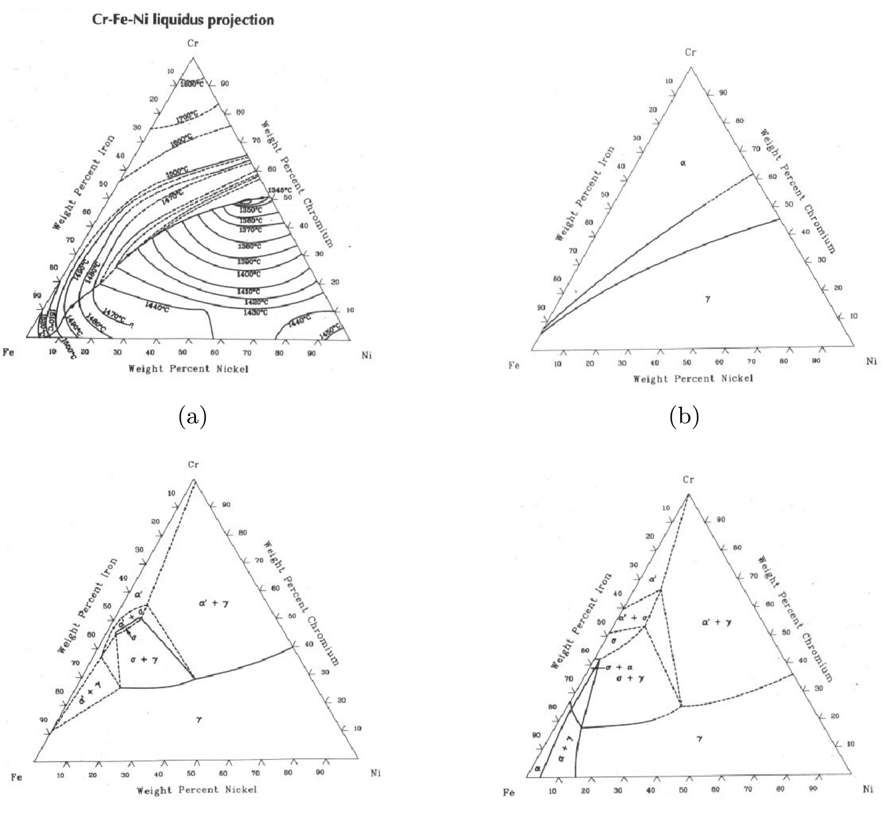

(a)

(b)

(c)

(d)

Figure 1.2 – (a) Projected Ni-Fe-Cr ternary liquidus diagram. (b) Ni-Fe-Cr ternary phase diagram at 1300°C. (c) Ni-Fe-Cr ternary phase diagram at 900°C. (d) Ni-Fe-Cr ternary phase diagram at 650°C [31].

Carbides, titanium nitrides and carbon nitrides are all present in the microstructure. The carbides form readily as the carbon solubility of the alloys is low, equations (1.1) and (1.2) show the carbon solubility as a function of temperature. The M_7C_3 carbides form predominantly at higher temperatures and have a hexagonal type unit cell comprising of 80 atoms, $M_{23}C_6$ have a cubic unit cell comprising of 116 atoms (Note: other authors have stated that the $M_{23}C_6$ carbides are crystalline deposits while M_7C_3 carbides are amorphous deposits [32]). The precipitates do not act to strengthen the alloy, though the alloys can be work hardened.

$$\log(\%C) = 3.14 - \frac{6397}{T} \qquad Alloy\ 690 \tag{1.1}$$

$$\log(\%C) = 2.90 - \frac{5834}{T} \qquad Alloy\ 600 \tag{1.2}$$

T is the absolute temperature and %C is the carbon solubility limit.

The location of the carbides can be used to categories the microstructure into three types (illustrated in Figure 1.3):

- Type I: The carbides are purely intergranular (this can be sub-divided into continuous or discontinuous depending on the carbide density).
- Type II: The carbides are intragranular, but located on the previous grain boundaries (i.e. boundaries prior to recrystallisation). This is referred to as a ghost microstructure.
- Type III: The carbides are uniformly precipitated.

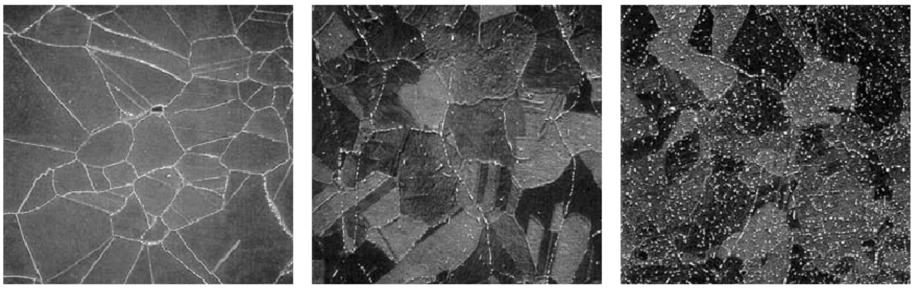

(a) Type I (b) Type II (c) Type III

Figure 1.3 – Examples of the different carbide distributions [11].

1.3 Production

The process used for producing both alloys are similar. For the formation of a component, a billet is commonly used as a starting point, the thermo-mechanical process (TMP) used in production of a billet is shown in Figure 1.4. The melting processes are carried out under vacuum to reduce contamination.

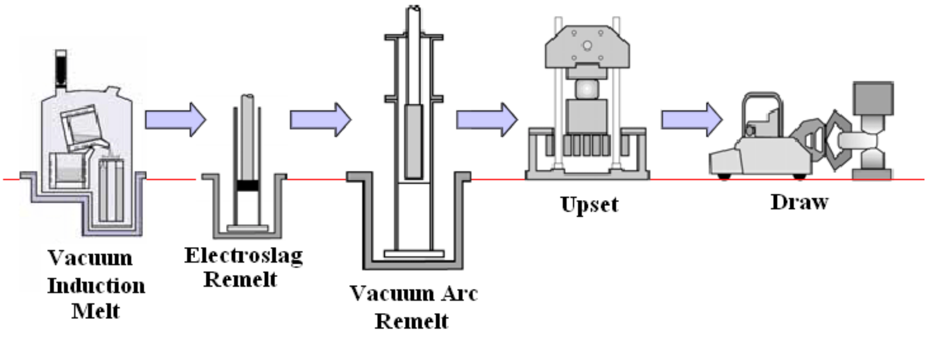

Figure 1.4 – Typical Thermo-Mechanical-Process used for the production of Ni-Fe billets [33].

From the billets, the main production methods can be generalised as forging or rolling processes. The production process can significantly cold work the material. The amount of energy stored in the materials depends upon a number of factors:

- Amount of deformation,
- Temperature of deformation, relative to its melting point,
- Initial grain size,
- Stacking fault energy, linked to the metal purity and composition.

The stored energy work hardens the material, but can also be used to induce recrystallisation in post processing of the material.

1.3.1 Annealing

The produced components are mill annealed. The purpose of the mill annealing is twofold. Firstly to fully recrystallise the microstructure. Secondly, the annealing dissolves the carbides, so that the carbon forms an interstitial solid solution. The temperature required to dissolve the carbides is greater than the temperature required to recrystallise the microstructure.

Carbides can precipitate during the cooling stage of the annealing, these carbides are typically of the form M_7C_3 and their distribution and size depend on the cooling rate. The recrystallisation converts the cold worked material into a strain free microstructure and can refine the grain size. The end result of annealing is a strain free material which is supersaturated in carbon. The annealing process can be modified to alter the resulting microstructure, i.e. it may be desirable to retain some of the work hardening to increase the material yield point. The annealing process is carried out between 940 - 1040 °C [5].

1.3.2 Thermal Treatments

After the material has been mill annealed, it can be thermally treated. The purpose of this treatment is to obtain the desired carbide distribution and reduce chromium depletion at the grain boundaries. The chromium concentration can be reduced at grain boundaries as the carbide formation uses the chromium from the surrounding area (referred to as sensitisation), holding the sample at an elevated temperature allows the chromium to diffuse back reducing the sensitisation.

In Alloy 690, the desired carbide distribution is a continuous type I microstructure. This is achieved by heating the sample to the range of 700 - 730 °C (the temperature required to activate the formation of carbides) and holding it there 5 h to 15 h. The temperature required for carbide precipitation is reduced in cold worked samples as the increased dislocation density increases the carbon mobility, hence reducing the activation energy for the formation of carbides [34]. The length of the treatment is to reduce the sensitisation of the microstructure. Figure 1.5 shows a typical heat treatment for the alloys superimposed on Alloy 690's time temperature precipitation (TTP) curve for carbides. The carbides formed from this heat treatment are $M_{23}C_6$, M_7C_3 can precipitate during the cooling from the mill anneal.

Alloy 600 has a TTP curve similar to Alloy 690, except that intragranular carbides form more readily, hence all three types of carbide distribution can be created by altering the thermal treatments. M_7C_3 can also be found in Alloy 600 after the thermal treatments.

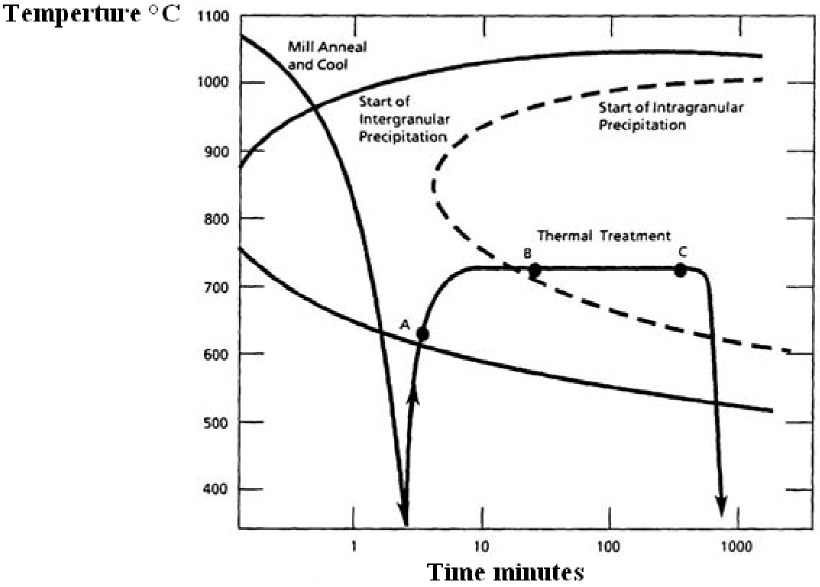

Figure 1.5 – Carbide precipitation curve for Alloy 690 with a typical thermal treatment overlayed [13].

CHAPTER

TWO

OXIDATION

Oxidation is a chemical reaction in which the oxidation state of the reactant increases, most commonly associated with the addition of oxygen but not necessarily the case. For oxidation to occur, there must be sufficient oxidising reagent to produce a thermodynamically stable oxide (a reduction of the Gibb's free energy occurs in the system by the formation of the oxide). The Gibb's free energy of formation is a function of the metal and of the valency of the oxide formed (i.e Chromium can form oxides with valancies of 2 to 6, including the possibility of a mixed valancy oxide).

The rate at which oxidation occurs is defined by a rate constant (k). The rate is dependent upon a number of factors; the most significant factor to affect the oxidation rate is the rate limiting step.

$$k_{l,p,n}t = \left(\frac{\Delta m}{A}\right)^{1,2,n} \tag{2.1}$$

where Δm is the weight change in the sample, $1 < n < 3$ and A is the total area being oxidised. The exponent is dependent upon the oxidation system in question, a linear relationship is the result of oxidation being limited by the chemical reaction, a parabolic (n=2) relation is an indication of a diffusion controlled process [35]. In the cases of a thin film formation, the relationship may be logarithmic. Wagner's theory includes a relationship between the diffusivity of the anions and cations to the observed oxidation rate [36]. The relationship derived from Wagner is

$$k_c = \frac{1}{2}\int_{PO_2(metal/oxide)}^{PO_2(oxide/gas)} \left[D_{anion} + \left(\frac{b}{a}\right) D_{cation}\right] d\ln PO_2 \tag{2.2}$$

where a and b are such that M_aO_b is the formed oxide, D_{anion} is the diffusivity of the anion, D_{cation} is the diffusivity of the cation and the limits of integration are the partial pressure of oxygen at the oxide/gas interface and the partial pressure of oxygen at the metal/oxide interface required for oxide formation.

2.1 PWR Oxidation

The PWR environment is pure water with hydrogen, lithium hydroxide and boric acid additives. The systems can experience temperatures of operation up to 360 °C. The oxidation is of significant interest due to the issues of PWSCC and release of nickel into the system which can become active when irradiated.

2.1.1 Oxide Structure

The oxide formed in simulated PWR environments on Alloy 600 has been investigated by a number of authors [37–41]. The oxide is a dual layer oxide, as illustrated by Figure 2.1. A thin layer (1-10 nm) of Cr_2O_3 oxide forms the inner layer of the oxide [37]. The outer layer is formed from a mixture of large and small octahedral crystals which create a non-protective and iron rich oxide [42]. The larger crystals are reported to be $NiFe_2O_4$ whist the smaller are of the form of a NiFeCr spinel, a number of theories exist for the formation of these crystals [42–44].

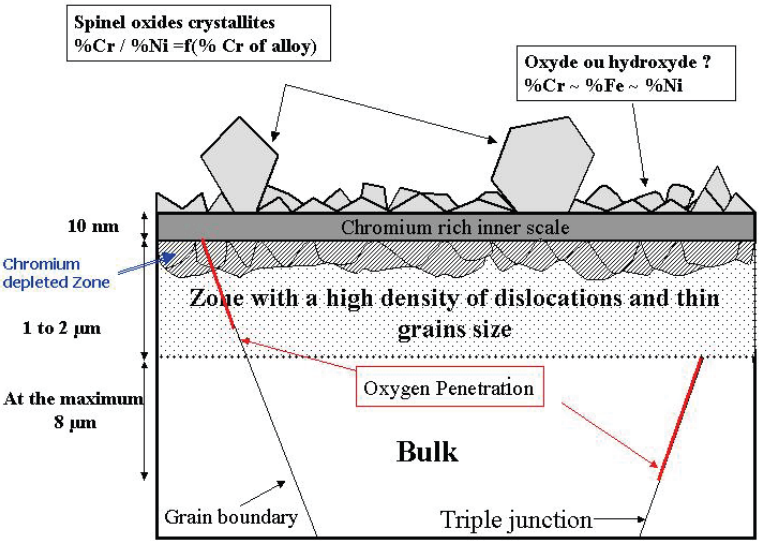
Spinel oxides crystallites
%Cr / %Ni =f(% Cr of alloy)
Oxyde ou hydroxyde ?
%Cr ~ %Fe ~ %Ni
10 nm
Chromium rich inner scale
Chromium depleted Zone
Zone with a high density of dislocations and thin grains size
1 to 2 µm
Oxygen Penetration
At the maximum 8 µm
Bulk
Grain boundary
Triple junction

Figure 2.1 – Schematic representation of the oxide formed on Alloy 600 under PWR conditions [38].

Some authors [38] have suggested that there is a "affected zone" below the oxide similar to that observed in Alloy 690 oxidation [45]. The affected zone takes the form of a fine sub grained region similar in appearance to a deformed layer. Given that this work was carried out on Alloy 600 with a P1200 grit surface, it is likely that the "affected zone" is a deformed layer, not a result of oxidation.

The early stages of the oxide growth have been investigated by XPS [43,46] whilst electron optic techniques were used on the latter stages of growth [37]. The process by which the oxide forms is believed to be as follows:

- Small particles of Cr_2O_3 form and selective dissolution of nickel occurs.
- A thin ($\approx 1nm$) oxide film of Cr_2O_3 forms by the coalescence of the oxide with an outer layer of $Cr(OH)_3$ preventing additional growth.
- Transport of Cr allows the $Cr(OH)_3$ to be converted to more stable Cr_2O_3.
- Nickel transport through the oxide produces a $Ni(OH)_2$ outer layer and releases nickel ions into the solution. It is believed that the vacancies generated by this process are accelerating the transport of chromium in the alloy to the metal/oxide interface and thus allow the oxide to grow.
- Spinel oxides form on the Cr_2O_3 outer oxide.
- Porous nickel ferrite forms on the outer layer when the solution is near saturation, possibly by redeposition.

The early stages of this process are illustrated by Figure 2.2.

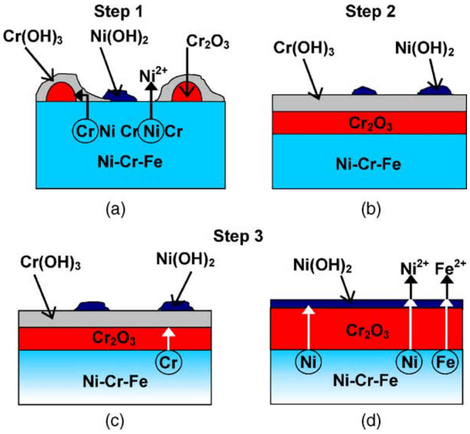

Figure 2.2 – Early stages of oxide formation on Alloy 600 [46].

Intergranular penetrations of chromium rich oxides in Alloy 600 were first reported by Newman and subsequently in other works [47]. The oxide has been reported to be Cr_2O_3 [48]. Short circuit diffusion has been implied by introducing O^{18} tracers, these indicated an increased oxygen diffusivity in the intergranular penetrations [49, 50].

2.1.2 Chromium Effect

The effect of chromium content on the oxidation of nickel based alloys has been directly investigated by Delabrouille [38, 39] and indirectly by comparison of similar alloys such as Alloy 690. The oxide formed on the higher chromium Alloy 690 has the same structure, but due to the increased chromium the produced crystals are reported to be ≈ 0.5 the size as that observed on Alloy 600.

Legras et al. investigated a range of nickel alloys containing between 5% and 30% chromium and 10% iron [51]. The oxide associated with Alloy 600 and 690 formed when the chromium content exceeded 10% on a P1200 grit surface, however 15% was required on a 1 µm surface. The crystal size decreased and the chromium content of the crystals increased with an increasing chromium content of the alloys. The chromium oxide film remained a constant thickness. The alloys with less than 10% chromium did not form a passive layer and had filament based oxide [51].

2.1.3 Environment

The effect of dissolved hydrogen (oxygen content) on the oxide formation in simulated PWR conditions has been investigated by Terachi et al. [44] at a temperature of 320°C. This work showed that the oxide formed changed as a result of the changing environment, the results of which are summarised in Figure 2.3. At low hydrogen content, NiO is stable and able to form a continuous oxide layer, as it becomes less stable it forms a needle like oxide. An increased hydrogen content beyond the Ni/NiO transition point yielded a oxide consistent with that obtained in simulated PWR conditions, it was indicated that an increasing hydrogen content produced a thicker spinel layer [44]. A layer rich in metallic nickel was reported below the chromium oxide.

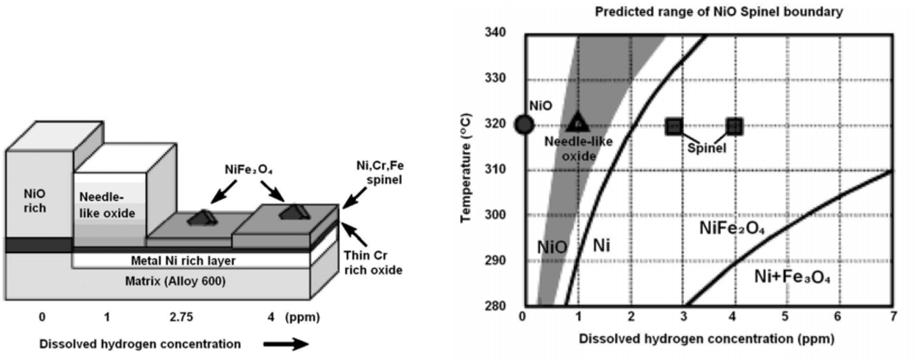

(a) (b)

Figure 2.3 – Oxide structure of Alloy 600 as a function of the dissolved hydrogen at 320°C [44].

Nickel oxide is a p-type semiconductor with a band gap energy range of 3.6-4.0eV [52]. However, work by Loucif et al. showed that the oxide formed on both Alloy 600 and 690 in low hydrogen environments is in the form of a n-type semiconductor; at high hydrogen pressures, the oxide was still a n-type semiconductor for low energy but acted as an insulator for higher energies [53]. The formation of an n-type nickel oxide has been shown to be a result of a change in character of the point defects present in the oxide layer, depletion in oxygen produced by low partial pressures results in oxygen vacancies and metallic nickel in the oxide [52, 54]. Work by Gupta et al. has indicated that a n-type nickel oxide can be generated by ultraviolet-laser irradiation and indicated that the formed n-type oxide could be converted to p-type by thermal annealing (300-700°C) in oxygen [52]. Lithium doping of the p-type oxide has been shown to increase the conductivity as the Li^+ ions substitute the Ni^{2+} thus to maintain charge neutrality O^- holes are formed [55].

2.1.4 Surface Finish

The surface finish has a marked effect on the oxidation of the alloy. It was noted by Legras et al. that the chromium required to produce a passive layer varied as a result of surface finish, it was suggested that a more deformed surface had a greater chromium mobility and thus more readily formed a passive oxide [51]. A similar effect has been noted in internal oxidation studies. Rapp [56] noted that the internal oxidation was suppressed in preference of an external oxide as a result of a scratch at the surface of a Ag-In alloy, this was attributed to the enhanced diffusion of the indium allowing it to form a passive layer. Loucif et al. reported that the semiconductor properties of the formed oxide did not change as a result of the surface preparation [53].

2.2 Internal Oxidation

Internal oxidation (IO) is defined as an oxidant diffusing into an alloy and reacting with the less noble components to form discrete particles [57]. Wagner's model of internal oxidation assumed that the process is controlled by the inward diffusion of the oxidant into the alloy. It follows that the thickness of the IO zone (ξ) has a parabolic relationship with the exposure time (t). The relationship between time and IO thickness is given by Wagner's equation, equation 2.3 [58, 59] for a binary alloy.

$$\xi = \left(\frac{2N_O^s D_O t}{v N_B^0} \right)^{\frac{1}{2}} \tag{2.3}$$

Where N_O^s is the solubility of oxygen, D_O the diffusivity of oxygen, t is the time, v is the stoichiometric coefficient of oxygen in the reaction to form the oxide and N_B^0 is the concentration of the less noble solute. In the derivation of this, a number of assumptions are made, the particles of oxide formed are spherical, the particles do not affect the diffusion rate of the oxidant, no external oxide formed and there is no enrichment of the reactive solute as a result of the oxidation [57, 58, 60].

The transition from internal to external oxide is observed to occur when a critical concentration of the reactive solute is reached, tests conducted in Rhines packs have reported this critical value to be 9 at.%In in Ag-In, 8.3 at.%Al in Ni-Al and 10 at.%Cr in Ni-Cr [61, 62]. The cause of this transition was proposed by Wagner to be a result of the formed oxides physically blocking the inward diffusion of oxygen, this would occur when the volume fraction of the oxide reached a critical value (g^*) relative to the volume of the matrix [58]. Rapp [56] reported the critical value to be 0.3 in Ag-In, this value can be seen as comparable to the value expected in the Ni-Cr system as the volume changes associated with the formation of an oxide in both systems are comparable. The blocking effect of the oxide can be countered by an increased inward diffusion as a result of the incoherent oxide/matrix interface. Wagner derived the critical oxygen solubility required for IO to occur as

$$N_O^s = \frac{2v(N_B^O)^2 V_{OX} D_B}{\pi g^* V D_O} \tag{2.4}$$

where D_B is the diffusivity of the reactant in the alloy, V_{OX} is the molar volume of the formed oxide and V is the molar volume of the alloy. Subsequent work by Onishi et al. investigated the oxide formation in Fe-Si alloys relative to critical oxygen solubility at a temperature of 850°C [63]. The results showed that the calculated critical oxygen solubility was in good agreement with the experimental results. Preferential grain boundary oxidation could however occur below the critical oxygen solubility in addition to the formation of an external oxide (Figure 2.4).

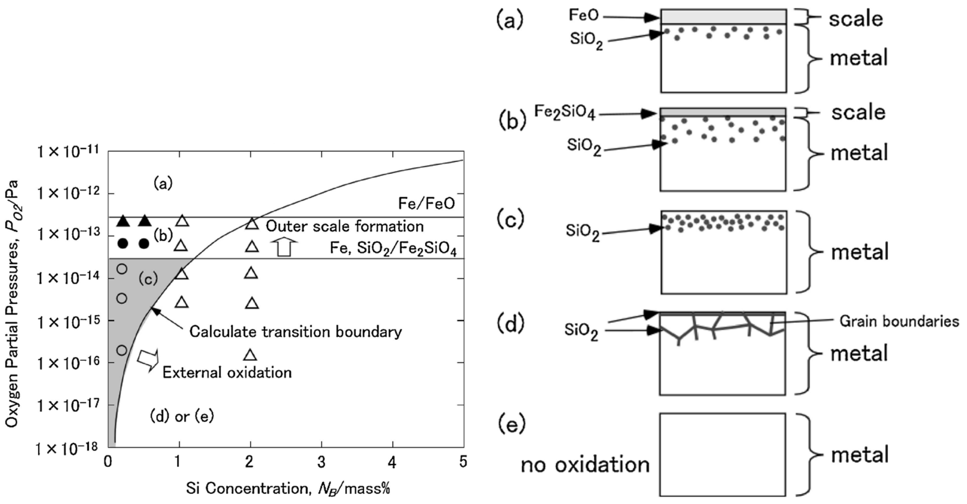

(a) (b)

Figure 2.4 – Internal oxidation morphologies as a function of oxygen partial pressure and reactive solute concentration in Fe-Si binary system [63].

Wood et al. examined the IO morphology on grain boundaries in Ni-Cr and indicated that at lower temperatures or greater Cr content, grain boundary oxidation was more significant [64]. This work summarised four morphologies which could form in the region of the grain boundary (Figure 2.5):

- Type 1: The grain boundary oxide consists of discontinuous particles and is of equal depth to the internally oxidised zone. The particles of oxide appear to increase in size with increasing penetration depth.

- Type 2: As type 1, but the particles of oxides observed on the grain boundary exceed the depth of the internally oxidised zone.
- Type 3: The near surface intergranular oxide is continuous, laterally formed branches deviating from the grain boundary are observed. Beneath the continuous oxide, particles of oxide form on the grain boundary which continue deep beyond the internally oxidised zone.
- Type 4: A near continuous layer of Cr_2O_3 forms at the surface of the alloy in the region of the grain boundary. Under the semi-continuous surface oxide, relatively large particles of internal oxide form, both on the grain boundary and in the adjacent region.

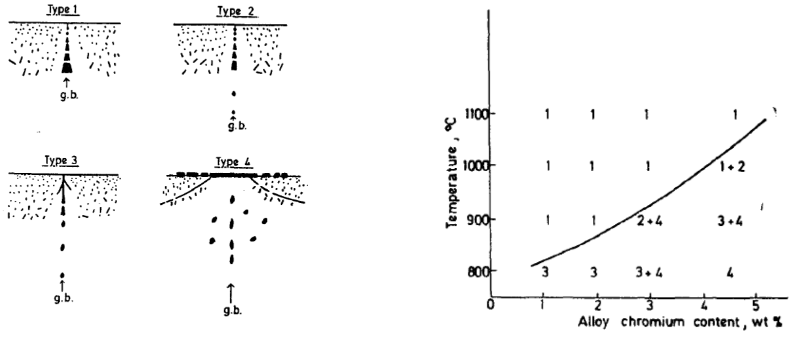

(a) (b)

Figure 2.5 – Types of IO observed in Ni-Cr alloys after high temperature (900-1100°C) oxidation in Ni/NiO powder Rhines packs [64].

The formation of an oxide can be seen to generate a significant stress in the material as a result of the volume changes. Wood et al. [64] calculated that the volume change created by the formation of an oxide in Ni-Cr was

$$\frac{\Delta V}{V_{alloy}} = 1.17 N_{Cr}^{0} \tag{2.5}$$

The result of this expansion is a compressive stress within the alloy [65, 66]. At high temperatures in Ni-Al, grain boundary sliding has been observed to accommodate the generated stress, this process is summarised in Figure 2.6 [67]. It was noted that the morphology of the IO particles changed as the penetrations increased. In addition to the sliding, regions free from oxides, near the grain boundaries, appeared extruded out from the surface; at lower temperature grain boundary oxidation was more significant [67]. The work noted that the effect of stress generation is more significant at oxygen partial pressures less than that required to oxidise the nickel as the oxidation process would lead to an injection of vacancies when forming the NiO scale and thus accommodate the volume change [67].

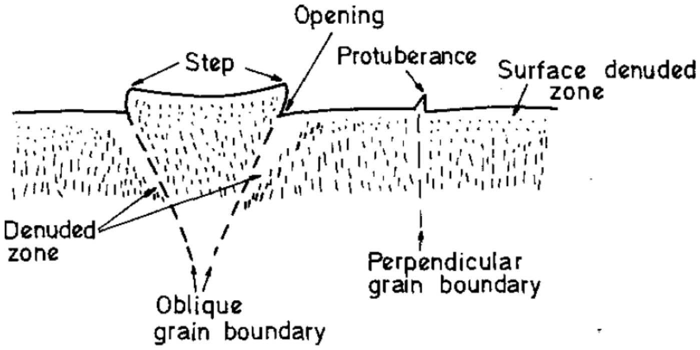

Figure 2.6 – Mechanism of grain boundary sliding observed in high temperature Ni-Al as a result of volume expansion caused by IO [67].

In Ag-In nodules of the less reactive silver were observed to form at the surface as a result of the stress [68]. It was concluded that the stress relief observed to form the nodules of silver was the result of a pipe diffusion, as the Nabarro-Herring creep mechanism proposed by Mackret [69] was unable to account for the rate of formation for the nodules. Extrusion of the Ag nodules as a stress relief mechanism was considered, but rejected as it would be expected that small particles of internal oxides would be trapped in the nodules as they were extruded. Trapped particles of oxide were not observed in the nodules [68].

In Ni-Cr and Ni-Al at low oxygen partial pressures, nickel was observed to form at the surface. In Ni-Al the nickel formed a layer at the surface whilst in the Ni-Cr alloy it had formed nodules. The different formations were attributed to the different IO structures permitting variable levels of plastic deformation [60]. The nickel nodules were also observed in Ni-Al when internally nitridized [57].

During work investigating the transition point from internal to external oxidation, Rapp noted that effect of surface finish had a marked effect. Electrochemically etched samples were used, however in the region of damage (a scratch), it was noted that internal oxidation which occurred on the alloy (silver-6.8%indium) was replaced by external oxidation; this was attributed to an increased diffusivity of the indium [56].

2.3 Considerations for Steam Oxidation

The possibility of using low pressure steam oxidation is being looked at in this thesis, steam has been used by a number of authors to investigate SCC, with both high pressure [70–73] and low pressure [13, 50, 74–77] systems. The work carried out in steam relative to PWSCC has focused on the cracking tests and not the produced oxide. The use of steam opposed to high pressure water leads to a number of considerations which are different to that of water.

2.3.1 Oxygen Partial Pressure

PWR's primary circuit operating conditions can be defined by the operating potential. However, steam as a non-conductive medium means the potential is viewed as an abstract concept as the value cannot be physically measured, only calculated. Alternatively, the oxygen partial pressure is used to define the environment, the PWR environment operates at an oxygen partial pressure in the region of the Ni/NiO transition point [50, 70, 78]. The partial pressure of oxygen can be controlled by the addition of hydrogen, as defined by equations 2.6 and 2.7 [79]. The addition is achieved via mixing the two components in known quantities or passing hydrogen through a water bath at a set temperature [70, 74]. The method of hydrogen uptake is of questionable relevance as calculations indicate that there is insufficient uptake of water to produce a system which is oxidising relative to nickel as reported by Capell [70, 71]:

$$2H_2O \rightleftharpoons 2H_2 + O_2 \tag{2.6}$$

$$pO_2 = \left(\frac{pH_2O}{pH_2}\right)^2 exp\left(\frac{-\Delta G^0}{RT}\right) \tag{2.7}$$

2.3.2 Volatile Species

The cation solubility in steam is near zero, as such the iron rich spinel layer which is believed to be formed by a re-deposition mechanism will not be expected in the system [13]. A large concern in the use of steam is the production of volatile species which can evaporate and thus change the oxidation process. The volatilisation reactions relevant to PWSCC testing are [79]:

$$2Cr_2O_3 + 4H_2O^{(g)} + O_2^{(g)} \rightleftharpoons 4CrO_2(OH)_2^{(g)} \tag{2.8}$$

$$SiO_2 + 2H_2O^{(g)} \rightleftharpoons Si(OH)_4^{(g)} \tag{2.9}$$

$$SiO_2 + H_2O^{(g)} \rightleftharpoons Si(OH)_2^{(g)} \tag{2.10}$$

$$Al_2O_3 + 3H_2O^{(g)} \rightleftharpoons 2Al(OH)_3^{(g)} \tag{2.11}$$

Chromium oxide evaporation has had significant investigations in the literature, the results have shown that the process in equation 2.8 is more prevalent in high

pO_2 environments and unlikely to occur at temperatures less than 700 °C [80]. It has however been suggested that the volatilisation of chromium may be more significant in high pressure steam [79, 80].

The volatility of iron ($Fe(OH)_2$) has been noted to be significant in low pO_2 environments over the temperature range 450-600°C [79, 81]. However, it is noted that the provided explanation for this behaviour was on the CO present in a water/CO_2 environment used to deoxygenate the system and not the low oxygen partial pressure.

The occurrence of a volatile silicon oxide is of relevance as quartz reaction chambers are often used for steam oxidation; as such volatilisation could act to contaminate a test. The volatility of silicon is seen to increase at lower oxygen partial pressure (Figure 2.7); however, it's volatility only becomes significant above 800°C or in high pressure systems [79, 82].

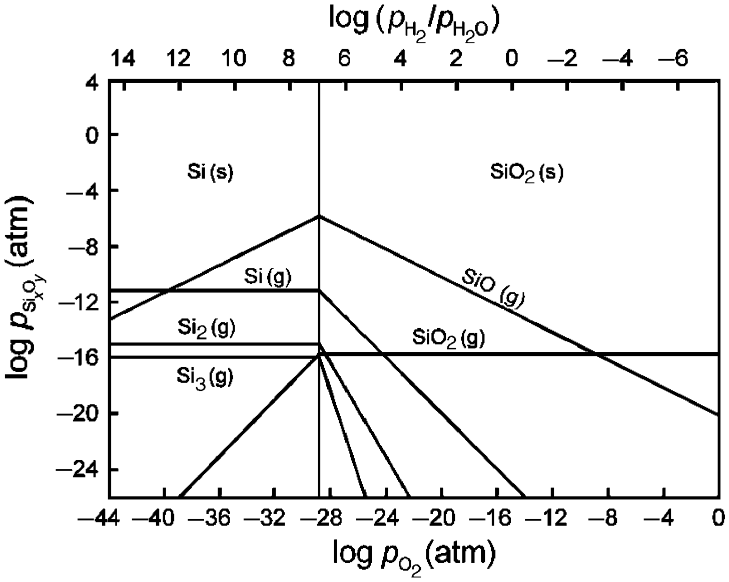

Figure 2.7 – Partial pressure of SiO at 1000°C as a function of the oxygen partial pressure [82].

2.3.3 Pressure

An increase in the pressure of steam in a system is generally considered to increase the oxidation rate; Montgomery et al proposed that an increased steam pressure would reduce the integrity of the formed oxide scale [83]. Otoguro et al showed that on an austenitic steel. The oxidation rate increased with pressure; this was attributed to the voids and cavities observed in the oxide having a destabilising effect [72]. The generation of these cavities and voids has been suggested to occur due to a number of mechanisms [72]:

- A differential metallic ion diffusion rate between the inner and outer oxide scale.
- The grain boundaries in the oxide being unstable at higher pressures.
- Local variations in the oxide growth rate producing a less compact structure

However, tests carried out on P92 (a martensitic steel) have indicated that the steam pressure has little to no effect on the oxidation process [84]. Figure 2.8 shows the oxidation rate of different steels as a function of pressure, it implies that there is no general relationship between pressure and oxidation rate.

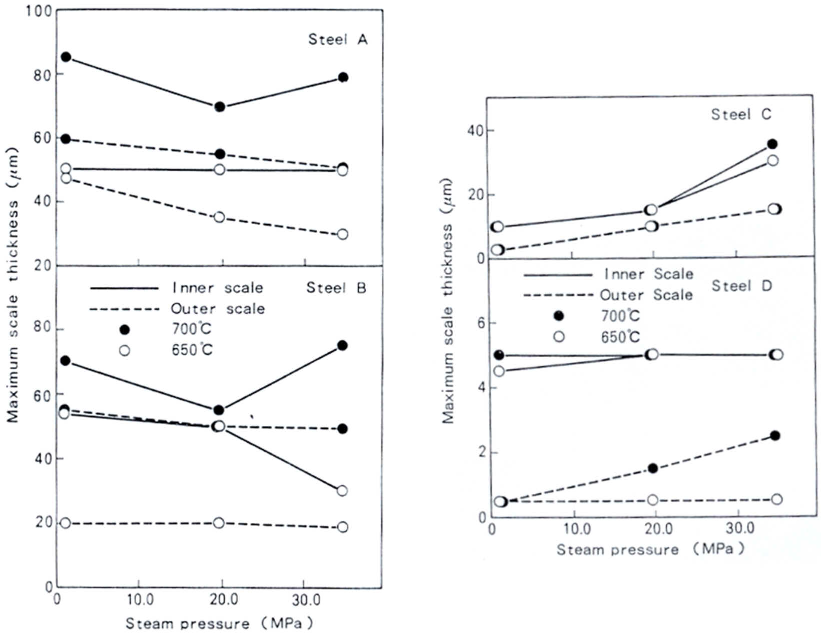

(a)

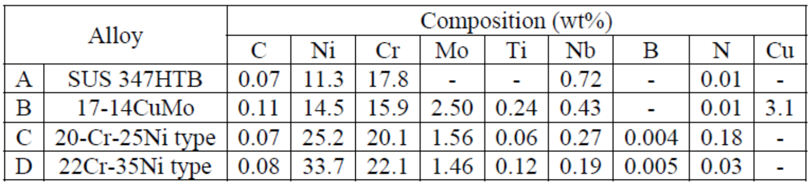

Alloy		Composition (wt%)								
		C	Ni	Cr	Mo	Ti	Nb	B	N	Cu
A	SUS 347HTB	0.07	11.3	17.8	-	-	0.72	-	0.01	-
B	17-14CuMo	0.11	14.5	15.9	2.50	0.24	0.43	-	0.01	3.1
C	20-Cr-25Ni type	0.07	25.2	20.1	1.56	0.06	0.27	0.004	0.18	-
D	22Cr-35Ni type	0.08	33.7	22.1	1.46	0.12	0.19	0.005	0.03	-

(b)

Figure 2.8 – (a) Oxidation rate of steel at 650°C and 700°C as a function of steam pressure showing both increasing and decreasing trends in oxidation rates dependant on the material composition (b) chemical compositions of the materials used in (a) [72].

CHAPTER

THREE

STRESS CORROSION CRACKING

Stress corrosion cracking (SCC) is cracking of a material as a result of a corrosion process coupled with a stress on the material. The process of SCC has three requirements, as shown in Figure 3.1. Removal of any one of these perquisites will inhibit the process of SCC, though other problems may arise. The stress required for SCC can be a result of loading, residual stress or stress generated by the corrosion. The material is one which is susceptible to SCC; the environment is one which will induce SCC in the specified material.

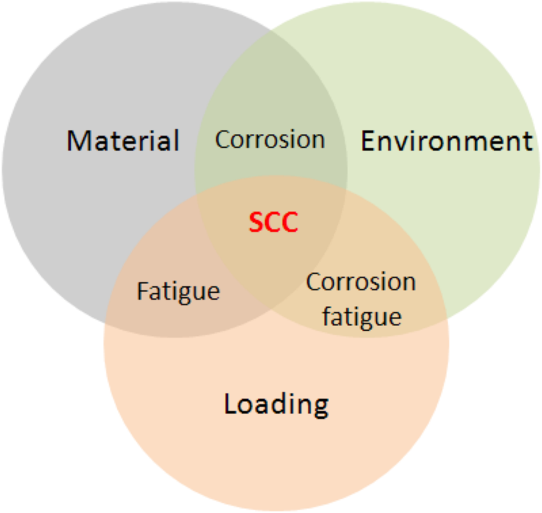

Figure 3.1 – Influencing factors for SCC.

The earliest known example of SCC is brass in ammonia, referred to as season cracking. The first occurrences of season cracking were in the 19th century when brass bolts in coffee pots left on during the night in the vicinity of ammonia (believed to be from babies nappies) failed [85]. This type of SCC became a significant problem for the British army in India as brass rifle cartridges failed, resulting in a misfire. The term season cracking is believed to originate from the fact that the rifle cartridges would fail more in the rainy seasons.

Probably the most well-known example of SCC is steel in caustic environments (caustic cracking). This combination was discovered as a result of a number of steel steam engine boilers failing in a catastrophic way.

3.1 The SCC Problem

Alloy 600 is used extensively in the PWR primary circuit. Alloy 600 was chosen for a number of reasons (see chapter 1) as a replacement for the previously used stainless steel (austenitic 18Cr-10Ni) which was prone to serious SCC. In 1959, Coriou et al. identified that Alloy 600 was susceptible to primary water stress corrosion cracking (PWSCC) [8]. This result was initially disputed as other facilities struggled to reproduce the cracking, however, in 1971, PWSCC was detected in operating components at the Obrighiem plant in Germany. Figure 3.2 shows the time line of major events in the detection of SCC in Alloy 600.

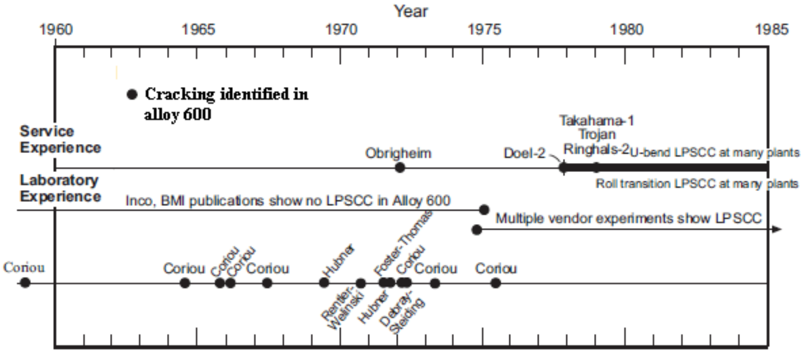

Figure 3.2 – Time line showing incidents of SCC detection in Alloy 600 [86].

The environment that induces the cracking is primary water. Primary water is pure, deaerated water with boron, lithium and hydrogen additives. Lithium is added in the form of lithium hydroxide and is used to maintain a neutral pH in the system. Boric acid is added to control the neutron flux. Hydrogen is added to maintain a reducing environment and to prevent the radiolysis of water [87]. The loading (stress) of the component can be due to both design and/or residual stress. For nickel alloys to suffer SCC, the load is often required to be comparable to that of the yield stress [88].

The SCC in Alloy 600 can be described in a number of ways. Hence multiple abbreviations are used to describe the problem, the most common are:

- Stress corrosion cracking (SCC), though not specific,
- Primary water stress corrosion cracking (PWSCC), specific to an environment,
- Intergranular stress corrosion cracking (IGSCC),
- Low potential stress corrosion cracking (LPSCC).

The terms listed here are used interchangeable throughout this report.

3.2 Influencing Factors

There are many factors affecting the process of SCC in Ni-Fe-Cr alloys. Many of the factors affecting SCC are related, this can make it difficult to fully define their effect as most tests will have multiple variables (i.e. changing carbon content of the alloy will affect the carbide distribution). This section looks at the work carried out in understanding of the factors that affect SCC.

3.2.1 Nickel and Chromium

The chemical composition significantly affects an alloy's susceptibility to SCC. The nickel and chromium concentrations are generally considered to be significant factors on the susceptibility of a material to PWSCC. Assessing the effect the nickel and chromium concentrations have on SCC is complicated as altering the chemical composition can significantly alter the materials mechanical properties and microstructures, hence making it difficult to distinguish the factors which are significant to SCC and those which are not.

Coriou et al. were the first to study the effect of nickel on SCC in pure or chlorinated water in 1969 [89]. The result of this experimentation is presented in Figure 3.3. This shows that an increased nickel content increases the susceptibility to PWSCC. It can be noted that iron rich alloys (low nickel) are more susceptible to chloride ion induced SCC (which resulted in the nickel alloys use), but the nickel alloys are more susceptible to PWSCC. It should be noted that these experiments were carried out at the Ni/NiO potential, hence inhibiting the formation of an external NiO in the high nickel alloys. This could significantly affect the results. Further work by Coriou et al. has however shown that PWSCC can occur at concentrations of nickel as low as 45%.

The effect of chromium and nickel was studied by Yonezawa et al. [90]. This study found that increasing the chromium content significantly increases the resistance

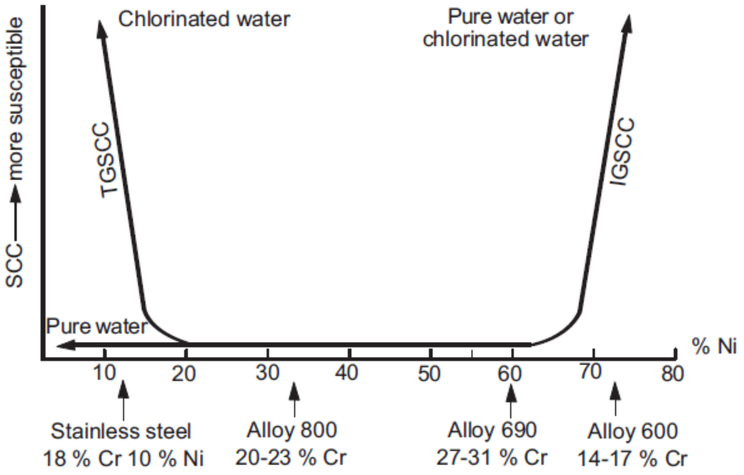
SCC ⟶ more susceptible
Chlorinated water
Pure water or
chlorinated water
TGSCC
IGSCC
Pure water
% Ni
10
20
30
40
50
60
70
80
Stainless steel
18 % Cr 10 % Ni
Alloy 800
20-23 % Cr
Alloy 690
27-31 % Cr
Alloy 600
14-17 % Cr

Figure 3.3 – Effect of nickel content on the alloy susceptibility to transgranular and intergranular SCC in pure or chlorinated water [8].

of the alloy to PWSCC, up to 17% chromium at which point no cracking was observed (Figure 3.4). Was et al. [91] however observed that cracking occurred in alloys containing up to 30% chromium, a result which has been repeated by Delabrouille [38]. With classical SCC tests (SSRTs, RUBs, constant load), EDF has demonstrated that cracking could occur up to 22% chromium (SCC decreases with % chromium content), no SCC occurred at chromium contents above 25%, with the exception of some structures involving intragranular carbides and/or specific cold work (1D with complex strain path) [92].

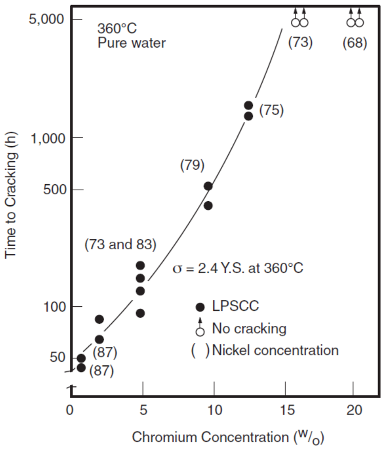

Figure 3.4 – Effect of chromium content on nickel alloys susceptibility to PWSCC [90].

The improved resistance to PWSCC as a result of increased chromium is complex as its addition has multiple effects. The chromium forms a protective chromium oxide layer on the sample. This layer however is continuous at concentrations greater than 10%, the thickness of the oxide becomes constant at concentrations greater than 15% [38]. An increased chromium content has a favourable effect on the repassivation kinetics [88]. The chromium content also affects the creep rate and it has been suggested that this is responsible for the beneficial role of chromium [88], the reason for chromium's effect on the creep rate is not clear. It could even be attributed to chromium being a solid solution strenghtener in the alloy matrix or promoting the formation of grain boundary carbides which could mechanically prevent slip at grain boundaries.

3.2.2 Carbon Content and Carbide Distribution

The effect of carbon cannot be analysed without looking at the carbide distribution. The carbide distribution has a significant effect on the alloy susceptibility to PWSCC, while the carbon content effect is minimal. Elemental carbon acts as a solid solution strengthener, reducing the carbon content in solution (either by carbide formation or using a purer alloy) can increase the creep rate. The creep rate has been shown to be an important factor in the initiation and propagation of PWSCC cracks, higher creep rates are worse [93].

The effect of the carbide microstructure type, on PWSCC susceptibility, is illustrated in Figure 3.5. This shows that the most resistant carbide structure is when the intergranular carbides are continuous. The term continuous does not imply a film coating of the grain boundaries; it implies a high density of carbides on the grain boundary such that under low magnification it appears continuous. The type of carbide is also considered to be important as it has been found that M_7C_3 are more resistant than the more common $M_{23}C_6$, however this may result from the M_7C_3 carbides forming a more favourable microstructure opposed to the carbide structure [94].

This may be seen as counter intuitive as carbides at the grain boundary may result in sensitisation of the material (chromium being depleted at the grain boundaries). Sensitisation is a significant problem in stainless steels, as it makes them significantly more susceptible to SCC. Experimental and theoretical work has shown that sensitisation occurs in nickel alloys [29], however the affect is not significant relative to beneficial properties of the carbides and reducing nature of the environment. The effects of sensitisation can be reduced by maintaining the thermal treatments for a prolonged time. This allows the chromium consumed in the carbide formation to be replaced by chromium in the bulk diffusing to the areas of lower concentration.

The reason for the beneficial effect of grain boundary carbides is unclear, a number of possibilities have being proposed. The carbides may act as a physical ob-

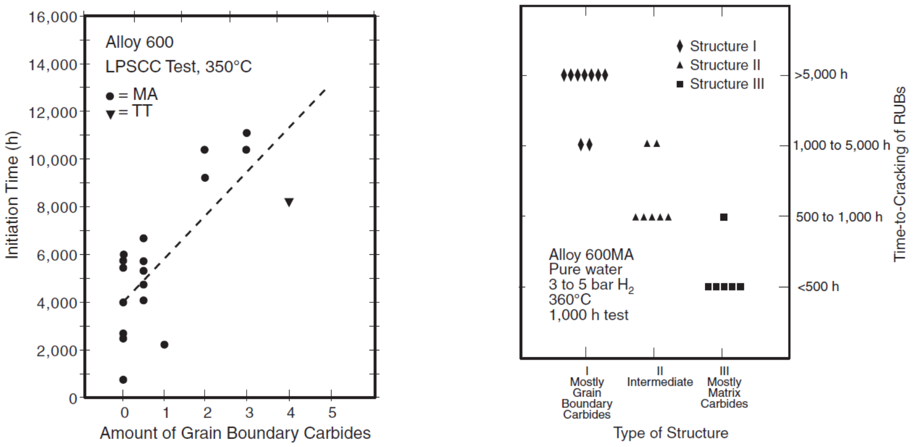

(a) (b)

Figure 3.5 – Effect of carbide distribution on PWSCC in Alloy 600 [95].

struction to grain boundary sliding, hence restricting initiation and propagation. It has also been suggested that they act as a physical barrier to grain boundary diffusion, hence reducing the rate at which the boundary can be embrittled. They could also act as oxygen or hydrogen traps, hence having a similar effect as if they were a physical obstruction to grain boundary diffusion.

Brummer et al. suggested that the carbides may act as dislocation sources [96], hence resulting in the crack tip blunting, this would explain the detrimental effect of intergranular carbides (detrimental in this case means worse than, not necessarily negative effect as to the authors knowledge there has being no testing of carbide free alloys) as it would result in strain localisation at grain boundaries. Recent work has indicated that SCC initiation is controlled by intergranular carbides, while propagation is controlled by misorientation in the material [12]. This would imply that the absence of intergranular carbides would result in PWSCC initiation occurring more readily, but with a low propagation rate. The dislocation source argument is interesting, but an increased dislocation density on the grain boundary would result in an enhanced diffusion rate. This would increase the rate of embrittlement (unless the carbides act as an obstruction) and hence reduce the required initiation time.

Alloy 690 is thermally treated to produce a continuous intergranular carbide structure; this however is not always possible in Alloy 600 due to different carbide precipitation curves. It should be noted at this point that alloy 600 (at least industrial steam generator tubes) was generally mill annealed at low temperature (980°C), resulting in significant intragranular carbides, while alloy 690 was generally mill annealed at higher temperature ($\geq$ 1050°C), resulting in IG carbides [12]. This factor is seen as a major contributor to Alloy 600 having significantly worse

PWSCC resistance, despite alloy 690 only having $M_{23}C_6$ carbides.

3.2.3 Grain Size and Orientation

The effect of grain size is difficult to determine as altering this requires using different post processing heat treatments, hence variable mechanical properties. Gorman [70] has attempted to measure the behaviour of Alloy 600 steam generatora tubes a function of grain size, the results of this are shown in Figure 3.6. These results are plotted as a function of the ASTM grain size (n), this is defined as:

$$N = 2^{n-1} \tag{3.1}$$

where N is the number of grains per square inch, when measured at magnification of a hundred.

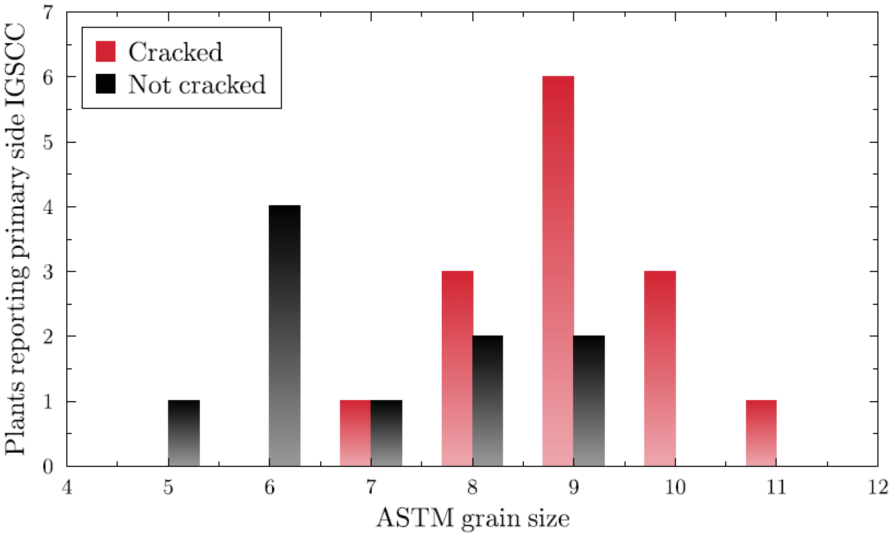

Figure 3.6 – Effect of grain size on PWSCC susceptibility [11].

The work by Gorman shows that an increasing grain size decreases the susceptibility of the alloy to PWSCC. However, the PWSCC is also dependant on the yield stress and the yield stress is related to grain size by the Hall Patch relationship, equation (3.2):

$$\sigma_y = \sigma_0 + kd^{-1/2} \tag{3.2}$$

Where σ_y is the yield stress, d is the grain size and σ_0 and k are material constants. The production of the samples may also have affected this result, as a high temperature anneal will increase the grain size but limit the formation of intragranular carbides. As shown in the previous section, this would increase the resistance to PWSCC, hence these results may be a result of the carbides and not the grain size.

In addition to the grain size, the orientation of the grains is important. Grain boundary structure can be described by the coincident site lattice (CSL) model. The CSL model produces a CSL boundary (CLSB) value, Σ. Σ is the reciprocal of the frequency of coincident site lattice points, i.e. Σ 3 implies that every third lattice point at the boundary is the same for both grains. The CLSB value has been shown to correlate with the energy stored in the grain boundary [97].

It was believed that grain boundary energy is related to stress corrosion cracking, with low energy being beneficial. Gertsman and Brummer showed that the tendency of a boundary to crack was linked to the Σ value (Figure 3.7(a)), however, only Σ3 boundaries were immune [98]. Σ3 boundaries however may crack as the authors noted that there frequency was low, hence making it impossible to produce a statistically valid conclusion.

The result of high angle grain boundaries (HAGB) preferentially cracking over low angle grain boundaries (LAGB) could be attributed to the fact that carbides form preferentially on high energy grain boundaries (Figure 3.7). However work by Alexandreanu et al. [97] showed that this tendency was independent of the microstructure.

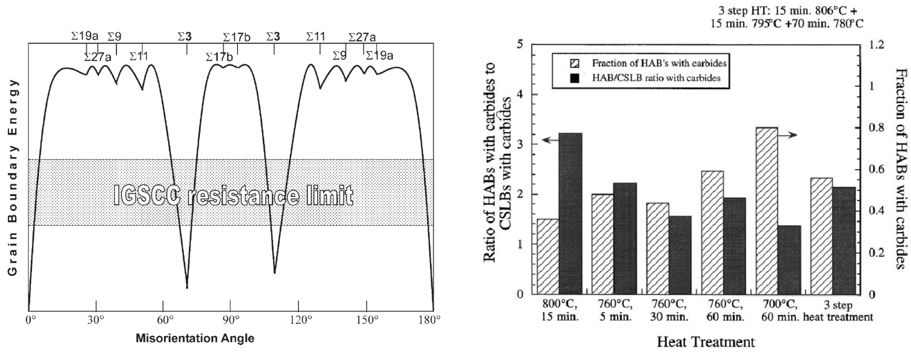

(a) (b)

Figure 3.7 – (a) Susceptibility as a function of grain boundary orientation. (b) Effect of grain boundary orientation on carbide precipitation [98, 99].

3.2.4 Stress, Strain and Creep

The stress applied to the material can be considered to be important for both the initiation of a crack from a smooth surface and the propagation of an existing crack. There appears to be a stress threshold (the stress required to initiate a crack) for the PWSCC cracking of the alloys of around the yield stress. Figure 3.8 shows the stress threshold for PWSCC as a function of the materials yield point (at testing temperature).

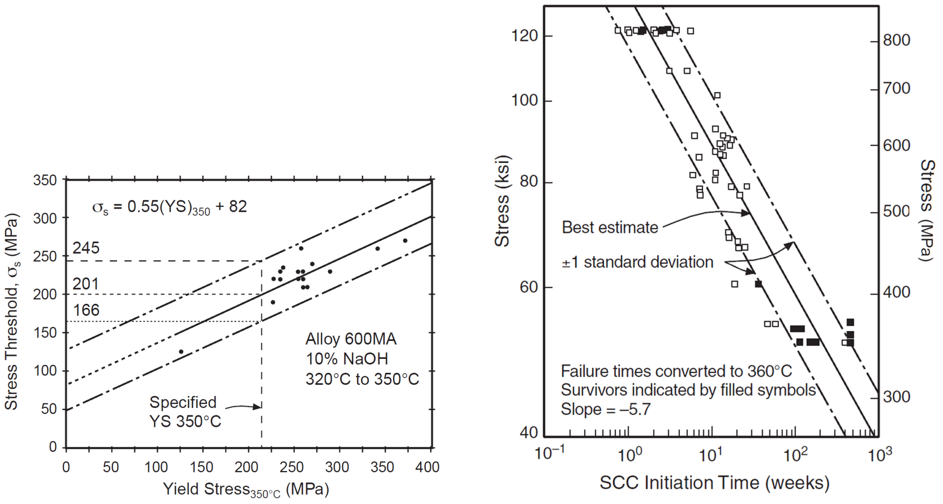

(a) (b)

Figure 3.8 – (a) Tests showing the stress threshold for SCC initiation as a function of yield stress [100]. (b) Dependence of initiation on applied stress [101].

The time to component failure (t_f) has been linked to the applied stress by

$$t_f = k\sigma^{-n} \tag{3.3}$$

where k is a constant accounting for material and environmental conditions, σ is the stress and n is the stress exponent. The exponent n has been measured experimentally by separate laboratories to be 4 and 5.7. The creep rate of the alloys is also dependent on a power law relationship. The exponent in creep rate is 4, this has resulted in exponent n in equation (3.3) being taken as 4 [11]. It has already been noted that the creep rate and yield point are dependent on the alloy grain size.

The stress dependence is often referred to as the time to initiation (Figure 3.9(b)) due to the high threshold stress for initiation and a relatively low stress intensity factor for propagation (K_{ISCC}). The value of (K_{ISCC}) for the alloys has been measured by Rebak to be in the range of 5 to 15 $MPa\sqrt{m}$ [102] (K_{ISCC} for the materials to be used in this project has been measured to be 9 $MPa\sqrt{m}$ and 5 $MPa\sqrt{m}$ for AR-WF675 and 15%CW-WF675 respectivly [12]).

The dependence of PWSCC on applied stress is debated as other work (Figure 3.9(a)) has shown that the relationship between stress and initiation is not as clear as Figure 3.8(b) suggests. As a result of this, it has been suggested that the plastic strain on the material is a more suitable parameter. Work by Morton et al. showed the relationship between the plastic strain and the initiation time (Figure 3.9(b)) [103].

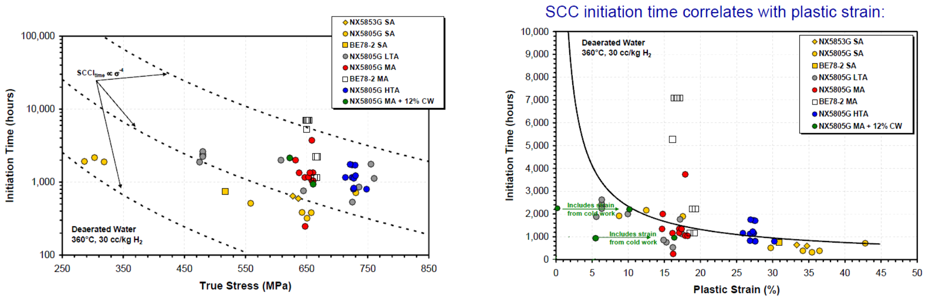

(a) (b)

Figure 3.9 – Work by Morton et al. showing the relationship between stress and initiation time and strain and initiation time for alloy 600 [103].

3.2.5 Cold Work and Strain Path

In addition to the stress and strain on a sample, the level of cold work has been found to be important. Cold work can introduce additional stress and strain to the material which is not expected.

Inducing cold work to a material has been found to reduce the crack initiation time (at equivalent loading relative to the yield stress [11, 12]) and increase the rate of propagation [104–106]. A reduction in the critical crack length required to transition between slow and fast propagation combined with a reduced critical stress intensity factor (K_{ISCC}) have also been reported as a result of cold work [12]. A number of authors have indicated that the detrimental effect of cold work is limited to a critical quantity (in the region of 20-30%) above which additional cold work improves the cracking characteristics relative to the lower cold work levels [107,108]. Hou et al. attributed the phenomenon to the increased cold work removing any strain localisation and producing a homogenous strain distribution, as their results in Figure 3.10 illustrate [107].

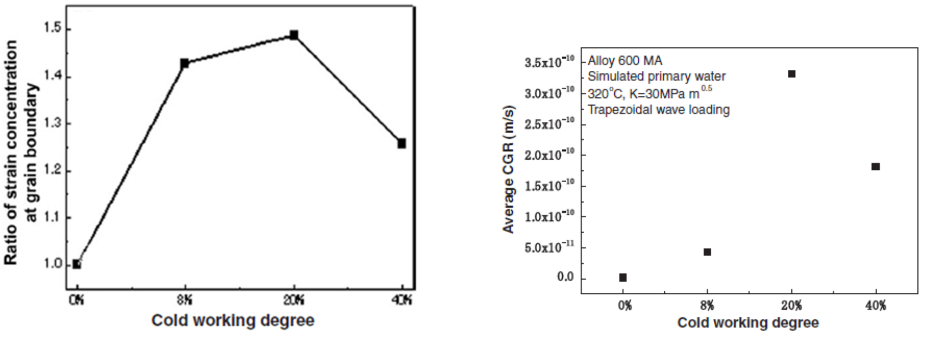

(a) (b)

Figure 3.10 – Results showing the observed localisation of strain at the grain boundaries (a) and the subsequent crack growth rates observed (b) [107].

In addition to affecting the SCC properties of a material, cold work affects the oxidation. Feron et al. studied the effect of cold work on the oxide formed on 304 SS and 316L SS, their results indicated that the predominant effect on the oxidation was on the inner chromium rich oxide layer [109]. The inner layer was reported to be continuous on solution annealed materials and dis-continuous when cold worked (Figure 3.11), however the surface finish on the samples used in this study is not well defined (the sample surface was prepared to a mirror polish but this could imply a range of finishes, which can be seen to yield different oxidation results [13,14,110,111]), as such the effect of local cold work at the surface (Bibly layer) was not defined.

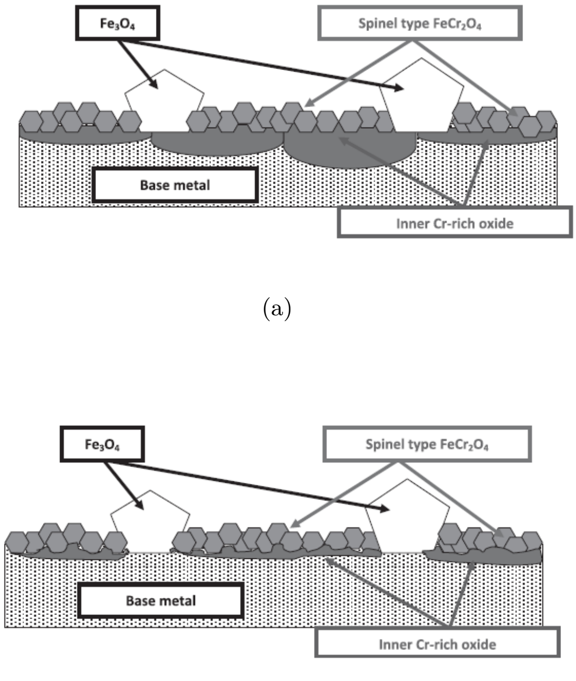

(a)

(b)

Figure 3.11 – Oxide formed on annealed (a) and cold worked (b) 316L stainless steel when exposed to simulated PWR conditions at 300 °C [109].

Lozano-Perez [112] used sequential slice and view FIB to produce 3D reconstructions of oxidised 304 SS, the work showed that both cold work and applied tensile strain increased the mean oxide depth, in contrast to that reported by Feron et al. The use of 3D imaging was reported to produce results of high statistical significance, but the number of grains observed is a severe limitation to this technique. The sunfish finish used in this study is also questioned as it is reported as an OPS finish, but surface scratches inconsistent with this are clearly visible.

The level of cold work has typically been measured as the reduction of the material. However Moshier and Brown [113] showed that the strain path of the material was important. This work showed that the crack growth rate of a rolled material is depended on the orientation of the sample been cracked, relative to the rolling direction, hence the strain path of the material (Figure 3.12(b)).

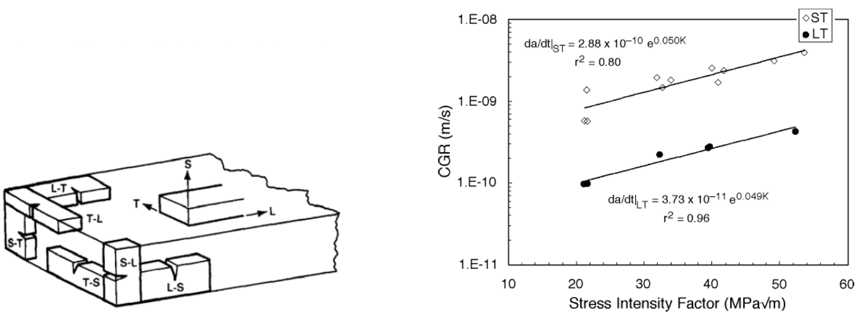

(a) (b)

Figure 3.12 – CGR as a function of orientation, experiment by [103], image reproduced from [11].

The quantification of prior strain is complex; the β parameter (also referred to as α by Schmitt et al. [114]) is one method of quantification. The β parameter is defined as:

$$\beta = \frac{\epsilon_1 : \epsilon_2}{\|\epsilon_1\| \cdot \|\epsilon_2\|} \tag{3.4}$$

Such that ϵ_1 is the initial strain vector and ϵ_2 is a subsequent strain vector [114–117].

The strain history is considered to be significant as it can affect the strain localisation which occurs at grain boundaries due to the different grains hardening at different rates as a result of their orientations [118]. Studies by Couvant et al. on Alloy 182 showed that the prior deformation paths had a significant effect on the strain localisation which occurred in the material, this was supported by FE modelling of complex strain path on a polycrystalline material. The strain path was noted to affect the crack morphology on 304 SS, with uniaxial strain path producing transgranular cracking and a complex strain path required for IGSCC [115]. Tribouilloy et al. noted a similar effect when comparing tensile cold worked SS to cold rolled SS [119].

Recent work by Leonard has shown that the misorientation may be an appropriate quantity for the susceptibility to PWSCC [11,120]. The misorientation is the rotation of the grain' lattice relative the grain's average orientation (Note: the term can also be used to represent the rotation of the material lattice relative to the neighbouring points, this can however be dependent on the measurement resolution).

Surface strain (due to handling) has been observed in steam generator divider plates to produce a significant strain gradient, with the surface being pre-strained up to 0.2 whilst the bulk is only 0.05. SCC CERT tests of materials with a cold-worked surface layer in the region of $\approx 2\ mm$ lead to the conclusion that crack propagation within the cold worked layer was significantly greater than that of the bulk, with the possibility of the cracks arresting when propagating into the bulk [121].

3.2.6 Temperature

PWSCC has been found to predominantly affect the hot leg of steam generator tubes. These tubes operate at ≈ 325°C and PWSCC has not been observed at temperatures less that 250°C [96]. PWSCC is linked to temperature by a Arrhenius relationship of the form

$$k = Ae^{\left(\frac{-Q}{RT}\right)} \tag{3.5}$$

where k is the reaction kinetic, A is a constant, Q is the apparent activation energy, R is the ideal gas constant and T is the absolute temperature.

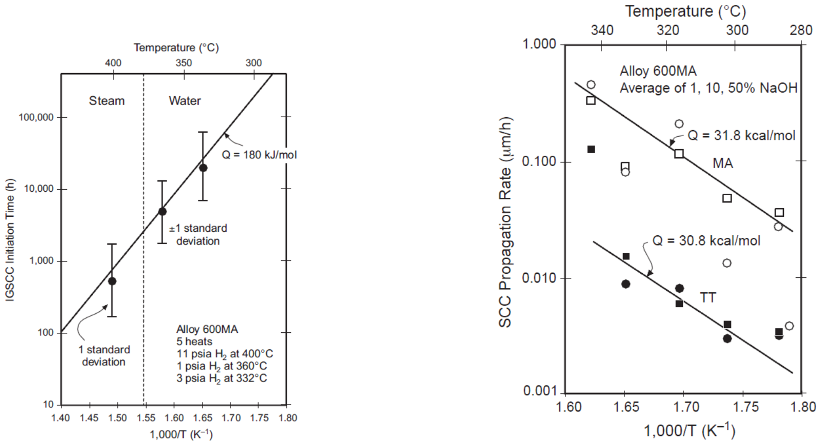

(a) (b)

Figure 3.13 – Initiation time and propagation rate of PWSCC cracks as a function of temperature [11, 101].

The activation energy for the initiation and propagation of a PWSCC crack vary. The variation in activation energy suggests that the mechanism governing them may be different, but the large scatter in the available data means this point is debatable. The measured range for the activation of initiation and propagation are 79 to 330 kJ/mol and 80 to 225 kJ/mol respectively [70, 80, 101, 122–128]. The large variation may be attributed to the fact that tests were carried out at a constant hydrogen partial pressure. The susceptibility to PWSCC has been found to be a maximum at the Ni/NiO redox potential. The location of the redox potential is dependent on the temperature, the potential of the system is controlled by the hydrogen content of the water. Testing at a constant hydrogen partial pressure may bias the results as different temperatures will be at different points relative to the Ni/NiO redox potential, hence variable susceptibilities. More recent tests have been conducted at a constant distance from the Ni/NiO equilibrium potential and the consensus is that the values for initiation and propagation are 190±40 kJ/mol and 140±25 kJ/mol, respectively (Figure 3.13) [103].

3.2.7 Environment

The environment in PWSCC is primary water; primary water is pure, deaerated water with boron, lithium and hydrogen additives. The pH of the environment has been found to affect the PWSCC susceptibility (Figure 3.14). The effect of the pH however has been questioned as its value was controlled by varying the lithium hydroxide and boric acid concentrations. It was suggested that a lithium content greater than 3.5 ppm could increase the time to initiation of PWSCC [129]. The boron (added as boric acid), has to date not been reported to directly affect PWSCC.

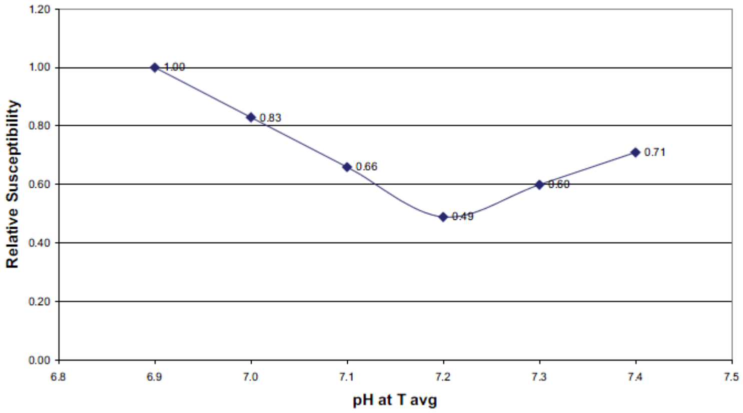

Figure 3.14 – PWSCC susceptibility measured as a function of pH [129].

The effect of the added hydrogen is considered to be one of the most important factors affecting PWSCC. The concentration is often related to the Ni/NiO equilibrium point. This is the transition point at which the formation of nickel oxide goes from being stable to unstable. The reaction for the formation of NiO is shown in equation (3.6), it can be seen from this that increasing the hydrogen content inhibits the formation of NiO and hence stabilises the Ni.

$$Ni + H_2O \rightleftharpoons NiO + H_2 \tag{3.6}$$

The concentration of hydrogen in the system is often described in terms of a potential relative to the Ni/NiO transition point. The potential can be calculated from the electrochemical half-cell equations of (3.6) and the Nernst equation. The result of this is that the relative potential can be calculated by equation (3.7).

$$E_{Ni/NiO} = -\frac{2.303 \times R \times T}{2 \times F} \times \log\left[\frac{pH_2}{pH_{2NiNiO}}\right] \tag{3.7}$$

Where $E_{Ni/NiO}$ is the potential, R is the universal gas constant, T is the temperature in Kelvin, F is Faraday's constant, pH_2 is the hydrogen pressure and pH_{2NiNiO} is the hydrogen pressure at the Ni/NiO redox potential.

The susceptibility to PWSCC has been found to experience a strong maximum in the region of the Ni/NiO redox potential. A number of studies have been carried out to assess the effect of potential on the initiation and propagation of PWSCC cracks. Figures 3.15(a) and 3.15(b) are an accumulation of data taken from these studies [10, 77, 123, 130–135]. It is generally agreed that there is a parabolic relationship between the potential and the initiation time. The relationship between crack growth rate and potential is less clear. Some studies have found there to be a step in the growth rate centred on the transition point whilst others have found there to be a parabolic relationship similar to that of initiation.

The minimum in initiation time at the transition point has been explained in a number of ways, each to support a different proposed mechanism. In general, the explanations are all related to an unstable oxide resulting in a higher rate of grain boundary embrittlement or the oxide itself becoming brittle. The explanation for the variation in crack propagation results is unknown, though there is evidence that the hydrogen content can affect the critical stress intensity factor (K_{IGSCC}) [136]. This could be interpreted as the environment changing the structural integrity of the formed oxide.

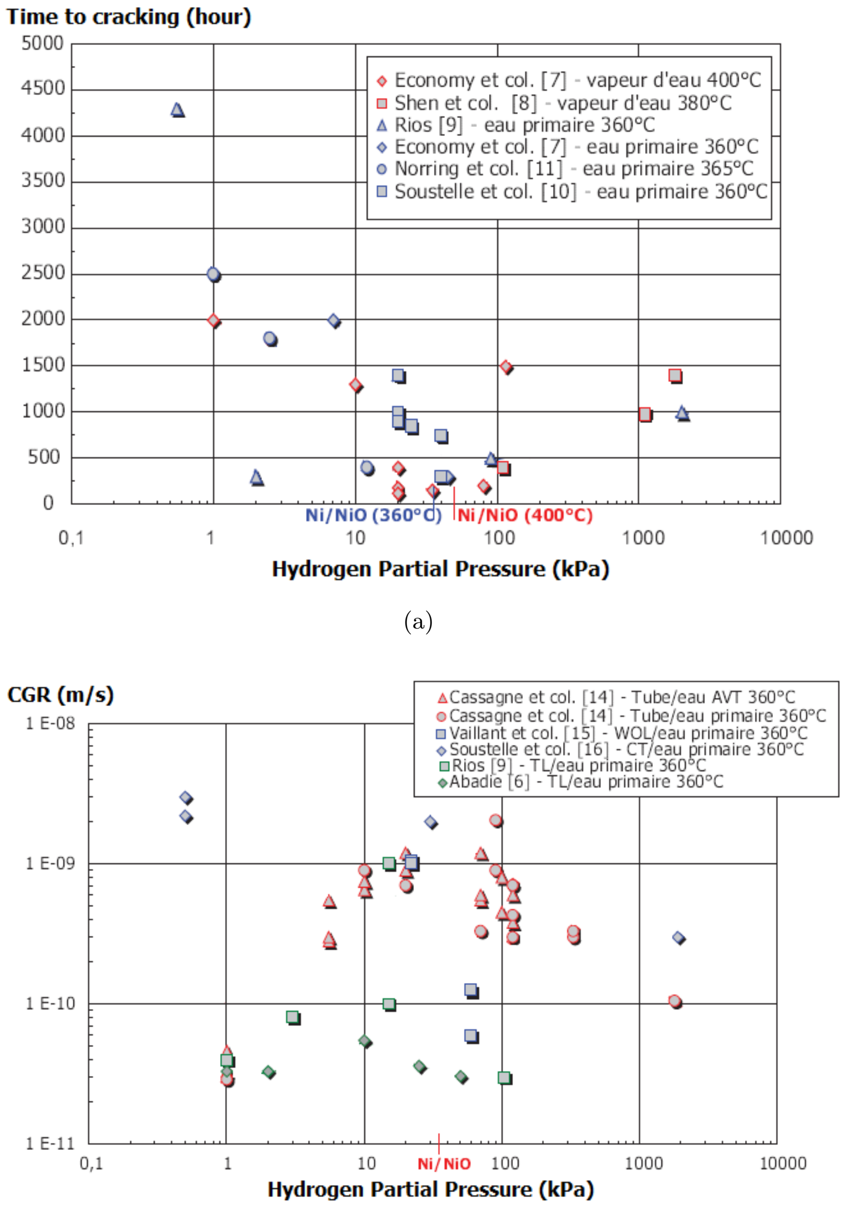

(a)

(b)

Figure 3.15 – Relationship between the hydrogen partial pressure and the crack propagation and initiation time [137].

3.3 Stress Corrosion Cracking Mechanisms

The mechanism of PWSCC in Ni-Fe-Cr alloys is unclear. Since the discovery of PWSCC in Alloy 600, there have been a number of models proposed to explain the cracking. Despite the numerous models proposed, no single model has been able to explain completely the process of PWSCC.

Of the proposed mechanisms, the three leading models are considered in more detail in this thesis. These mechanisms are the film rupture (slip-dissolution) model, the corrosion enhanced plasticity model and internal oxidation. Other models proposed for SCC which may account for PWSCC include, hydrogen induced local plasticity (HELP) by Birnbaum [138], film-induced cleavage model (FICM) by Sieradzki and Newman [139], Lynch model by Lynch [140], Jones model by Jones [141], adsorption theory by Petch [142], decohesion theory by Troiano [143], internal pressure theory by Zapffe [144, 145] and creep deformation coupled with intergranular sliding by Angeliu and Was [146, 147].

For anyone of these models to be viable for PWSCC they must be able to account for the consistently observed experimental characteristics of PWSCC cracking, the main characteristics of PWSCC are [6, 11, 148]:

- Variable and large initiation times in PWR primary water.
- Significant variation in between batches, despite all other influencing parameters remaining constant.
- Significant influence of the carbide distribution.
- Detrimental effect of cold-working on the material.
- Perceived continuous mechanism of cracking between 286°C sub-cooled water and 400°C superheated steam.
- Significant variations in susceptibility with hydrogen partial pressure, most susceptible as the value approaches the Ni/NiO equilibrium potential.
- Relatively high activation energy of crack initiation (190 kJ/mol) and propagation (140 kJ/mol).
- Stress exponent of 4-6 for time to failure and a high stress threshold relative to the yield point.

3.3.1 CEPM

The corrosion enhanced plasticity model (CEPM) was proposed by Magnin et al. to describe the brittle failure of ductile 316 alloy when exposed to $MgCl_2$ at 153°C. The failure of 316 stainless steel is predominately transgranular compared to Alloy 600 which cracks intergranularly [149].

The process of CEPM is as follows: micro-rupture on a slip plane results in a break down in the passivity at a crack tip. The re-passivation results in an increase in hydrogen production and vacancy injection. The crack tip deformation is limited to 111 planes, preventing crack tip blunting. The hydrogen segregates to the slip planes' increasing the local plasticity and resulting in an increase in dislocation generation. Dislocations pile-up in the slip planes, resulting in work hardening. The work hardening increases the slip planes susceptibility to hydrogen embrittlement [9]. Micro-rupture occurs in the embrittled slip planes and the process repeats [10]. This process is illustrated in Figure 3.16.

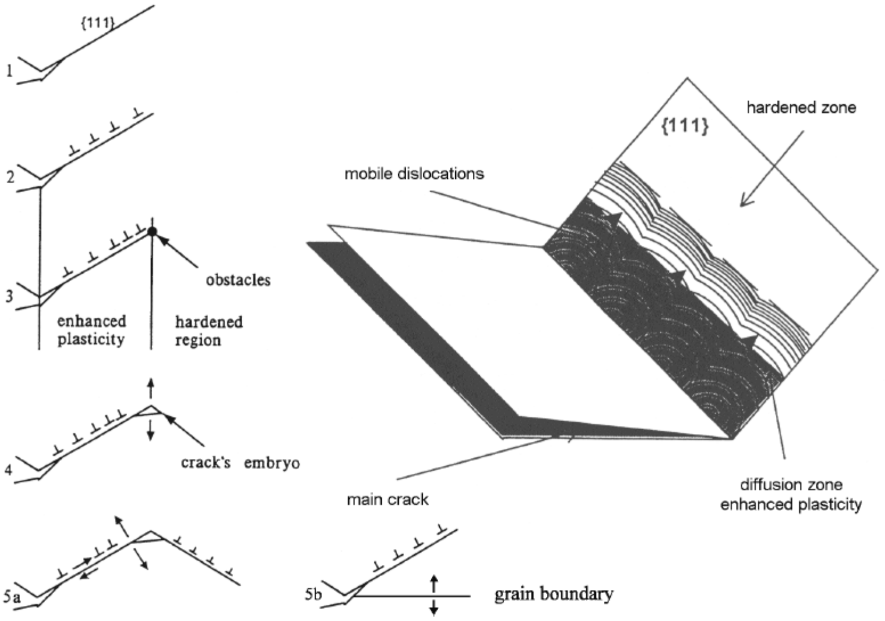

Figure 3.16 – Graphic illustration of the CEPM process [150] .

The CEPM is very effective at describing the detrimental effect of cold working the material. The cold work results in the material being more susceptible to hydrogen embrittlement, hence having a detrimental effect on PWSCC susceptibility. The carbides can be accounted for as they act as hydrogen traps, preventing the embrittlement. It should however be noted that in the original CEPM for 316SS, the enhanced plasticity would result in a stress build up at obstacles (precipitates and grain boundaries), hence cracking.

The CEPM is a propagation model and as such it makes no attempt to account for the initiation stage of PWSCC. The CEPM also struggles to explain the observed effects of hydrogen partial pressures as an increased pressure should imply a greater rate of embrittlement and hence faster cracking. The hydrogen partial pressure variation may be explained by the oxide formed being unstable, hence generating more hydrogen or allowing a greater volume of hydrogen into the material. The CEPM does not account well for the temperature dependence of PWSCC. In addition to this, the model is only pseudo intergranular cracking. The original model was for transgranular cracking and in the case of PWSCC, the cracking is transgranular located around a fast diffusion point (grain boundary).

3.3.2 Film Rupture

The film rupture mechanism, a variant of which is the slip step dissolution has been used successfully to describe incidents of SCC in a number of systems. The pure model of film rupture was first developed by Logan in 1952 and has gone through a number of modifications since [151, 152].

The film rupture mechanism is composed of three stages. The oxide film will crack; the cracking of the oxide exposes the bulk material. There is anodic dissolution of the exposed metal. The re-passivation of the oxide will protect the material. Under this description, the crack growth rate is given by equation (3.8) [153]. This process is illustrated in Figure 3.17.

$$\dot{a} = \frac{M \cdot q}{F \cdot t_r \cdot z \cdot \rho} \tag{3.8}$$

where M is the atomic weight of the metal at the crack tip, ρ is the mass density of the crack tip metal, F is Faraday's constant, z the number of electrons involved in the oxidation of the metal atom, q the corrosion charge density per oxide rupture event, and t_r the period of oxide rupture events.

The main advantage of the film rupture model is that it quantifies the crack growth rate. The predicted crack growth rates are comparable to those experienced in Alloy 600. The model however predicts a discontinuous acoustic emission, where as a continuous acoustic emission is observed in PWSCC. There are also issues in describing the effect of the potential as re-passivation rate is controlled by the potential. The susceptibility should be linked to the re-passivation rate and hence the potential; but the link between susceptibility and potential is not as expected. Another significant problem with the film rupture model is that grain boundary oxidation is observed when no stress is applied. Like the CEPM, the film rupture model only describes the propagation of the crack and makes no attempt to account for the large initiation times.

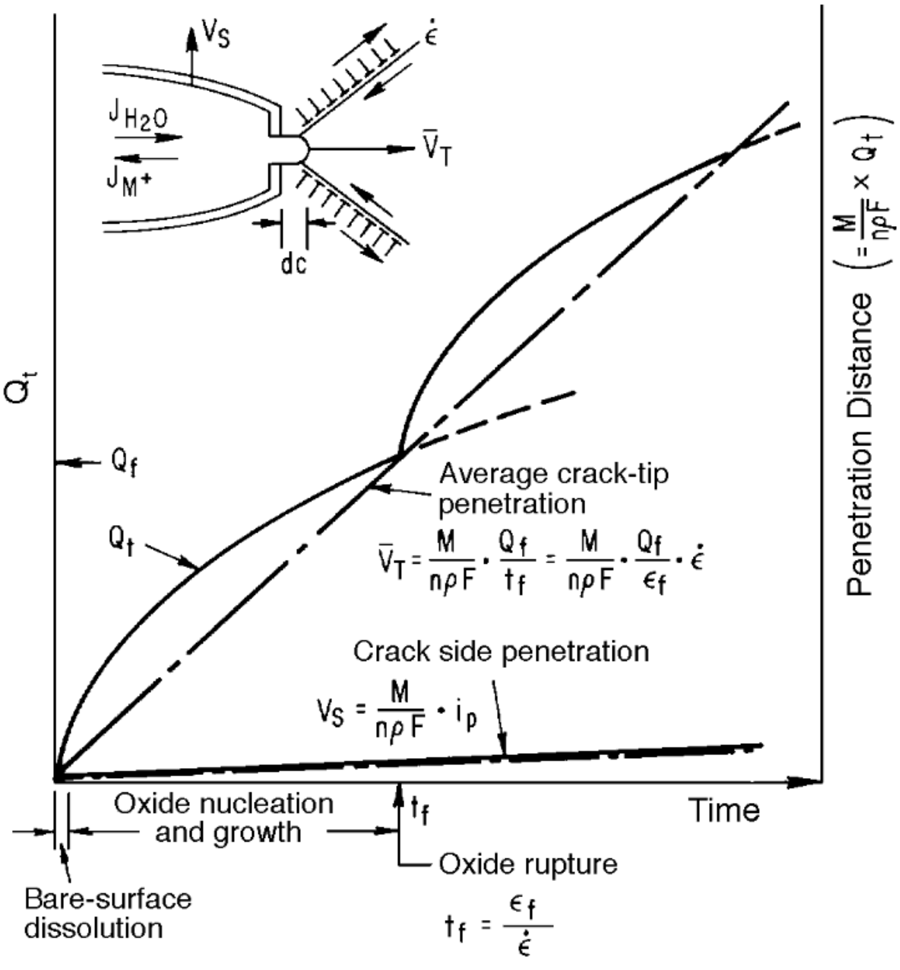
V_S
$\dot{\epsilon}$
J_{H_2O}
J_{M^+}
$\bar{V}_T$
dc
Q_t
Q_f
Q_t
Average crack-tip penetration
$\bar{V}_T = \frac{M}{n\rho F} \cdot \frac{Q_f}{t_f} = \frac{M}{n\rho F} \cdot \frac{Q_f}{\epsilon_f} \cdot \dot{\epsilon}$
Crack side penetration
$V_S = \frac{M}{n\rho F} \cdot i_p$
Penetration Distance $\left(= \frac{M}{n\rho F} \times Q_t\right)$
Time
Oxide nucleation and growth
t_f
Oxide rupture
$t_f = \frac{\epsilon_f}{\dot{\epsilon}}$
Bare-surface dissolution

Figure 3.17 – Graphic illustration of the film rupture process [154] .

3.3.3 Internal Oxidation

The final model to be discussed is internal oxidation (IO). IO was first proposed as an explanation of PWSCC by Scott and Le Calvarr in 1993. The process of IO was first proposed in 1959 by Wagner et al. to explain the high temperature embrittlement of nickel based super alloys operating in jet engines [155]. The model was proposed as the PWSCC appeared to have large activation energies for crack initiation and propagation, these energies were consistent with those associated with solid state diffusion.

IO is the preferential corrosion of a less noble metal element in an alloy by the inward diffusion of oxygen. In the case of Alloy 600, the process refers to the diffusion of oxygen along grain boundaries, it is thermodynamically favourable for the minor elements such as chromium, iron and carbon to oxidise preferentially [125]. The resultant oxide is brittle and under an applied stress, produces micro cracks. Propagation occurs with alternating grain boundary oxidation and micro cracking [156]. This process is illustrated in Figure 3.18.

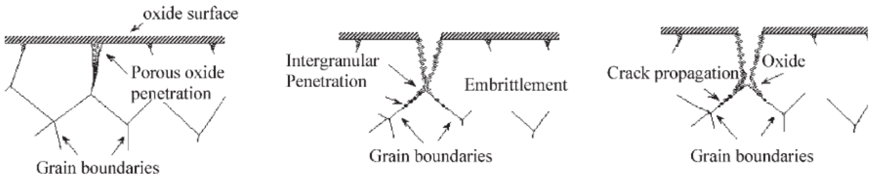

Figure 3.18 – Graphic illustration of the internal oxidation process at grain boundaries [156].

The model assumes that the crack propagates following linear elastic fracture mechanics. Based on a parabolic oxidation rate to a critical depth, the time to a detectable crack formation can be calculated by:

$$t_i \propto (K_{ISCC}/\sigma)^4 \tag{3.9}$$

where t_i is the initiation time, K_{ISCC} is the stress intensity factor and σ is the applied stress. This shows that there is a stress exponent of 4, as experimentally measured [156].

A major advantage of the IO model is its ability to predict the initiation of cracks as well as the method by which they propagate. There is also evidence for IO by the fact that grain boundary oxidation has been reported from unstressed samples [70]. The internal oxidation model can also be used to quantify the crack growth rates observed with a similar accuracy of film rupture [153].

The influence of carbides in the IO model is not explicit, but they can be accounted for in a number of ways. The two main ways are that the carbides act as a chemical and/or physical barrier to the transport of oxygen along the grain boundaries, hence preventing the embrittlement. The second explanation is that the carbides mechanically strengthen the grain boundaries preventing slip, the inhibiting of slip then prevents the formation of cracks and slows the propagation of existing cracks. However, this argument is questionable as the IO model of PWSCC does not imply that slip occurs as it is a brittle fracture model.

The model has been used to describe the effect of potential in a number of ways and it has been noted that there has been similar trends observed in high temperature internal oxidation. Staehle has pointed out that the susceptibility model of

PWSCC should be linked to the solubility of oxygen in the material and as a result of the potential. The dependence of solubility on potential however does not match the potential dependency of PWSCC [157].

The biggest objection to the IO model however is the oxygen diffusion rate. The diffusion rate required to support the IO model has been calculated by Scott. The rate required however appears to be significantly higher than the expected (Figure 3.18).

It should however be noted that the majority of the date shown in Figure 3.19 is obtained at significantly higher temperatures than those experienced in the primary circuit and extrapolated to lower temperatures. The result of the extrapolation is that there is a variation of 6 orders of magnitude at the temperatures where PWSCC occurs. Although Figure 3.19 has been used extensively in the debate about internal oxidation, it should be noted that the given diffusion rates refer to the bulk and apparent rates, not the grain boundary diffusion rates which relate to IO. The lack of diffusion data means it is difficult to produce an accurate propagation model (though as previously stated it is possible to create a qualitative model).

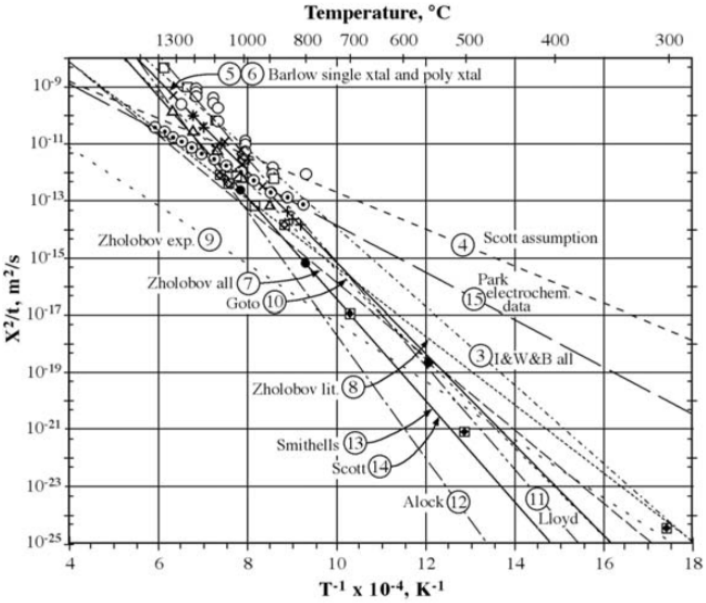

Figure 3.19 – Comparison of experimental diffusion rates for oxygen in nickel with the rate required for IO included [157].

It has been suggested that there could be an enhanced diffusion rate at the grain boundaries by the injection of vacancies created by the corrosion process [156]. This would be consistent with the detrimental effect of cold working the material as this would increase the dislocation density, thus the ability of vacancies. The low diffusion rate could also be accounted for by the crack propagating beyond the embrittled zone before blunting.

The best way to test the IO model is to experimentally measure the grain boundary diffusion rate of oxygen at low temperatures as it has been noted that "There are no experimental observations that uniquely support the IO model" [157]. An accurate measurement of the diffusion rate would however provide substantial evidence for or against the IO model.

The concept that the oxide/crack act as a fast transport path for the transport of oxygen has recently been demonstrated by Laghoutaris et al [158]. The work used tensile stressed specimens of Alloy 600 exposed to a simulated PWR environment for ≈ 1000 h followed by a short (≈ 66 h) exposure to a simulated PWR environment doped with a O^{18} tracer (H_2O^{18}). SIMS detected the O^{18} throughout the oxide, not just at the surface, as such there is a question to the rate limiting step in PWSCC [158]. The suggestion has been made that the availability of chromium to oxidise is the limiting factor.

Part II

Experimental and Analytical Techniques

CHAPTER

FOUR

MATERIAL PREPARATION

A wide range of techniques have been used for preparing samples for both imaging and testing, the procedures used are outlined in this section. The specific samples used in each test/analysis method are detailed in their own sections. The aim of each method is to produce samples which are consistent and reproducible.

4.1 Surface Finish

Knowledge of a samples condition prior to testing is of particular importance for both oxidation and SCC tests, as such extensive analysis of the samples has been carried out, prior to testing to fully characterise the surface finish. The condition of the surface can affect the structure and composition of the formed oxide. This change can be due to the presence of a deformed layer or a slight change in chemical composition at the surface due to the method of preparation. This can have a dramatic effect on the oxidation and PWSCC behaviours observed in testing and may explain some of the differences between laboratory testing relative to in service observations.

The testing surfaces predominately used in this thesis are those finished with a 60 nm oxide polishing suspension (OPS) or a 600 grit silicon carbide grinding paper (P600). An OPS finish is used to produce a stress free surface with no deformed layer, the P600 to produce a finish with a deformed layer.

4.1.1 Grinding and Polishing

Sample surfaces were prepared to the required finish by grinding and polishing. The progressive steps used in grinding were P80, P220, P360, P600, P800, P1200, P2500 and P4000. The starting step of the grinding depended on the prior preparation of the sample, P600 was typical unless removing a melted layer produced by electric discharge machining (EDM) or significant thinning of a sample was required. The final grinding step depended on the application, P600 if the sample were to be tested with a deformed layer, P4000 if the sample needed subsequent polishing steps. Each stage of grinding was applied for a minimum of 2 minutes per sample; the samples were rotated 90 degrees between papers to allow visual examination of the surface to confirm all previous grinding damage had been removed. In-between grinding steps, the sample is rinsed with water before moving to the next stage.

Polishing steps of 5 µm, 3 µm and 1 µm were used for a minimum of 5 minutes per step. In-between polishing steps, the sample was washed with soap and rinsed with ethanol before drying. It should be noted that a poly-crystalline polishing solution (water based) was used; a diamond paste had been used but was found to produce a pitting like appearance on the sample surface; alcohol, water and oil based lubricants were used in an attempt to solve the problem, but to no avail. The spray was found to work with all lubricants; an alcohol based lubricant was used preferentially.

The final step used to produce a stress free surface with a mirror finish was a 60 nm oxide polishing suspension (OPS). Each sample was cleaned as in the previous polishing steps and polished for a minimum of 20 minutes with the OPS. After OPS, the sample was cleaned immediately with soap and ethanol; if residual OPS dried to the surface, the only method reliable of removing it was to re-polish the sample with the OPS for an additional 2 minutes and repeat the cleaning.

4.1.2 Electrochemical Polishing

Electrochemical polishing was used in some cases to remove additional material; this was used for residual stress measurements and in some cases electron backscatter diffraction (EBSD) mapping. 8% perchloric acid in acetic was used as the electrolyte and was chilled in ice. A voltage of 47 V was applied to the sample (anode), with a current density in the region of 1.7 Acm^{-2} for 3 minutes, a stainless steel was used for the cathode. This was performed three times; the sample was washed and cooled with methanol in-between each polish. The process would remove $\approx$ 3 microns per minute.

4.1.3 Cleaning - Plasma Cleaning

Samples were first cleaned with an undiluted thick soap (an industrial soap intended to be diluted with ten parts water was used), thus allowing the sample to be rubbed with a finger without damaging the surface. The samples were then ultrasonically cleaned for 15 minutes progressively in acetone, ethanol and deionised water; the samples were then dried by a heat gun to avoid water marks.

For SEM observations and EBSD mapping, plasma cleaning was used to remove contaminations when required (the cleaning was not suitable for post-exposure samples). The plasma cleaning was carried out by either glow discharge optical emission spectroscopy (GDOES) unit or a Horiba TENSEC. Both methods resulted in a 3 mm disk being cleaned on the sample, however both units required the sample to have a minimum diameter of 1.5 cm so as to create a seal on an outer O-ring. Due to the small area cleaned, relative to the sample size the method is not well suited to oxidation and SCC tests.

4.1.4 Etching

4.1.4.1 Grain Boundary Etching

An electrochemical etch was used for grain boundary etching, prior to etching the samples had been polished to 1 μm. 5% Nitric acid in methanol (5% Nital) was used as the etchant, 8 V was applied to the sample for 10 seconds as suggested by [14].

4.1.4.2 Carbide Etching

The carbides were revealed by etching away the matrix; this was achieved indirectly by the electrochemical polishing method used for TEM sample preparation. The electrochemical TEM sample preparation only etched the matrix. As such in the non-electron transparent parts of the foils, the carbides were left exposed and there distribution revealed.

4.2 Introducing Cold Work

The purpose of introducing cold work is twofold, it will introduce an uniform stress with a clearly defined strain path, such that it can be quantified by a number of methods (the beta parameter was used by [11]) and it will increase the susceptibility of the material to PWSCC. The cold work can be applied in two ways, tensile extension or cold rolling.

Tensile straining was used by Leonard, this testing found that the most susceptible orientation was at a 45 ° orientation with respect to the applied tensile stress (as shown in Figure 4.1). This corresponds to a beta parameter of 0.25 [11]. The production of samples with the 45 ° orientation requires a large volume of material and produces significant wastage.

To produce cold worked material for the SCC tests, rolling was used. The material was rolled on the tube axis direction to a 19% reduction in thickness.

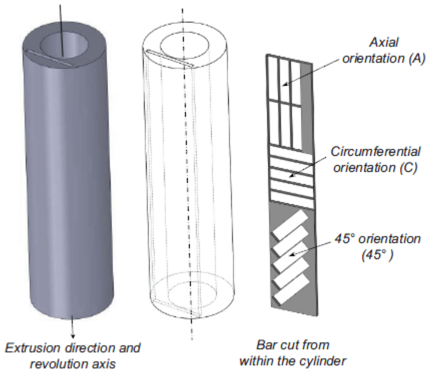
Axial orientation (A)
Circumferential orientation (C)
45° orientation (45°)
Extrusion direction and revolution axis
Bar cut from within the cylinder

Figure 4.1 – The orientations used by Leonard when analysing SCC susceptibility in WF675 and cold worked WF675. The cold worked material was strained in the axial direction thus the given definitions are used for both sets of samples [11].

4.3 Samples

Two main sample types were used in the completion of this thesis, corrosion coupons and dog bone tensile samples. The geometry of these samples is shown in Figure 4.2.

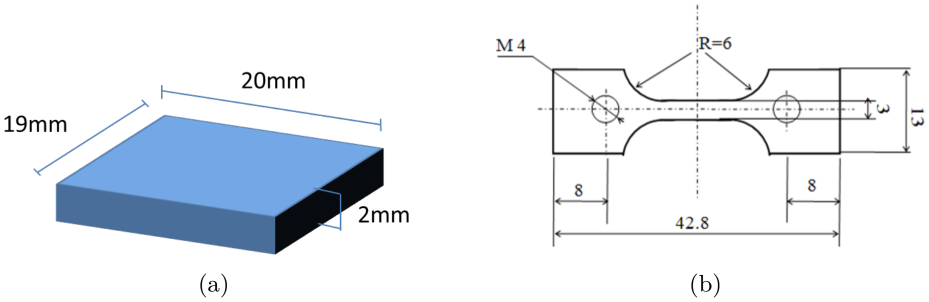
20mm
19mm
2mm
(a)
M 4
R=6
3
13
8
8
42.8
(b)

Figure 4.2 – (a) $2 \times 19 \times 20\text{mm}^3$ corrosion coupons used in oxidation exposures. (b) 1 mm thick dog bone samples used for SCC tests.

The corrosion coupons were machined and supplied by EDF from the as forged and 15% cold worked materials, electric discharge machining (EDM) was used. Non-square samples were used such that the orientation could be noted. For the as-received coupons, the 20 mm length was along the tube axis whilst the 19 mm was along the circumference of the tube. For the cold worked coupons, the 20 mm length was in the direction of cold work and the 19 mm along the circumference of the tube. The orientation of the samples was known, but the location relative to the tube was not.

Tensile specimens were used for the SCC tests. These samples were extracted from WF675 which was cold-rolled to 19%. The specimen orientation was such that the applied load in the SCC tests was in the transverse direction of cold-rolling and crack propagation would occur in the longitudinal direction.

CHAPTER

FIVE

ENVIRONMENTAL EXPOSURES

5.1 Hydrogenated Steam Testing Systems

PWSCC testing is generally carried out in high temperature, pressurised autoclave loops, which are costly and complex due to the high pressures required. The possibility of using low pressure hydrogenated steam, which is capable of reproducing similar oxidising electrochemical potentials, is being examined. Hydrogenated steam exposures benefit from reduced costs as a result of the low test pressures, this also reduces the risk associated with test and allows the tests to be conducted at higher temperatures than that obtainable in conventional autoclave testing.

The environment produced in the hydrogenated steam system can be characterised by the ratio (R). This is the ratio of the partial pressure of oxygen at the Ni/NiO transition point to the partial pressure of oxygen in the system which is used, such that a value of eight implies that there is eight times less oxygen than required to oxidise nickel. For comparison of steam tests to autoclave tests, the test parameter R for steam tests can be converted to an equivalent cc/kg of hydrogen at a given temperature. Details of this calculation can be found in Appendix A.

The first system (Rig 1) is used for the oxidation of coupons. Rig 2 is based on the same design as Rig 1, but modified to accommodate a tensile tester, thus allowing it to carry out SCC tests under constant load conditions.

5.1.1 Calculations

PWSCC susceptibility increases significantly in the region of the Ni/NiO transition point; for this reason it was decided that tests should be carried out at potentials within this region. The measure of the steam environments potential can be seen as an abstract value as the potential of a non-conductive medium has no physical meaning. As such the potential of the system is defined by R_{test}, this is the ratio of the partial pressure of oxygen at the Ni/NiO transition point ($PO2_{Ni/NiO}$) to partial pressure of oxygen in the system (PO_2), such that a value of eight implies that there is eight times less oxygen than required to oxidise nickel.

$$R_{test} = \frac{PO2_{Ni/NiO}}{PO_2} \tag{5.1}$$

The calculations for the oxygen partial pressure of the system is not trivial, the following details these calculations in terms of the flow rates with the aim of calculating the required flow rate of hydrogen for the system to be at the Ni/NiO transition point. Based on this methodology, the effect of any variable and defining of the environment of the system can be extracted.

The starting point is calculating the required oxygen partial pressure at the equilibrium point and the oxygen partial pressure in the steam (the hydrogen directly controls this). The oxygen partial pressure is derived from the Gibbs free energy (5.3) of reaction (5.2).

$$Ni + \frac{1}{2}O_2 \rightleftharpoons NiO \tag{5.2}$$

$$\Delta G_{NiO} = \Delta G^0_{NiO} - RT\ln\left[\frac{a[NiO]}{a[Ni]a[O_2]^{\frac{1}{2}}}\right] \tag{5.3}$$

where ΔG_{NiO} is the Gibbs free energy of the reaction, Δ^0_{NiO} is the Gibbs free energy of formation, R is the universal gas constant, T is the absolute temperature and $a[NiO, Ni, O_2]$ is the activity of NiO, Ni and O_2 respectively.

The Ni/NiO transition point is the equilibrium point, therefore ΔG_{NiO} is zero. The activity of a solid is unity, therefore $a[NiO] = a[Ni] = 1$. The activity is equivalent to the partial pressure (p), hence it can be written as (5.4):

$$0 = \Delta G^0_{NiO} - RT\ln\left[\frac{1}{pO_{2_{Ni/NiO}}}^{\frac{1}{2}}\right] \tag{5.4}$$

This rearranges to give:

$$pO2_{Ni/NiO} = \exp\left[\frac{2\Delta G^0_{NiO}}{RT}\right] \tag{5.5}$$

The partial pressure of oxygen in steam is calculated from reaction (5.6).

$$H_2O \rightleftharpoons H_2 + \frac{1}{2}O_2 \tag{5.6}$$

The Gibbs free energy associated with this reaction is given by:

$$\Delta G_{H_2O} = \Delta G^0_{H_2O} - RT \ln \left[\frac{p[H_2]p[O_2]^{\frac{1}{2}}}{p[H_2O]} \right] \tag{5.7}$$

where ΔG_{H_2O} is the Gibbs free energy of the reaction, $\Delta G^0_{H_2O}$ is the Gibbs free energy of formation, R is the universal gas constant, T is the absolute temperature and p is the partial pressure.

Assuming the system is at equilibrium ($\Delta G_{H_2O} = 0$), it rearranges to give the oxygen partial pressure to be:

$$pO_2 = \left(\frac{pH_2O}{pH_2} \right)^2 \exp \left[\frac{2\Delta G^0_{H_2O}}{RT} \right] = R^2_{steam/H_2} \exp \left[\frac{2\Delta G^0_{H_2O}}{RT} \right] \tag{5.8}$$

R_{steam/H_2} is the ratio of steam to hydrogen. In the steam oxidation rig, this value is known at room temperature (it is assumed that the ratio of flow rates is equivalent to the ratio of pressure). The flow rates at the operating temperature can be calculated from equations (5.9) and (5.10).

$$F_{steam} = \frac{F_{H_2O} D_{H_2O_{steam}}}{D_{H_2O}} \tag{5.9}$$

$$F_{H_{2HT}} = \frac{F_{H_{2RT}} T_{HT}}{T_{RT}} \tag{5.10}$$

where F_{steam} is the flow rate of steam, F_{H_2O} is the input flow rate of water, $D_{H_2O_{steam}}$ is the density of the steam and D_{H_2O} is the density of water at the input temperature. $F_{H_{2HT}}$ is the hydrogen flow rate at high temperature, $F_{H_{2RT}}$ is the hydrogen input flow rate, T_{HT} is the operating temperature and T_{RT} is the input temperature.

Hence R is given by:

$$R_{steam/H_2} = \frac{F_{steam}}{F_{H_{2HT}}} = \frac{F_{H_2O} \cdot D_{H_2O_{steam}} \cdot T_{RT}}{F_{H_{2RT}} \cdot T_{HT} \cdot D_{H_2O}} \tag{5.11}$$

The values of ΔG^0 can be calculated by equation (5.12).

$$G^0 = A + BT \log T + CT \tag{5.12}$$

The book values of A, B and C are given in Table 5.1.

Table 5.1 – Book values for the Gibbs free energy [159].

	NiO	H_2O
A ($Jmol^{-1}$)	-232450	-239648
B ($Jmol^{-1}K^{-1}$)	0	18.75
C ($Jmol^{-1}K^{-1}$)	83.435	-9.25

From the combination of equations (5.8), (5.11) and defining the oxygen partial pressure in (5.5), the hydrogen flow rate can be calculated by (5.13).

$$F_{H_2RT} = \left(\frac{F_{H_2O} \cdot D_{H_2O_{steam}} \cdot T_{RT}}{T_{HT} \cdot D_{H_2O}}\right) \frac{1}{pO_2} \exp\left[\frac{2\Delta G_{H_2O}}{RT}\right] \tag{5.13}$$

5.1.2 Calibration

The calculated environment is dependent on the hydrogen and water flow rates, as such for the knowledge of the produced steam environments, these flow rates must be calibrated. However, as there is variation in the book values required for the calculations the produced environment should subsequently also be tested. The following outlines the methods used for the calibrations, the results of which can be found in Appendix B.

5.1.2.1 Flow Rates

The flow rate of water in the tests is controlled by a variable speed peristaltic pump. The flow produced by the pump is not entirely constant, but oscillates around a mean value as a result of the pumps nature. As a result of the pump variation the stated environment is a time averaged environment not static as might be expected. The small fluctuations will produce a slight variation in the produced oxygen partial pressure, the time period of the oscillation corresponds to a single rotation of the pump head. The time for a single rotation is dependent on the pumps flow rate, but in the region of one minute.

The variable speed pumps can be calibrated by measuring the volume of liquid displaced over a given time, the time of the measurement should be sufficiently long to allow multiple rotations of the head to occur, thus allowing an accurate time average measurement. Due to the low flow rates used (≈ 1 dm^{3}min^{-1}), the measurements are made by connecting the pump to the bottom of a burette and recording the volume filled in a given time, as illustrated in Figure 5.1.

By the use of a liquid impermeable to the hydrogen, the flow rate of hydrogen can be measured much in the same way as the pump calibration. The liquid used was

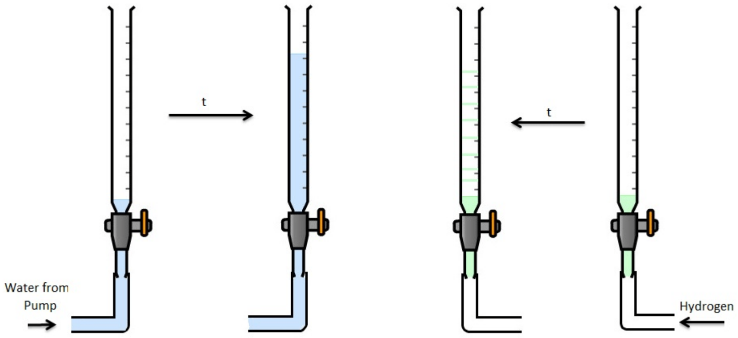

Figure 5.1 – Calibration set up used for calibrating the water pump and hydrogen flow rates.

a concentrated soap which is intended for dilution; however any thick liquid soap should be suitable. A small amount of the liquid is placed in the bottom of the burette and hydrogen allowed to flow into the burette from the bottom, as it flows, due to the impermeable nature bubbles form. The flow of theses bubbles allows the hydrogen flow to be visualised and thus the flow rate can be measured (Figure 5.1).

5.1.2.2 Environment

The environment can be calibrated by the use of nickel 200 (99% pure nickel). Small samples of the alloy prepared with a P600 surface are placed into the system for a short 24 h test at 400 °C. Running tests around the Ni/NiO transition point and checking for the presence of nickel oxide on the surface allows a quick check of the environment the sample was exposed to. The nickel oxide is visually observed via a colour change in the samples, this is further checked by grazing angle X-ray diffraction used to identify the phases present.

5.1.3 Oxidation Rig (Rig 1) - Samples

Rig 1 is the hydrogenated steam rig used for oxidation tests. The system was built and operated in a fume cupboard, Figure 5.2 shows a schematic of the system.

The rig operates by a deionised water source being pumped by a variable speed peristaltic pump into a preheating brass block. The brass block is preheated to 150°C to vaporise the water and generate steam. The preheating stage also acts as a mixing point for the hydrogen and water to form the hydrogenated steam mixture. The hydrogen flow rate was controlled by a needle valve flux meter.

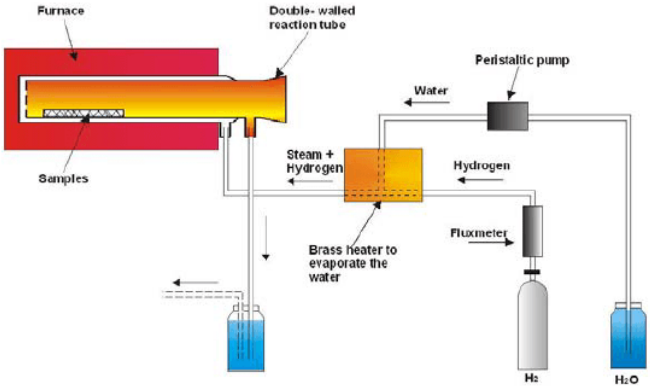

Figure 5.2 – Schematic of the steam oxidation rig used to test samples [14].

During the course of the project, the needle valve control system was upgraded to an electronic flow meter, the electronic flow meter was installed before the needle valve flux meter. As such the flow rate was controlled by the electronic flow meter, but measured by the needle valve flux meter. This allowed the same calibration to be used, but with a more consistent flow. The hydrogenated steam mixture was then passed through the outer section of the double walled reaction vessel; this heats the mixture to the desired temperature. The heated mixture is then passed back through the inner tube and over the samples. The mixture was disposed of by condensing the mixture, allowing the hydrogen to be released and safely vented via the fume cupboard. The procedure for the operation of this system is summarised in Appendix C.

The samples used in the oxidation were corrosion coupons ($2 \times 19 \times 20$ mm^3); coupons of both the as received and the 15% cold worked WF675 were used. The samples were placed on a quartz sample boat and placed with the surface of interest face up, the reverse of the samples were not analysed as the flow in this region was limited by the geometry of the quartz sample boat. Tests were conducted on samples with both a OPS and P600 surface finish. In all tests, the reverses of the sample were prepared to a minimum of a P600, this was to ensure any contamination in the sample from the EDM was removed and thus not to compromise the exposure. All samples were cleaned prior to exposure.

5.1.4 SCC Test Rig (Rig 2) - Samples

The steam generation in Rig 2 is much the same as that in Rig 1, with the exception that a stainless steel block is used in the preheater. The gas flow is controlled and monitored via a needle valve flux meter.

A Ni 200 tube is used for the construction of the reaction chamber; this is vertically mounted within a 10 kN Instron tensile machine. The steam gas mixture is heated via coiling of the inlet pipe through the chamber. The Pull-rod seals to the chamber are cooled by a 2 kW chillier to prevent any leakage. The experimental setup is summarised in Figure 5.3. The procedure for the operation of this system is summarised in Appendix D.

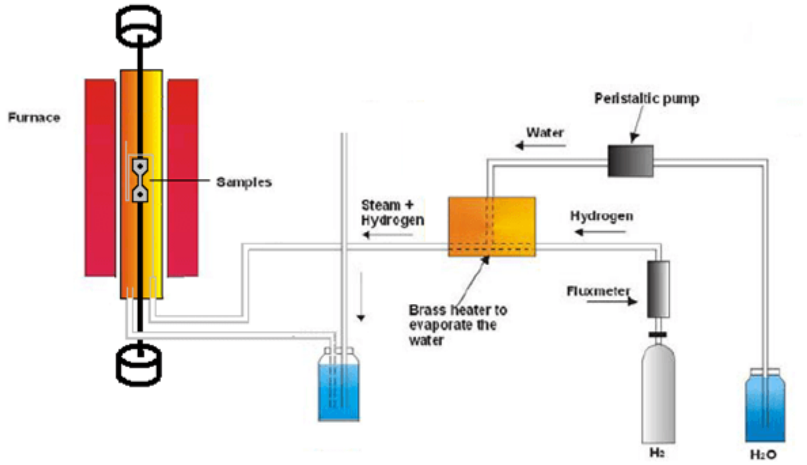

Figure 5.3 – Schematic of the steam oxidation rig built to conduct SCC tests.

Dog-bone samples were used for the SCC tests. These samples were extracted from WF675 which was cold-rolled to 19%. The specimen orientation was such that the applied load in the SCC tests was in the transverse direction of cold-rolling and crack propagation would occur in the longitudinal direction. This orientation was chosen as it has been shown to be one of the most susceptible to PWSCC [113]. The samples were finished to an OPS standard on one side with the reverse being P600 (note the OPS finish was applied after the P600 to mitigate the possibility of the finish being compromised), thus allowing the effect of surface finish to be investigated in the SCC tests. All samples were cleaned prior to testing.

5.2 Autoclave Testing - Samples

For reference to the hydrogenated steam tests, exposures were conducted in pure water with a hydrogen overpressure. A 316L SS autoclave which was designed and built by Cormet was used for the exposures. The autoclave (Figure 5.4) has a 1 litre capacity and can be operated up to 350°C at 200 bar. The autoclave was originally designed for conducting tests in oxygenated environments and subsequently had to be modified for the hydrogenated testing.

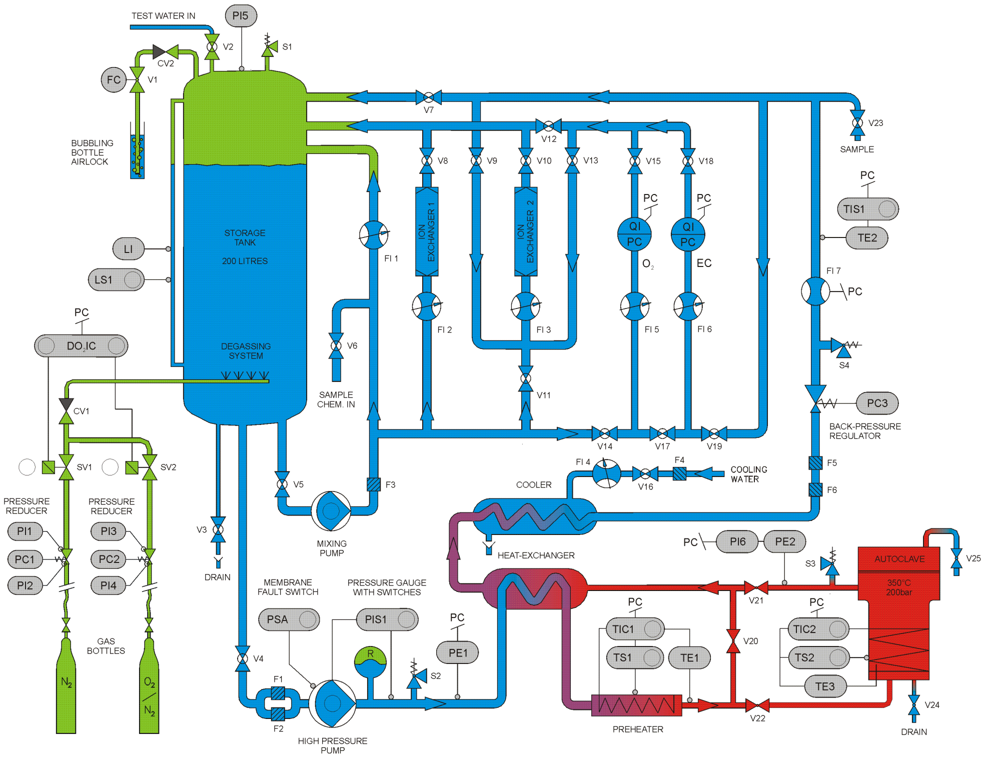
TEST WATER IN
PI5
V2
S1
CV2
FC
V1
BUBBLING BOTTLE AIRLOCK
STORAGE TANK
200 LITRES
DEGASSING SYSTEM
LI
LS1
PC
DO,IC
CV1
SV1
SV2
PRESSURE REDUCER
PRESSURE REDUCER
PI1
PC1
PI2
PI3
PC2
PI4
GAS BOTTLES
N_2
O_2
N_2
V3
DRAIN
V4
F1
F2
HIGH PRESSURE PUMP
V5
F3
MIXING PUMP
V6
SAMPLE CHEM. IN
FI 1
V7
V8
V9
V10
V12
V13
V15
V18
ION EXCHANGER 1
ION EXCHANGER 2
FI 2
FI 3
V11
QI PC
QI PC
PC
PC
O_2
EC
FI 5
FI 6
V14
V17
V19
FI 4
V16
F4
COOLING WATER
COOLER
HEAT-EXCHANGER
MEMBRANE FAULT SWITCH
PRESSURE GAUGE WITH SWITCHES
PSA
PIS1
R
S2
PC
PE1
V23
SAMPLE
PC
TIS1
TE2
FI 7
PC
S4
PC3
BACK-PRESSURE REGULATOR
F5
F6
PC
PI6
PE2
S3
AUTOCLAVE
350°C
200bar
V25
V21
V20
V22
PC
TIC1
TS1
TE1
PC
TIC2
TS2
TE3
PREHEATER
V24
DRAIN

Figure 5.4 – Cormet supplied schematic of the used autoclave.

The autoclave was converted from an oxygenated environment to a de-aerated environment by closing off both the N_2 and N_2/H_2 cylinders. A hydrogen over-pressure was introduced to the system breaking in to the pipe between CV1 and the degassing system and connecting to a hydrogen cylinder. Both a manual and non-return valves were installed to prevent the hydrogen cylinder back filling with water should the gas supply be exhausted. The hydrogen over-pressure was controlled by regulating the cylinder outlet pressure.

The samples used for the autoclave exposure were corrosion coupons ($2 \times 19 \times 20$ mm^3). Samples of the as received and 15% cold worked forms WF675 were exposed. The surface finish on all samples was a P600 on one side and the reverse being polished down to OPS, multiples of each material were placed in the 1 litre chamber to allow both surfaces to be fully examined in the post test analysis. The samples were spot welded to a nichrome wire and suspended from a custom build clothes line like assembly (Figure 5.5).

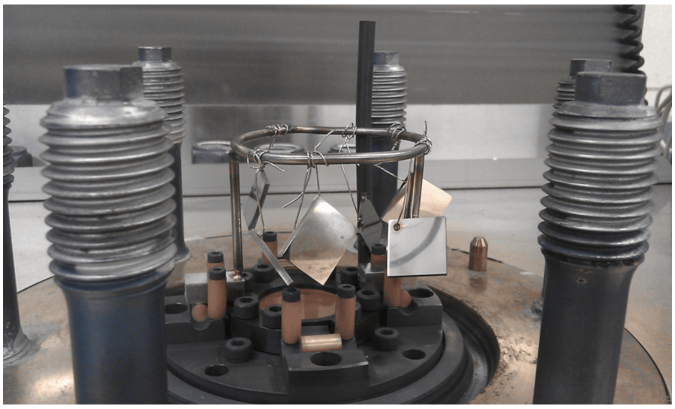

Figure 5.5 – Photo of the samples suspended in the autoclave prior to exposure.

CHAPTER

SIX

MICROSCOPY AND ANALYSIS TECHNIQUES

A number of microscopy and analytical techniques have been used in the completion of this thesis, the majority of which can be classed as analytical electron microscopy (AEM). X-ray diffraction, optical microscopy and heavy ion milling have been used in addition to the AEM.

6.1 SEM

6.1.1 Overview

Scanning electron microscopy (SEM) is an electron optic method by which an electron beam is focused on to the surface of a sample; this beam is scanned across the region of interest. A number of possible interactions can occur between the incident beam and the sample. The detection of these interactions can be used for imaging different features of the sample. The possible interactions and the location at which they occur relative to the sample surface can be seen in Figure 6.1.

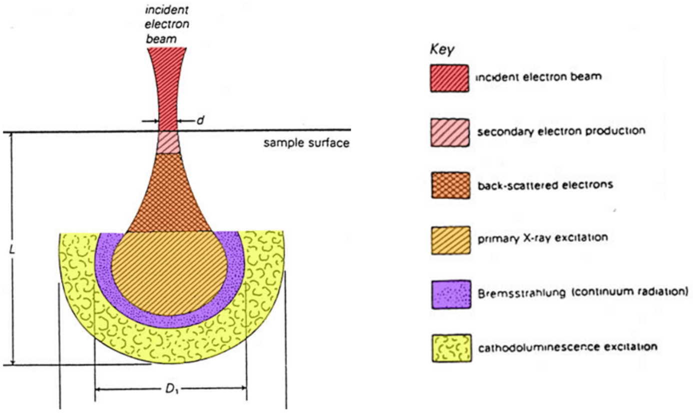
incident electron beam
d
sample surface
L
D₁
Key
incident electron beam
secondary electron production
back-scattered electrons
primary X-ray excitation
Bremsstrahlung (continuum radiation)
cathodoluminescence excitation

Figure 6.1 – Schematic showing the location and geometry of possible electron beam interactions within a sample. Image adapted from [160].

Secondary electrons (SE) are the result of an electron exciting one or more atoms such that an outer shell electron is liberated, thus creating a secondary electron. Backscattered electrons are a result of electrons from the primary beam being reflected from scattering events.

6.1.2 Imaging Modes

The SE1 (Inlens) detector is used for detecting secondary electrons which are produced from a single (primary) interaction of the incident electron beam. The angle at which these electrons are generated is near parallel to the incident beam, as such the detector used must be placed in the lens (hence the name). The images produced from the Inlens are topographic dependent with a little influence of atomic number (Z).

The SE2 (SE) detector is used for detection of secondary electrons created by backscattered electrons. The SE2 electrons can be seen to be generated from a larger volume relative to the SE1 (Figure 6.1) and thus has a lower resolution, but a higher intensity and escape angle (easier detection). The SE2 image is dominated by the local topography of the sample.

The backscattered detector detects electron which are from the incident beam and as a result of elastic interactions have been scattered back out of the material. Given the number of interactions required to produce a backscattered electron (BSE), the intensity of the signal is less than that of the SE. In addition to a BSE detector, other detectors can be used to identify BSEs from specific interactions, theses include:

- Energy selective backscattered (EsB) detector
- Angle selective backscattered (AsB) detector

The BSE and EsB can be seen to produce images from which the contrast is dependent upon the atomic mass, AsB is dependent upon Z and the crystallographic orientation.

Electron backscatter diffraction (EBSD) mapping is a method by which produced diffraction patterns (Kikuchi lines) from a location on a sample are indexed to determine the crystallographic orientation. Unlike the previous detection methods which have no specific sample conditions other than electrical conductivity (and ideally that the sample is level), this requires that the sample surface be prepared such that it is strain free. This is achieved in this thesis via OPS or electrochemical polishing; the indexing rate has been improved in some cases by the use of plasma cleaning the surface.

Energy dispersive X-ray (EDX) detection, these X-rays are produced as the result of atomic excitations, the relaxation of the atom to the ground state is achieved via the emission of a X-ray, the energy of the emitted X-ray is characteristic of the element excited. Each element has a number of possible excitations, the probability of excitation decreases with Z.

It should be noted that a number of these excitations energies used for EDX overlap within the resolution of the EDX detectors ($\approx 130\ eV$), thus making quantification of specific elements complex. The most notable of the overlaps in this thesis is the chromium L peak and the oxygen K peak. The K peaks are the most intense and thus used for quantification, the result of this is that high chromium levels can lead to an artificial detection of oxygen, but not vice versa.

The accelerating voltage can be seen to affect the produced image; lower voltages result in a smaller interaction volume (the values of D_1 and L in Figure 6.1 can be seen to decrease) and greater elemental contrast. However, lower accelerating voltages are associated with a lower beam current and thus a reduction in signal (intensity).

6.1.3 Utilised SEM's

A number of SEM's have been used for the completion of this project, the following is a brief summary of all machines used and their capabilities:

- CamScan MX2000: FEG SEM with EBSD.
- FEI Quanta 650: FEG SEM with EDX (SDD) and EBSD.
- Philips XL30: FEG SEM with EDX and EBSD.
- Zeiss Evo 50: Tungsten filament SEM with EDX.
- Zeiss Evo 60: Tungsten filament SEM with EDX.
- Zeiss Ultra 55: Gemini column FEG SEM with EDX and EBSD.

Note: Field emission gun (FEG) is superior to the tungsten filament machines and the silicon drift detector (SDD) for EDX is far superior to the other EDX detectors.

Although a large number of SEM's have been utilised for the completion of the project, the results presented have in the majority come from the Ultra 55 (low voltage imaging), Quanta 3D FIB SEM (discussed in a following section) and the CamScan (used for EBSD work).

6.2 FIB

6.2.1 Overview

The focused ion beam (FIB) used in this project was a Quanta 3D, a dual beam FIB SEM (has a gallium ion beam and a electron beam). The electron beam in the FIB SEM is orientated at 52 ° relative the ion beam, normal operation is carried out such that the sample surface is normal to the ion beam (Figure 6.2).

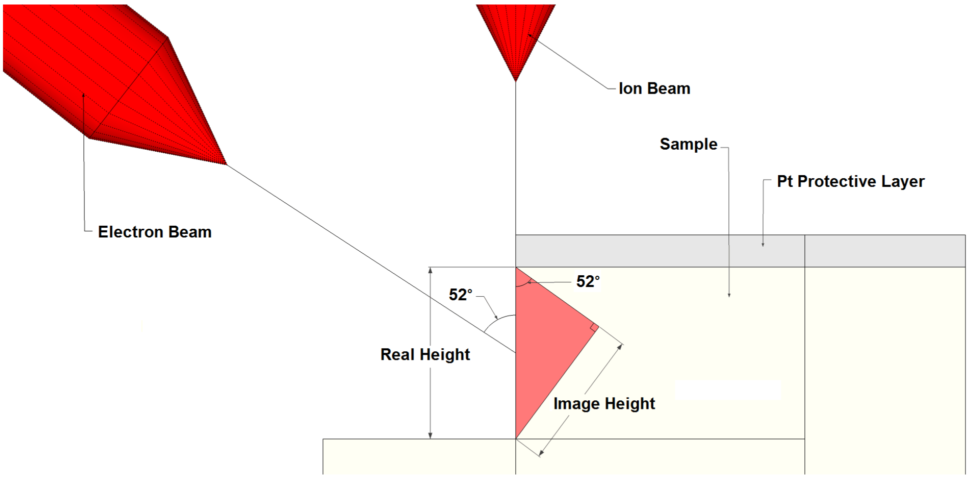

Figure 6.2 – Schematic representation of the geometries present in the operation of the FIB. Image adapted from [161].

The gallium ion beam allows milling of the sample to be achieved. Platinum can be deposited on the sample via a needle injecting a platinum hydrocarbon based gas, the electron or ion beam can be used to ionise the gas thus depositing the platinum onto the surface in a user defined pattern, beam current and deposition time can be used to control the deposited depth. An Omni probe micro manipulator allows for the manipulation and removal of created samples.

The main uses of the FIB were for the production of cross-sections, 3D serial sections and TEM samples. The following is intended as a brief overview of these techniques and not a comprehensive guide to the operating procedure.

6.2.2 Cross-Sectioning

The production of a FIB cross-section can be divided into four steps, these are:

1. Identify a region of interest.
2. Deposit a protective layer on the order of $2 \times 15 \times 1$ µm^3 ($h \times w \times d$) on the region of interest (the depth is dependent on the size of any features at the surface, it should be sufficiently deep to produce a flat surface obscuring

any surface features). This layer acts to protect the surface in the region of interest during the subsequent milling.

3. An initial "rough cut" trench is milled in advance of the platinum layer. The trench should be as long as it is deep, and slightly wider than the protective layer applied. The depth is dependent upon the feature to be imaged, ≈ 2× depth of feature should be considered a minimum. This milling is carried out simultaneously (the entire area is milled at the same time). This trench can be milled at high current.
4. Polish the surface of interest, this is achieved by sequential milling (mills carried out as a set of line scans) carried out at decreasing beam currents until no striations are present on the surface of interest and the region is under the protective layer.
5. Image the region of interest, this can be achieved via the FIB SEM or other SEM's, depending on the required imaging modes.

This sequence is summarised in Figure 6.3.

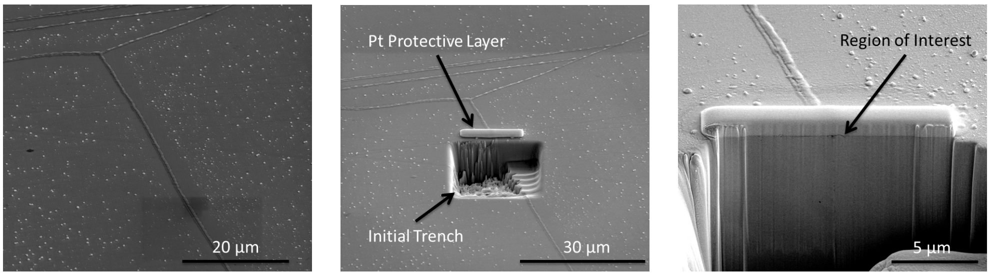

(a) (b) (c)

Figure 6.3 – Outline of stages in the preparation of a FIB cross-section.

6.2.3 Serial Sectioning

Serial sectioning can be seen as an extension of the cross-section method; however instead of producing a single cross-section, a series are produced from a selected region. The preparation follows that of the previously described for a cross-section with a number of small alterations.

Platinum is deposited on the region which is to be imaged, typical on the order of $15 \times 15 \times 1$ µm^3 ($h \times w \times d$). As with the cross-sectioning a rough trench is placed in front of the region which is to be imaged. In addition to this the sides of the region to be imaged are removed (Figure 6.4(a)). All three sides surrounding the platinum are polished to an imageable quality. The slice and view software is then used to sequentially remove slices from the surface of interest and image the resulting surface. Figure 6.4 shows the results of the preparation done prior to useing the slice and view software; note that the cross at the top of the image is used for drift correction and is produced via the software if user defined.

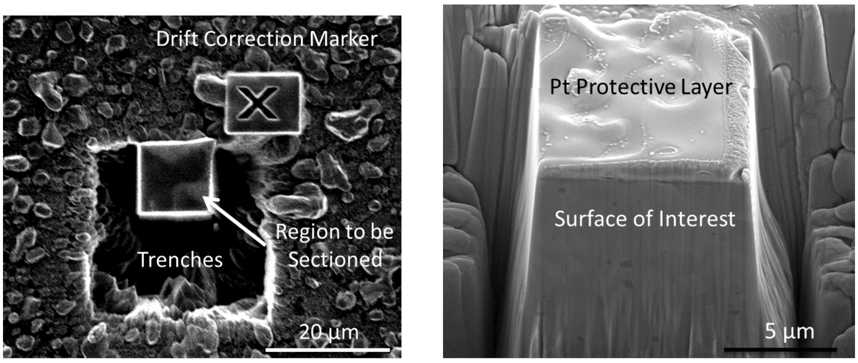

(a) (b)

Figure 6.4 – Ion beam (a) and electron beam (b) images showing a sample prepared for serial sectioning.

6.2.4 TEM Sample Preparation

The initial stages of TEM sample preparation is similar to that of the cross-sectioning method outlined. A protective platinum layer on the order of $2 \times 15 \times 1$ µm^3 ($h \times w \times d$) is applied to the surface over the region of interest. The sample is then milled as if it was being prepared for a cross-section, but the milling is conducted from both sides such that on completion a 1 µm lamella is produced. The milling should be conducted with each step being completed on both sides before moving to the next, i.e. both rough cuts are produced before any polishing.

The next stage is to undercut the sample such that it can be removed, the TEM sample preparation used in this thesis uses the in-situ lift-out method, and as such a J undercut is used. The J undercut leaves a small region of the sample attached to the bulk thus preventing the sample from falling over. The Omni probe is used to lift out the sample, the probe is attached to the sample by the use of platinum deposition, the join to the bulk left by the J undercut is then milled, freeing the lamella and allowing it to be lifted out.

Once the lamella is lifted out, it needs to be attached to a TEM grid, a half crescent FIB TEM grid (both 3 and 4 post grids have been used, but it is recommended that no more than one sample be placed on a single grid, regardless of available posts) is used. The lamella is joined to a post on this grid via platinum deposition, once connected it is milled free from the Omni probe.

The final stage is to thin the sample to electron transparency. This is achieved in the same way as the final polishing stages in the cross-sectioning. The sample should be thinned evenly from both sides to ensure re-deposition from the lift out process is removed.

The stages in the production of the TEM lamella are summarised in Figure 6.5.

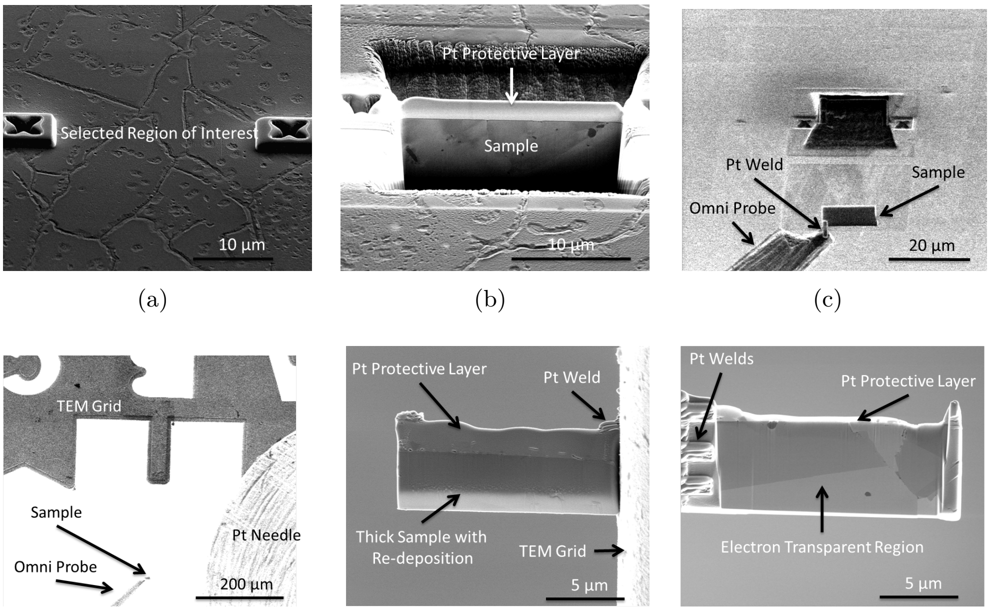
Selected Region of Interest
10 µm
Pt Protective Layer
Sample
10 µm
Pt Weld
Sample
Omni Probe
20 µm
TEM Grid
Sample
Pt Needle
Omni Probe
200 µm
Pt Protective Layer
Pt Weld
Thick Sample with Re-deposition
TEM Grid
5 µm
Pt Welds
Pt Protective Layer
Electron Transparent Region
5 µm

(a) (b) (c)

(d) (e) (f)

Figure 6.5 – Outline of stages in the preparation of a FIB TEM sample.

6.3 TEM

6.3.1 Overview

Transmission electron microscopy (TEM) is an electron optic method in which the electrons transmitted through a sample are analysed to produce images. The TEM used in the completion of this thesis was a FEI Tecnai TF30 300keV STEM (Scanning transmission electron microscopy). The Tecnai is capable of producing a wide range of images from multiple modes, the imaging modes predominately used are:

- Bright field (BF) imaging: This is a projection produced by the beam as a result of transmission, higher atomic masses or thicker parts of a sample will produce a higher attenuation of the beam and a darker contrast, a hole on contrast will suffer no attenuation and hence produce a bright spot.
- Diffraction imaging (part of the BF image): Image produced as a result of Bragg scattering of the electron beam, the resulting image is highly dependent on the crystallography (and thus the orientation of the sample).

- High angle annular dark-field imaging (HAADF): The image produced via HAADF is a result of high angle incoherent scattering of the electron beam, the incoherent nature of the scattering results in there being little to no crystallographic information in the image. HAADF images contrast can be seen to be proportional to Z^2 [162].

The Tecnai is also equipped with an Oxford instruments X-max 80 SDD EDX detector. The EDX used in STEM operates by the same principle as the EDX in SEM, however the thin nature of the sample implies a significantly improved spatial resolution. The produced spectra are still however susceptible to the overlapping peak issue as stated in the previous section (chromium oxygen).

A generalised schematic of the electron optics associated with a TEM can be found in Figure 6.6, however it should be noted that there can be significant variation between different systems.

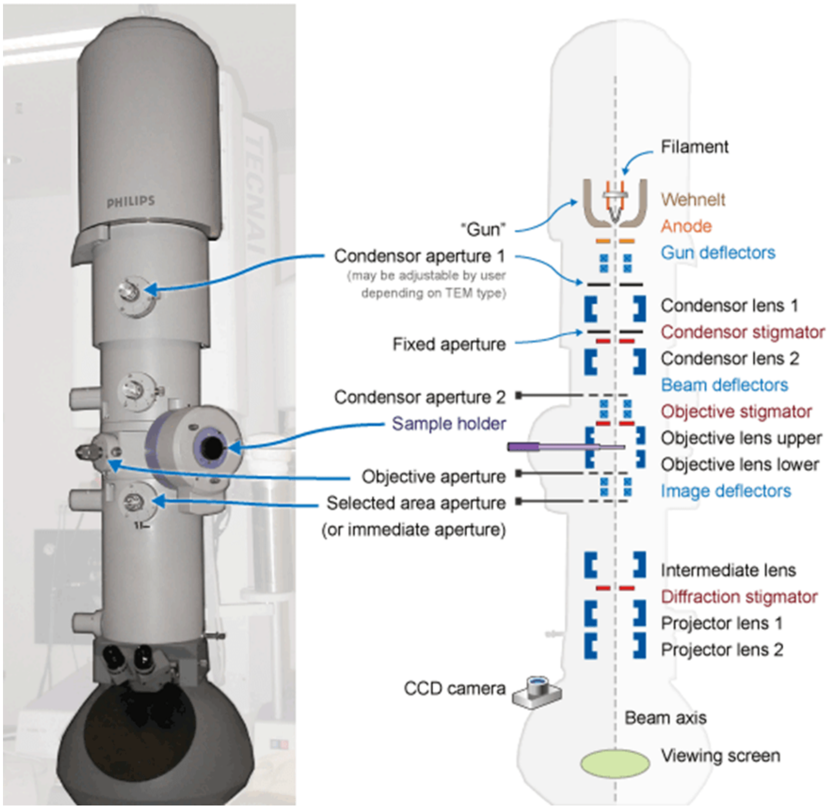
PHILIPS
TECNAI
Filament
Wehnelt
"Gun"
Anode
Gun deflectors
Condensor aperture 1
(may be adjustable by user depending on TEM type)
Condensor lens 1
Fixed aperture
Condensor stigmator
Condensor lens 2
Beam deflectors
Condensor aperture 2
Objective stigmator
Sample holder
Objective lens upper
Objective lens lower
Objective aperture
Image deflectors
Selected area aperture
(or immediate aperture)
Intermediate lens
Diffraction stigmator
Projector lens 1
Projector lens 2
CCD camera
Beam axis
Viewing screen

Figure 6.6 – Schematic representation of the electron optics associated with TEM and example instrument [163].

6.3.2 Sample Preparation

Despite TEM having significantly improved resolution relative to SEM, its use is severely limited by the required sample preparation; three methodologies have been used for the production of TEM samples.

Mechanical preparation combined with ion beam thinning was used to produce samples from the bulk and surfaces (the surface TEM work published all originated from the FIB). Electrochemical preparation can produce samples from the bulk with relative easy, but the method is not suitable for surface samples. Focused Ion Beam (FIB) can produce samples from a specific location, but is not suitable for bulk samples, in addition the equipment cost and availability can be seen as a severe limitation.

6.3.2.1 PIPS

The preparation of TEM samples from the bulk first required the production of thin (sub 250 µm) wafers of the material, 3 mm discs were then punched from the wafers. The discs were then polished to a 4000 grit finish on both sides, in the process the samples were thinned to sub 100 µm. The produced discs were then thinned by dimpling on both sides using a 1 µm diamond paste. Once dimpled the final thinning was achieved via ion beam thinning. A gatan PIPS^{TM} (Precision Ion Polishing System) 691 was used for this process.

The method used for surface samples was the same as the bulk, except for the production of the initial 3 mm discs. The initial discs were produced using the inserts outlined in [164], the material placed in the inserts consisted of two surface samples with the surface of interest glued together, such that the surface of interest was in the centre of the insert.

6.3.2.2 Electrochemical Polishing

A Struers tenupol-5 with a closed cycle refrigeration unit was used for the electrochemical preparation of TEM samples. 3 mm discs were first produced from the bulk alloy and mechanically thinned to sub 100 µm with a 1200 grit finish, as in the previous method but with the surface finish being less critical. The produced discs were electrochemically thinned to electron transparency in the tenupol, a 20% perchloric in methanol electrolyte maintained at 17°C was used.

6.3.2.3 Focused Ion Beam

The TEM sample preparation via FIB is outlined in section 6.2.4.

Part III

Results and Discussion

CHAPTER

SEVEN

MATERIAL CHARACTERISATION

The material predominately used in this thesis is heat WF675 (EDF Reference U589) and was manufactured by Imphy. WF675 is a forged heat of Alloy 600 which has been used for control rod drive mechanism (CRDM) nozzles. The material is examined in three conditions:

- As-Received (AR): This material is in the state it was supplied; forged, then subjected to a final heat treatment of 2 h at 820°C.
- 15% Cold Worked (15%CW): This material has been cold-worked in tension along the tube axis to a strain of 15%.
- 19% Cold Worked (19%CW): This material has been cold-rolled along the tube axis to a 19% reduction.

The AR and 15%CW materials were supplied by EDF, whilst the 19%CW was produced from the supplied AR material at Manchester University. The microstructure of these materials is examined and the general effect of surface finish on Alloy 600 is explored.

Given the complex strain path present in the forging and the highly strained nature of the cold worked alloys, it was decided that a reference, solution annealed (SA) alloy, should be investigated. The material used in the solution annealing was from pressure vessel tubing; this was produced by B&W Tubular Products Division and was designated heat HT93510. The work carried out on the solution annealed alloy was in collaboration with Giacomo Bertalli (a master's student on a corrosion MSc) as part of his masters project.

The chemical composition of WF675 has previously been characterised by EDF, this work was published in [11]. The results were obtained by combustion/infrared absorption for the light elements and X-ray fluorescence for the heavy elements.

The chemical composition of HT93510 was supplied by the manufacturer. These compositions are shown in Table 7.1 along with the specification of production, RCC-M 4102. WF675 is within specification for all elements with the exception of titanium and aluminium, which are less than specified for the alloy.

Table 7.1 – Chemical composition of WF675 and HT93510 compared to the specification (wt. %).

Element	**RCC-M 4102**	**WF675**	**HT93510**
Ni	> 72.0	73.20	74.43
Cr	14.0 – 17.0	16.05	15.42
Fe	6.0 – 10.0	8.80	8.94
C	< 0.10	0.058	0.047
Mn	< 1.0	0.81	0.23
Si	< 0.5	0.45	0.30
S	< 0.015	< 0.001	0.002
P	< 0.025	0.007	0.005
Cu	< 0.5	0.02	-
Co	-	0.04	0.057
Al	0.2 – 0.8	0.29 (Al+Ti)	-
Ti	0.65 – 1.15		-

7.1 WF675

The microstructure of the AR (WF675) material has had some characterisation carried out previously, most notably the work based on the lattice strains (calculated from lattice curvature observed in EBSD) in the alloy and how this was related to the PWSCC susceptibility [11,165]. The work suggested that there is an inhomogeneous grain size within the microstructure of WF675; as a result there are regions of large grains within the relatively fine grained microstructure. There are also conflicting reports on the carbide distribution within the alloy, mostly with respect to the grain boundary coverage.

The work in the literature is used as a point of reference in the proceeding microstructural characterisation. Where possible, explanations of the reported and observed discrepancies are suggested.

7.1.1 Grain Size

The grain size of the materials has been investigated; this was achieved via processing of produced EBSD maps (optical observations made were found to be consistent with the EBSD results). Figure 7.1 shows typical EBSD maps obtained from the three materials[1]. The materials for oxidation studies (AR and 15%CW) were examined from the surface which was to be oxidised and the 19%CW material used for SCC was examined in the plane normal to the loading axis.

The results from these maps showed that all the materials had a non-equiaxial grain structure (the results discussed here exclude the abnormal grains, which are discussed at the end of the section). The AR material had $\approx 2:1$ aspect ratio in favour of the tube direction in all analysed EBSD maps; however the measured grain size varied significantly with the average grain size in the tube direction ranging between $11 - 25$ µm ($6 - 15$ µm in the circumferential direction) when measured from different samples of the same material.

In both the cold worked alloys, the grain structure appeared to be more uniform relative to the AR; this is concluded from the performed analysis of EBSD maps which showed consistent average grain sizes, but an insufficient number of samples were mapped for this analysis to be statistically confirmed. It can also be noted that during analysis of the oxidation tests, in which thermal etching had occurred, a more variable grain size was observed on the cold worked material. The 15%CW had a $\approx 3:1$ aspect ratio in favour of the tensile direction. The 19%CW samples were mapped from TEM samples; as a result of this method, the orientation of the sample was unknown. The maps were obtained from the plane of propagation; the primary purpose of the mapping was to determine the grain boundary character.

The EBSD maps shown in Figure 7.1 show the homogenous grain structure observed in the alloy, the grain size variation mentioned was a result of taking maps from different samples; however regions in which an extreme grain growth had occurred were observed. Examples of this grain growth are shown in Figure 7.2, it should be noted that the map scale bars in these images are comparable to the like materials shown in Figure 7.1.

These coarse grains (up to 0.5 mm) have previously been report in [11] and were found to occur more frequently in samples from the outer wall of the forging, given that the samples were provided with only orientation data and not location relative to the forging this hypothesis could not be confirmed.

---

[1] EBSD maps taken from AR-WF675 and 15%CW-WF675 are low resolution (1.5µm step size) maps taken during the initial characterisation of the material. The 19%CW-WF675 material was produced significantly later in the project to examine PWSCC in steam; as such the maps taken from 19%CW-WF675 are from a smaller region, but at a higher resolution (0.4µm step size) . As such the maps taken from 19%CW-WF675 are of a different scale.

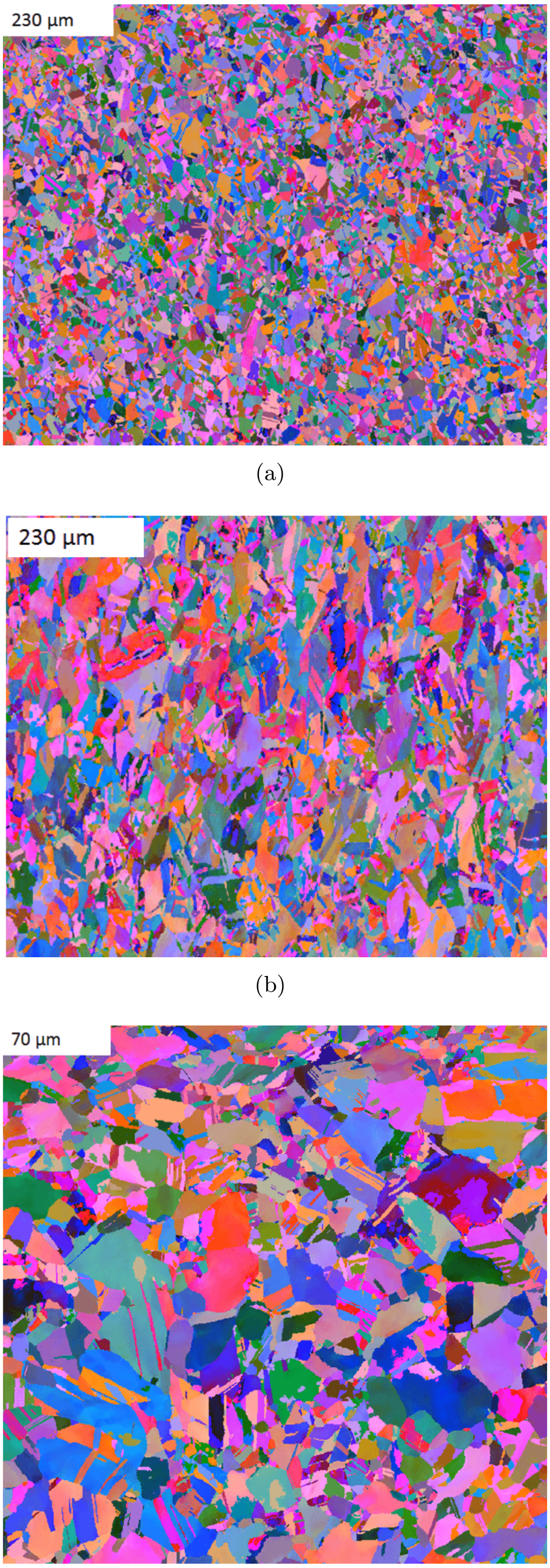

(a)

(b)

(c)

Figure 7.1 – Representative EBSD maps obtained from the AR (a), 15%CW (b) and 19%CW (c) materials used in this study.

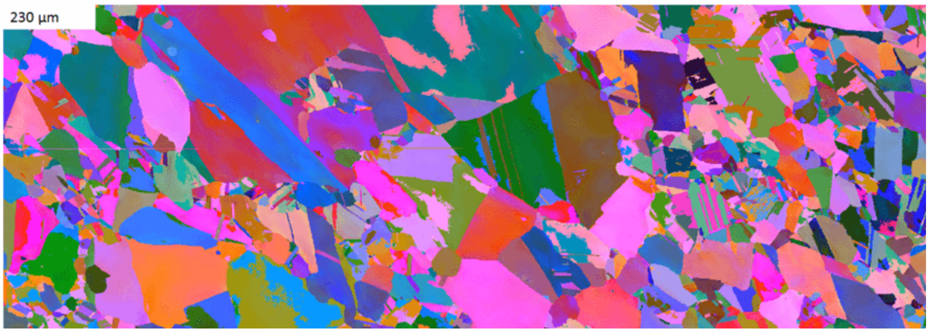

(a)

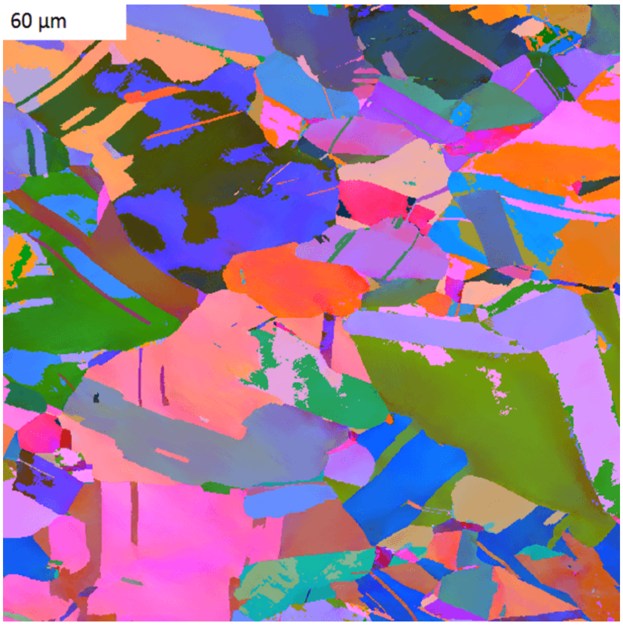

(b)

Figure 7.2 – EBSD maps taken from the AR (a) and 19%CW (b) material which show examples of the large grains observed in the microstructure of all the used alloys. It should be noted that 19%CW (b) map is taken from the same TEM sample used to produce the map in Figure 7.1. The AR (a) is a result of two EBSD maps being stitched, the region on the left shows the abnormal grains, whilst the right side shows the microstructure returning to that typically observed.

7.1.2 Grain Boundary Statistics

The analysis of the grain boundary nature in terms of HAGB and LAGB in this report has been based on a HAGB being defined as an orientation change in excess of 15° and a LAGB being less than this, but greater than 2°, values less than 2° were excluded from the calculations. This analysis was carried out on all produced EBSD maps, including those with the abnormal grains. However, it is noted that the result from the maps with the coarse grains was within the range produced by the homogenous regions of the sample and the inclusion of these maps did not alter the results. The results produced from this analysis are summarised in Table 7.2.

Table 7.2 – Grain boundary statistics of WF675 and its cold worked form, in terms of the percentage of HAGB, LAGB and Σ3 present.

Material	**HAGB**	**LAGB**	Σ3
AR	39 - 75	25 - 61	16 - 35
15% CW	22 - 34	66 - 78	5 - 10
19% CW	60 - 72	28 - 40	33

The results show that the grain boundary character varies significantly within the AR material and that the values previously reported were not reproduced, with the exception of Σ3 boundaries which was within the observed range. As with the grain size, the grain boundary character appeared to vary significantly between maps taken from different samples of the same material, no correlation between the observed grain size and grain boundary character was observed.

The cold worked samples appear to produce more consistent results, interpreted as a result of the uniform deformation of the sample producing a more homogenous material, however the data set for the cold rolled 19%CW is from a limited data set (15%CW data set is from a comparable number of maps as the AR set).

In all the EBSD maps, no other Σ boundary type accounted for more than 1% of the total boundaries analysed.

7.1.3 Grain Structure

TEM analysis of electro-polished samples has been utilised to identify the subgrain structures present within the alloy. The work by Leonard et al. had suggested that the variable grain size may be a result of recrystallized grains experiencing grain growth whist the smaller recovered grains do not, this theory was also linked to the low stored energy present in the coarse grains [11]. However, examinations of other forged Alloy 600 microstructures (un-published) have shown that hot working may produce a mixed microstructure of recrystallized and recovered grains with the recrystallized grains not always experiencing grain growth.

7.1.3.1 As Received

TEM analysis of the AR forging indicated that it consists of a mixed recrystallized/recovered hot worked microstructure. The recovered grains had formed a subgrain to accommodate the deformation induced in the forging whilst the recrystallised grains had no such subgrain structure and had a low density of dislocations (Figure 7.3). In addition to the mixed microstructure, jagged grain boundaries were observed, as in Figure 7.3(c).

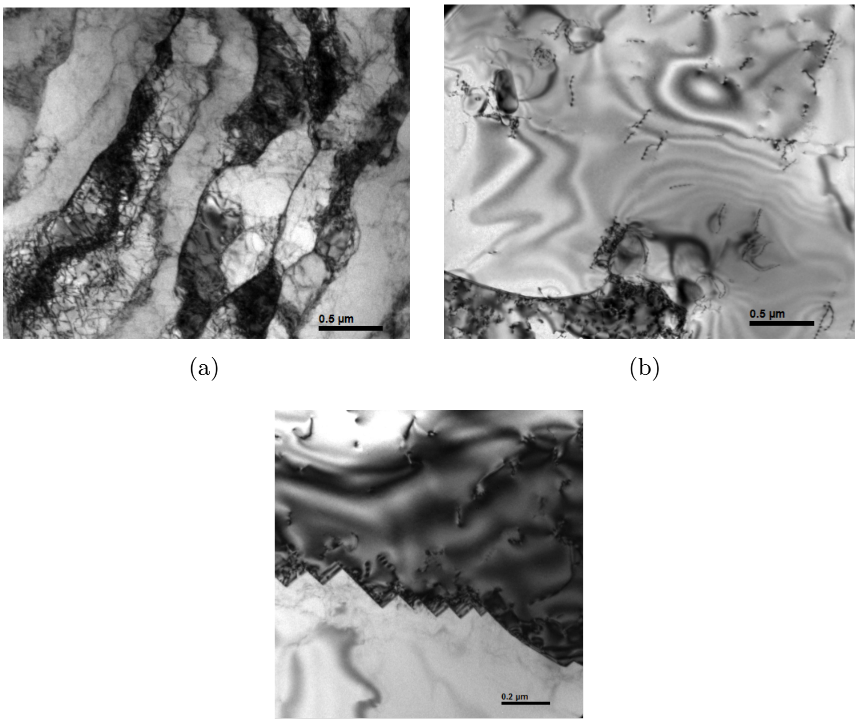

(a) (b)

(c)

Figure 7.3 – TEM images showing microstructural features observed in WF675 in the AR condition. (a) A grain which has recovered by the formation of a subgrain structure. (b) A recrystallized grain, a carbide is observed to pin the grain boundary thus preventing additional growth. This feature may contribute to the duplex grain structure observed. (c) A jagged grain boundary.

7.1.3.2 Cold Worked

The 19%CW material exhibited a very high proportion of fine slip bands and dislocations (Figure 7.4(a)), the extent of the plastic deformation experienced is illustrated by the physical deflection observed on a twin boundary Figure 7.4(b)). This highly-deformed structure overwhelmed the subgrain structure observed in the as forged material to produce a homogenous microstructure.

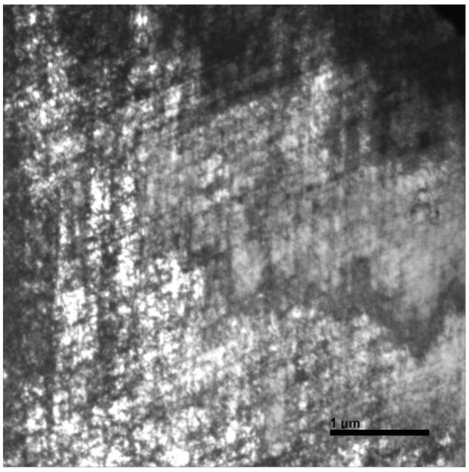

(a)

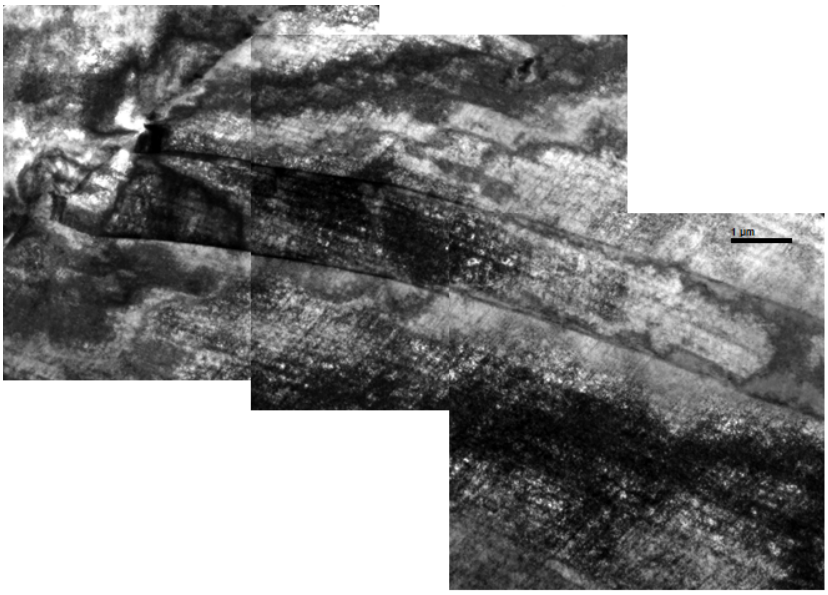

(b)

Figure 7.4 – TEM images showing the microstructure of WF675 in the CW condition.

7.1.4 Precipitates and Inclusions

The analysis of the precipitates present in the alloy has been conducted predominantly on the AR material as it is expected that the cold-working of the alloy will not alter the chemistry or density of the precipitates present in the alloy.

7.1.4.1 Carbides

The distribution of the carbides was a mixture between a ghost microstructure and random (predominantly intragranular) precipitation (Figure 7.5). The carbide distribution was quantified by imaging the thick parts of electrochemically prepared TEM foils. In these regions, the matrix had been etched away and left the carbides proud to the surface. The proud nature of the carbides resulted in them imaging brightly in secondary electron mode, this allowed the images to be threshold for analysis (Figure 7.5(b)), the analysis yielded the volume fraction of the carbides to be 1.7%, consistent with that reported by Leonard [11].

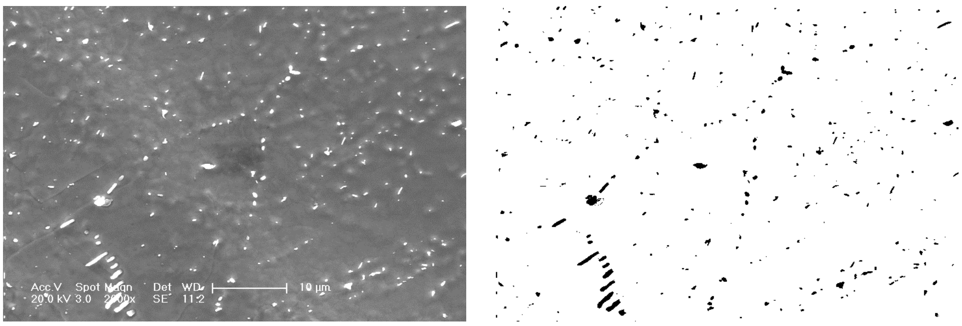

(a) (b)

Figure 7.5 – Mixed Ghost/ intragranular structure of the observed precipitates (a) and the corresponding binary image used for analysis (b).

A high proportion of the carbides observed in the microstructure were chromium rich M_7C_3 carbides (Figure 7.6), on supply of the material it had been believed that these were the only carbides present in the alloy. The M_7C_3 carbide has pseudo hexagonal crystal structure with $a_0 = 13.98$ Å and $c_0 = 4.523$ Å [166]. The produced diffraction patterns appear to contain streaks (Figure 7.6(b)). The streaking is a result of stacking faults within the carbide, the faults can be observed in bright field images (Figure 7.6(a)) [167].

However, high magnification imaging of the samples showed a number of very fine (<50 nm in size) intergranular $M_{23}C_6$ carbides along portions of some grain boundaries (Figure 7.7). The fine $M_{23}C_6$ had previously been missed due to insufficient magnification being used in analysis, this is illustrated by the fact that Figure 7.7(a) is a higher magnification image of Figure 7.5(a), note that these carbides are also missed in the threshold based analysis. The grain boundary coverage of carbides has not been calculated due to the size variation of the grain boundary carbides.

A small fraction of the carbides observed in the cold worked alloys were observed to have been cracked (Figure 7.8), subjectively the frequency at which cracked

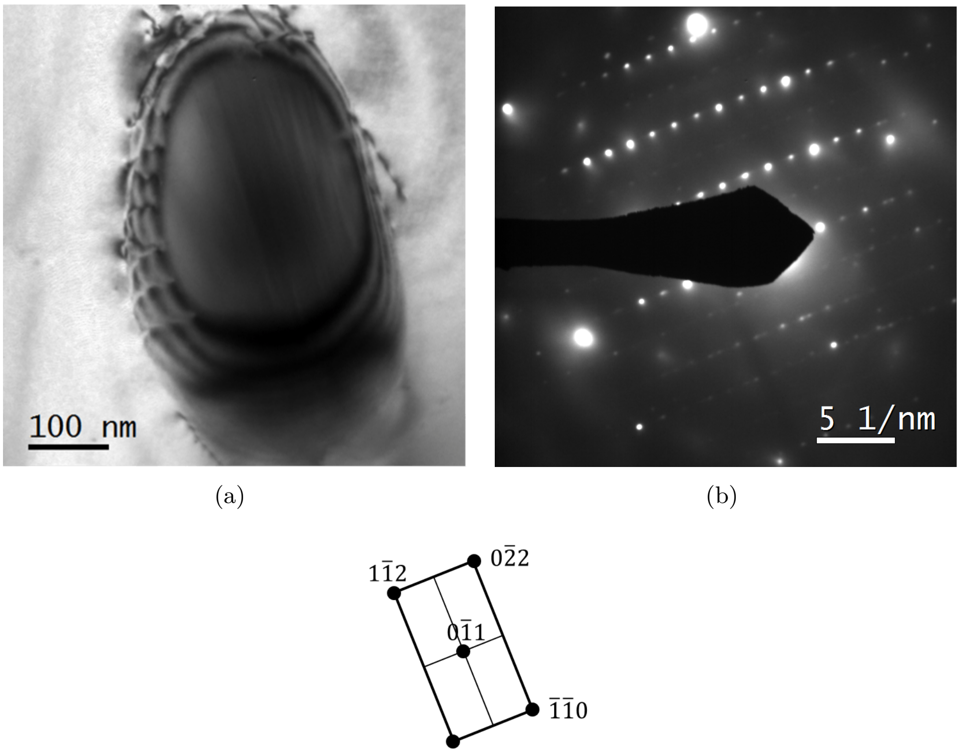
100 nm
5 1/nm
$1\bar{1}2$
$0\bar{2}2$
$0\bar{1}1$
$\bar{1}\bar{1}0$

(a)

(b)

(c)

Figure 7.6 – (a) Bright field image of a chromium carbide, (b) diffraction pattern from the imaged carbide, (c) solution to the diffraction pattern confirming it as a M_7C_3.

carbides were observed was considered to be significantly higher in the cold rolled material relative to the tensile strained material.

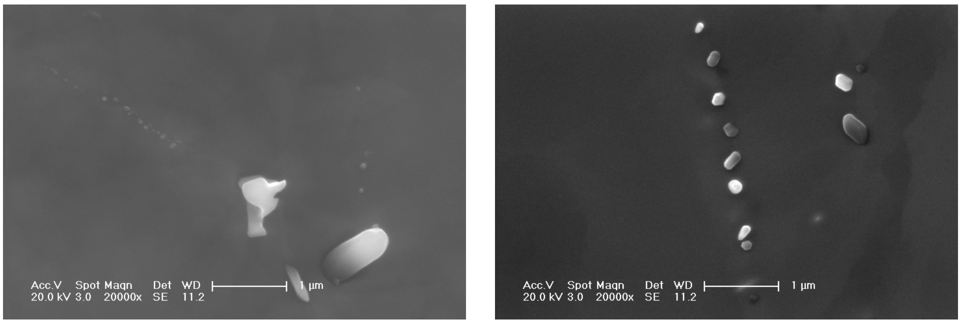
Acc.V Spot Magn Det WD 1 µm
20.0 kV 3.0 20000x SE 11.2
Acc.V Spot Magn Det WD 1 µm
20.0 kV 3.0 20000x SE 11.2

(a) (b)

Figure 7.7 – (a) Mixture of $M_{23}C_6$ and M_7C_3 carbides in the alloy showing the size discrepancy. (b) $M_{23}C_6$ carbides in the alloy. (a) is a higher magnification image taken from the centre of Figure 7.5 (the dark spot in the centre is a result of this image). This illustrated the size discrepancy between the two carbide types and thus the difficulties created for analysis.

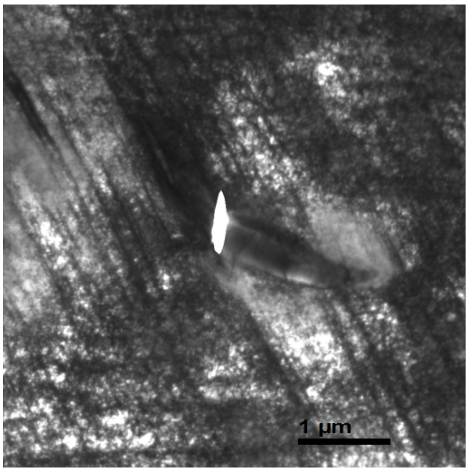

Figure 7.8 – Cracked carbide observed in the 19%CW material.

7.1.4.2 Titanium Nitrides

Titanium rich particles (identified by EDX analysis), believed to be titanium nitrides (due to their morphology), were observed within the material (Figure 7.9). The distribution of the particles was sporadic with vast regions being observed to be nitride free, yet others would have several nitrides visible in the same field of view (for reference, the description is based on images observed at ≈ 1000 times with a field of view of 300 × 300 μm^2). The titanium nitrides were observed to have initiated on magnesium rich inclusions (Figure 7.9). In some cases, it was observed that a titanium nitride had acted as an initiation site for the precipitation of carbides (Figure 7.10).

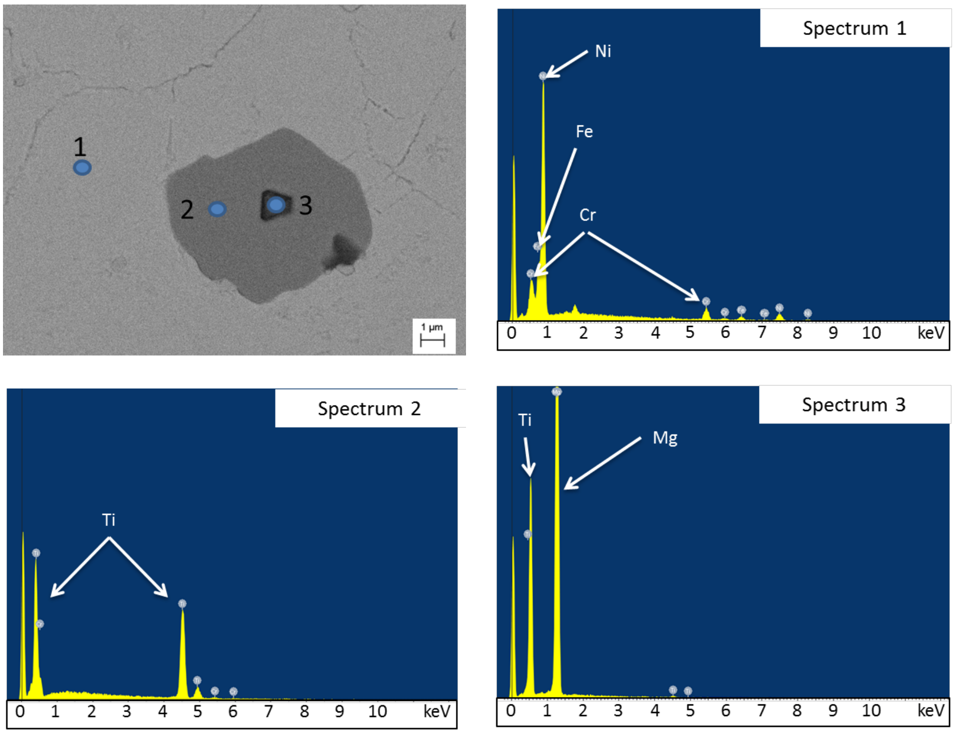

Figure 7.9 – Titanium nitride observed in the matrix, with corresponding EDX spectra for points 1, 2 and 3. Spectrums 1-3 were quantified and the results indicated the compositions of the matrix, greater than 90% Ti and greater than 90% Mg respectively.

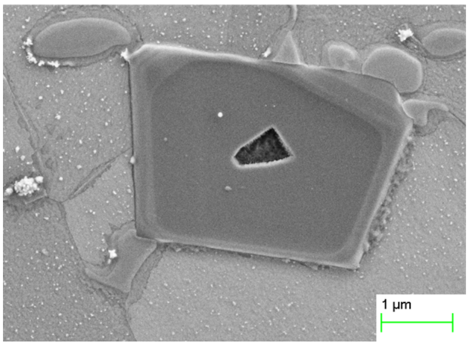

Figure 7.10 – Titanium nitride observed to act as a initiation site for carbides in the alloy.

7.1.5 Surface Preparation

The coupons supplied were EDM machined and the surface of which was visibly tarnished. SEM examination showed a rough surface finish that is a melted and re-solidified layer produced by the EDM process (Figure 7.11(a)). FIB cross-sectioning showed a layer of contaminated material which contained voids and cracks and muck (Figure 7.11(b)). As a result of this, all samples were polished with a P600 paper prior to any testing or subsequent surface preparation, this ensured the contamination was fully removed.

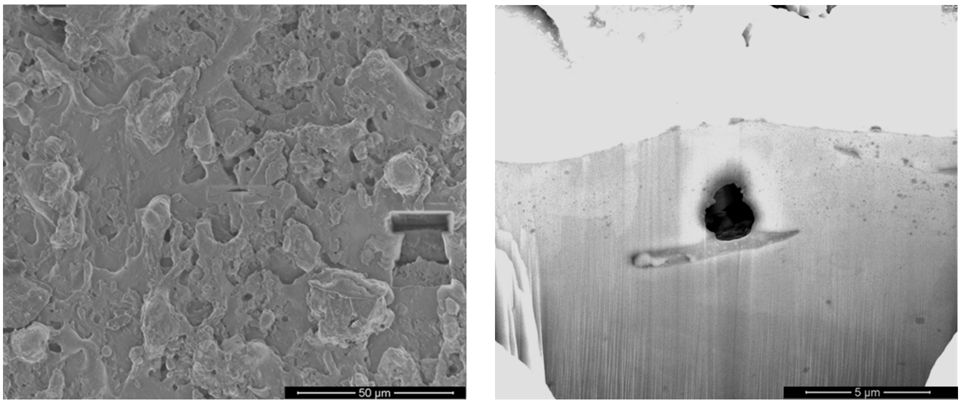

(a) (b)

Figure 7.11 – (a) EDM surface on the coupons as they were received. (b) Cross-section obtained from this surface illustrating the contamination and presence of voids.

The OPS-polished samples were considered to be a strain-free surface on the basis that it is commonly used to prepare samples for EBSD analysis when the Beilby layer (amorphous layer at the surface created by the mechanical deformation) must be removed. It is assumed that the strain free surface is devoid of any deformed layer, this is supported from cross-sections of oxidised samples present in the later sections which show no indication of a deformed layer, both in SEM and TEM examinations.

An OPS surface was used in favour of an electrochemically polished surface as the surface finish could be reproduced consistently; the surface finish produced was a mirror finish with no scratches. The finish could produce a slight topography due to different grain orientations being etched at different rates, but this was not significant as the grain boundaries were not attacked. The topography was comparable to that observed in electrochemically polished samples (Figure 7.12)

The P600 finish produced a rough surface with a deformed layer in the region of 2 μm (Figure 7.13). This deformed layer was observed to be consistent in depth on all materials examined in these studies and consistent with the value reported for stainless steel with a comparable finish.

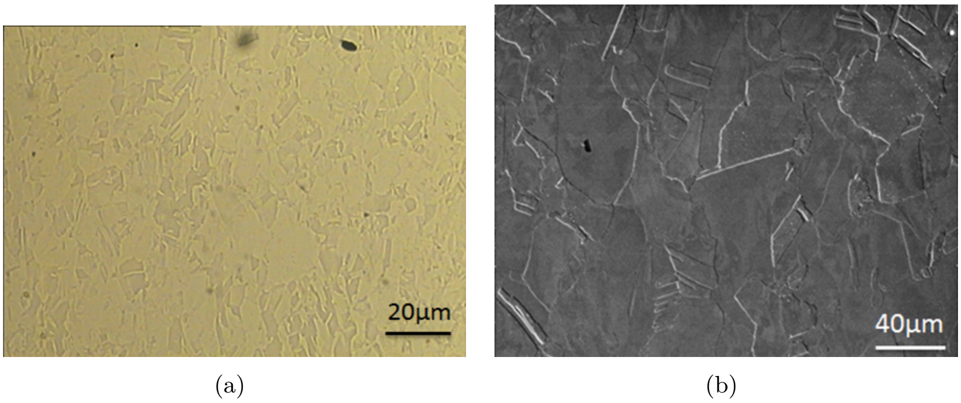

(a) (b)

Figure 7.12 – Optical image of the OPS surface finish (a) and SEM SE image of the electrochemically polished surface finish (b) at comparable magnifications.

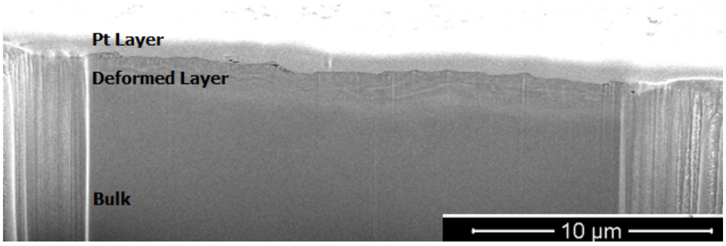

Figure 7.13 – FIB Cross-section of the P600 surface finish showing the deformed layer produced via this surface finish.

7.2 Solution Annealed Alloy 600

The alloy used was supplied in the solution annealed condition and was the same as that used by Scenini et al. [13, 14]. The process for solution annealing was given defined as 1100°C for 30 minutes and subsequently water quenched. This was reported to produce a material devoid of carbides and all carbon present in the matrix to form a supersaturated solid solution. The time spent at the elevated temperature allowed significant grain growth to occur [14].

7.2.1 Grain Size

The grain structure was revealed by a 5% Nital etch on a 1 µm prepared surface (Figure 7.14). The grains observed ranged from 50 µm to 500 µm, with the average grain size being determined by the linear line intercept method to be 180 µm. The grain size characterisation is consistent with that of previous work. The etch did not attack twin boundaries as severely as the bulk boundaries, however twins in the alloy were resolvable and can be observed in Figure 7.14. The twins observed in the solution annealed alloy are believed to be annealing twins.

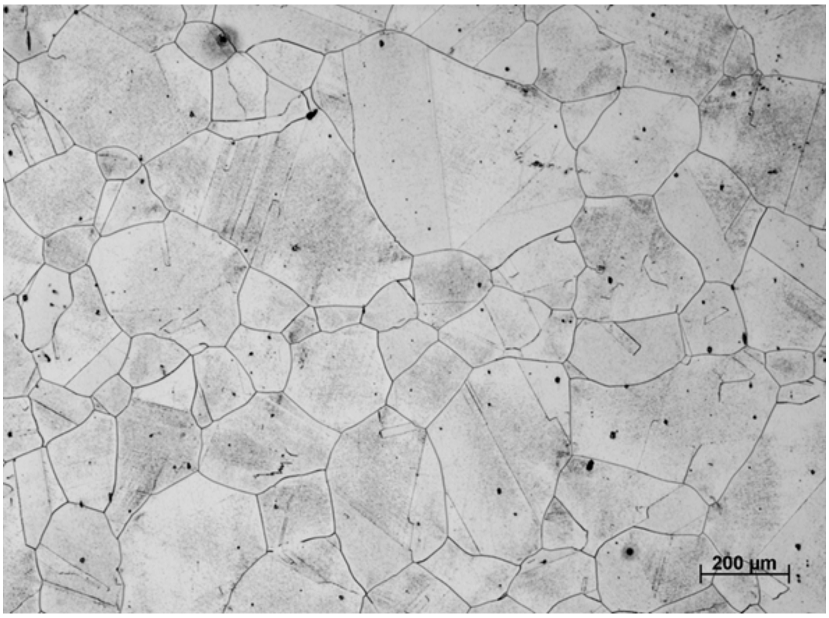

Figure 7.14 – Optical image of the SA alloy etched to reveal its grain structure.

7.2.2 Precipitates and Intermetalics

Phosphoric acid etching of the alloy had previously been used to confirm that the alloy was free of carbides, however TEM characterisation of the material showed that small (< 50 nm) chromium rich $M_{23}C_6$ carbides were present on a number of grain boundaries (Figure 7.15(a)). Given that the heat treatment on the material was in excess of the carbide dissolution temperature, it is deduced that the carbides formed during the quenching process.

In addition to the carbides, titanium nitrides were observed in the alloy (Figure 7.15(b)). The temperature of the solution anneal was not sufficient to dissolve the titanium nitrides, as such the observed nitrides are believed to be relics from the original form of the alloy. As with those observed in WF675, magnesium inclusions were observed in the titanium nitrides, these inclusions are believed to act as initiation sites for the titanium nitrides.

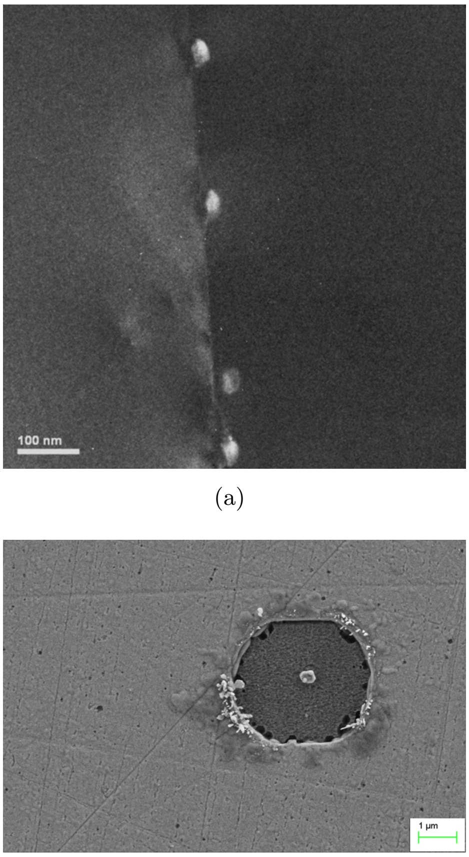

(a)

(b)

Figure 7.15 – (a) BF image of grain boundary carbides observed in the solution annealed material. (b) Titanium nitride with a magnesium rich inclusion acting as an initiation point.

CHAPTER

EIGHT

STEAM OXIDATION

The hydrogenated steam oxidation of WF675 has been conducted on samples in the AR and 15%CW state. The tests were carried out in the temperature range of 350 - 500 °C and for durations of 66 - 500 h. The majority of the testing was conducted in a reducing environment relative to the Ni/NiO transition point with a ratio of 20, however some limited testing was conducted at 400°C at variable R values to verify the calculated environment and to act as a point of reference for the SCC samples produced from a hydrogenated steam environment.

The effect of cold work vs as-received will be examined in section 8.2.4 and 8.3.4, until these sections, images will be taken from both forms of the alloy, without the effect of material being discussed. This is justified as the points being made are applicable for both forms of the alloy.

A number of the results presented in this section have been obtained by sequential slice and view via FIB SEM. This data allowed a number of features (i.e. does a carbide contact a grain boundary at any point or is there an alternative shorter path for the oxide) to be investigated which could not be obtained by conventional imaging. The raw data from the slice and view of the as-received and cold worked forms of WF675 after oxidation at 500°C for 500 h with an R of 20 can be found in appendix E and F respectively.

8.1 Calibration of the Environment using Nickel 200

The environment of the hydrogenated steam system as previously shown in section 5.1.1 is defined by R, the ratio of the partial pressure of oxygen at the Ni/NiO transition point relative to the partial pressure of oxygen in the environment. The steam is generated from deionised water with no lithium or boron additives.

To verify the calculated Ni/NiO transition point samples of nickel 200 were used, these samples should form a nickel oxide when R<1 and not oxidise for R>1. The samples were finished to a P600 surface and exposed for 24 h at 400°C. Exposures were carried out with a decreasing R in each subsequent test; the testing was stopped when oxidation was seen to have occurred. The presence of nickel oxide was identified by grazing angle XRD, the results of which are shown Figure 8.1. These results showed that the first detection of nickel oxide occurred at an R of 0.5, and that the sample exposed to an R of 0.8 had not oxidised.

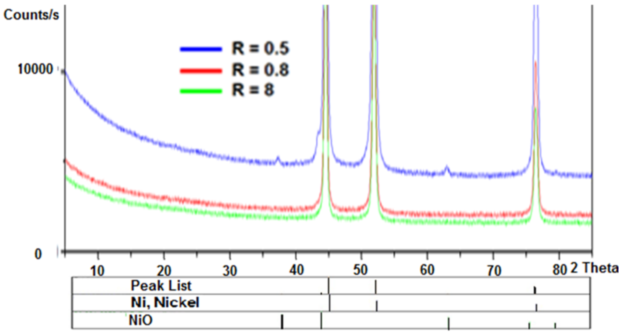

Figure 8.1 – Grazing angle XRD results from Ni 200 samples exposed to different R values for 24 h at 400°C. Note only the R=0.5 shows a NiO peak, this peak is very faint and only the most intense peak is identifiable from the spectrum implying a thin oxide.

It should be noted that the produced oxide is thin; as such the peak associated with NiO is faint. The results show that the calculated environment may be slightly out as the test at R=0.8 did not oxidise as it was expected to. The XRD results were backed up by visual inspection (Figure 8.2).

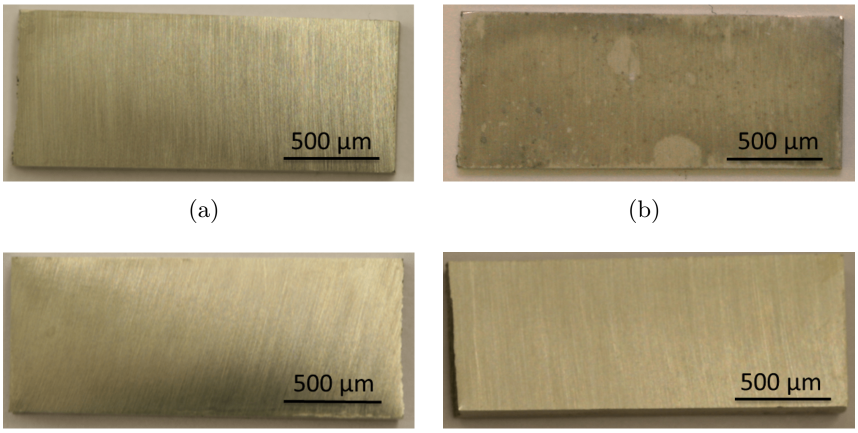

(a) (b)

(c) (d)

Figure 8.2 – Photos taken of the Ni 200 samples used for calibration tests at 400°C for 24 h: before exposure (a) and after exposure (b) at R of 0.5. Before exposure (c) and after exposure (d) at R of 0.8.

8.2 Observations of the Oxides Formed on the Surface

The role of surface oxidation on PWSCC is not clearly defined, but it is believed to be influential. As such the produced oxides in hydrogenated steam should be characterised and contrasted to those formed in PWSCC test conditions. The oxides formed in hydrogenated steam should theoretically show similarities to those formed in PWR conditions; any differences observed in the oxides may consequently produce differences in the SCC behaviour observed in steam relative to PWSCC. The surface oxides explored in this section are from samples of AR and 15%CW WF675 with an OPS surface finish, the effect of different surface finishes is explored in section 8.5.

8.2.1 Oxidising Environments (R<1) at 400°C

The focus of the study in this thesis has been on tests at R>1, however, a small number of test have been conducted with R<1. These tests were to observe if a change in the oxidation behaviour of Alloy 600 was observed in the region of the Ni/NiO transition point and provided a reference for SCC tests conducted at R<1. The tests were carried out at 400°C, the temperature at which the system was calibrated and that of the conducted steam SCC tests (chapter 10).

Testing at an R of 0.1 for 100 h produced a surface which appeared to have suffered a pitting like attack within the grains, with the grain boundaries appearing to be etched. SEM images showed that the surface was covered with fine platelets of what is believed to be a nickel based oxide (Figure 8.3). The carbides in the matrix appeared to have been attacked in a similar manner to that of the grain boundaries. Repeating the test for a duration of 500 h produced a similar result, with the exception that the etching like attack of the grain boundaries and carbides appeared to be more severe.

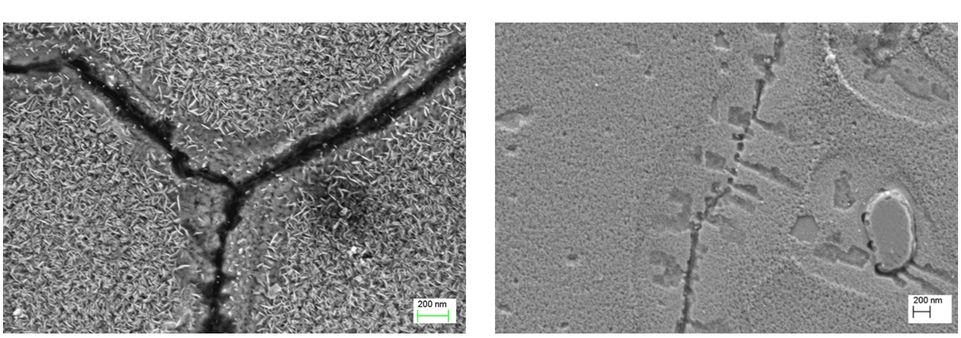

(a) (b)

Figure 8.3 – Inlens (a) and SE (b) images taken from AR-WF675 tested in a oxidising environment (R=0.1) at 400°C for 100 h (a) and 500 h (b).

The Inlens image of the 100 h exposure shows the platelets but losses detail of the etching (Figure 8.3(a), etching appears black), the SE image of the 500 h shows the detail of the etching and the increased size (relative to the 100 h exposure) but does not clearly show the platelets (Figure 8.3(b)). This implies that there is a change in the chemical composition of the platelets relative to the matrix with a small change in topography and that the etching is primarily a topographic effect, not a change in chemical composition.

To identify the oxide, grazing angle XRD was attempted on a sample tested for 500 h (Figure 8.4); however, no oxide was detected from the XRD. The observation that there was a colour change on the samples (taken to imply an oxide), which was similar to that observed on the nickel 200 reference samples led to the deduction that a thin oxide was formed (in the order of nm).

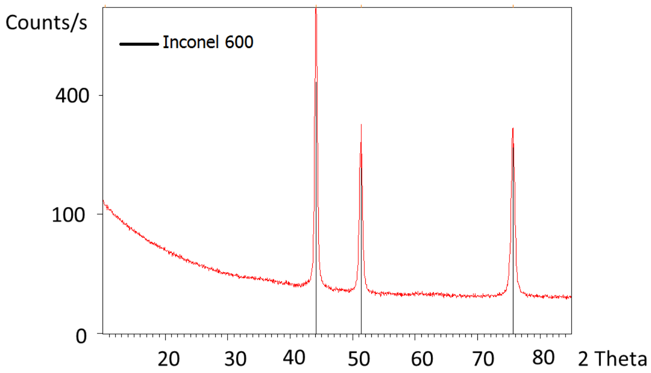

(a)

Figure 8.4 – Grazing angle XRD taken from AR-WF675 exposed to 400°C steam for 500 h with an R of 0.1.

A TEM foil was prepared by the FIB technique from a sample with a similar etched appearance. EDX line scans from the platinum protective layer to the matrix gave an indication that there was a nickel enrichment at the surface (Figure 8.5). This interpretation is based on the fact that as the platinum wt % drops, the nickel concentration rises without any increase in the iron or chromium concentrations (If the beam was passing through the matrix and platinum it would be expected that the Ni, Cr, Fe concentrations would all rise at the same rate). There is also an indication of a fine iron rich (or chromium depleted) layer being present at the surface. It is believed that this is most likely a chromium depletion as the ratio of Ni:Fe in the region is constant, but the evidence is not conclusive.

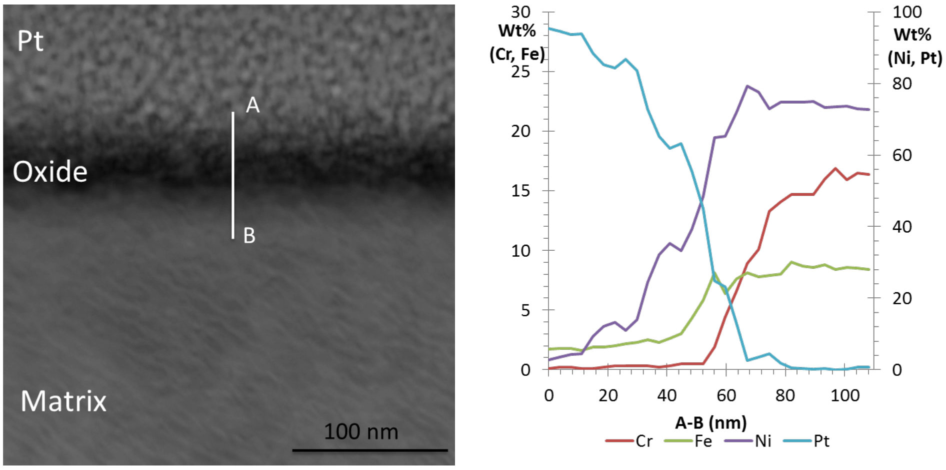

(a) (b)

Figure 8.5 – TEM EDX line scan and corresponding HAADF image form 15%CW WF675 oxidised at 400°C for 500 h with an R of 0.5.

8.2.2 Reducing Environments (R>1) at 400°C

Testing at 400°C with an R of 20 for 66 h produced samples which were visually unchanged. SEM observations of the samples indicated that the grain boundaries had been preferentially attacked, but unlike the etched boundaries in the oxidising environment, these boundaries were raised with what appeared to be an oxide at the surface (Figure 8.6). Backscattered imaging indicated that the grain boundary composition was of a lower average atomic mass than that of the matrix, but due to the interaction zone of the electron beam and the suspicion that the boundaries were preferentially oxidised, this observation could not conclusively be attributed to the surface oxide and may have been a feature of grain boundary within the alloy.

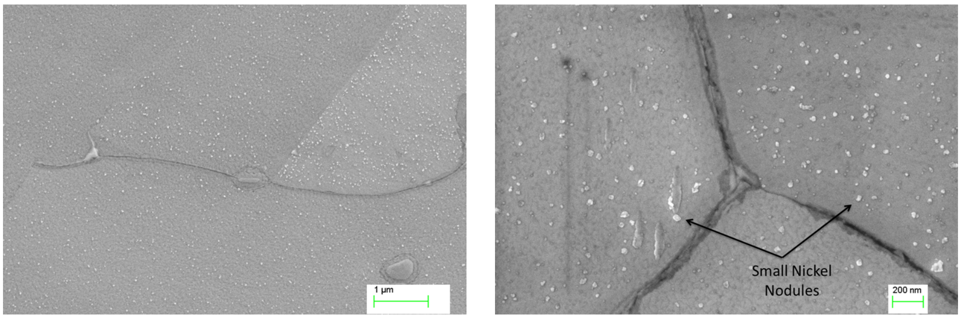

(a) (b)

Figure 8.6 – SE (a) and ESB (b) images of AR-WF675 surface after being tested at 400°C with an R of 20 for 66 h.

Within the grains, brightly imaging features of a few nm in size were observed. These small particles in the grains are suspected to be small particles of metallic nickel (based on observations seen in 500°C oxidation, section 8.2.3), but no evidence of this has been obtained.

The carbides in the alloy at the surface were oxidised in a similar manner to that of the grain boundaries. The oxide, when observed in backscattered images, appeared to have a contrast which matched that of the grain boundary oxide indicating it was similar in nature (the term oxide is used as a result of the subsequent analysis, not based on these images).

Grazing angle XRD has been utilised to characterise the oxide formed on this sample, however as with the previous samples at 400°C, no detection other than the matrix were obtained from the X-ray spectrum. TEM samples prepared by FIB have shown that the oxide in the surface region at the grain boundary is a chromium rich oxide (Figure 8.7), note the surface oxide is not to be confused with the preferential oxidised grain boundary also present in (Figure 8.7). The small brightly imaging particles observed by SEM were not observed in the TEM samples.

It should be noted that the angle of the preferential oxidation at this boundary means that any analysis by EDX from the surface in a SEM could yield false results in the grain boundary region. Any detected chromium rich oxide may be an artefact of the preferential oxidation of the grain boundary, not the surface (even at 10 keV, the minimum voltage for reliably quantifying Ni, the interaction volume of the electron beam is $\approx$ 500 nm, thus interacting with the preferential oxide).

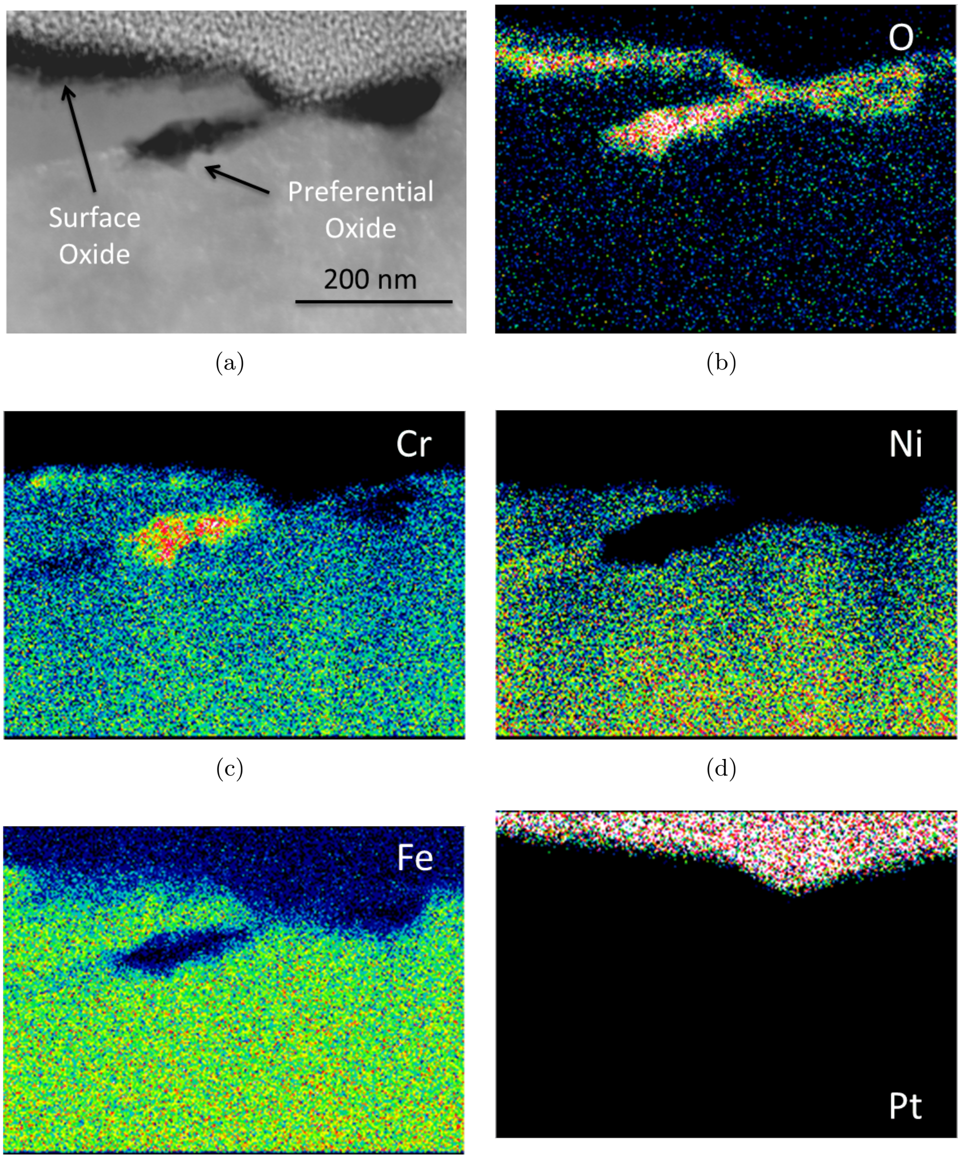
Surface Oxide
Preferential Oxide
200 nm
O
Cr
Ni
Fe
Pt

(a) (b)

(c) (d)

(e) (f)

Figure 8.7 – HAADF image of the oxide formed in the vicinity of a grain boundary in 15%CW-WF675 after 500 h in a reducing environment (R=20) at 400°C, (b-f) are the corresponding EDX elemental maps.

8.2.2.1 Oxidation at Grain Boundaries

The oxide formed at the grain boundaries in the reducing environments at 400 °C appeared to have a change in morphology relative to the bulk surfaces.

In the 66 h test at 400°C with an R of 20, it appeared that the grain boundaries were oxidising at a faster rate relative to the matrix, as a result the boundaries were protruding from the surface, this made them not only visible in the backscattered electron image but also in the secondary electron images (Figure 8.8). The fact that the boundaries were visible in the secondary electron image aided the analysis greatly, as it removed the concern that artificial features produced by the sub surface preferential oxidation of a grain boundary were being observed. The level of grain boundary attack changes as the nature of the boundary changes,but could also be observed to change without any apparent change in grain boundary character (Figure 8.8). However, a number of observations were made when the level of attack changed with no obvious change in the boundary character. Figure 8.8(d) shows a jagged boundary (like the one observed in Figure 7.3(c)) which has oxidised, but note that the oxidation is not continuous but changes in nature at each step, indicating that a change in grain boundary structure changes the nature of the oxidation.

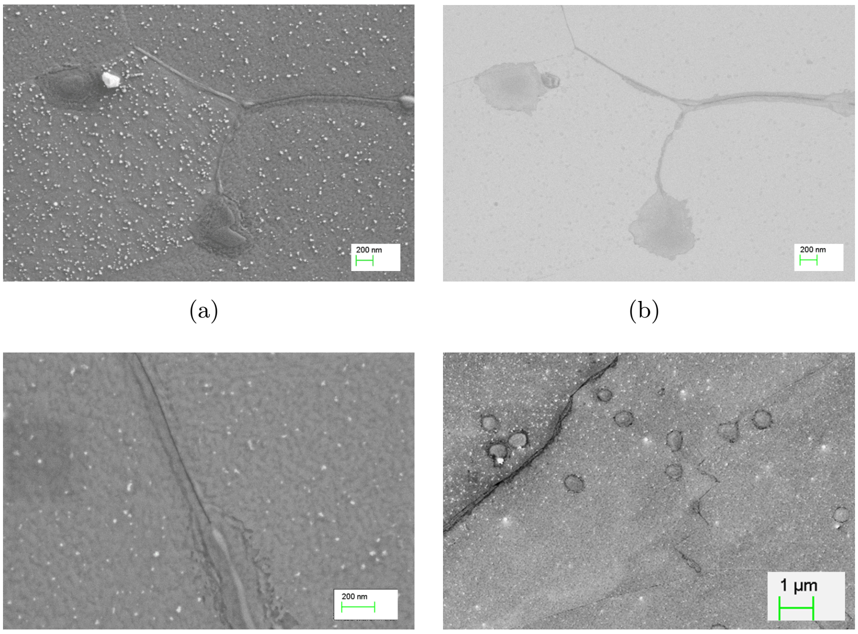

(a) (b)

(c) (d)

Figure 8.8 – (a, b) SE and ESB images respectively of oxidised grain boundaries and carbides observed on the surface of AR-WF675 after 66 h at 400°C with a R of 20. (c) SE image of the grain boundary oxide changing morphology with no obvious change in grain boundary character. (d) Carbides and a jagged grain boundary observed to oxidise.

8.2.3 Reducing Environments (R>1) at 500°C

Testing at 500°C with an R of 20 for 66 h and 500 h produced samples which were visually changed as they appeared to be slightly tarnished. Under SEM examination, the 66 h and 500 h samples were similar (Figure 8.9), however the large crystals which were on the 500 h test were larger and of a greater density relative to that of the 66 h test.

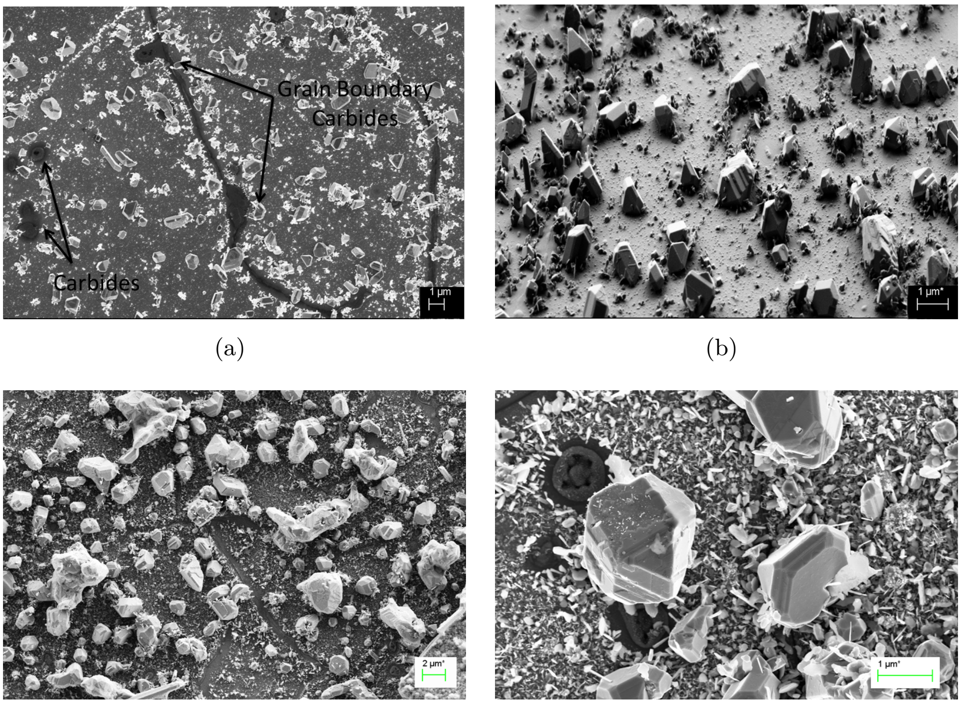

(a) (b)

(c) (d)

Figure 8.9 – SE images of the surface after exposure to 500°C hydrogenated steam with a R of 20 for 66 h (a,b) and 500 h (c,d). (a) is taken from 15%CW-WF675, b-d are from AR-WF675. (a) Shows the nickel nodules formed on the grains and the different morphology at the grain boundaries, a group of three carbides can be seen on the left of the image as well as two on the grain boundary. (b) Is taken from a single grain on a sample after tilting to 52 °, the twin boundaries can be seen on centre nodule as a result of the tilting. (c) After longer exposure it is observed that the larger nodules lost their well defined edges, the small nodules however maintain their crystalline shape. (d) Higher magnification of the surface showing the fine oxide which begins to form in between the nickel nodules, two carbides can be observed near the large nodule on the left.

The surface is covered with large crystals, some of the nodules had parallel bands of contrast which ressembled a twin; EDX point analysis indicated that the large features were more than 90% nickel. Some of the crystals on the 500 h test were less well defined as a crystal, this appeared to only occur on the larger crystals (≈ 2 µm). In addition to the crystals, less well defined sharp edged iron rich oxides were visible on the grain surface. Carbides observed from the surface appeared to be oxidised, but were free of the crystals and sharp edged oxides. The oxidised carbides imaged as dark region (the carbide) on the grain surface surrounded by a band of contrast (Figure 8.9(d)), this was identified by TEM as a chromium rich oxide.

The nature of the 500 h sample, with the larger features meant that grazing angle XRD was able to detect a number of the components forming the surface oxide on the sample (Figure 8.10). The grazing angle XRD detected Inconel, pure nickel and Trevorite ($NiFe_2O_4$).

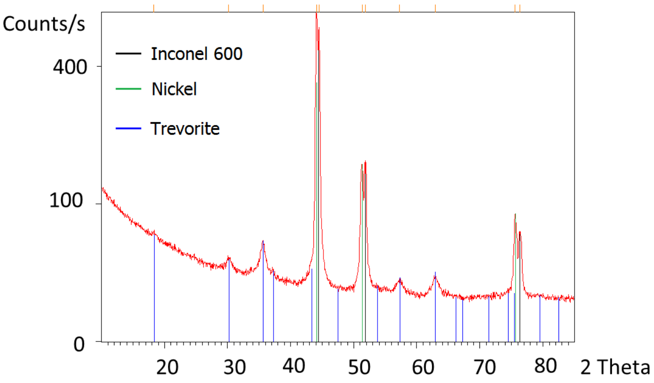

(a)

Figure 8.10 – Grazing angle XRD results from AR-WF675 after 500 h at 500°C with an R of 20. The results show the presence of an oxide in addition to metallic nickel.

The 3 peaks associated with pure (metallic) nickel are within 0.5° of the 3 peaks associated with Inconel 600, however at each location the two distinct peaks were identifiable. The metallic nickel is attributed to the large crystals formed at the surface of the sample.

The Trevorite is a spinel type oxide, the chemical composition defined by the grazing XRD was $Ni_{1.43}Fe_{1.7}O_4$, however it should be noted that other spinel oxides of the form $Ni_xCr_xO_z$ and $Fe_xCr_xO_z$ exist which have comparable lattice parameters, as such produce near identical XRD peaks to that of Trevorite.

TEM samples from the 66 h test were prepared by the FIB method. The 66 h samples were used as the nickel nodules were smaller and less frequent, thus did not impede the deposition of a protective platinum layer and allowed grain boundaries to be more readily identified. The large crystal nodules were identified as pure nickel from EDX mapping, it can also be noted that there is an internally oxidised layer in the sample which is depleted in nickel and is a probable source of the nickel which formed the nodules (Figure 8.11).

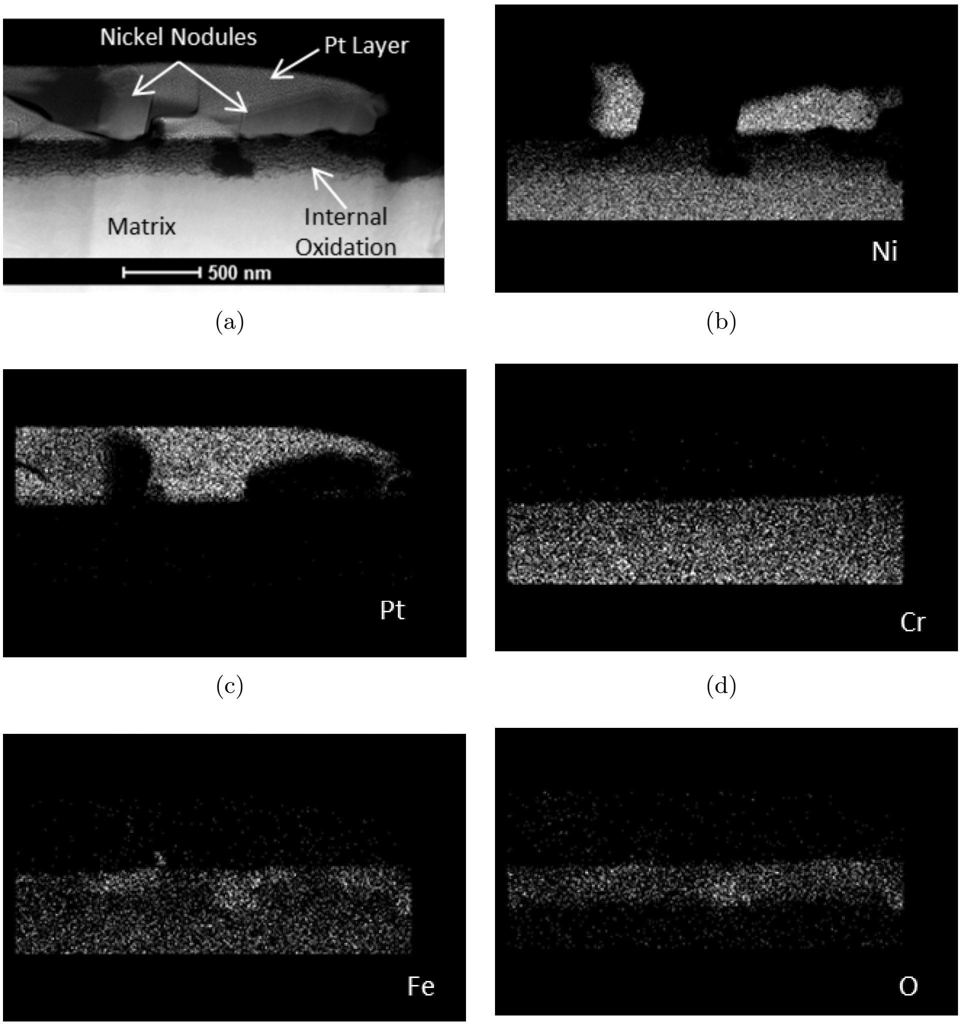

(a) (b)

(c) (d)

(e) (f)

Figure 8.11 – HAADF Image of the nickel nodules present on AR-WF675 after 66 h in a reducing environment (R=20) at 500°C (a) and the corresponding EDX elemental maps obtained from this region (b-f). It should be noted that as the nodules are at the surface, to preserve their structure in the FIB preparation they are completely encased in the platinum layer.

The small sharp oxides are observed to be iron rich (Figure 8.12). It can also be seen from Figure 8.11 and Figure 8.12 that there is no formation of internal oxides when a continuous surface oxide film or iron rich oxide is present. However internal oxidation was predominately observed, with a continuous surface oxides only being observed in the vicinity of grain boundaries, surface damage. In a small number of cases, a large region of iron rich oxide was observed in the internally oxidised region.

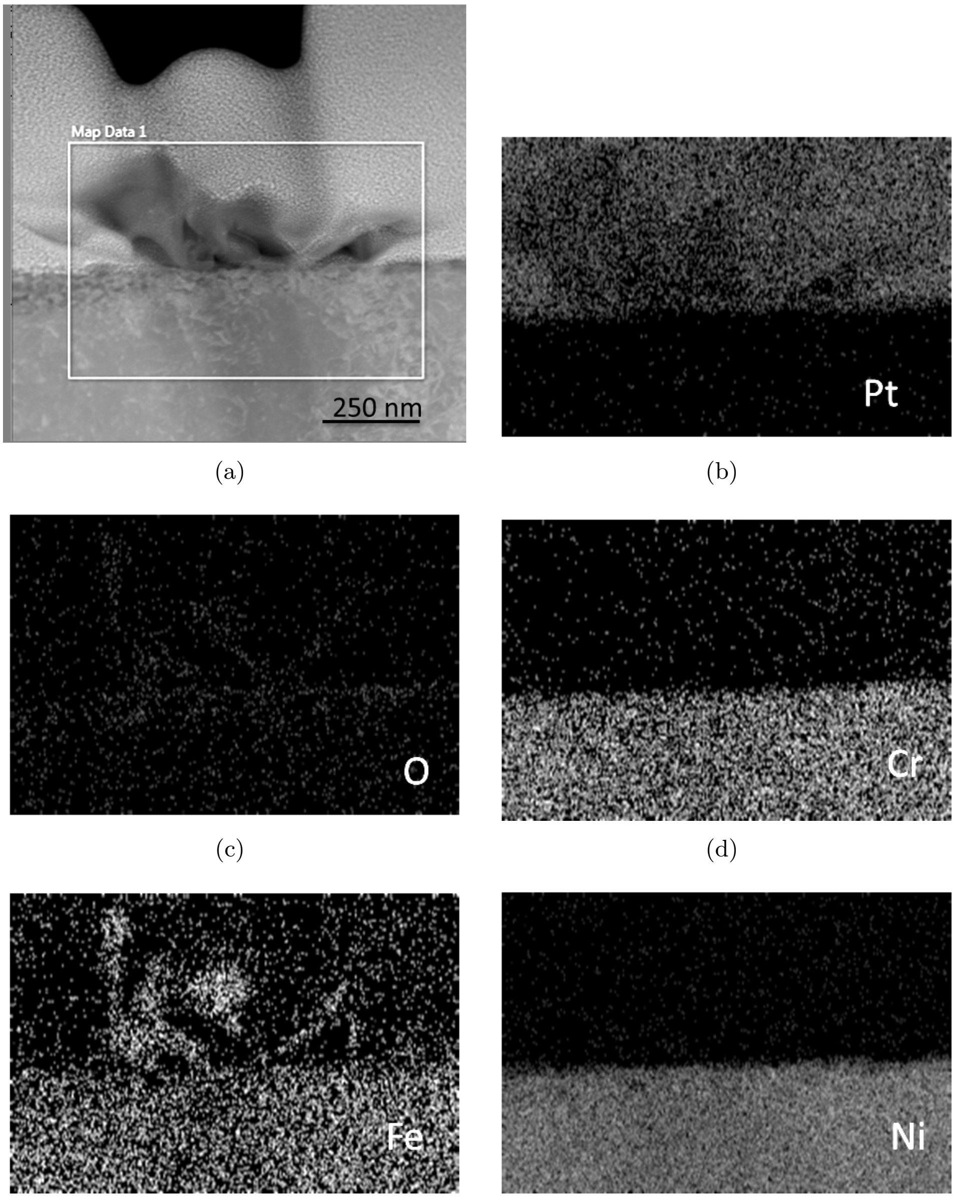
Map Data 1
250 nm
Pt
O
Cr
Fe
Ni

(a) (b)

(c) (d)

(e) (f)

Figure 8.12 – HAADF Image of the sharp edged oxide present at the sample surface (a) and the corresponding EDX elemental maps obtained from this region (b-f).

8.2.3.1 Oxidation at Grain Boundaries

The oxide formed at the grain boundaries in the reducing environments at 500 °C appeared to have a change in morphology relative to the bulk surfaces.

In both the 66 h and 500 h test at 500°C with an R of 20 (Figure 8.9), the grain boundaries were less visible relative to the 400°C exposures (Figure 8.6), this is due to the formed corrosion products (nickel nodules and surface oxides). However with the aid of the results presented in section 8.6, it became possible to identify 3 distinct morphologies of the grain boundary oxidation (Figure 8.13). The three boundary types have been labelled as nodule free zone (NFZ), no nodule free zones (NNFZ) and half and half (HH), Figure 11.1 gives a schematic representation of the three grain boundary morphologies observed.

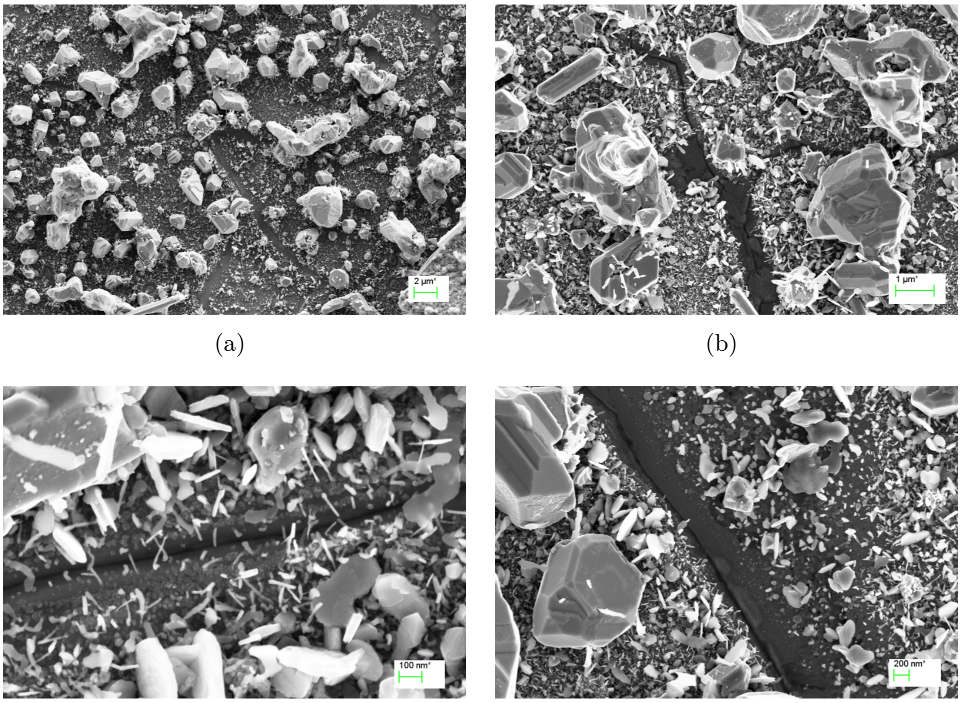

(a) (b)

(c) (d)

Figure 8.13 – Selection of SE images taken form the 500°C, 500 h test at R=20 illustrating the observed grain boundary types (Images taken from AR-WF675, but same observations were also made on 15%CW-WF675). (a) Low magnification image illustrating the difficulty in locating the grain boundaries. (b) An example of a NFZ boundary. (c) An example of a NNFZ boundary. (d) An example of a HH boundary.

A NFZ boundary is characterised by there being a small region on both sides of the boundary were no particles (nickel nodules or iron oxides) form (Figure 8.13(b)). The NNFZ is the opposite to the NFZ and has no region which is free from the surface oxide particles (Figure 8.13(c)). The HH has one side of the boundary which is representative of a NFZ, whist the other side is a NNFZ (Figure 8.13(d)). This method of classification can be seen more clearly in 8.6.1.

8.2.4 Cold Worked vs As-Received

Up-to now the AR and 15%CW material oxidation has been discussed as the same, with the illustrations given being from both materials, this is due to both forms of WF675 having the same oxide morphology, when tested in the same conditions. However, despite the same oxide morphology on both forms of the alloy, there was a marked difference between the oxides. In the cold worked alloy, the density of pits/thermal etching (R<1) and nickel nodules (R>1) was uniform between the grains; however in the forging (AR), the density of these features was seen to vary between grains (Figure 8.14).

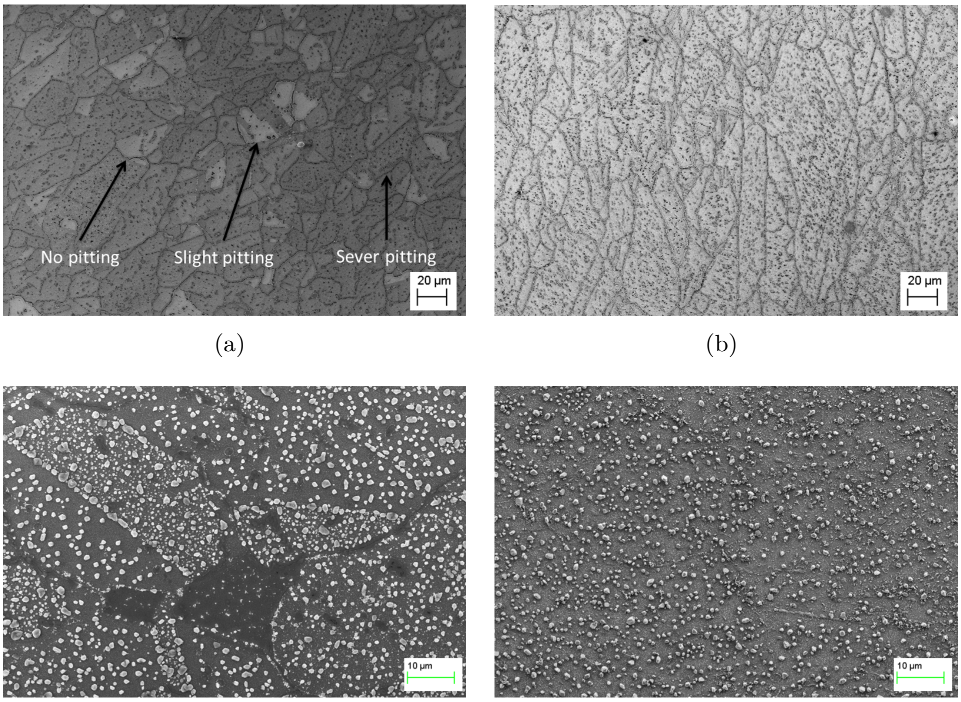

(a) (b)

(c) (d)

Figure 8.14 – SE images illustrating the effect of cold work on the oxidation of the alloy. (a - b) from R less than 1, the cold worked alloy (b) has a uniform density of pits on all grains whist the AR (a) is to have a variable density. (c - d) from R greater than 1, the cold worked alloy (d) has a uniform density of nodules on all grains pits whist the AR (c) is seen to have a variable density.

8.3 Internal Oxidation

Given the high temperatures used in these oxidation studies, it was a distinct possibility that classical internal oxidation would occur, by which discrete particles of oxide form in the matrix as a result of the inward diffusion of oxygen. The possibility of internal oxidation was examined by cross-sectioning of a set of samples produced with an R of 20, these samples were exposed to temperatures in the range of 350 - 500°C for up to 500 h.

8.3.1 Temperature Dependency

The effect of temperature on internal oxidation is significant, as a reduction in temperature reduces the diffusivity of oxygen and hence the ability of it to diffuse into an alloy before reacting. FIB produced TEM samples and cross sections showed that no internal oxidation was present in the test at 350°C for 500 h (Figure 8.15(a)). An exposure of 66 h to 500°C steam was sufficient to produce significant internal oxidation (Figure 8.15(c)). The results from the 400°C for 500 h was less clear, as with the 350°C test a surface oxide had formed, however a small amount of oxide was detected under this layer, it is however not clear if this oxide is in the form of discrete particles as expected by Wagner's model of internal oxidation or formed by the oxidised dislocations (Figure 8.15(b)).

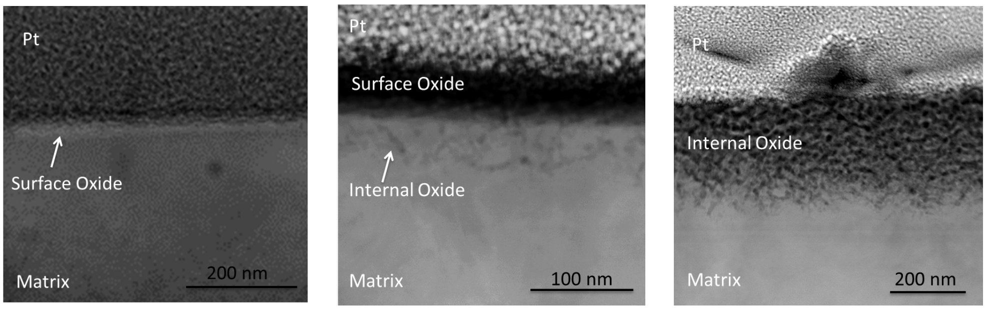

(a) (b) (c)

Figure 8.15 – T (a) Bright field image of the sub-surface oxidation of AR-WF675 after 500 h in 350°C steam with an R of 20. (b) HAADF image of the sub-surface oxidation of AR-WF675 after 500 h in 400°C steam with an R of 20. (c) HAADF image of the sub-surface oxidation of AR-WF675 after 66 h in 500°C steam with an R of 20.

The internal oxidation formed in the 500°C samples is identified as a chromium based oxide, this can be seen from Figure 8.16. The iron concentration varies around the bulk composition value whist the nickel concentration is reduced, the chromium in the region of the internal oxidation is enriched. This indicates that the fine oxide particles form in skeleton of the alloy. The oxygen line is included in the quantification to illustrate the region which is internally oxidised. The oxygen line does not shadow the chromium line, indicating that it is not a result of the chromium peak. It should be noted that on one of the 500°C samples, two large iron based oxides were observed in the internally oxidised layer (Figure 8.11). These features were however not observed in any other TEM sample or FIB cross-sections and are considered interesting but anomalous.

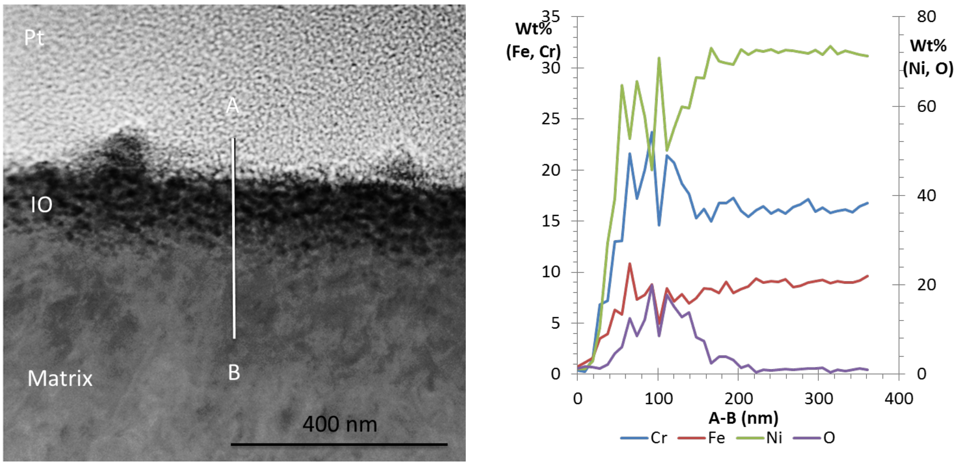

(a) (b)

Figure 8.16 – EDX line scan and corresponding HAADF image of the internal oxide formed on AR-WF675 after 66 h in 500°C steam with an R of 20.

The narrow (sub 10 nm) oxidised features observed in the first 100 nm from the surface of the 400°C sample indicate a slight chromium enrichment at the expense of iron (Figure 8.17).

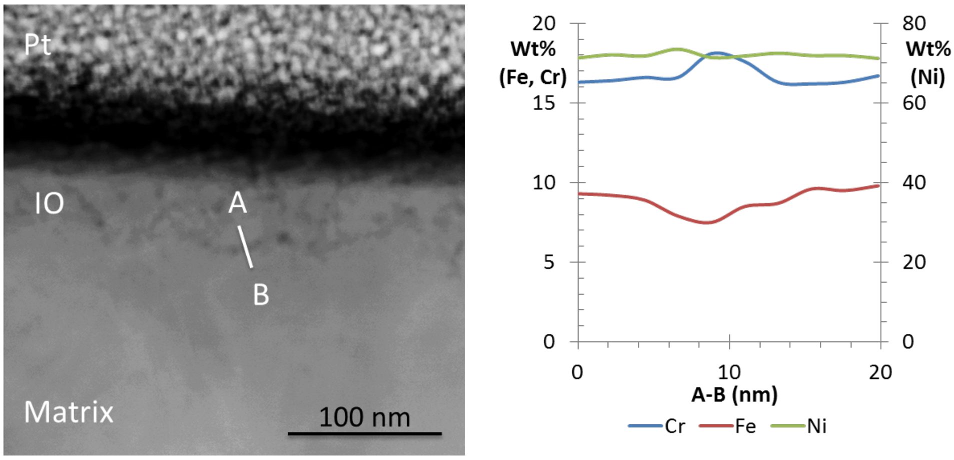

(a) (b)

Figure 8.17 – EDX line scan and corresponding HAADF image of the internal oxide formed on 15%CW-WF675 after 500 h in 400°C steam with an R of 20.

8.3.2 Effect of Exposure Time

The maximum observed internal oxidation in the 500°C tests can be seen in Figure 8.18 and are summarised in Table 8.1. These results show that the maximum internal oxidation observed in both forms of the alloy are consistent for the same exposure times. However it should be noted that the Wagner's equation would predict that the depth of the internal oxidation in the 66 h test be only 36% the depth of the 500 h test; it can be seen from Table 8.1 that this is not the case. This discrepancy produces a significant error in the calculated oxygen diffusivity, furthermore it questions the validity of using Wagner's equation for determining the oxygen diffusivity.

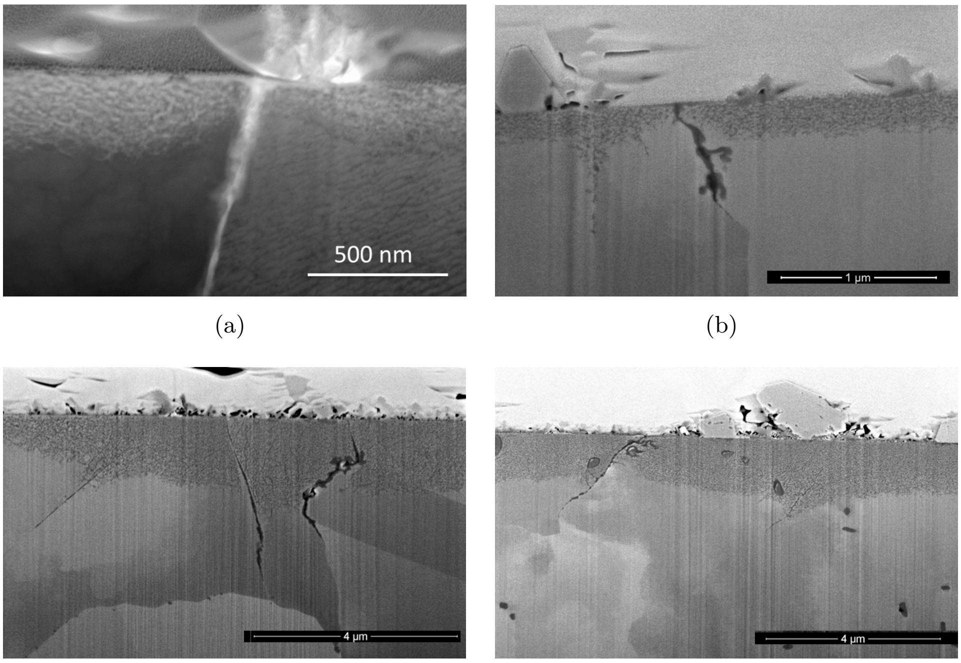

(a) (b)

(c) (d)

Figure 8.18 – Bright field (a) FIB SEM (b-d) images of the maximum IO penetrations observed in 500°C steam with an R of 20 for AR-WF675 after 66 h (a), 15%CW-WF675 after 66 h (c), AR-WF675 after 500 h (c) and 15%CW-"WF675 after 500 h (d).

Table 8.1 – The maximum observed internal oxidation in WF675 and 15%CW-WF675.

Temperature (°C)	Duration (h)	Maximum observed depth of internal oxidation (nm)	
		AR	CW
500	66	270	260
500	500	2070	1700

8.3.3 Observations of Slip Bands

Slip bands (based on morphology) within the materials have been observed to oxidise, initially the oxidation was believed to be preferential, however close inspection led to the conclusion that it was internal. The slip band oxidation did not only penetrate deeper than the internally oxidised layer, it was also seen in some cases to increase the IO layer in its vicinity.

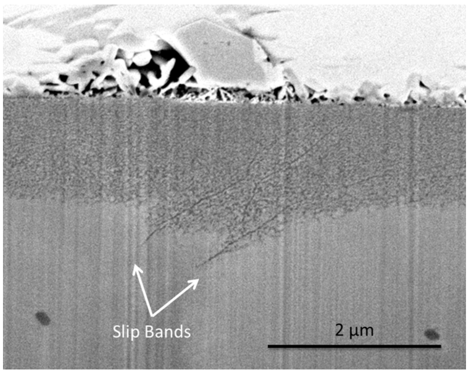

(a)

Figure 8.19 – FIB SEM image of what has been interpreted to be an internally oxidised slip bands on 15%CW-WF765 after 500 h in 500°C steam with an R of 20.

8.3.4 Cold Worked vs As-Received

The maximum depth of the internally oxidised layer was not significantly different between the AR and 15%CW forms of WF675. The consistency of the penetration depth between the two materials was however different Figure 8.20. The cold worked-material had a uniform penetration depth, whilst the forging had a variable penetration depth. The variation in the forging was not just between grains, but also within a single grain, whilst the 15%CW had a constant penetration in all observed grains (except when a surface oxide was observed and IO was suppressed).

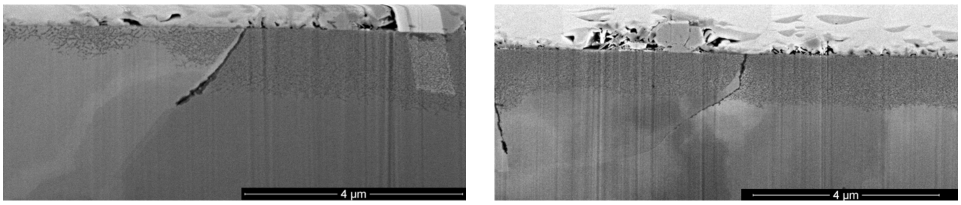

(a) (b)

Figure 8.20 – FIB SEM images of the internally oxidised layer created in 500°C steam (R=20) after 500 h in AR-WF675 (a) and 15%CW-WF675 (b). It can be seen that in the AR condition the depth of penetration varies whilst the 15%CW remains relatively constant.

Both the as-received and cold worked materials exhibited regions where no internal oxidation was observed (Figure 8.21). These regions were characterised by the formation of a continuous surface oxide. Furthermore, in Figure 8.20(b) it can be noted that there is a slight increase in the depth of the internally oxidised zone, the morphology of which is indicative of a slip band.

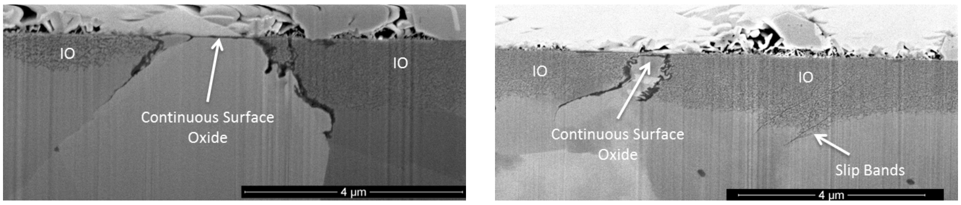

(a) (b)

Figure 8.21 – FIB SEM images of the internally oxidised layer created in 500°C steam (R=20) after 500 h in AR (a) and 15%CW (b) where a surface film has formed, thus preventing the inward diffusion of oxygen and hence internal oxidation.

8.4 Cross-Sectional Views of the Preferential Oxides

As with the surface oxidation studies the samples cross-sectioned and prepared for TEM analysis were produced in a hydrogenated steam environment of R=20. The samples were exposed for periods of 66 h and 500 h. The temperature range investigated was 350 - 500°C. The oxidation in this section is referred to as preferential oxidation, not internal, as it is continuous in nature, not formed by discrete particles, characteristic of traditional internal oxidation. Preferential oxidation was observed on grain boundaries and carbides.

8.4.1 Effect of Temperature on Oxidation Kinetics

Grain boundary preferential oxidation was observed at all temperatures after an exposure of 500 h, however from the 66 h exposed samples, grain boundary preferential oxidation was only observed on samples tested at 500°C. The formed oxide was continuous, in the case of the 500°C tests the oxide could be seen to deviate from the boundary. Figure 8.22 shows examples of theses oxides after 500 h of exposure.

The maximum preferential oxidation penetrations observed in the samples are summarised Table 8.2 and shown in Figure 8.23. The penetration depth given is the maximum length of oxide observed penetrating the material along a grain boundary from the surface, not the depth normal to the surface. This allows for the worst case scenario to be accounted for, it may be possible for an observed penetration to take a shorter path, if there is a more direct grain boundary route to the surface in the material which may not have been observed in a cross-section. It should be noted that the maximum penetrations observed were normally on boundaries which were near normal to the surface (the difference

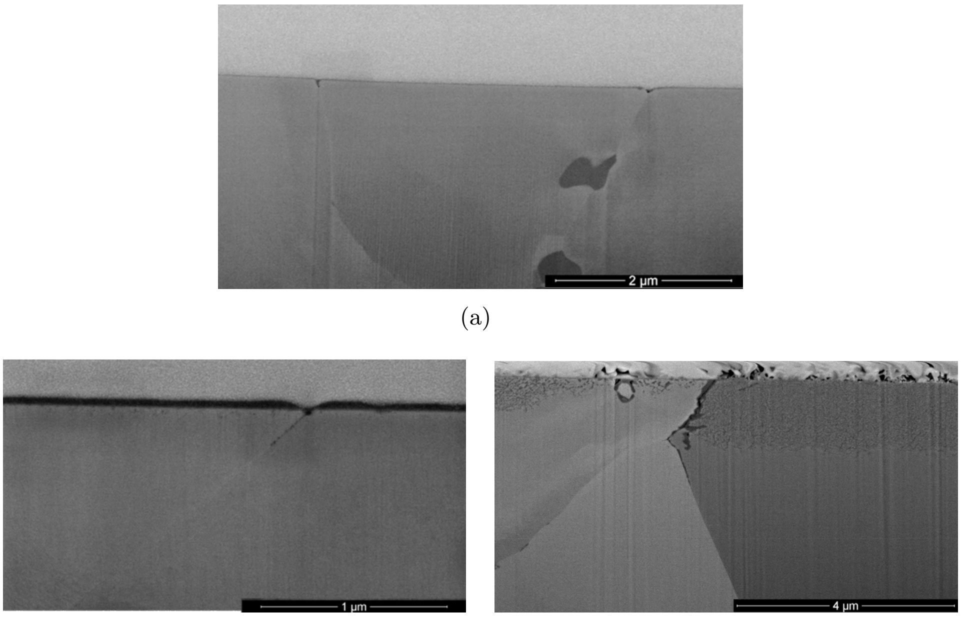

(a)

(b) (c)

Figure 8.22 – Preferential oxidation observed by FIB SEM from 15%CW-WF675 at 350°C for 500 h (a), 15%CW-WF675 at 400°C for 500 h (b) and AR-WF675 at 500°C for 66 h (c) exposures to steam with an R of 20.

between the length of oxide and depth normal to surface in the case of the maximums observed was never more than ≈ 15%).

Table 8.2 – The maximum observed grain boundary preferential oxidation depths in WF675 and 15%CW-WF675 after exposure to hydrogenated steam with R=20.

Temperature (°C)	Duration (h)	Maximum observed depth of grain boundary oxidation (nm)	
		AR	CW
500	66	1390	1460
500	500	3100	2500
400	500	210	300
350	500	50	100

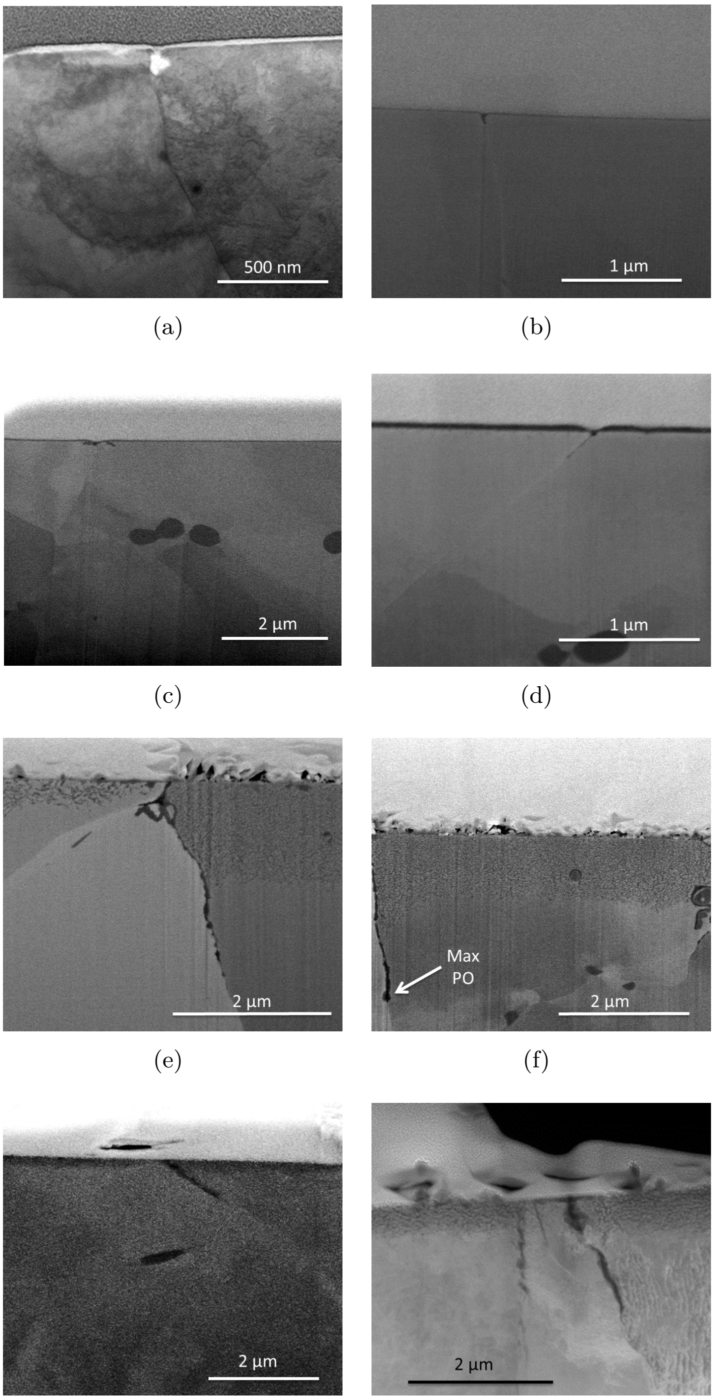
500 nm
1 µm
2 µm
1 µm
2 µm
Max PO
2 µm
2 µm
2 µm

(a) (b)

(c) (d)

(e) (f)

(g) (h)

Figure 8.23 – Bright field (a), FIB SEM (b-g) and HADDF (h) images showing the maximum observed preferential oxidation in steam (R=20). 350°C for 500 h AR (a) and CW (b), 400°C for 500 h AR (c) and CW (d), 500°C for 500 h AR (e) and CW (f), 500°C for 66 h AR (g) and CW (h).

Assuming that the preferential oxidation is diffusion controlled, a preferential oxidation rate constant (K_{oxide}) can be defined from the penetration depth via parabolic relationship. The value of K_{oxide} can be seen to have a comparable activation energy as the diffusion rate calculated by Scott [168]. Based on the maximum penetrations observed in steam, K_{oxide} has been calculated and can be seen in Figure 8.24.

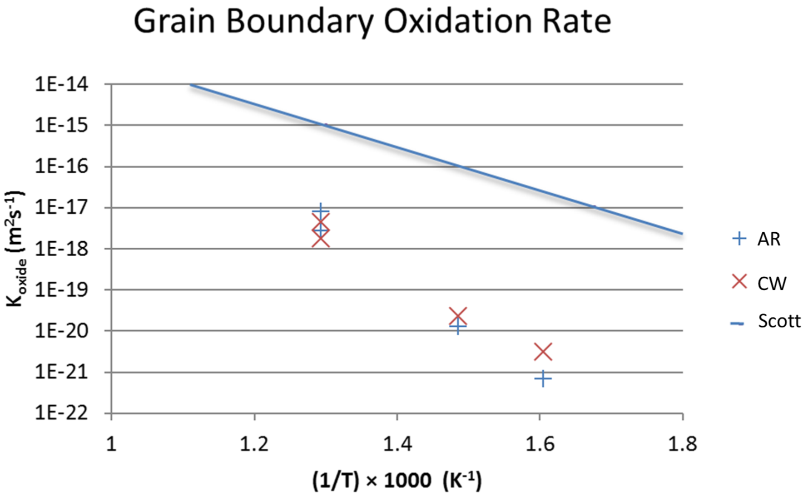

Figure 8.24 – Calculated preferential oxidation rates as a function of temperature for AR-WF675 (AR), 15%CW-WF675 (CW) and Scott's assumption of oxygen diffusivity required for the IO model of PWSCC (Scott).

Fitting of the data in Figure 8.24 with a equation in the form of

$$K_{oxide} = A \exp^{\frac{-Q}{RT}} \tag{8.1}$$

yields the activation energy of the process producing the preferential oxide. The results of which are $A = 2.27 \times 10^{-3}\ m^2 s^{-1}$ and $Q = 221$ kJ.mol^{-1} for AR-WF675 and $A = 5.04 \times 10^{-7}\ m^2 s^{-1}$ and $Q = 171$ kJ.mol^{-1} for 15% CW-WF675.

8.4.2 Dependency on Surface Oxide Morphology

The surface oxide formed at a grain boundary at 500°C has been divided into three types; NFZ, NNFZ and HH, the cross-sectioning of these boundaries by the FIB technique has shown that the preferential oxide formed (and internal oxidation) can be related to the surface oxide morphology. The observed relationship is more clear on the tests carried out for 66 h than that of the 500 h tests.

The NFZ boundary is seen to produce a preferential oxidation which in general was less severe than that observed on the other two boundary types. The region which is observed from the surface to be nodule free is seen to form a continuous oxide film at the surface. In this region under the continuous oxide it is observed that there is no internal oxidation present, this is associated with the formation of the continuous oxide at the surface preventing the inward diffusion of oxygen (Figure 8.25).

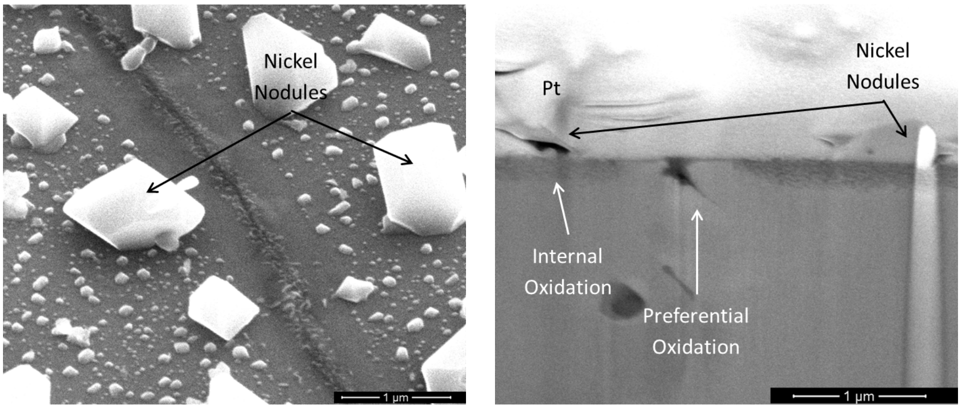

(a) (b)

Figure 8.25 – SE surface image of a NFZ boundary on 15%CW-WF675 in 500°C steam (R=20) after 66 h and the corresponding FIB SEM cross-section of the boundary.

The NNFZ boundaries have no continuous surface oxide (Figure 8.26); subsequently there is internal oxidation of the matrix all the way up to the grain boundary. In all the preferential oxidation observed on all of the boundary types, there is a significant variation in the observed penetration depths. However, the preferential oxidation observed on the NNFZ from the observed boundaries is perceived to be more penetrating relative to that of the NFZ boundaries (Figure 8.25).

The nature of the HH boundaries reflects its name; the side of the boundary which is free from nodules is seen to produce a continuous oxide under which is free from internal oxidation. The side which is observed to contain nodules at the surface has internal oxidation present up to the grain boundary and no observed surface oxidation (Figure 8.27). The severity of the preferential oxidation in terms of penetration depth can be seen to be comparable to that of the NNFZ boundaries.

The tests carried out for a duration of 500 h can be seen to oxidise in a manner similar to that of the shorter tests. However it should be noted that the identification of the boundary type becomes more difficult as the oxide grown obscures the boundary. In addition to the boundaries being obscured, boundaries which have the surface oxide related to the nodule free zone are observed to have small nodules form on the film, cross-sectioning of these boundaries show that there is limited internal oxidation under the film oxide formed at the surface. This can

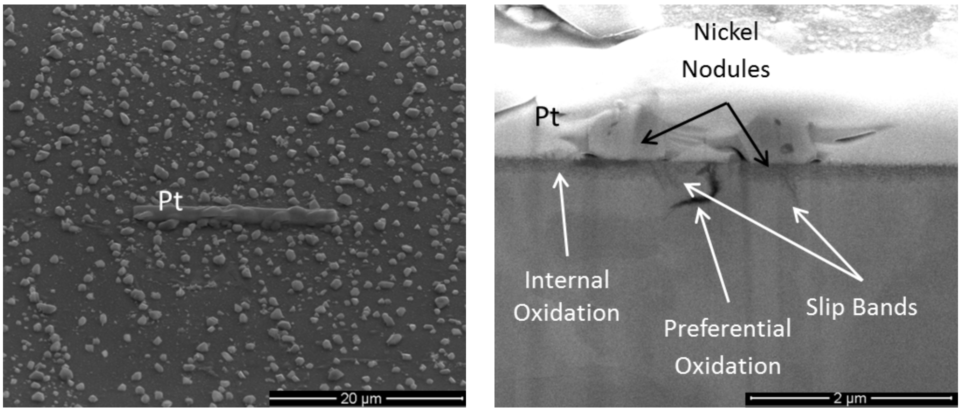
Pt
20 μm
Nickel
Nodules
Pt
Internal
Oxidation
Preferential
Oxidation
Slip Bands
2 μm

(a) (b)

Figure 8.26 – SE surface image of a NNFZ boundary on 15%CW–WF675 in 500°C steam (R=20) after 66 h and the corresponding FIB SEM cross-section of the boundary.

be interpreted as the surface oxide delaying the internal oxidation of the alloy, but not completely protecting it. Examples of all boundary types can be seen in Figure 8.28. It should be noted that the images 8.28(b)-8.28(d) are taken from the same boundary, thus indicating that the boundary type is not the dominate factor in the morphology which forms at a boundary.

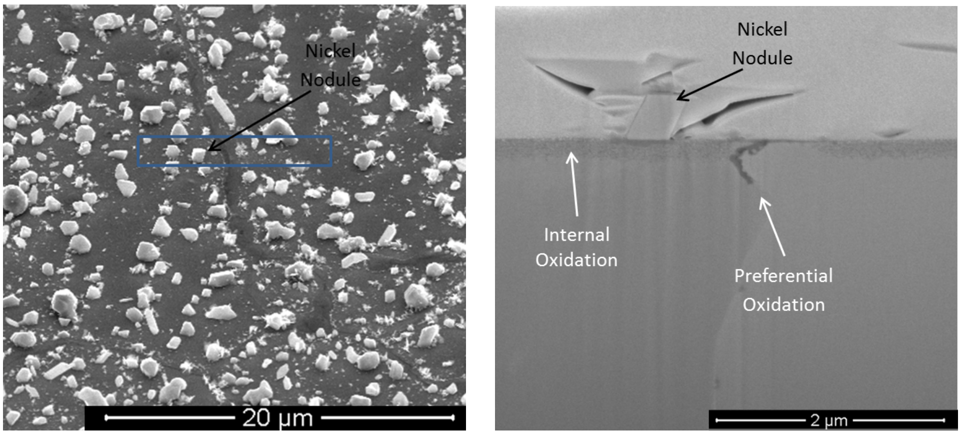
Nickel
Nodule
20 µm
Nickel
Nodule
Internal
Oxidation
Preferential
Oxidation
2 µm

(a) (b)

Figure 8.27 – SE surface image of a HH boundary on 15%CW–WF675 in 500°C steam (R=20) after 66 h and the corresponding FIB SEM cross-section of the boundary.

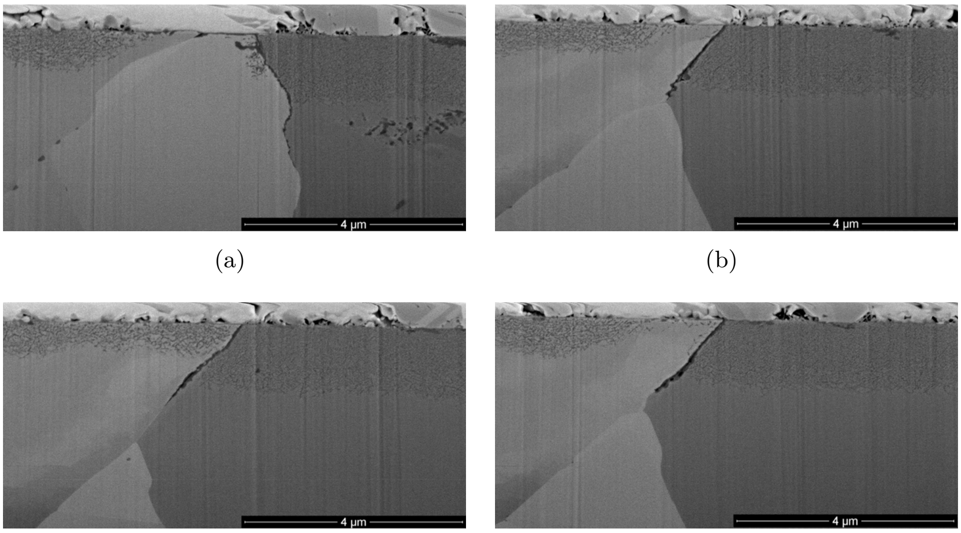
4 µm
4 µm
4 µm
4 µm

(a) (b) (c) (d)

Figure 8.28 – FIB SEM cross-sectional images of the preferential oxidation observed in a sample exposed to steam (R=20) for 500 h at 500°C, (a) is a NFZ (and a HH), (b) is a HH, (c) is a NNFZ and (d) is an example of a nodule free zone having slight internal oxidation. Cross sections (b) - (d) are taken from the serial sectioning of a single boundary, thus showing the GB Morphology can change without a clear change in grain boundary character.

8.4.3 The Effect of Carbides

Carbides observed in the internally oxidised layer were observed to be preferentially oxidised. The oxidation is implied by a dark ring of contrast forming around the carbide, this indicates a low atomic density. The observed oxidised carbides (the term oxidised carbide is refereeing to the oxide in the vicinity of the carbide, however it is probable that the oxide is a result of the incoherent interface acting as a fast transport path for oxygen, which subsequently reacts with the matrix material adjacent to the carbide, not the carbide oxidising) were not just present in the internally oxidised layer, but in the region beneath it, implying that the oxidation in the vicinity of the carbides was accelerated. Figure 8.29 shows an example of one of the preferentially oxidised carbide observed beyond the internally oxidised zone.

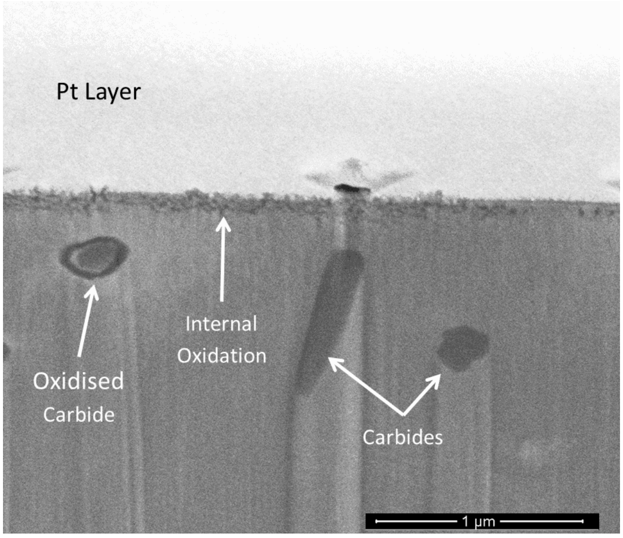

Figure 8.29 – Carbide observed by FIB SEM which appears to be below the internal oxidation zone, but still oxidised.

The oxide formed on the carbides is refered to as preferential not internal as it was continuous in nature. It should be noted that of the 176 carbides observed in the vicinity of the internally oxidised layer (at least part of the carbide could be identified to be within the IO layer), all but 3 were observed to be oxidised (form a ring or partial ring of dark contrast). It should be noted that the three carbides not observed to be oxidised were from the same region of a FIB serial sectioning and as such this may be a result of a poor focus/contrast as a result of drift during the process.

TEM EDX analysis of the dark ring of contrast produced on the carbides showed that there was a peak in the oxygen concentration, this peak was confirmed as a real feature by the analysis of the produced spectrums to confirm the presence of an oxygen peak (Figure 8.30). It should be noted that the presence of a peak is implied by the line scan as the oxygen profile does not shadow the chromium peak as would be expected, if the oxygen was a result of the chromium peak.

Serial sectioning of the 500°C samples showed that the oxidation observed on the carbides below the internally oxidised zone was a result of the oxidation proceeding down a carbide which was in part in the internally oxidised region (Figure 8.31), this was observed on multiple carbides. The illustration shown in Figure 8.31, shows a carbide producing a local acceleration in the oxidation rate, resulting in the oxide penetration being increased, it should be noted that the carbide given as an example is not completely oxidised, as the very tip of the carbide has no oxide.

Carbides observed beyond the internal oxide in the regions adjacent to, but not on the grain boundaries were in a number of cases observed to be oxidised Figure 8.32. The sequential sectioning indicated that the oxide bridged the gap between the carbide and grain boundary thus allowing the fast transport of oxygen.

The morphology of the oxide on the carbides was typically a shadow of that of the carbide, however frequently there was a small gap between the carbide and the oxide of what appeared to be matrix like material (Figure 8.33 and the first image of 8.31(a)). An extreme case of this is shown in Figure 8.33, note that the TEM EDX analysis shows that the material between the carbide and the oxide is representative of the matrix and has no elemental depletions. The influence of the chromium on the oxygen peak can also be observed in Figure 8.33 as despite the whole carbide being mapped as being slightly oxygen rich, no oxygen peaks were observed in the spectra from the carbide. The oxygen peak was observed in the outer parts, it can also be noted that the oxygen intensity in this region is greater than that of the carbide.

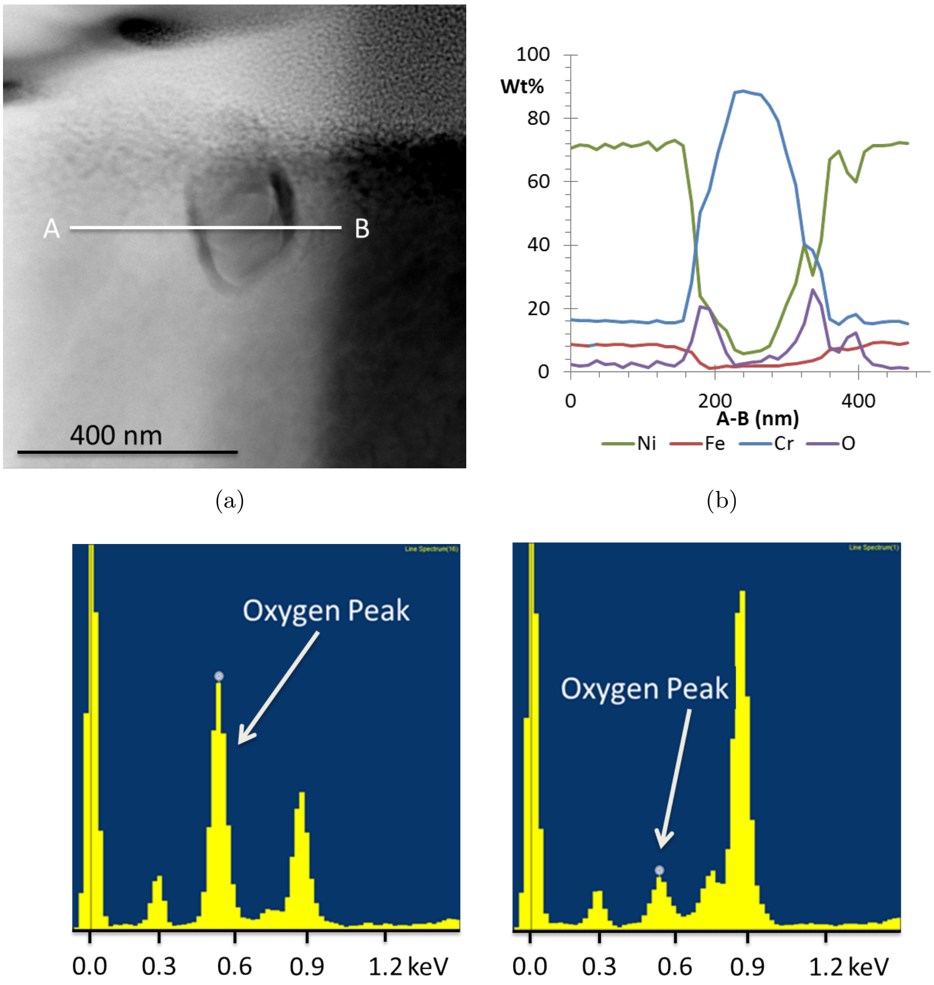

(a) (b)

(c) (d)

Figure 8.30 – HAADF image and EDX line scan obtained from an oxidised carbide (a-b), the oxygen peak obtained in the spectrum at 190nm (c) on the line A-B is given with a comparison to that obtained in the spectrum located at 0nm (d) on the line A-B.

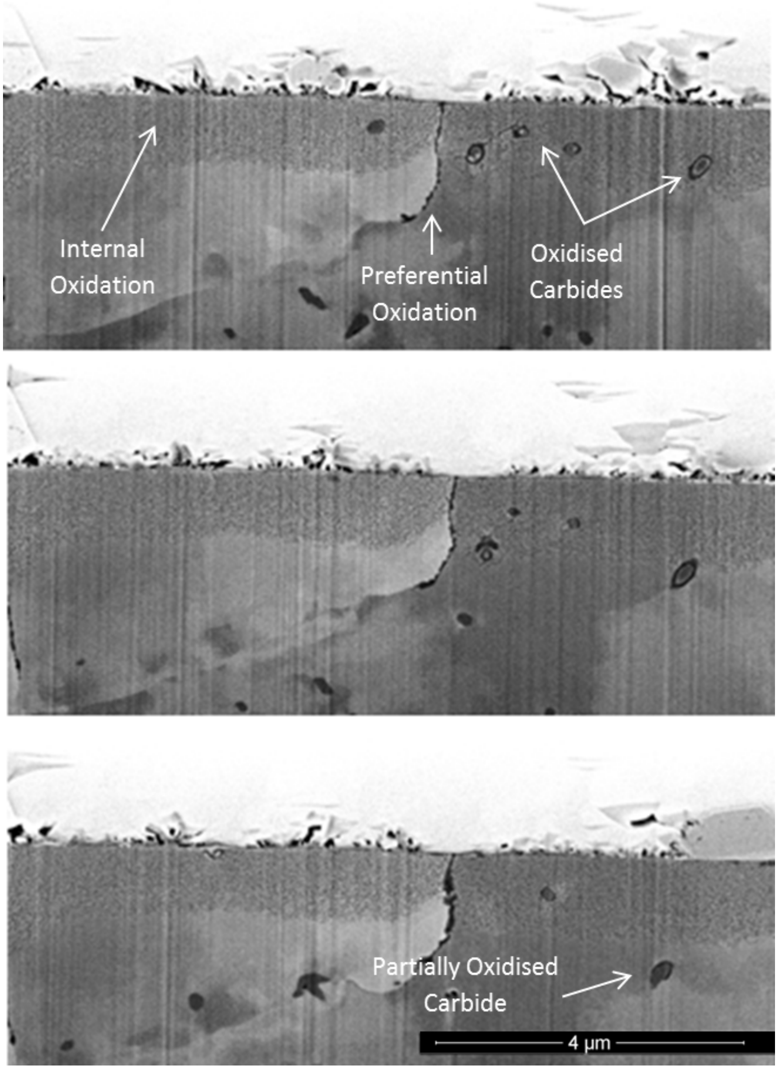
Internal
Oxidation
Preferential
Oxidation
Oxidised
Carbides
Partially Oxidised
Carbide
4 µm

(a)

Figure 8.31 – A sequence of images from FIB SEM serial sectioning showing an oxidised carbide which proceeds beyond the internally oxidised layer.

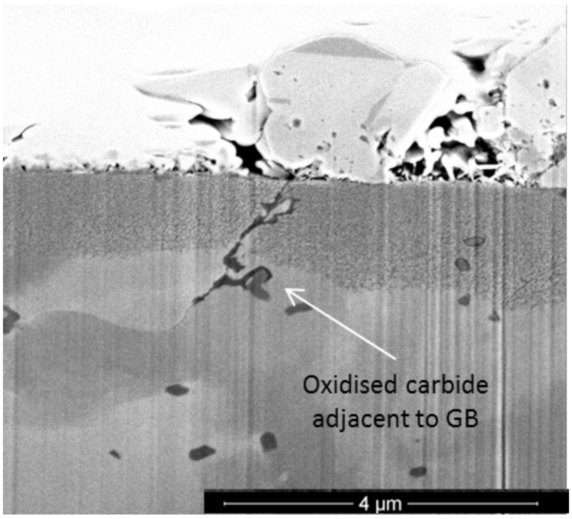
Oxidised carbide adjacent to GB
4 μm

(a)

Figure 8.32 – Carbide observed to be oxidised as a result of proximity to the grain boundary.

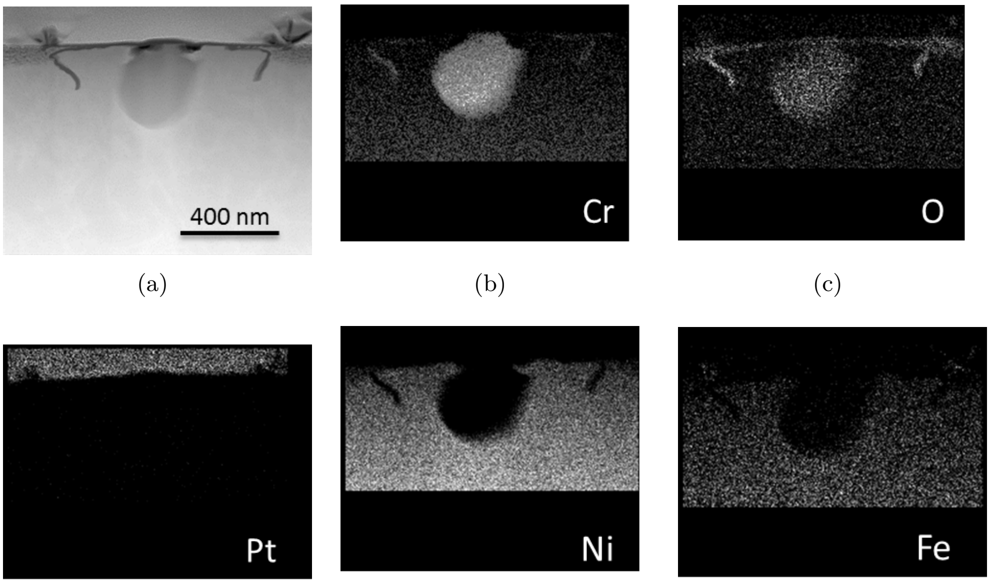
400 nm
Cr
O
Pt
Ni
Fe

(a) (b) (c)

(d) (e) (f)

Figure 8.33 – HAADF Image of a oxidised carbide (a) and the corresponding EDX elemental maps obtained from this region (b-f).

8.4.4 Elemental Analysis of Preferential Oxides

TEM samples of the preferential oxides formed on the AR and CW material after an exposure of 500°C for 66 h have been produced. A TEM sample of the preferential oxidation on the CW material exposed for 500 h at 400°C has also been produced. The purpose of these samples is to confirm the presence of oxygen in the suspected preferential oxide (the term preferential oxide has been used in the previous sections, however technically speaking it should have been described as a darkly imaging feature as the presence of oxygen has not yet been shown), identify any oxygen or fine oxides in advance of the preferential oxidation and observe any compositional changes as a result of the preferential oxidation.

NNFZ and HH boundaries were examined in the TEM analysis; no NFZ boundaries were observed via TEM, this is a result of the low frequency of this boundary type within the samples.

8.4.4.1 AR-WF675, 500°C, 66 h

From the AR material exposed at 500°C for 66 h, samples were produced from the NNFZ and HH boundaries. The darkly imaging region observed in the FIB cross-sectioning were confirmed to have a significant oxygen peak (Figure 8.34), supporting the previous assumptions that the darkly imaging features at the grain boundary were oxides.

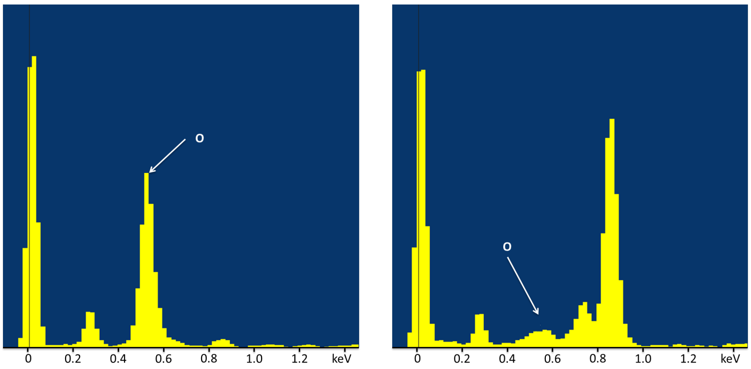

(a) (b)

Figure 8.34 – Oxygen peak obtained in the EDX spectrum from the preferential oxide (a) and a reference point in the matrix (b) of AR-WF675 after 66 h in 500°C steam (R=20). Spectrum (a) is taken from the 200 nm position of the line A-B in figure 8.35(b) whilst spectrum (b) is taken from 0 nm position of the line C-D in figure 8.35(c).

Line scans (generated from multiple point analysis producing individual spectra, not a continuous scan) produced from the oxide region showed that the oxide was chromium rich oxide (Figure 8.35). In addition to the chromium enrichment a slight enrichment was observed in both titanium and aluminium within all the preferential oxides observed (Figure 8.35(b)), the enrichment resulted in a depletion of nickel and iron. The formation of the preferential oxidation can be seen to produce a chromium depletion in the vicinity of the grain boundary. Note the chromium depletion can only be seen to occur on one side of the preferential oxide, thus exhibiting a strong asymmetry. The chromium depletion can also be observed as a nickel enrichment.

The chromium depletion (nickel enrichment) was not just observed adjacent to the preferential oxide, but in advance of the oxide down the grain boundary (Figure 8.35(c)). The chromium depletion along the grain boundary was present to beyond the end of the sample, however it should be noted that $M_{23}C_6$ carbides were detected in the mid-section of the TEM sample on the grain boundary (Figure 8.35(d)), thus the extensive depletion of chromium cannot solely be attributed to the preferential oxide as it may in part be a result of the small intergranular carbides.

In addition to the observed chromium depletion, the iron concentration is also depleted; the extent of which is not as large as that of the chromium. The iron is depleted adjacent to the grain boundary, in the same location as the nickel enrichment and chromium depletion and just ahead of the preferential oxide. However at the end of the TEM sample the iron concentration is not observed to vary over the grain boundary, whilst there is still a depletion of chromium (Figure 8.35(e)). This may indicate that the depletion within this region is a result of the observed carbides, not oxidation.

The sample shown in Figure 8.35 is from a HH boundary, elemental maps of the chromium and oxygen intensities of this preferential oxide are shown in Figure 8.36. The chromium map shows the large difference in chromium depletion observed, it can be noted that this depletion is observed in the region under the continuous film oxide where no internal oxidation is observed, this trend was observed in all samples analysed by TEM which were seen to have an internal oxidation free zone adjacent to the grain.

The asymmetric chromium depletion in adjacent grains was not however confined to the nodule free zones, a TEM sample from a NNFZ boundary showed that there was no chromium depletion initially at the surface, however beyond the internally oxidised zone a chromium depletion was observed to develop (Figure 8.37). As with the previous sample the depletion was only observed to occur on one of the grains and extended beyond the end of the TEM sample, it should be noted that the asymmetry in the depletion was not just confined to the region adjacent to the preferential oxide, but continued along the grain boundary.

The maps in Figure 8.37, in addition to showing the oxide also indicate that the internal oxidised zone is depleted in nickel and that the nickel is enriched in the chromium depleted region. The iron concentration in the vicinity of the preferential oxide shadows the chromium profile.

It can be seen in Figure 8.37 that the preferential oxide has a significant titanium concentration, as was indicated in the line scans of Figure 8.35. The presence of titanium is seen to extend beyond the chromium rich preferential oxide. Figure 8.38 shows point analysis taken from this region, the results of which show that there is a clear titanium (and aluminium) enrichment in the chromium depleted zone on the grain boundary. Analysis of the spectra shows that a faint oxygen peak is detected in the spectra exhibiting the titanium enrichment.

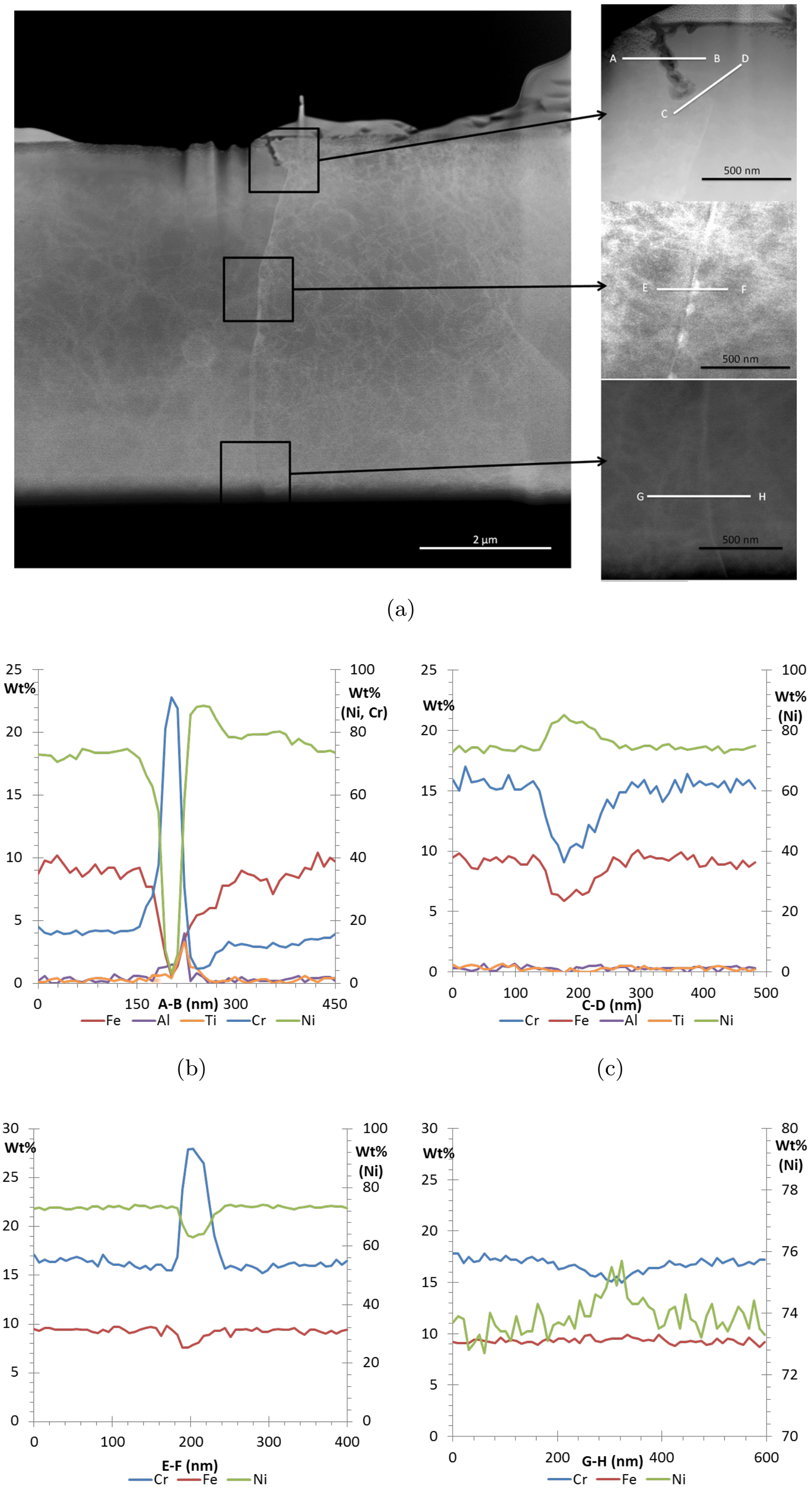

(a)

(b) (c)

(d) (e)

Figure 8.35 – HAADF image (a) and EDX line scans (b-e) of preferential oxidation on a HH boundary in AR-WF675 as a result of 66 h at 500°C in steam (R=20). (b) is from the preferential oxide, (c) is from the region just in advance of the oxide, (d) shows the presence of carbides in the central region of the sample and (e) is from the end of the sample.

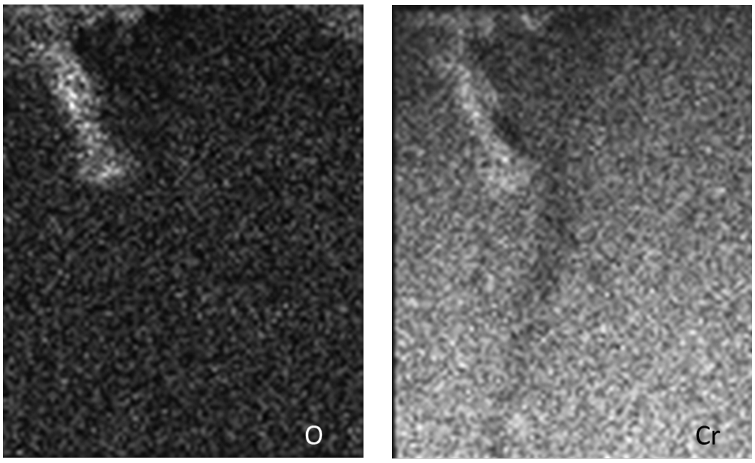

(a) (b)

Figure 8.36 – Chromium and oxygen maps obtained by EDX from the sample in Figure 8.35.

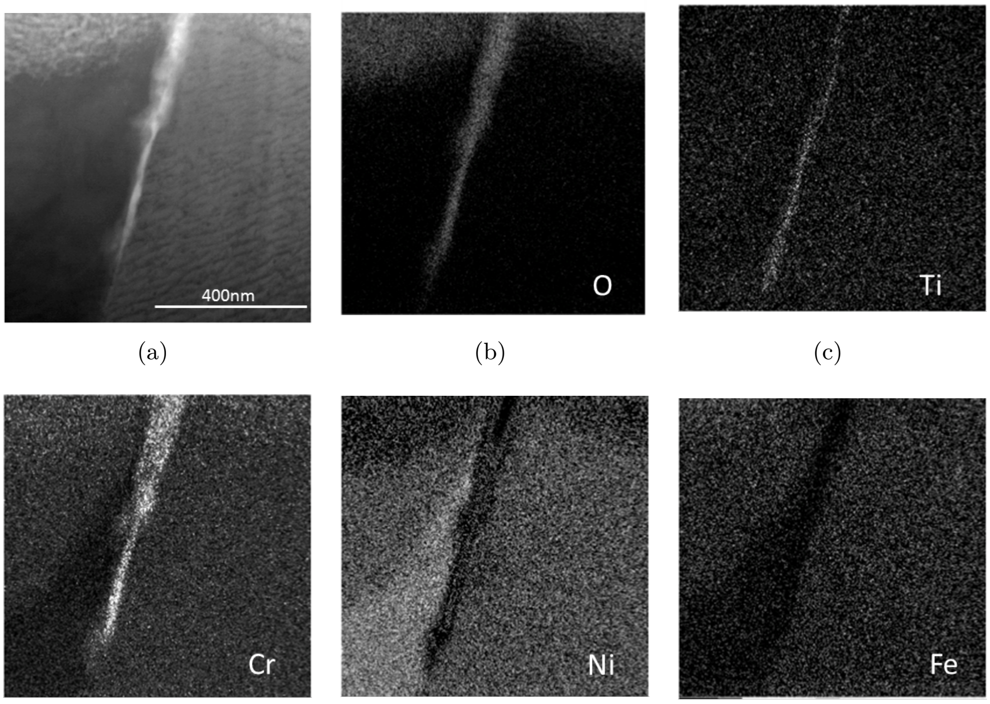

(a) (b) (c)

(d) (e) (f)

Figure 8.37 – Bright Field image of a preferential oxide under a NNFZ boundary in AR-WF675 as a result of 66 h at 500°C in steam (R=20) (a) and the corresponding EDX elemental maps obtained from this region (b-f).

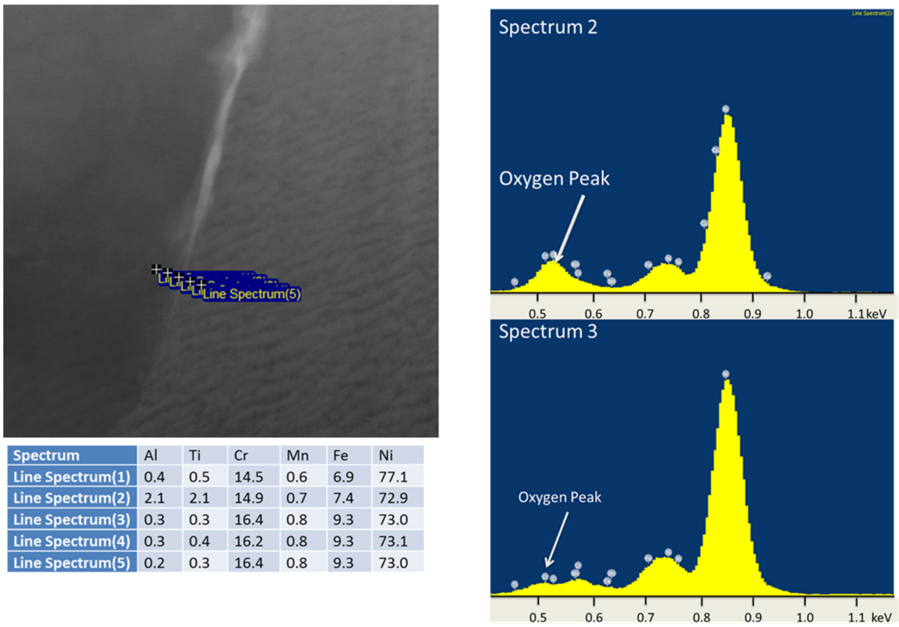

Spectrum	Al	Ti	Cr	Mn	Fe	Ni
Line Spectrum(1)	0.4	0.5	14.5	0.6	6.9	77.1
Line Spectrum(2)	2.1	2.1	14.9	0.7	7.4	72.9
Line Spectrum(3)	0.3	0.3	16.4	0.8	9.3	73.0
Line Spectrum(4)	0.3	0.4	16.2	0.8	9.3	73.1
Line Spectrum(5)	0.2	0.3	16.4	0.8	9.3	73.0

Figure 8.38 – Bright field image of the preferential oxide tip (from Figure 8.37) with EDX point analysis and spectra. These are indicating that there is an enrichment of titanium and oxygen in the chromium depleted zone just in advance of the chromium oxide.

8.4.4.2 15%CW-WF675, 500°C, 66 h

From the CW material exposed at 500°C for 66 h, samples were produced from HH boundaries. The result of the TEM analysis of these samples was much the same as the AR material.

The region observed to be free from internal oxidation was observed to have a significant depletion in chromium and iron, whilst being enriched in nickel (Figures 8.39(b)-8.39(c)). The preferential oxide was observed to have an enrichment in both titanium and aluminium, this enrichment was observed to proceed significantly into the chromium depleted region of the grain boundary (Figure 8.39(d)). In the region immediately under the surface oxide; the chromium depletion was not as severe, the zone of chromium depletion appeared to increase in size, up till ≈ half way down the preferential oxide before beginning to reduce (Figures 8.39(c)-8.39(e)).

As with the previous samples, the end of the grain boundary depletion could not be located, however as with the previous sample the presence of carbides may have influenced this result. The asymmetry observed in the chromium depletion can be seen to extend beyond the preferential oxide and continue down the grain boundary (Figures 8.39(d)- 8.39(e)).

Higher resolution analyses of the non-depleted grain was used to investigate if a small depletion zone was present, the results of this are shown in Figure 8.40. The results of Figure 8.40 indicate that if a depletion/enrichment was present within the grain, it would have to be less than 5 nm for it not to have been observed.

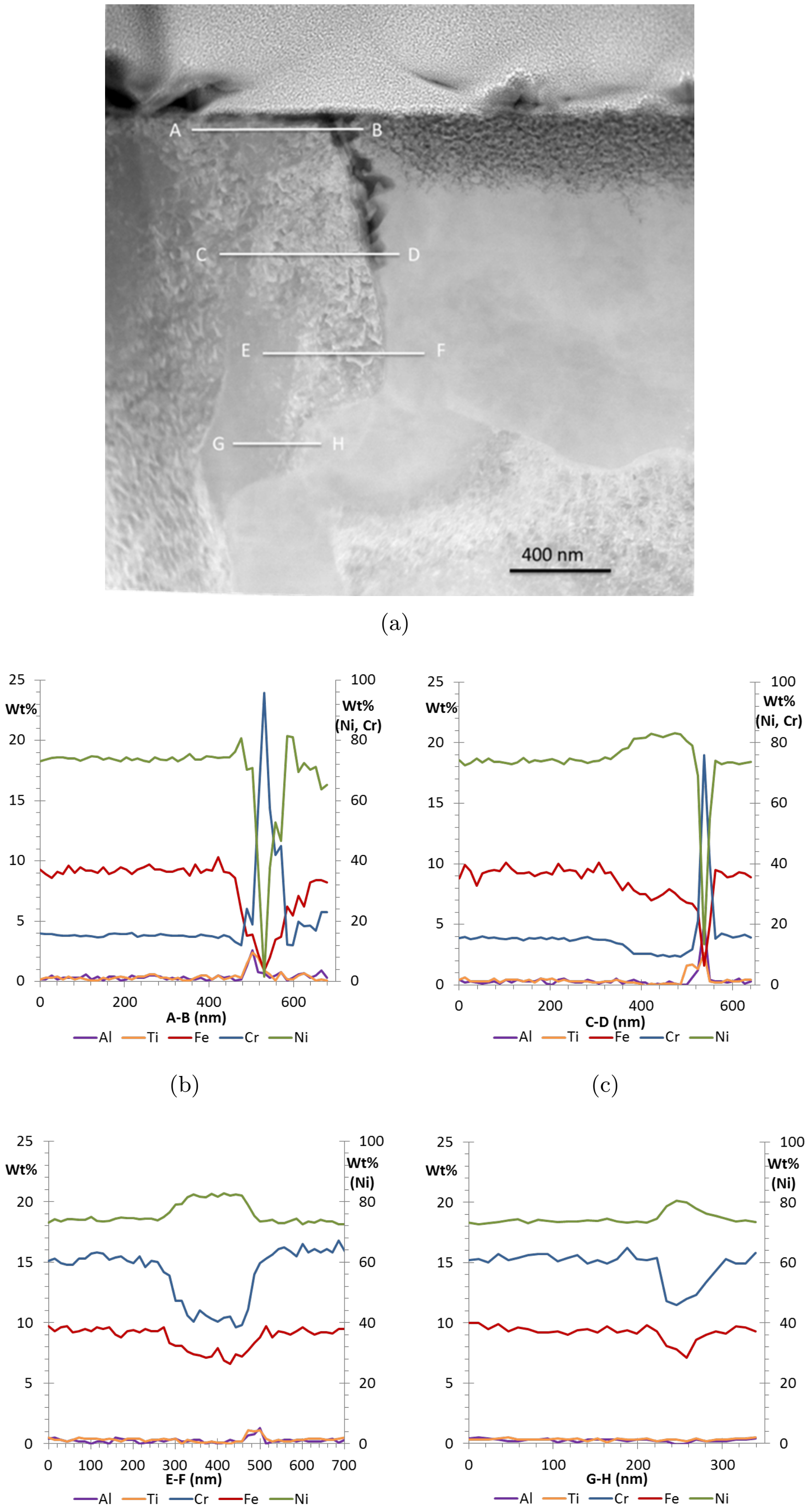

(a)

(b) (c)

(d) (e)

Figure 8.39 – HAADF image and EDX line scans of the preferential oxidation formed on a HH boundary in 15%CW-WF675 after 66 h at 500°C in steam (R=20). (b) is from the preferential oxide near the surface, (c) is from the preferential oxide near the tip, (d) is from the region just in advance of the oxide, (e) is far in advance of the preferential oxide.

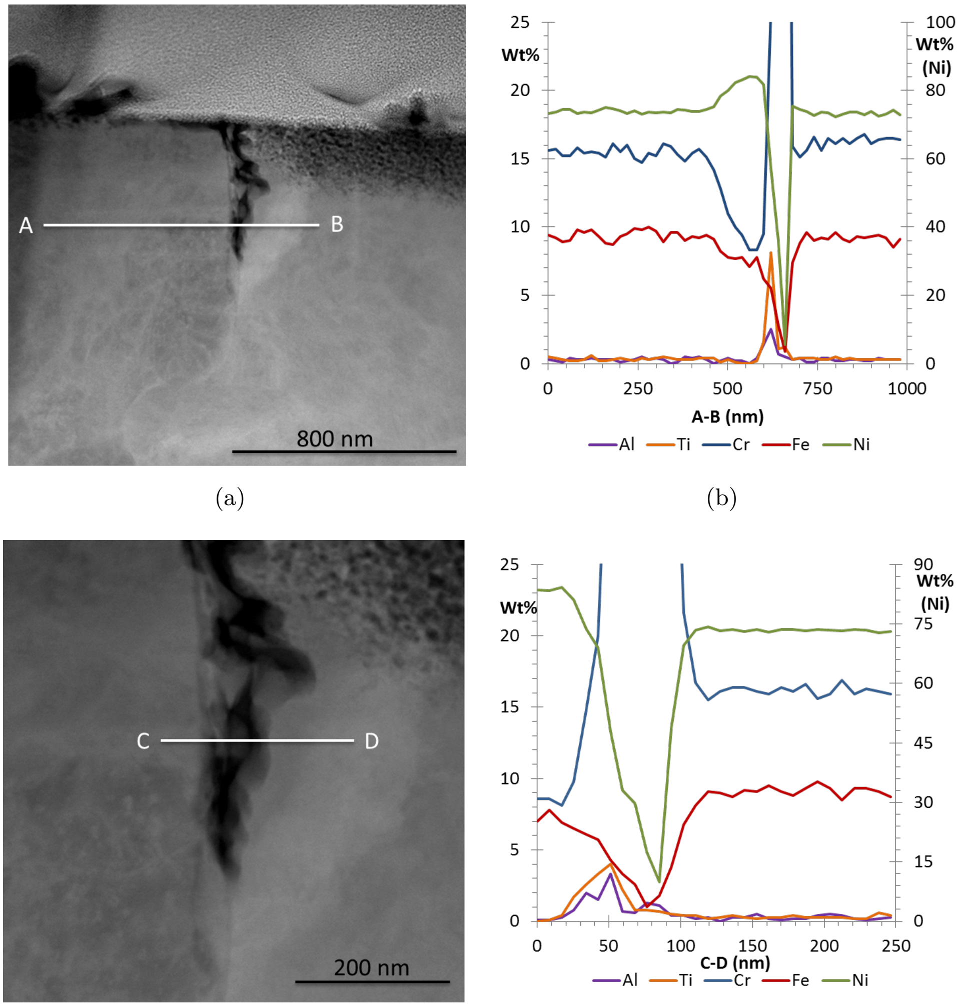

(a) (b)

(c) (d)

Figure 8.40 – HAADF image and EDX line scans of the preferential oxidation observed in Figure 8.39 at a higher magnification to identify any small depletion in the none depleted grain.

8.4.4.3 15%CW-WF675, 400°C, 500 h

Unlike the 500°C samples, the boundary types on the 400°C samples were not distinguishable into different types. TEM analysis of the CW 400°C sample exposed for 500 h showed that the preferential oxide was chromium and titanium rich, the same as the tests conducted at 500°C (Figure 8.41 and Table 8.3). The grain boundary can be seen to be depleted in chromium in advance of the preferential oxide, relative to the matrix. No titanium or chromium enrichment was observed in advance of the chromium oxide.

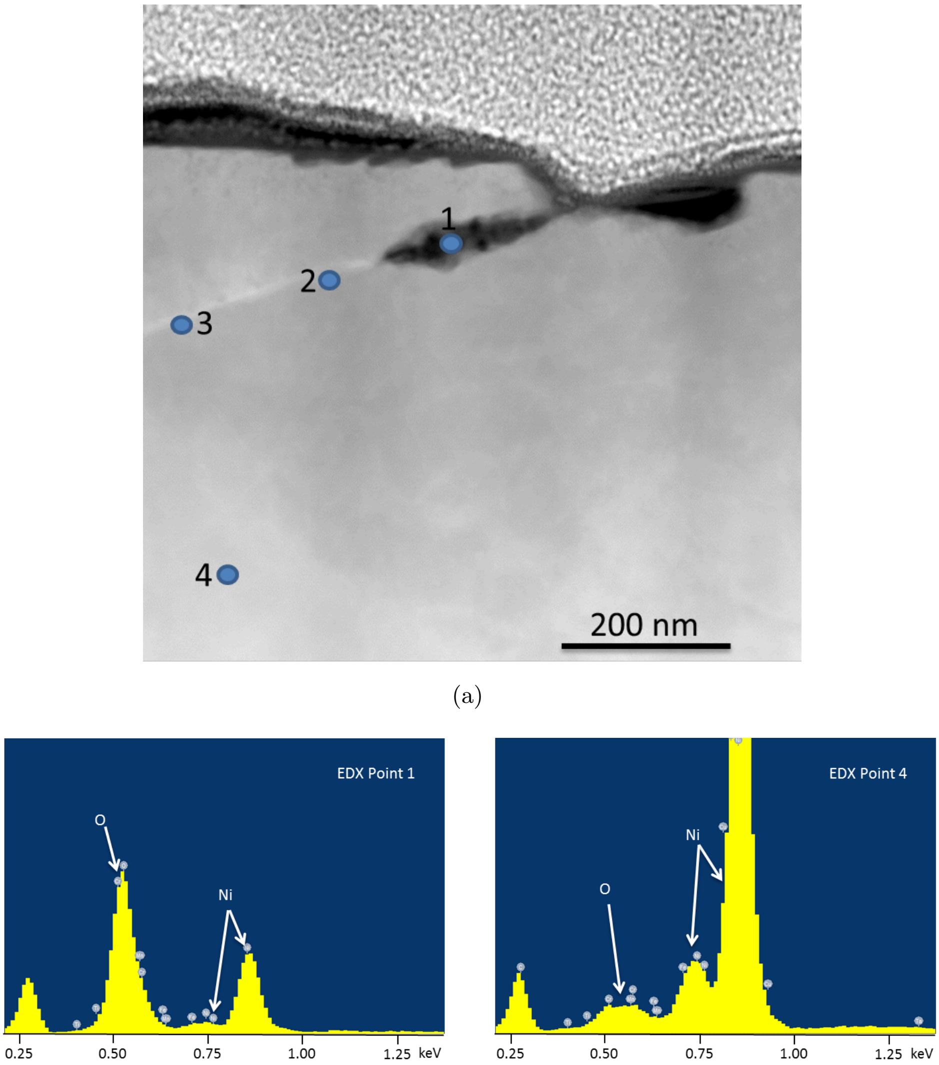

(a)

(b)

(c)

Figure 8.41 – HAADF image annotated with locations of EDX point analysis locations from a preferential oxide formed at 400°C. The spectrum in (b) is taken from EDX point 1 whist spectrum (c) is from EDX point 4, these spectra confirm the presence of oxygen. The results of the EDX is given in Table 8.3.

Table 8.3 – Results of the EDX point scans shown in Figure 8.41.

Point	Ni	Fe	Cr	O	Ti	Al
Spectrum 1	20.1	2.3	44.5	28.4	1.1	0.5
Spectrum 2	73.1	8.6	14.7	1.5	0.3	0.4
Spectrum 3	73.7	8.7	15.2	0.7	0.4	0.2
Spectrum 4	72.1	9.4	16.8	0.4	0.4	0.3

From the maps shown in Figure 8.42 it can be seen that there is a possible indication that the chromium depletion is from a single grain, however the small size of the depletion means that this maybe an effect of the boundary being inclined through the sample thickness. It can also be observed that a small chromium rich particle (presumed to be a carbide) is observed on the grain boundary, thus making the cause of the observed depletion questionable. A slight enrichment of titanium can just be made out in the tip of the preferential oxidation (also visable from EDX point 1 in Figure 8.41 and Table 8.3).

The range of the observed chromium depletion can be seen to be just over one micron from Figure 8.43, as the first two scans can be seen to be nickel rich, the third line has no compositional changes when passing over the grain boundary. The change in the chromium and nickel concentrations on the second line scan is within error, representative of the bulk, however there are 5 consecutive points at the grain boundary for which the nickel is enriched and chromium depleted, as such this slight change is interpreted as a real feature, not scatter from the data.

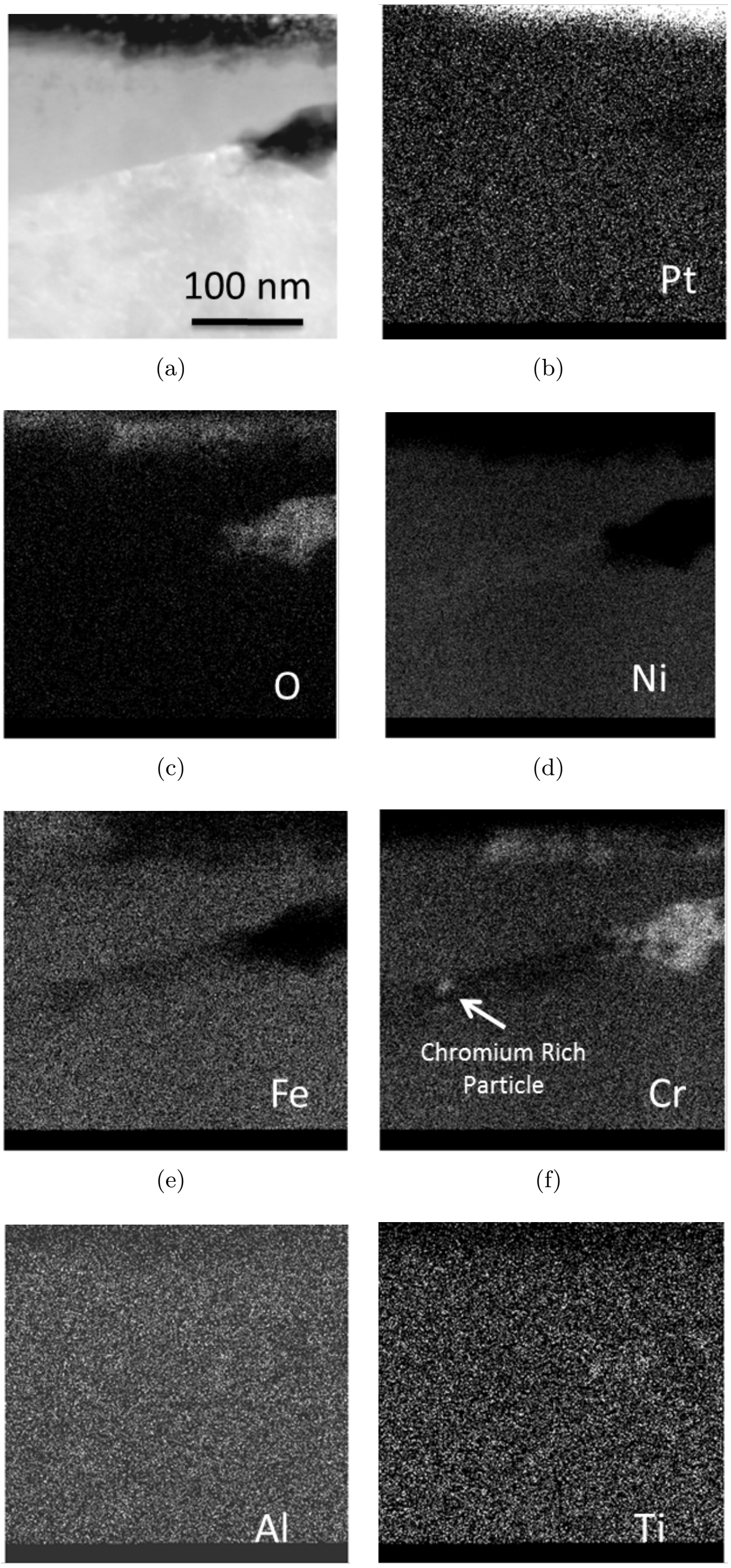
100 nm
Pt
O
Ni
Fe
Chromium Rich Particle
Cr
Al
Ti

(a) (b)

(c) (d)

(e) (f)

(g) (h)

Figure 8.42 – HAADF image of preferential oxidation formed in 15%CW-WF675 as a result of 500 h at 400°C in steam (R=20) (a) and the corresponding EDX elemental maps obtained from this region (b-h).

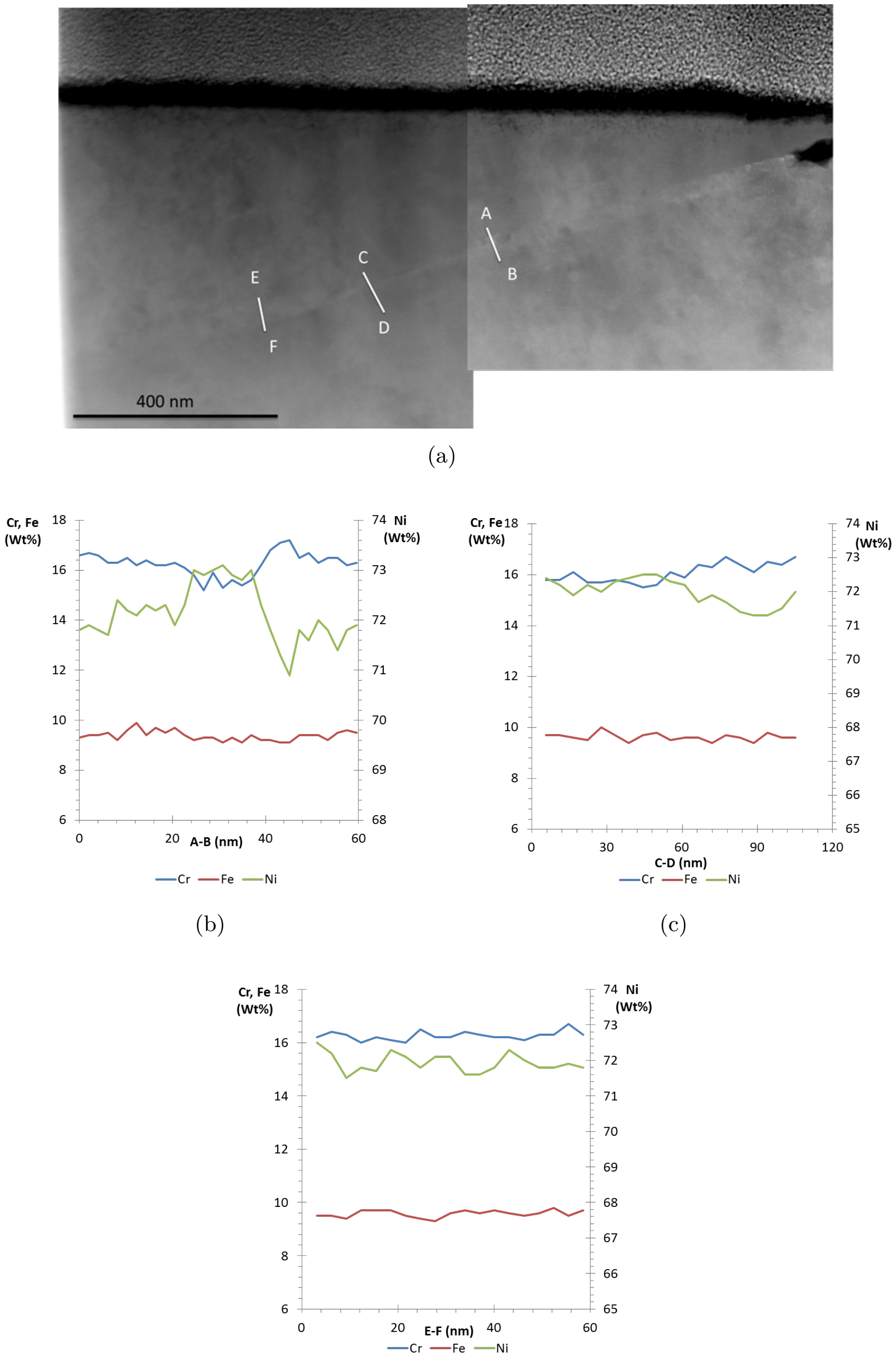

(a)

(b)

(c)

(d)

Figure 8.43 – Lower magnification HAADF image of the preferential oxidation in Figure 8.42, presenting the grain boundary in advance, with EDX line scans indicating chromium depletion. Lines 1, 2 and 3 are shown in (b), (c) and (d) respectively.

8.4.5 Discussion of the Mobility of Chromium During Oxidation

A region of particular interest in the preferential oxidation is the depletion of chromium, it has been suggested that this may be the rate limiting factor in PWSCC. As could be seen in 8.4.4, there was significant chromium depletion in the region of the preferential oxide. The morphology of the depleted regions was not consistent with that expected from a diffusion controlled process (all diffusion appeared to occur in a single grain (Figure 8.40), the depletion profile could be found to be significantly more pronounced beyond the preferential oxidation (Figure 8.37) and the grain boundary in the region of the depletion had an erratic path (Figure 8.35).

Treating the grain boundary chromium depletion in the same manner as the preferential oxidation (follows parabolic growth rate) a minimum grain boundary diffusivity can be estimated. The results of such a calculation imply that minimum grain boundary diffusivity at 500°C and 400°C are on the order of $\approx 1 \times 10^{-16} m^2 s^{-1}$ and $\approx 10 \times 10^{-18} m^2 s^{-1}$ respectively. For 500°C, this value is based on the length of the TEM sample being the size of the depleted zone ($\approx$ 5 μm) as depletion was observed to the end of all TEM samples, in reality this value is questionable due to the presence of carbides and the fact that no end to the depletion was observed. The value at 400°C is based on the grain boundary depletion of $\approx$ 1 μm as observed in Figure 8.43.

Following the same logic and using the maximum width of depletion ($\approx$ 1 μm) observed leads to a minimum value of $10 \times 10^{-18} m^2 s^{-1}$ for the bulk at 500°C. All the above calculations assume that the time is equal to the full duration of the test and that the concentration at the edge nearest to the oxide has a chromium concentration of zero, which in reality is unlikely.

It should be noted that this data cannot be used to extrapolate the diffusivity at lower temperatures as in 500°C samples the grain boundary depletion was found to extend beyond the end of the samples and as such the measured length is an underestimate. In addition the presence of M_7C_3 (of which the material was initially believed to be free from when supplied [11]) carbides on the grain boundaries in all produced TEM samples may contribute to the depletion and severely limited the ability to accurately determine the grain boundary diffusivity of chromium. With regard to the bulk diffusivity , the odd morphology of the bulk depletion leads to the mechanism of depletion to be questioned.

An observation made on numerous FIB cross-sections of 500°C exposures was that the grain boundaries would appear to kink in an un-natural fashion. The region between the kinked preferential oxide and an extrapolation of the expected grain boundary path, was found to correspond with the region of nickel enrichment and chromium depletion (Figure 8.44). As a result of this observation, grain boundary migration must be considered as a possible occurrence.

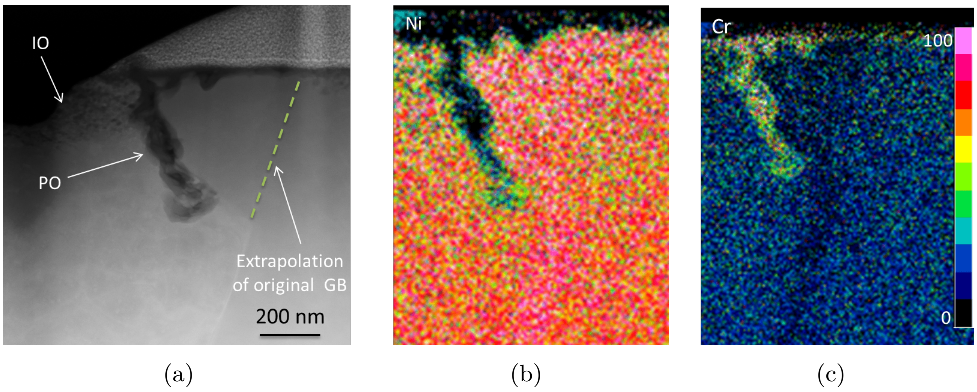

(a) (b) (c)

Figure 8.44 – Dark field image (a) and EDX maps showing nickel enrichment (b) and chromium depletion (c) along the trace of the original grain boundary, a lower magnification image of the sample (HH boundary in AR-WF675 exposed for 66 h to 500°C steam with an R of 20) can be found in Figure 8.35.

The occurrence of chromium depletion occurring up to what is postulated to be the original grain boundary is not just limited to the region adjacent to the oxide but could extended further into the grain. Figure 8.45 gives an example of this occurrence, with the results of the EDX point analysis in Table 8.4.

What is considered the original boundary appeared to form two humps, this is believed to be a result of a small M_7C_3 carbide pinning the grain boundary during thermal treatments of the material, the carbide was identified by EDX mapping of the grain boundary region Figure 8.46 (Figure 8.37 and Figure 8.38 shows additional EDX analysis of the same oxide).

It is noted that the tip of the preferential oxide in Figure 8.45 is on what is considered to be the original GB. This would suggest that if migration is occurring, a small quantity of oxide is insufficient to pin the grain boundary. Indications that this may be the case have been observed in the 500 h test at 500°C, during the cross-sectioning of the samples a number of occurrences were observed where the oxide would branch away from the grain boundary, this path would then shortly terminate (Figure 8.47).

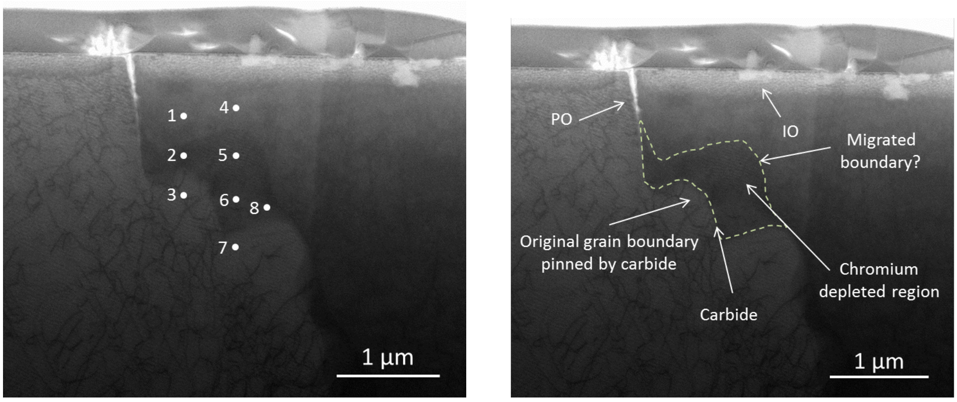
1
2
3
4
5
6
7
8
1 µm
PO
IO
Migrated boundary?
Original grain boundary pinned by carbide
Chromium depleted region
Carbide
1 µm

(a) (b)

Figure 8.45 – Dark field image (a) with location of EDX point scans and annotated version showing key features. Additional characterisation of this sample (NNFZ boundary in AR-WF675 exposed for 66 h to 500°C steam with an R of 20) can be found in Figure 8.37.

Table 8.4 – Results of the EDX point scans shown in 8.45(a).

Point	Ni	Fe	Cr
Spectrum 1	73.9	9.4	16.7
Spectrum 2	76.6	8.4	15.0
Spectrum 3	74.0	9.1	16.8
Spectrum 4	74.3	8.8	16.9
Spectrum 5	76.9	8.2	15.0
Spectrum 6	76.2	9.3	14.5
Spectrum 7	73.6	9.6	16.8
Spectrum 8	77.4	8.2	14.5

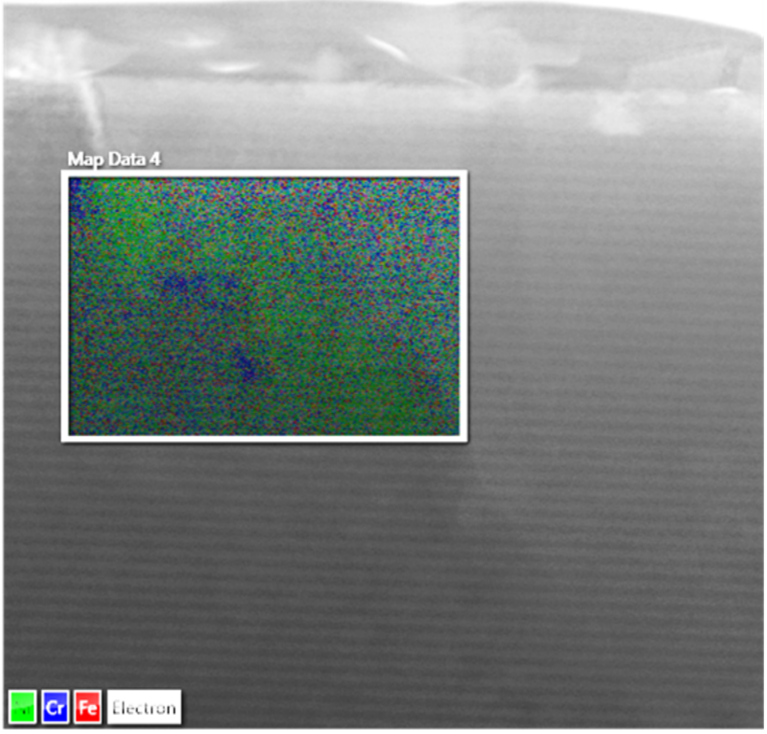
Map Data 4
Cr
Fe
Electron

(a)

Figure 8.46 – Dark field image with layered EDX map indicating the presence of a carbide, from Figure 8.45.

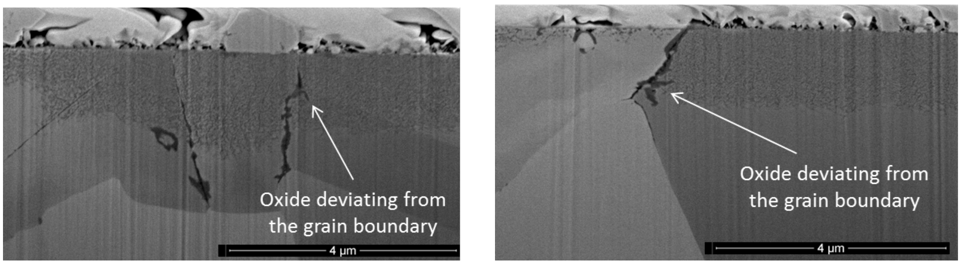
Oxide deviating from the grain boundary
4 µm
Oxide deviating from the grain boundary
4 µm

(a) (b)

Figure 8.47 – FIB SEM images with the preferential oxide appearing to deviate from the grain boundary in AR-WF675(a) and 15%CW-WF675 (b) after 500 h exposure to 500°C steam with an R of 20.

8.5 The Effect of Surface Finish

In the set of samples exposed to 500°C hydrogenated steam for 500 h, samples from both forms of the alloy were included which had a P600 surface finish (all samples were prepared with one face OPS, the other P600, however the possibility of a geometry effect lead to only the top faces being analysed). The effect of the surface finish had a dramatic effect on the surface, internal and preferential oxidation of the alloy.

8.5.1 Surface Oxidation

The morphology of the surface oxide formed on the two surfaces was in stark contrast to each other. As previously described the oxide formed on the OPS surface in 500°C steam was a mixture of metallic nickel nodules with some iron rich oxides at the surface, there was no chromium oxide film at the surface, instead there was internal oxidation of the matrix to produce a chromium rich oxide. The P600 surface however is observed to have undergone little visible change, a colouration change in the sample implied that an oxide had been produced, SEM analysis showed that there was no visible features formed on the sample surface (Figure 8.48).

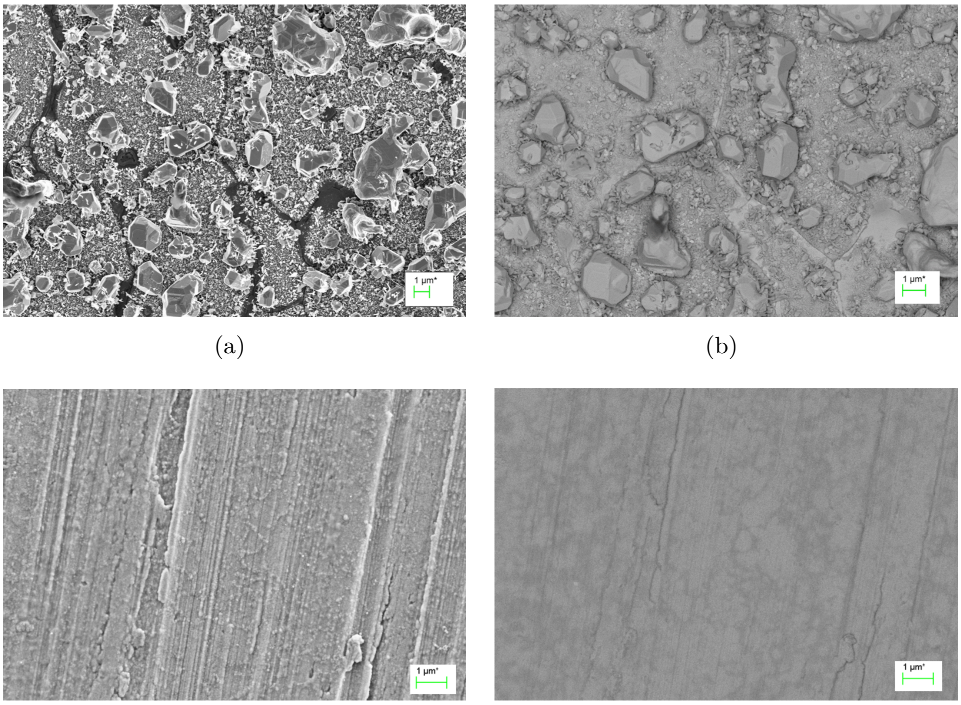

(a) (b) (c) (d)

Figure 8.48 – SE (a) and ESB (b) images of the oxide formed on an OPS surface in 500°C hydrogenated steam (R of 20) after 500 h. SE (c) and ESB (d) images of the oxide formed on a P600 surface in 500°C hydrogenated steam after 500 h.

8.5.2 Preferential and Internal Oxidation

The FIB cross-sectioning of the OPS surface had shown that there was significant internal and preferential oxidation of the OPS surface (Figure 8.49). The cross-sectioning of the P600 surface after oxidation however showed that the features observed in the OPS tests were not present. The cross-sections gave the indication that a continuous oxide film had formed at the surface. The formation of this oxide film appeared to have suppressed any internal oxidation occurring, the deformed layer in the P600 surface gives the impression of a fine grained microstructure, however none of the subgrain structure appeared to be oxidised (this is in contrast to the result present in section 9 which shows this structure to oxidise).

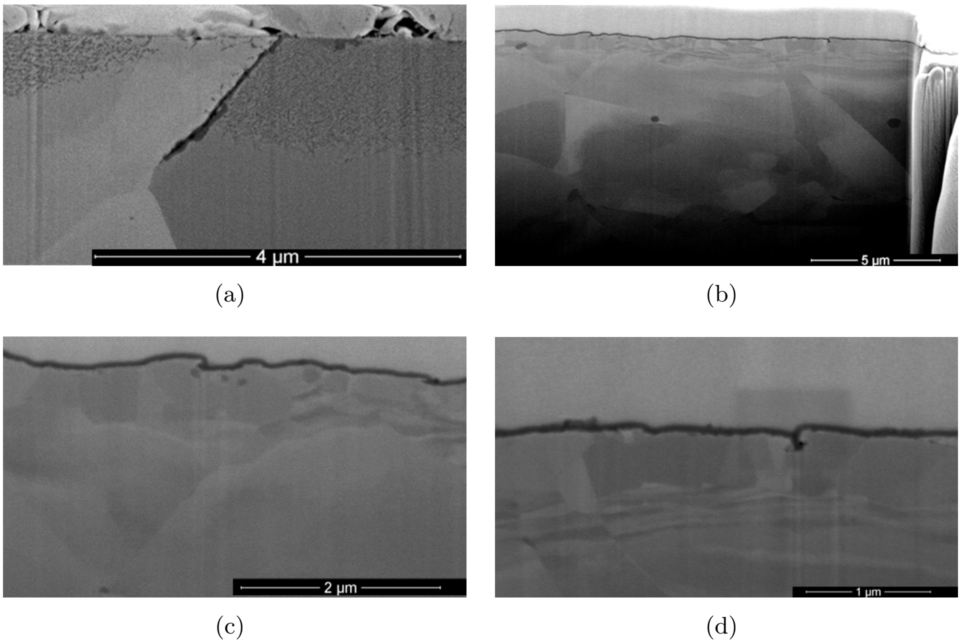

(a) (b)

(c) (d)

Figure 8.49 – FIB SEM cross-sections of the OPS (a) and P600 (b-d) surface, after a 500°C exposure for 500 h.

8.6 Solution Annealed Alloy 600

Hydrogenated steam oxidation was carried out at 480°C for 66 h with a ratio (R) of 20 on solution annealed HT93510 (SA-HT93510, described in 7.2), the samples had an OPS surface finish. These test parameters are consistent with tests in [14], which were carried out on electrochemically polished samples of the same material. The produced oxide is comparable to that reported to form on an electrochemical polished surface.

The oxide formed on solution annealed Alloy 600 (Figure 8.50) was predominately nodules of metallic nickel, however there were regions on the surface with iron based oxide present (deduced from morphology being consistent with that observed in Figure 8.12), in these regions the nickel nodules were still present.

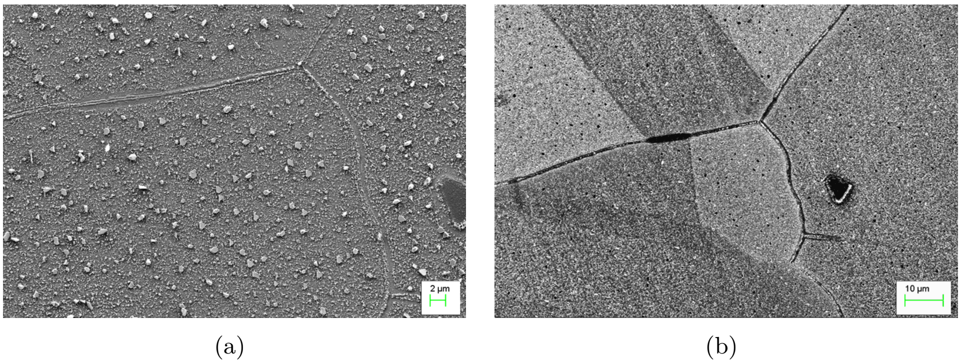

(a) (b)

Figure 8.50 – Low magnification SE images of the surface oxidation of SA-HT93510 after 66 h at 480°C with a R of 20.

It was observed that a number of distinct morphologies of the oxide existed at the grain boundaries. It is noted that these morphologies did not occur at twin boundaries, as can be seen from Figure 8.50.

8.6.1 Morphologies of Grain Boundary Oxides

The solution annealed alloy was EBSD mapped after oxidation. The EBSD mapping (Figure 8.51) indicated that the features previously assumed to be the grain boundaries were indeed grain boundaries.

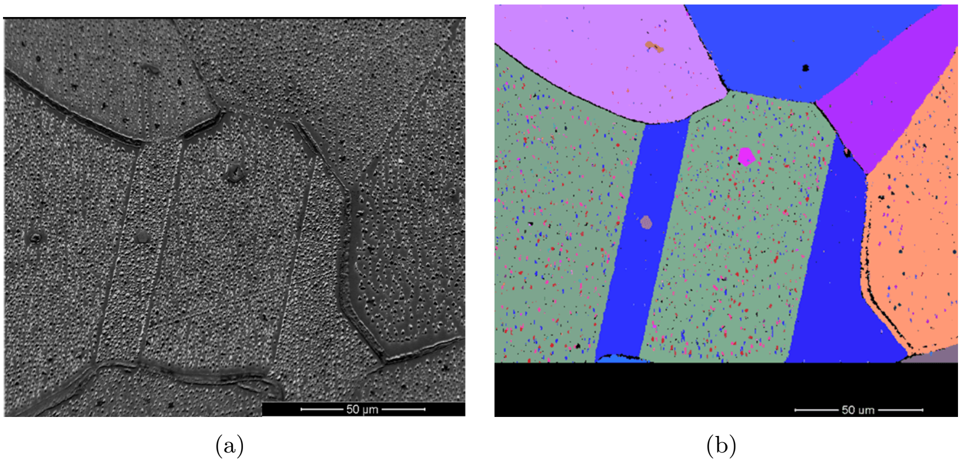

(a) (b)

Figure 8.51 – EBSD map taken on an oxidised sample (SA-HT93510 after 66 h at 480°C with a R of 20) indicating that the grain boundary oxide changes morphology's when the grain boundary character changes.

It can be seen from Figure 8.51 that the grain boundary's oxide morphology would only change when the character of grain boundary altered. Twin boundaries did not have the same morphologies as the grain boundaries, but were notably different from the matrix. This was in part due to the different crystallographic orientations oxidising at variable rates, hence producing a contrast change at the twin boundary. In some cases, but not all, a line of metalic nickel nodules formed along the twin boundary.

The grain boundary's oxide morphology can be divided into three distinct categories:

Nodule Free Zone (NFZ) grain boundaries (Figure 8.52): These grain boundaries presented a ridge at the boundary and the area adjacent to the boundary (approximately 1 µm) was devoid of any nodules.

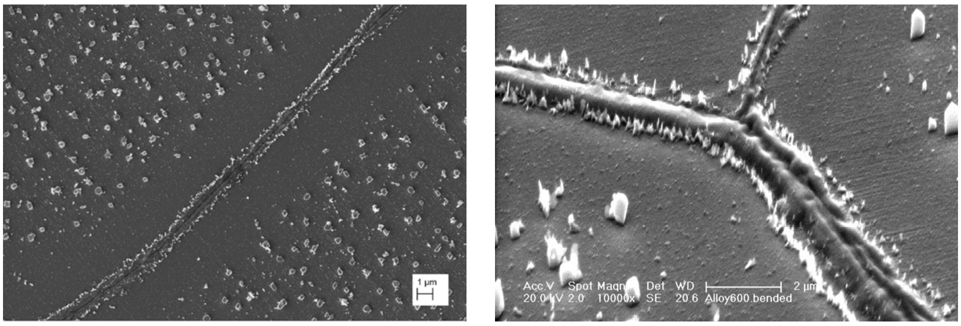
1 µm
Acc.V Spot Magn Det WD 2 µm
20.0 kV 2.0 10000x SE 20.6 Alloy600 bended

(a) (b)

Figure 8.52 – NFZ grain boundaries observed on SA-HT93510 after 66 h at 480°C with a R of 20. (b) is tilted to 52°.

No Nodule Free Zone (NNFZ) grain boundaries (Figure 8.53): These grain boundaries presented a ridge at the boundary, but the size of the ridge appeared to vary and the surface oxide formed in a continuous manner all the way to the boundary.

Half and Half (HH) grain boundaries (Figure 8.54): These boundaries were infrequent but appeared to have the morphology of a NFZ on one side and that of a NNFZ on the other.

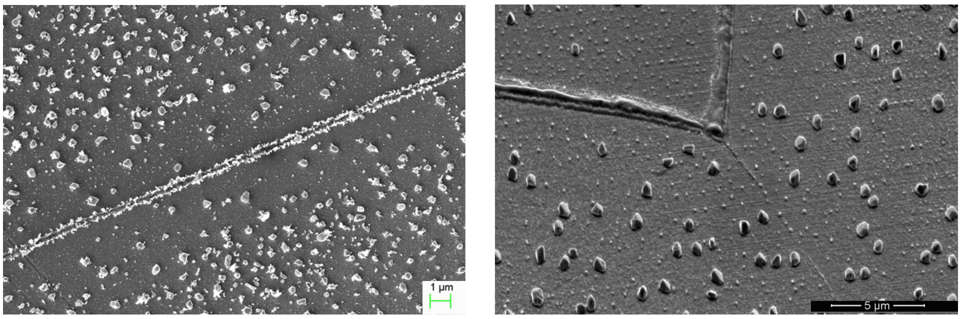

(a) (b)

Figure 8.53 – NNFZ grain boundaries observed on SA-HT93510 after 66 h at 480°C with a R of 20. (b) is tilted to 52°.

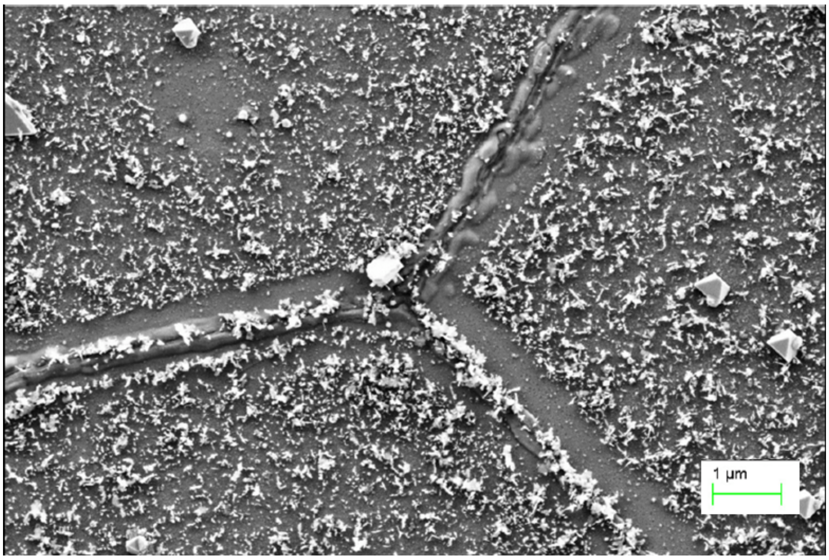

Figure 8.54 – HH grain boundary observed on SA-HT93510 after 66 h at 480°C with a R of 20.

8.6.2 Preferential Oxidation

The FIB method of producing cross-sections was utilised on the oxidised solution annealed samples to observe if preferential and internal oxidation had occurred. Prior to the cross-sectioning, some of the samples were carbon coated to increase the conductivity, this however produced a band of contrast change in-between the platinum and sample surface which is similar in appearance to an oxide layer. The grain boundary morphologies were noted before milling.

The cross-sections produced from the NNFZ showed the preferential oxidation of the grain boundary had occurred and that there was slight internal oxidation of the matrix (Figure 8.55). The internal oxidation of the matrix occurred uniformly and is seen to be present next to the preferential oxidation. No surface oxide was observed in these regions, the contrast produced in Figure 8.55 is a result of the carbon coating.

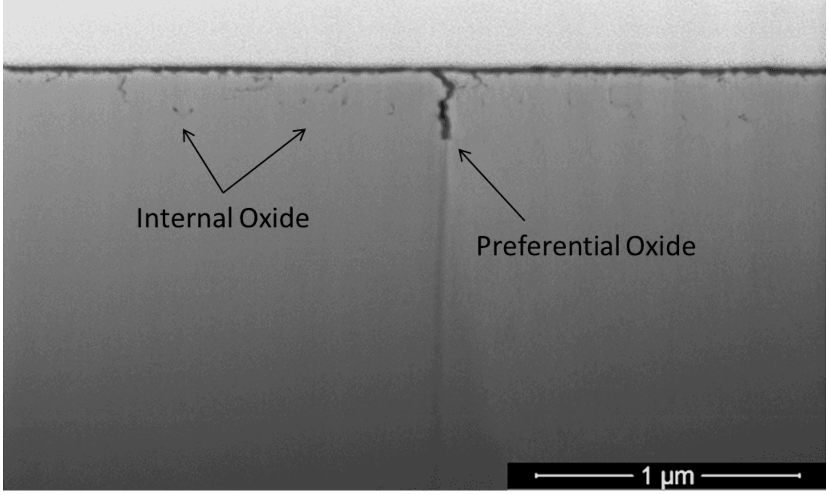

Figure 8.55 – FIB SEM cross-section of a NNFZ grain boundary observed in SA-HT93510 after 66 h at 480°C with a ratio of 20.

Cross-sections on the NFZ showed a very different morphology to that of the NNFZ's, these boundaries had little to no preferential oxide on the grain boundary; a thick surface oxide had however formed in the region which was free of nodules (Figure 8.56). Internal oxidation of the grain is observed, however this is suppressed in the region of the external oxide layer (Figure 8.56). The sample from which Figure 8.56 is taken is a carbon coated sample.

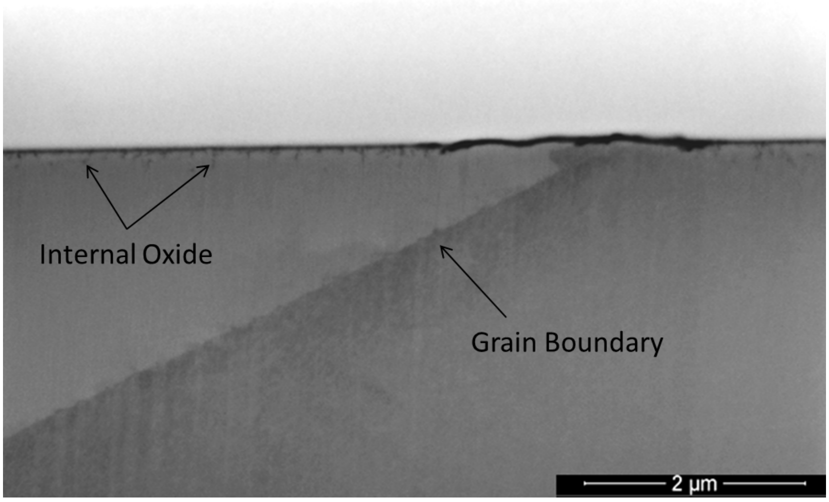

Figure 8.56 – FIB SEM cross-section of a NFZ grain boundary observed in SA-HT93510 after 66 h at 480°C with a ratio of 20.

A pair of twins from a non-carbon coated sample cross-sectioned (Figure 8.57) showed that no surface film (observable by FIB SEM) formed in the oxidation process, the internal oxidation observed in the region of the twins in Figure 8.57

is seen to be unaffected by their presence.

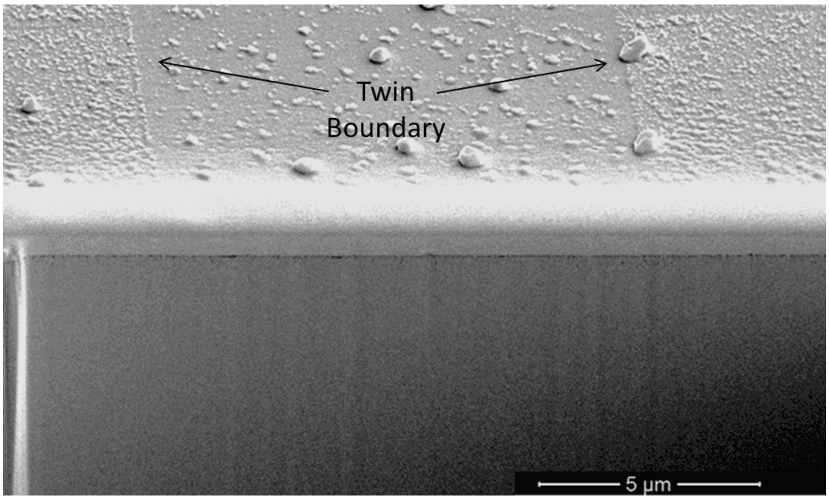

Figure 8.57 – FIB SEM cross-section of a twin grain boundary observed in SA-HT93510 after 66 h at 480°C with a ratio of 20.

The oxidation which has been reported in this section (the internal, preferential and grain boundary surface oxides) have all been confirmed as chromium rich oxide by TEM analysis [111]. The presence of titanium and aluminium enrichment in the preferential oxides has also been observed as shown in WF675 [1].

8.6.3 Metalic Nickel Nodules

A result of the EBSD mapping was that the fine step size used allowed the individual nickel nodules to be indexed, this can be seen in Figure 8.51, where they appear in the form of many small grains within the larger grains, these small grains correlate with the locations of the nickel nodules. The crystallographic relationship between the nodules and the matrix is such that there was a 60° rotation in the crystal lattice, the same as a twin boundary ($\Sigma3$). This can be seen by overlaying the $\Sigma3$ boundaries on the map, a method often used to highlight twinning (Figure 8.58).

---

[1] The TEM work is not published in this thesis as it is to form part of another student's future thesis, as per the required declaration at the beginning of this thesis, it cannot be published here. Some of the results can be found in [111]

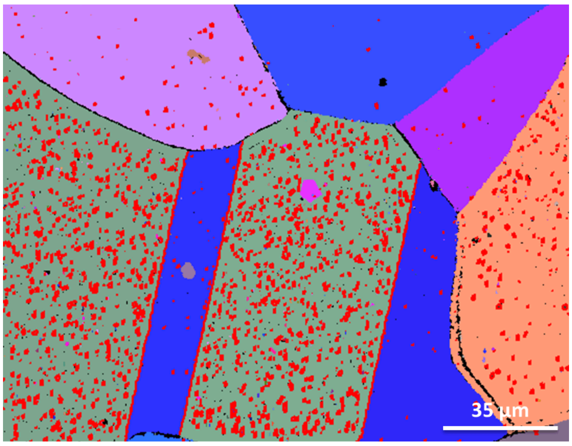

Figure 8.58 – EBSD map showing nodules on the grains appear to be mapped as $\Sigma3$ boundaries on SA-HT93510 after 66 h at 480°C with a R of 20.

8.6.4 Surface Finish

As with WF675, the effect of surface finish has been investigated on the SA-HT93510. The effect of surface finish was conducted in the same conditions as the previous results (480°C for 66 h with an R of 20). Three sample surfaces were used; an OPS, 1 µm and a P600 finish. The results of this test are shown in Figure 8.59. The results showed the OPS surface forming nodules of metallic nickel with regions of iron based oxide, as previously shown. The 1 µm and a P600 finishes however, showed no visible sign of oxidation and were almost indistinguishable from the un-oxidised samples with the exception of the titanium nitrides on the 1 µm sample which were attacked (the titanium nitride shown in 7.15(b) is actually an image taken from this test).

Given the dramatic change in external appearances the P600 sample was cross-sectioned to investigate the preferential oxidation. However as the grains were not visible from the surface and the large grain size meant the chance of a cross-section intersecting a grain boundary was low, a grid approach as shown in 8.60(a) was used. This grid of cross-sections was used to maximise the chances of locating a grain boundary, but unfortunately no grain boundaries were observed in the cross-sections. The cross-sections did however reveal that a film oxide had formed on the surface (sample is not carbon coated) and that no internal oxidation was observed (Figure 8.60(b)). The sample had a deformed layer of ≈ 2 µm (Figure 8.60(c)).

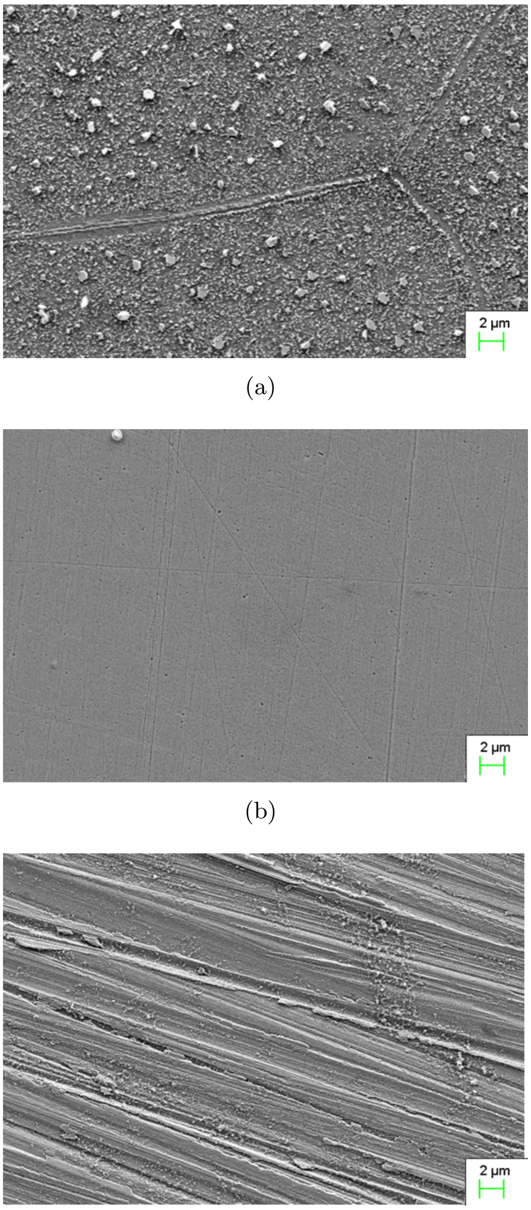

(a)

(b)

(c)

Figure 8.59 – SE images of the oxides formed on the OPS (a), 1 µm (b) and a P600 (c) surface after oxidation on SA-HT93510 after 66 h at 480°C with a ratio of 20.

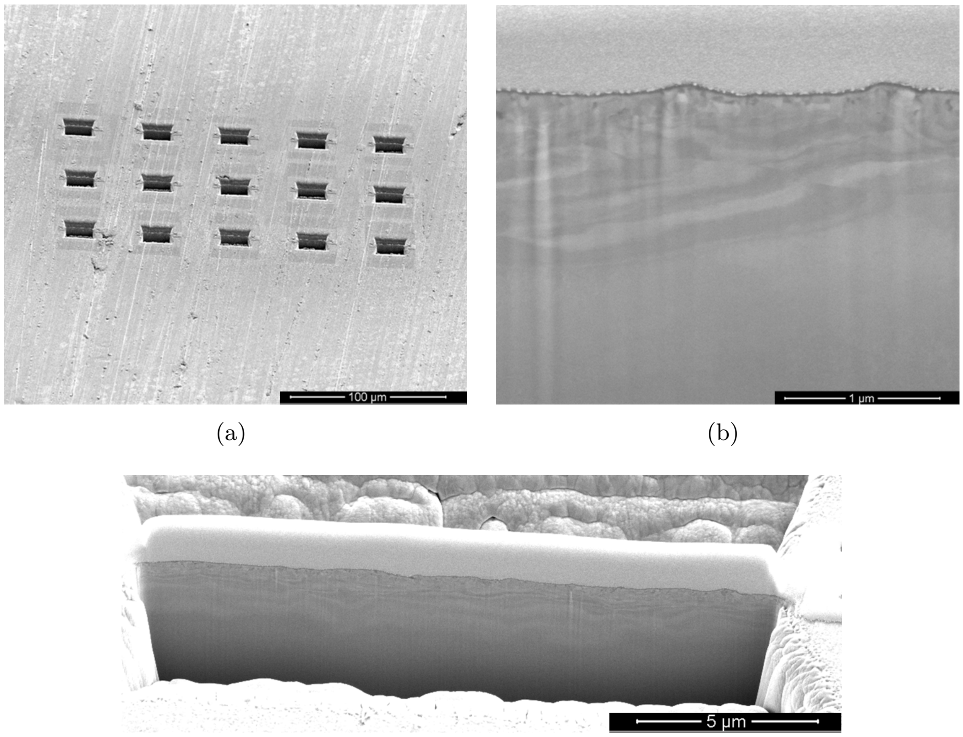

(a) (b)

(c)

Figure 8.60 – FIB SEM images taken in a attempt to locate a grain boundary on the P600 surface of SA-HT93510, after 66 h at 480°C with a ratio of 20.

CHAPTER

NINE

AUTOCLAVE OXIDATION

For comparison to the hydrogenated steam results, autoclave tests were performed on WF675. These were carried out at 350°C with a hydrogen overpressure of 30 cc/kg. As in the steam testing no lithium hydroxide or boric acid were added. The test was for a duration of 500 h. It should be noted that a failure of a preheater during the test (after $\approx$ 400 h) resulted in the remainder of the test being conducted at 325°C.

In general, tests simulating primary water are conducted with $\approx$ 1000ppm of boric acid and $\approx$ 2ppm lithium hydroxide. Considering a test temperature of 350°C, this results in the environment with a $pH_{350^{\circ}\mathrm{C}}$ of 7.9. The removal of these additives will alter $pH_{350^{\circ}\mathrm{C}}$ to $\approx$ 6.1. As can be seen from Figure 3.14, a reduction in pH will reduce the susceptibility of a material to PWSCC. The reduction in susceptibility is considered a necessity to allow the direct comparison of the low and high pressure oxidation samples.

9.1 Observations of the Oxides Formed on the Surface

The surface oxide formed on the reference tests has been examined to ensure that the test produced an oxide comparable to that reported in the literature, the oxide formed on a mechanically polished surface is well defined. Given the results obtained from steam, samples with an OPS surface are also examined.

9.1.1 The Effect of Surface Finish

The oxides formed in the autoclave tests on contrasting surfaces were significantly different (Figure 9.1). The OPS surface had formed a chromium rich oxide. The nature of the oxide suggested that its formation was crystallographic (possibly epitaxial). The oxide formed platelets, the platelets on a single grain protruded out at the same angle, other grains however formed a continuous film without the platelets (Figure 9.1(a)). The crystallographic behaviour of the oxide is illustrated by the twin in Figure 9.1(a), the orientation of the oxide on the twin is rotated relative to the grain, but the oxide orientation on either side of the twin is the same.

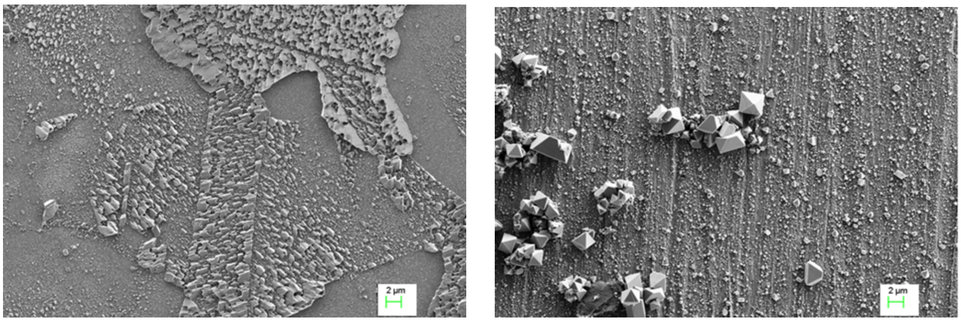

(a) (b)

Figure 9.1 – SE images of the oxide formed on the OPS (a) and P600 (b) surface of AR-WF675 after 500 h autoclave exposure to 350°C water with a hydrogen overpressure of 30cc/kg.

The P600 surface was morphologically consistent with the oxidation of Alloy 600 reported in the literature [37, 41]. It has previously been sugested that the large spinels (Figure 9.2(a)) formed on the oxide layer are a result of deposition, not growth. The deposition would occur in the cooling stage of the test when the cation solubility in the water decreases.

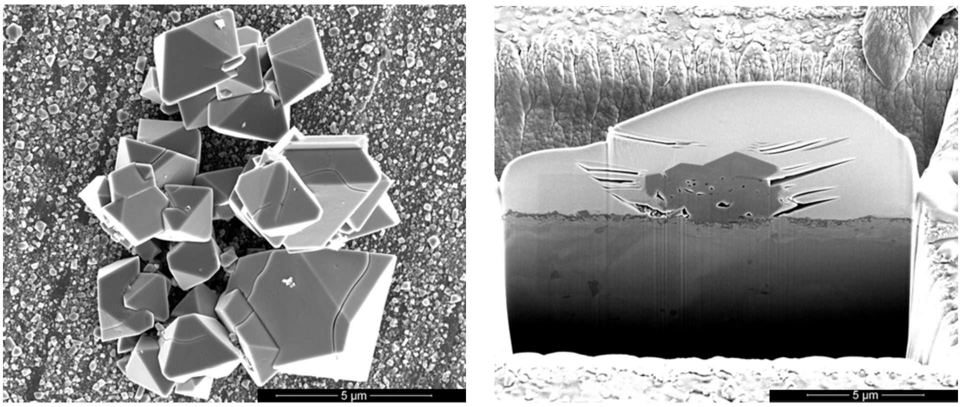

(a) (b)

Figure 9.2 – SE Image of a oxide spinel formed on the P600 surface of AR-WF675 (a) after 500 h exposure to 350°C water with a hydrogen overpressure of 30 cc/kg and the corresponding FIB SEM cross-section (b).

However this does raise the question of why no depositions were observed on the OPS surface; given that all the samples were in the same orientation in the same test (all samples tested had an OPS surface with P600 on the reverse side and were suspended such that both surfaces were vertical). It had been suggested that the large crystals may have been the result of a precipitate in the alloy, however these would have been present on both surfaces. Manual FIB sectioning of a crystal also showed no indications of a particle acting as an initiation point (9.2(b)). Furthermore the crystal appeared to be formed over the surface oxide and contained defects, adding to the view that the large crystals were deposited.

9.1.2 Oxidation at Grain Boundaries

Low voltage SEM imaging used to obtain an improved elemental contrast has in the cases (on the OPS surface) allowed grain boundary attack to be identified from surface imaging. When the oxide is thin (thin is defined as no plates protruding from the surface in this case) on at least one of the boundaries imaged, a change in contrast could be observed which implied a lower average Z in the region (light elements are less likely to produce backscattered electrons, so darker region implies a lower average Z); this was interpreted as an oxidised grain boundary. The observed attack was not visible in the SE detector and it could be seen that the boundaries were not attacked uniformly (Figure 9.3).

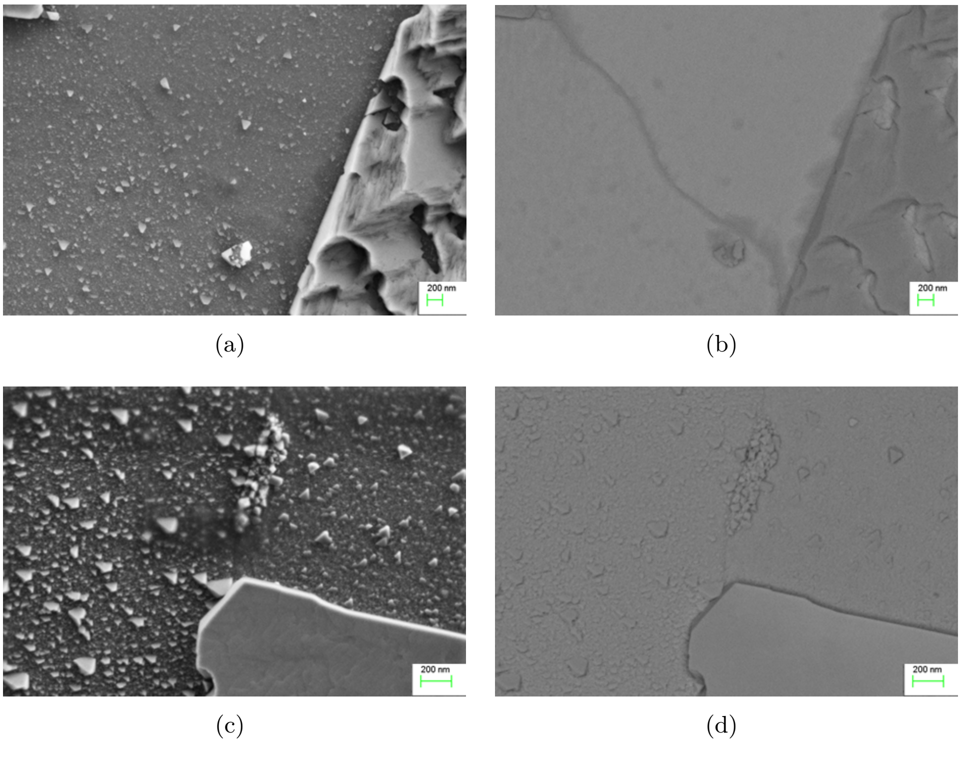

(a) (b)

(c) (d)

Figure 9.3 – SE images of the OPS surface of AR-WF675 after 500 h in 350°C water with a hydrogen overpressure of 30 cc/kg. (a, c) showing low visibility grain boundaries. (b) Backscattered image giving an indication that the grain boundary in (a) has been oxidised. (d) Backscattered image giving an indication that the grain boundary in (c) has not been oxidised.

Unfortunately the FIB-SEM (unfortunate in the sense that it would allow boundaries for analysis to be selected) used in the cross-sectioning was not equipped with a backscattered detector and the following cross-sectioning was based on random boundaries. The advantage of this method however is that there is no bias to selecting more attacked boundaries and the results can be seen as more representative of the material.

9.2 Cross-Sectional Views of the Preferential Oxides

FIB cross-sectioning has allowed what is interpreted as intergranular preferential oxidation to be observed, the oxidation is referred to as preferential and not internal due to the continuous nature. The maximum preferential oxidation observed (as measured along the oxide not depth from surface) in both AR-WF675 and 15%CW-WF675 can be seen in Figure 9.4 and is summarised by Table 9.1. It should be noted that the values given in Table 9.1 are excluding grain boundaries on which large M_7C_3 carbides were observed, the effect of which is covered in 9.2.4. The $M_{23}C_6$ carbides were not detected in the preferential oxides, however this is most probably due to them not been distinguishable from the oxide.

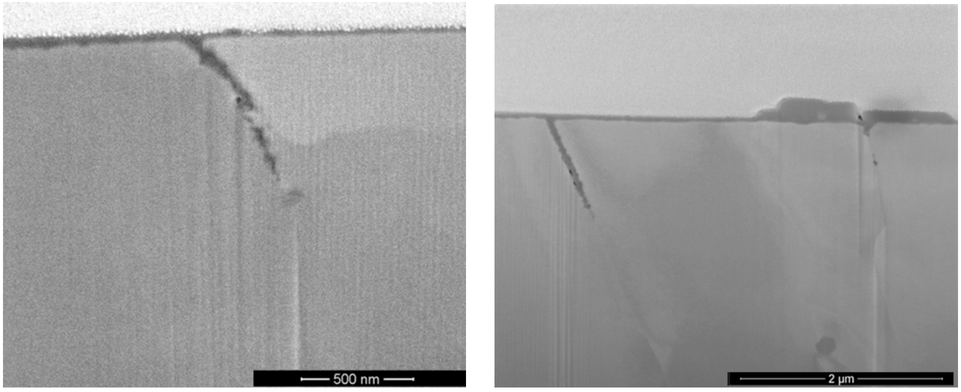

(a) (b)

Figure 9.4 – FIB SEM images of the maximum preferential grain boundary oxidations observed in AR-WF675 (a) and 15%CW-WF675 (b) as a result of autoclave exposure to 350°C water with a hydrogen overpressure of 30 cc/kg.

In the initial cross-sectioning, there had been a suspicion that the surface morphology of the oxide could be used to predict the form of the preferential oxidation. However, it became apparent after a number of cross-sections that this was not the case and that the surface morphology was not linked to the observed preferential oxidation.

Table 9.1 – Summary of the preferential oxidation observed in AR-WF675 (from 13 grain boundaries) and 15%CW-WF675 (from 14 grain boundaries) as a result of autoclave exposure to 350°C water with a hydrogen overpressure of 30 cc/kg for 500 h. A statistical outlier is defined as exceeding the mean by 3σ or more.

	Material	
	AR	CW
Average preferential oxidation depth (nm)	340	530
σ (nm)	200	200
Average preferential oxidation depth (nm) excluding statistical outliers	340	480
σ (nm), excluding statistical outliers	200	100
Maximum preferential oxidation depth (nm)	730	1130

9.2.1 Cold Worked vs As-Received

In the analysis of the preferential oxidation formed by autoclave testing, multiple grain boundaries from both the AR and 15%CW material were cross-sectioned, based on these observations the average penetration has been calculated as 340 nm and 530 nm for the AR and 15%CW material respectively, both had a standard deviation of 200 nm. These calculations were based on data from the OPS surface and did exclud twins or grain boundaries which contained carbides.

The fact that the standard deviation was consistent between the two materials was found as a surprise as in the production of the cross-sections the subjective opinion was that the 15%CW sample was significantly more consistent. Figure 9.5 is considered to show a representative image of a typical cross-section in both materials.

It should be noted that the maximum observed penetration in the 15%CW material was nearly double that of any other observed boundary in the material, treating this value as a statistical anomaly and removing from the data set yields an average penetration of 480 nm with a standard deviation of 100 nm. As can be seen by this the average is relatively unaffected by the values removal, but the scatter in the data relative to the AR is half, this is consistent with the impression grain in the production of the cross-sections.

Although the maximum oxidation can be viewed as anomalous, it is important to keep in mind that should the oxide be responsible for the PWSCC it is these outlying points which would crack first. The indication from the data is that the 15%CW is more susceptible to preferential oxidation but the relatively small data set ($\approx$ 30 grain boundaries in total) should be noted.

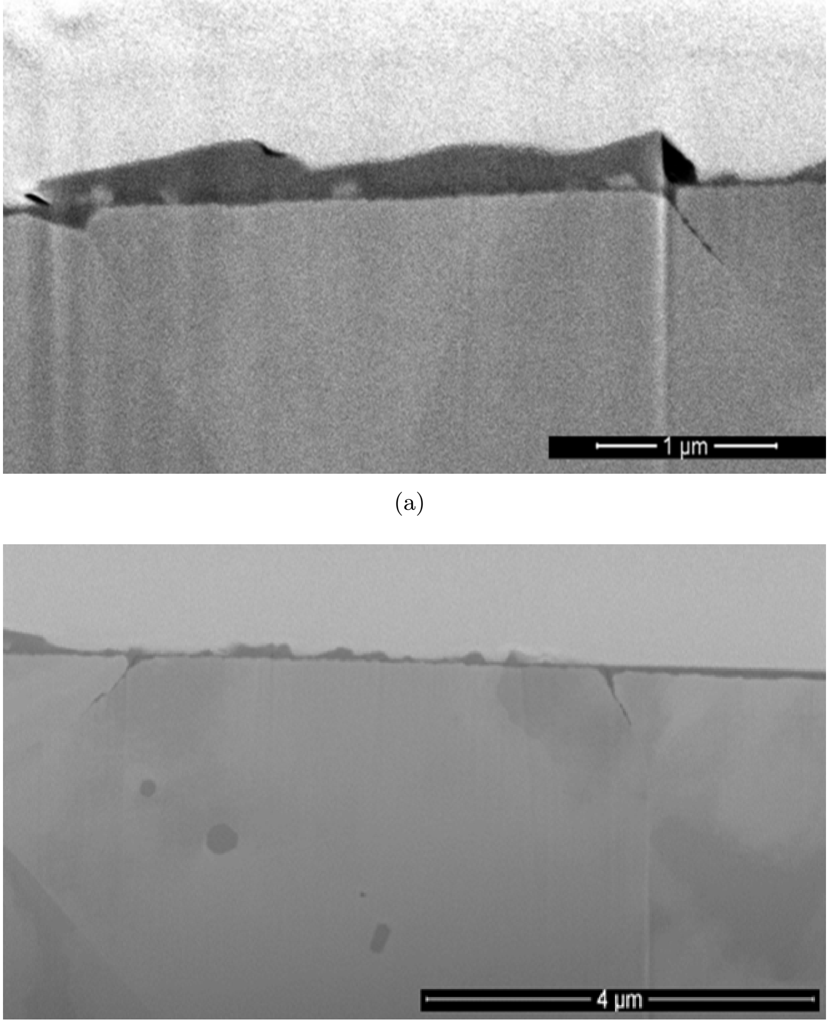

(a)

(b)

Figure 9.5 – FIB SEM images of the typical grain boundary preferential oxidation observed in the AR (a) and 15%CW (b) state after a 500 h exposure to 350°C water with a hydrogen overpressure of 30 cc/kg.

9.2.2 The Effect of a Deformed Layer

The surface finish, as in steam produced a dramatic, if slightly less pronounced change in the oxidation of the alloy. As previously illustrated, the grain boundaries from the OPS surface were preferentially oxidised (Figure 9.4 and Figure 9.5), the grain boundaries in the P600 surface were not oxidised (sugrain boundaries in the deformed layer were however attacked) (Figure 9.6). In addition to the unattacked grain boundaries, the bulk oxidation varied, with penetrations of oxidation proceeding into the deformed layer on what is believed to be the subgrain structure, this is in stark contrast to the continuous film formed on the OPS surface.

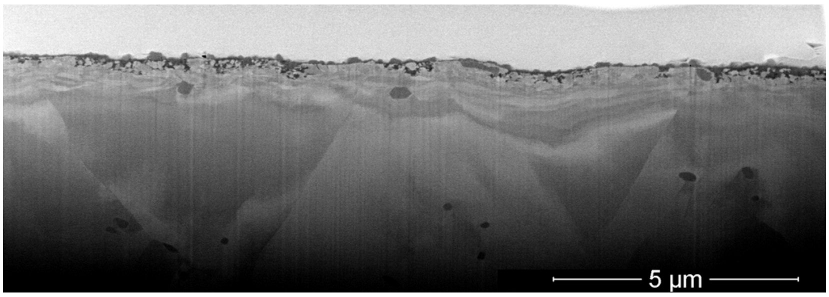

(a)

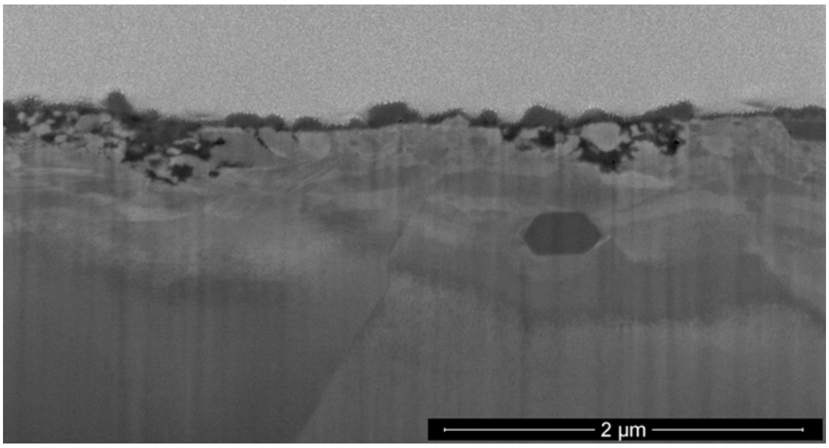

(b)

Figure 9.6 – FIB SEM cross-sectional images of the P600 surface on AR-WF675 after autoclave oxidation (500 h, 350°C water with a hydrogen overpressure of 30 cc/kg), showing no grain boundary preferential oxidation, but preferential oxidation of the deformed layer.

9.2.3 Cross-Sections of Twins

Twin boundaries were cross-sectioned from both the OPS and P600 surface; in both cases no preferential oxidation of the boundaries was observed (Figure 9.7). The nature of the oxide at the surface of the OPS surface would however change, lending support to the previous deductions that the formed oxide was crystallographic.

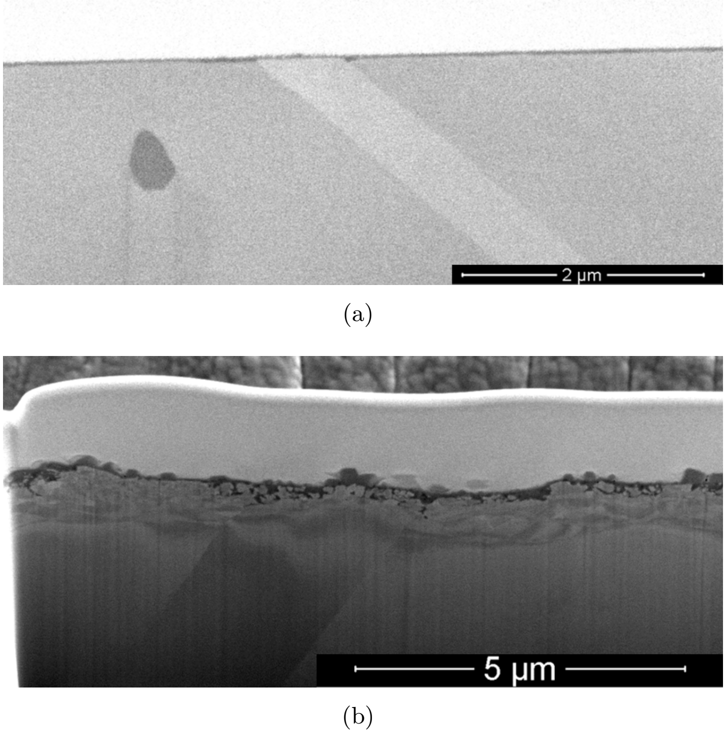

Figure 9.7 – FIB SEM cross-sectional images of twin boundaries in 15%CW-WF675 from the OPS (a) and P600 (b) surface after a 500 h in 350°C water with a hydrogen overpressure of 30 cc/kg.

9.2.4 The Role of Carbides on Oxidation

Carbides observed from the surface of the OPS side could be seen to be visibly oxidised, when not obscured by the surface oxide (Figure 9.8(a)). Cross-sectioning of these carbides revealed that they are preferentially oxidised (Figure 9.8(b)). The oxide followed the outline of the carbide, in some cases there was a small gap observed between the carbide and the oxide.

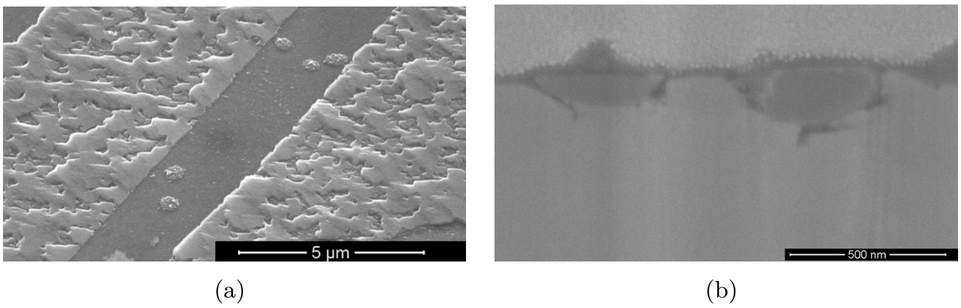

Figure 9.8 – SE image showing visibly oxidised carbides from the surface (a) and FIB SEM cross-section produced from the carbides (b) in AR-WF675 after a 500 h in 350°C water with a hydrogen overpressure of 30 cc/kg.

The intragranular carbides did not appear to impede the oxidation of the grain boundary. There were however suggestions from the observations that the presence of a carbide on a grain boundary actually accelerated the oxidation rate relative to the neighbouring boundaries (Figure 9.9). It should be noted that the maximum preferential oxidation observed did not occur on a boundary with a carbide present.

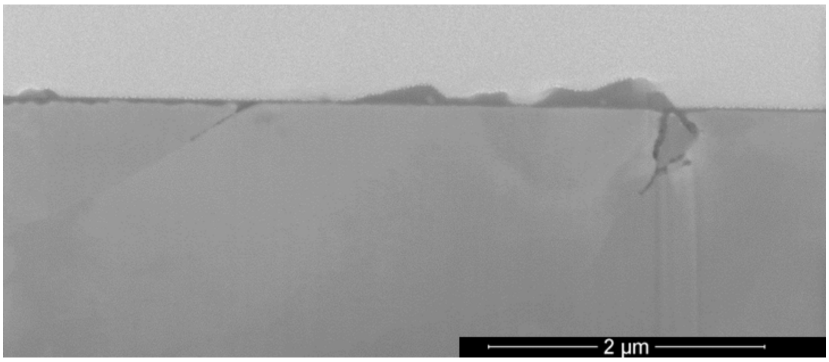

Figure 9.9 – FIB SEM cross-section showing two adjacent grain boundaries in 15%CW-WF675 after a 500 h in 350°C water with a hydrogen overpressure of 30 cc/kg. The grain boundary with a carbide is seen to have a deeper preferential oxide.

The presence of a deformed layer significantly altered the behaviour of the carbides. Both carbides in the bulk and on the grain boundary, within the deformed layer, were observed to have no visible signs of oxidation (Figure 9.10). The oxidation rate in there vicinity of the carbides, reflected that of the carbide free regions (no notable change).

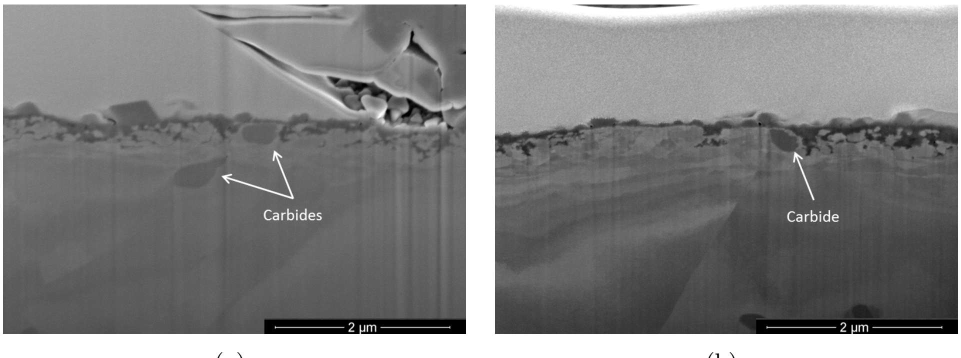

(a) (b)

Figure 9.10 – FIB SEM cross-section showing carbides in the deformed layer after oxidation (500 h in 350°C water with a hydrogen overpressure of 30 cc/kg) of the P600 surface on 15%CW-WF675.

CHAPTER

TEN

STRESS CORROSION CRACKING TESTS

SCC tests have been conducted in hydrogenated steam whilst the reference samples provided were tested in pressurised water. The tests conducted in hydrogenated steam are referred to as SCC tests, not PWSCC tests as despite being intended to investigate the mechanism of PWSCC they are technically not PWSCC test as they are not conducted in primary water. Due to material limitations, the SCC tests conducted in steam were on 19% cold rolled WF675, whilst the reference samples provided were of AR-WF675.

10.1 Stress Corrosion Cracking in Steam

The SCC tests conducted in steam were all carried out at 400°C with an applied load (630 MPa) just above that of yield (610 MPa). The SCC tests performed were intended to look at the relationship between the SCC in steam and the observed phenomena of PWSCC, in addition to this the effect of surface finish is examined.

10.1.1 Fractography

SCC samples from hydrogenated steam tests (R=8) loaded to 630 MPa were found to fail by SCC after $\approx$ 500 h (SCC tests performed with R values of 1.5, 20 and 70 also resulted in cracking). The fracture morphology showed clear regions of intergranular SCC (10.1(a)-10.1(c)) which transferred to ductile tearing (10.1(d)) after the sample was weakened by the SCC. High magnification imaging of the fracture surfaces showed that the intergranular fracture was pure and did not transgress from the grain boundary, as opposed to that observed on the reference PWSCC samples of non-cold worked WF675.

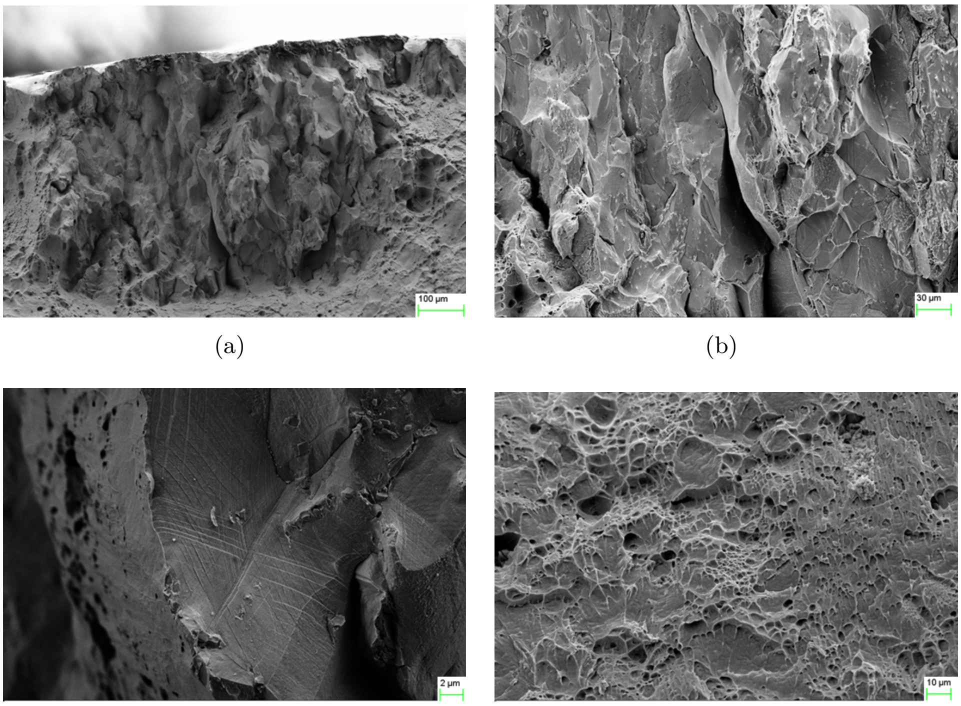

(a) (b)

(c) (d)

Figure 10.1 – Fractography of the fracture surface produced in hydrogenated steam with R=8. (a) Shows a low magnification micrograph of the fracture surface originating from the OPS surface. (b) and (c) are higher magnification images of the intergranular cracking observed on the SCC fracture surface. (d) shows the region of the sample which suffered ductile failure due to the SCC cracks reducing the integrity of the sample.

10.1.2 Environment and Susceptibility

The effect of the environment on the SCC was analysed by running tests at variable oxygen partial pressures (variable R values), the largest observable crack from each SCC test was then identified (the cracks were observed from the sample surface). The values of R used for these tests were 0.1, 8, 20 and 66. The largest cracks observed in these tests are shown in Figure 10.2; for the failed sample, the largest initiation site was used as this was also the largest crack present on the sample. Given that the size of the crack required to produce failure may vary (multiple smaller cracks may produce failure), it was decided that any other samples found to fail by SCC would be assumed to have the same maximum crack length (600 µm).

Figure 10.3 shows a plot of the maximum crack length vs. R, the plot of R is on a logarithmic scale as log(R) can be equated to the potential and as such the graph can be compared to the previous data on the susceptibility of PWSCC vs. potential.

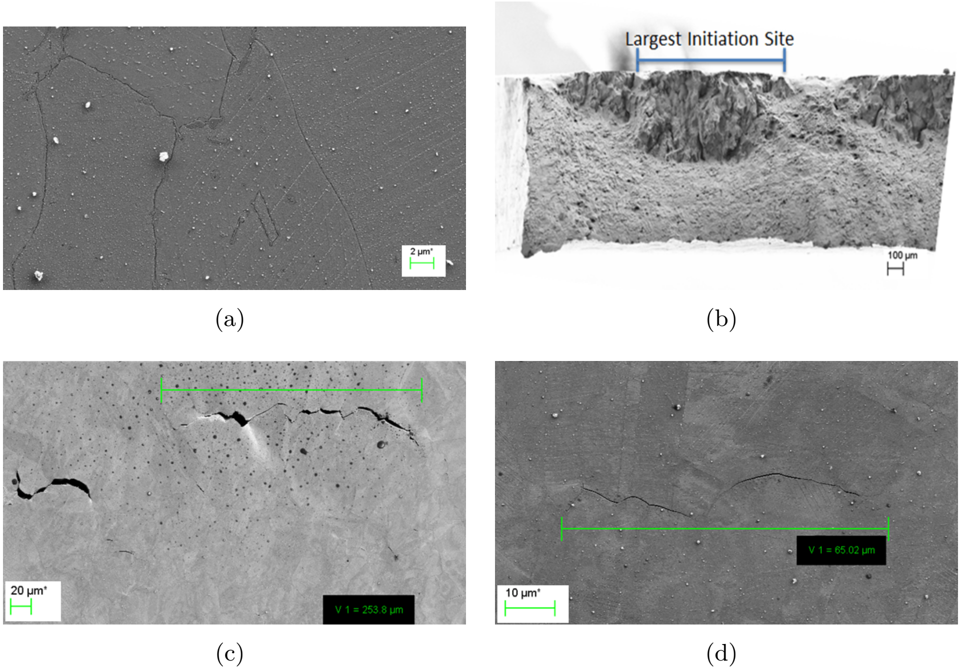
2 µm*
Largest Initiation Site
100 µm
20 µm*
V 1 = 253.8 µm
10 µm*
V 1 = 65.02 µm

(a) (b)

(c) (d)

Figure 10.2 – SE images of the largest observed cracks from SCC tests on 19%CW-WF675 at 400°C with R values of 0.1 (a), 8 (b), 20 (c) and 66 (d).

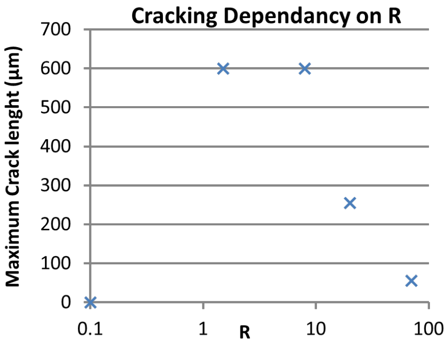

Figure 10.3 – Plot of SCC susceptibility (19%CW-WF675 with an OPS polish) vs R (on a logarithmic scale, such that it can be seen as a comparable to the plots in the literature relating PWSCC susceptibility to potential).

10.1.3 Surface Finish and Susceptibility

As previously stated, the samples used in the SCC tests had one surface prepared to an OPS finish and the reverse finished to P600. This allowed the effect of surface finish on SCC to be investigated. The result of the different surface finish was dramatic, all the samples which failed by SCC were found to have the SCC initiate from the OPS surface (Figure 10.4), the failure from the P600 side was in all cases purely ductile (there was no indication that the failure initiated from the OPS side, went ductile and subsequently connected with SCC cracks from the P600 surface).

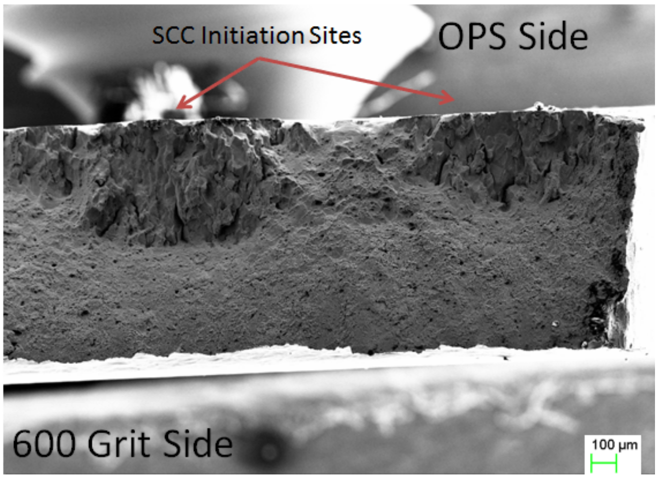

Figure 10.4 – Low magnification SE image showing that all initiation sites on a failed 19%CW-WF675 SCC sample(R=8) originate from the OPS surface, a observation made on all SCC samples which were tested to failure.

The effect of surface finish is illustrated in Figure 10.5. These images are taken from a SCC test in hydrogenated steam which was loaded to 630 MPa with an R of 8, the sample failed by SCC after 480 h, the adjacent images are taken at the same magnification, at the same location, but on the opposite surfaces of the sample. It should be noted that all the cracks in Figure 10.2 were taken from a OPS surface, this was because the maximum sized cracks were always located on the OPS surface and not because of a choice made in the analysis.

A series of images taken at the same magnification but on opposite sides was used to quantify the effect of surface finish. The magnification used meant that the limit of a resolvable crack was 1 µm width and 5 µm in length. The magnification was used as cracks less than these dimensions on the P600 surface were difficult to resolve at any magnification and the use of a higher magnification would have skewed the data towards the OPS surface. The result of this quantification is shown in Figure 10.6 and Table 10.1.

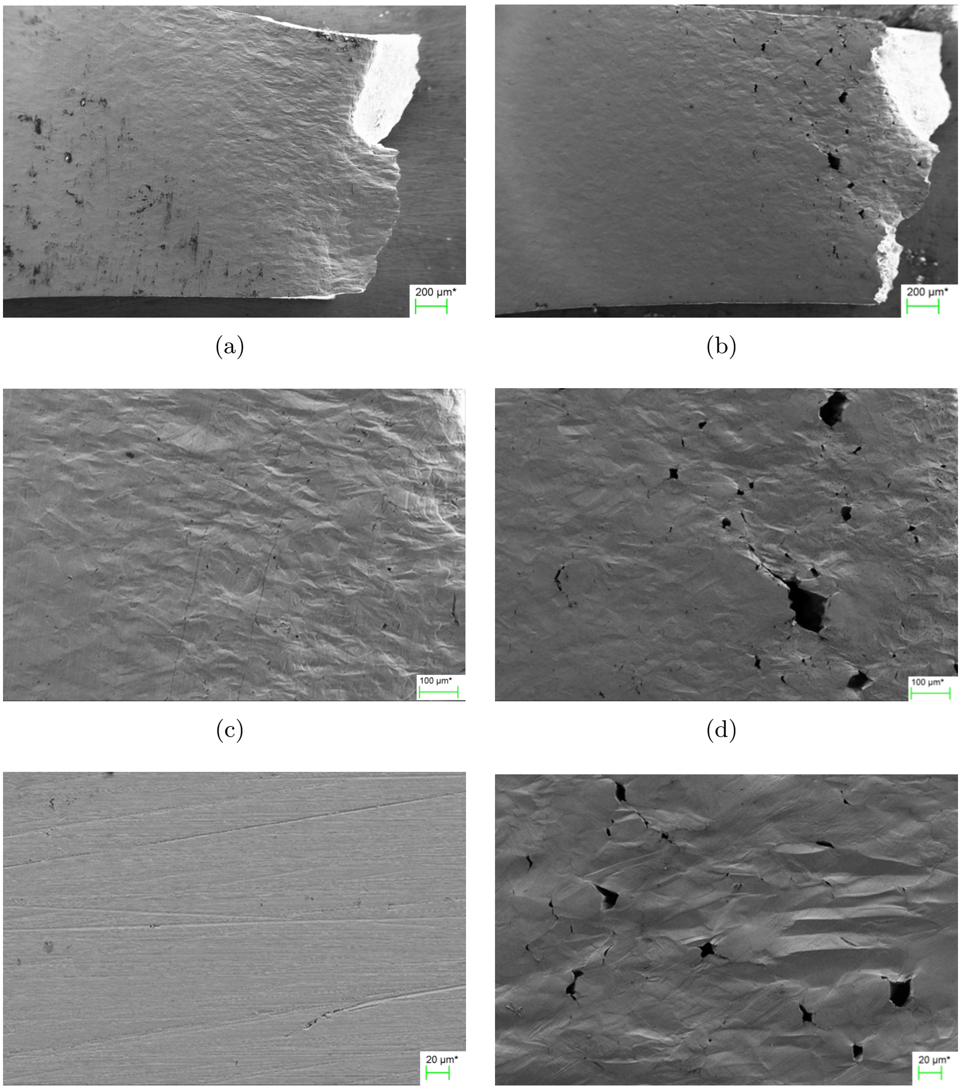
200 µm*
200 µm*
100 µm*
100 µm*
20 µm*
20 µm*

(a) (b)

(c) (d)

(e) (f)

Figure 10.5 – Sequence of SE images taken from the same failed SCC sample (19%CW-WF675, R=8) but on opposite side at a range of magnifications, (a), (c) and (e) are from the P600 surface whilst (b), (d) and (f) are from the OPS surface.

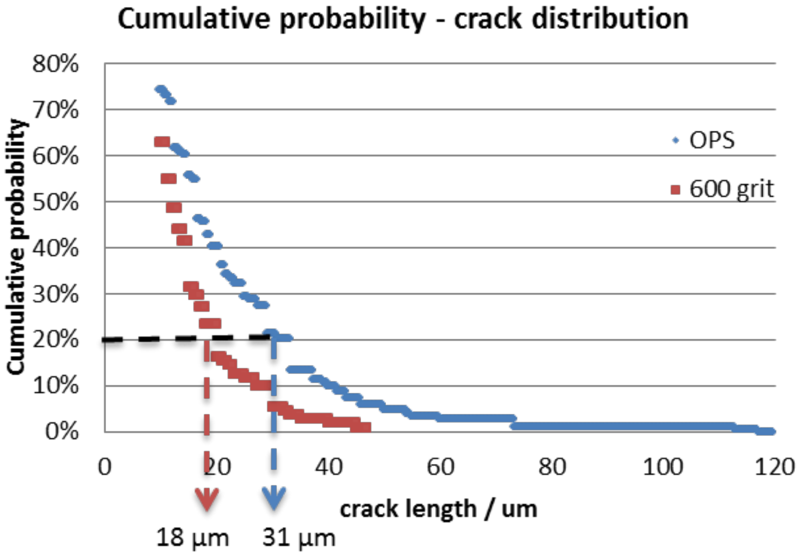

Figure 10.6 – Cumulative probability crack distribution for the OPS and P600 surface as a function of crack length.

Table 10.1 – Summary of results from the crack counting on a SCC tested sample of 19%CW-WF675, R=8.

	OPS Surface	600 Grit Finish
Number Of Cracks	149	96
Average Crack length (µm)	21.8	15.2
Cumulative Crack length (mm)	3.25	1.46
Max Crack length (µm)	117	47

10.1.4 Summary of Steam SCC Tests

A full list of the tests conducted in Rig 2 which were relevant to this thesis are given in Table 10.2. The majority of these test results have been outlined in the previous sections, this section is intended to summarise the key results of each of these tests. Samples which failed due to SCC had their maximum crack length taken to be 600 µm.

Table 10.2 – Summary of all relevant hydrogenated steam tests conducted in the SCC rig on 19%CW-WF675.

Test	**Duration**	**Load**	**R**	**Max Crack length Observed** (µm)
1	100h	-	4	Environment Calibration
2	-	-	4	Stress Strain curve
3	473 h	626 MPa	8	600 µm (Failed)
4	550 h	630 MPa	8	Power Cut (Failed)
5	480 h	630 MPa	8	600 µm (Failed)
6	1000 h	630 MPa	70	55 µm
7	1000 h	630 MPa	20	255 µm
8	1000 h	630 MPa	0.1	0 µm
9	625 h	630 MPa	1.5	600 µm

Tests 1 was a calibration test with no applied load, this was used to verify that the environment generated in the nickel 200 tube was comparable to that of the quartz tube in Rig 1, there had been concerns of a buffering effect of the nickel 200 tube altering the oxygen content of the system. The result showed that the two rigs were equivalent.

Test 2 was to measure the yield point and UTS of the alloy whilst in Rig 2, these values only apply to this specific system at the given temperature as the pull-rod and seal frictions were not corrected for.

Test 3 was the first SCC test conducted, however the location of the failure suggested that the sample was misaligned and as a result loaded with a shear stress. It was however noted that the sample did fail by SCC and that it was initiated from the OPS surface, in addition there was significantly more cracking on the OPS surface relative to the P600, however this could not be confirmed to be as a result of surface finish as the misalignment of the sample may have played a role.

Test 4 was a repeat of test 3, however a fault in the power supply led to a power cut (one of many!), and the subsequent contraction of the pull-rod caused the sample to fail in a ductile fashion. The test is included in the summary for two reasons, first is that the location of the failure was central and as such proved that the work on the system to solve the misalignment had been successful; secondly the duration of the testing prior to failure had produced a significant number of SCC cracks, on ductile failure these were opened up, hence providing a good illustration of the surface finish effect (Figure 10.7).

The tests 5-9 were used to investigate the effect of potential; in all cases more significant cracking was observed on the sample surface finished to OPS relative to the P600. In the case of Test 6, no cracking was observed on the P600 surface, in test 8, no cracking was observed on both surfaces, but the OPS surface had appeared to be etched by the oxidation process as seen on previous samples from the oxidation studies when R<1.

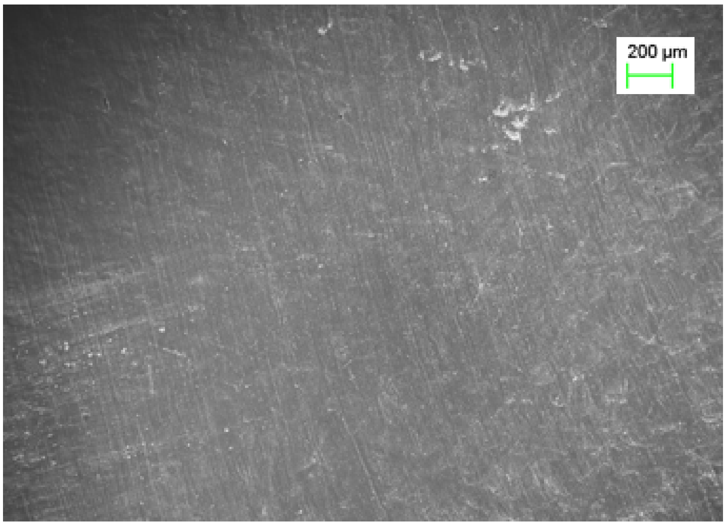

(a)

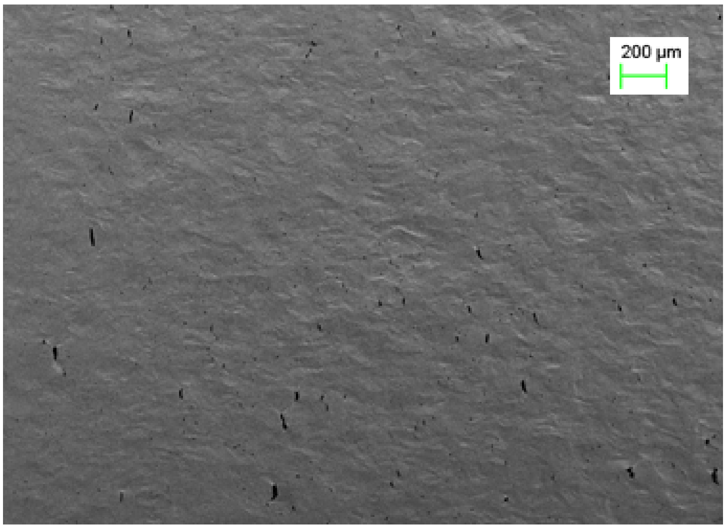

(b)

Figure 10.7 – SE images of test 4 from the P600 (a) and OPS (b) surfaces.

10.2 Reference PWSCC Samples

The samples used in this section are PWSCC samples, the samples are of AR-WF675 and were created during previous PhD projects. The fracture surface analysed is from a wedge open loading (WOL) specimen in simulated PWR conditions, the test was used to measure the crack propagation rate. The cross-sectioned samples are from constant load tests in simulated PWR conditions (1000 ppm boric acid, 2 ppm lithium hydroxide, and 30 cc/kg of hydrogen at 360°C). High resolution SEM examination of these samples has been used to further the understanding of the crack propagation path.

10.2.1 Carbides on the Crack Path

SEM imaging of the reference PWSCC samples after cross-sectioning and polishing allowed a two dimensional view of the crack path to be observed. Carbides observed on the crack path were seen to affect the propagation. Cracks could be seen to propagate beyond the carbides. However, in the presence of the carbide, no crack was observed implying the crack path diverted out of the plane of the image to bypass the carbide. In some cases, partial cracking of the grain boundary with a carbide is observed (Figure 10.8). Given that the carbides in the material are observed to readily oxidise, this observation suggests that the oxide formed on a carbide is of a greater mechanical strength or that the carbides pin the boundary, thus preventing slip and limiting the cracking.

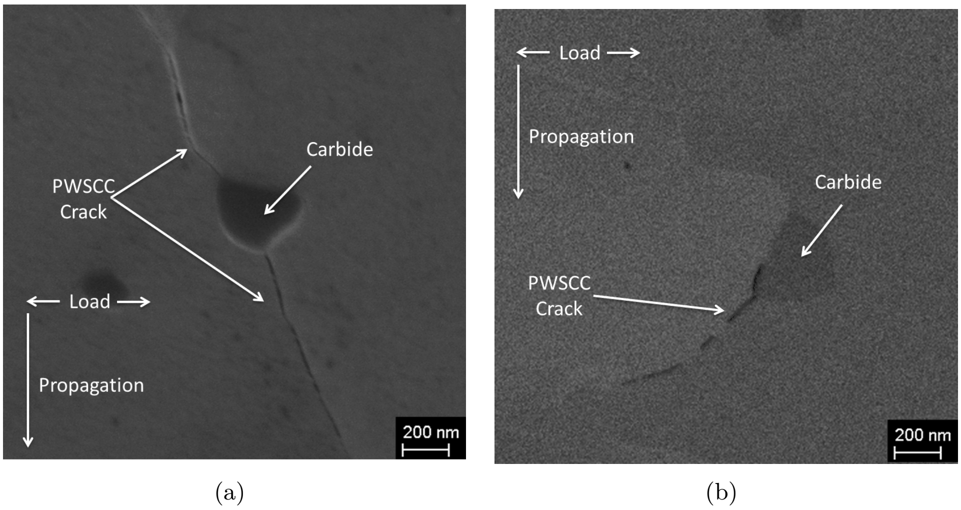

(a) (b)

Figure 10.8 – SE image of a PWSCC crack propagating in AR-WF675 beyond a carbide, with no visible PWSCC crack path around the carbide (a) and a backscatter image showing a PWSCC crack partially cracking the boundary just beyond a carbide (b).

One observation of a crack propagating around a carbide was made, Figure 10.9. However, no observation was made of a crack propagating through a carbide, despite the observation of carbides cracking when the material is cold worked.

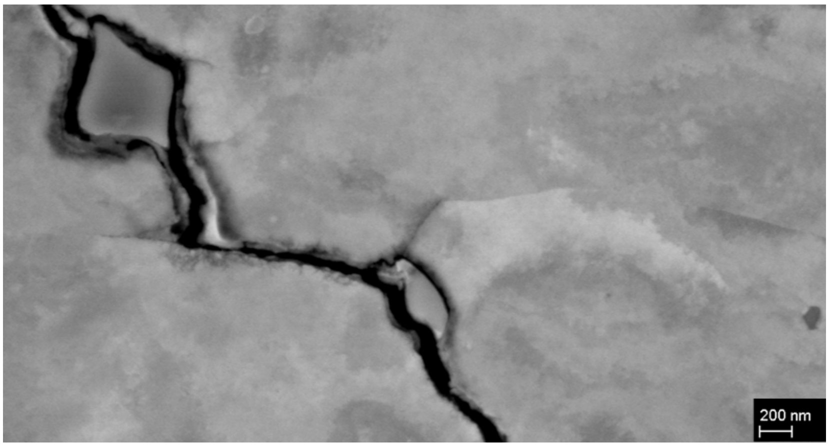

Figure 10.9 – PWSCC crack propagating around a carbide.

10.2.2 Surface Finish

In addition to using the AR-WF675 cross-sectioned PWSCC samples investigating the fracture path, they were used to interpret the surface preparation and the effect this may have on the result, this was achieved by measuring the deformed layer present on the sample (Figure 10.10). The PWSCC samples in question were prepared to a 4000 grit finish, this at the time was considered a good surface finish. The cross sections showed that there was a deformed layer at the surface of the sample which was ≈ 2 μm deep. Previous work by Carrette et al. [169] have shown that the magnitude of this deformed layer has a significant effect on the oxidation mechanism of Alloy 690.

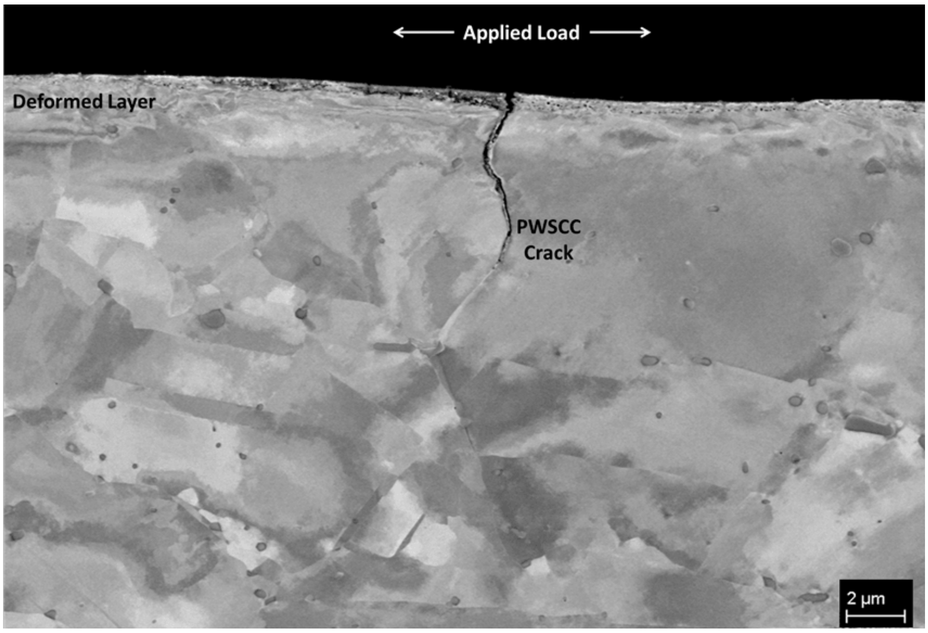
Applied Load
Deformed Layer
PWSCC Crack
2 μm

(a)

Figure 10.10 – AsB image of a mechanically cross-sectioned PWSCC sample of AR-WF675, the deformed layer present can be observed at the surface.

Part IV

Further Discussion

CHAPTER

ELEVEN

OXIDATION OF ALLOY 600

The initial aim of the project was to determine the oxygen and chromium diffusivity at temperatures lower than those used in previous studies and thus draw conclusions on the viability of IO as a mechanism of PWSCC. Hydrogenated steam was used as to replicate environments with a similar electrochemical potential as those experienced in the PWR primary circuit. The oxygen diffusivity has been successfully measured by Wagner's equation and the observed internal oxidation at 500°C (Table 11.1).

However, the more interesting result obtained from this thesis was related to the oxides formed in both the low pressure steam and high pressure water, of particular note was the effect of surface preparation and how the resulting oxide differed. The observed oxides can be divided into three types:

- Internal Oxides: Discrete discontinuous oxides formed within the material, IO has been observed within the matrix and accelerated by what is suspected to be slip bands in high temperature tests (500°C). Based on the previous work on Ni-Cr alloys, it is believed these particles are of Cr_2O_3, this is supported by the EDX data obtained. Using the IO penetration, the oxygen diffusivity is calculated.
- Surface Oxides: Oxides and features formed on the surface of the material, the features formed in a reducing environment are linked to the internal oxidation of the alloy within the local vicinity and the samples surface finish.
- Preferential Oxides: This is the formation of a continuous oxide within the material and occurred along grain boundaries and at carbide/matrix interfaces. The discussion of which includes aspects of both the internal and surface oxidation. The preferential oxidation will be discussed in terms of the produced elemental enrichments and kinetics of growth, which is comparable to the oxygen diffusivity.

The surface oxide present at grain boundaries in reducing environments is divided into three types, defined by the morphology of the nickel nodules in the vicinity of the grain boundary. The subsequent internal oxide could be predicated from the morphology observed at the surface (section 11.1.2). Figure 11.1 gives a schematic representation of the three grain boundary morphologies observed.

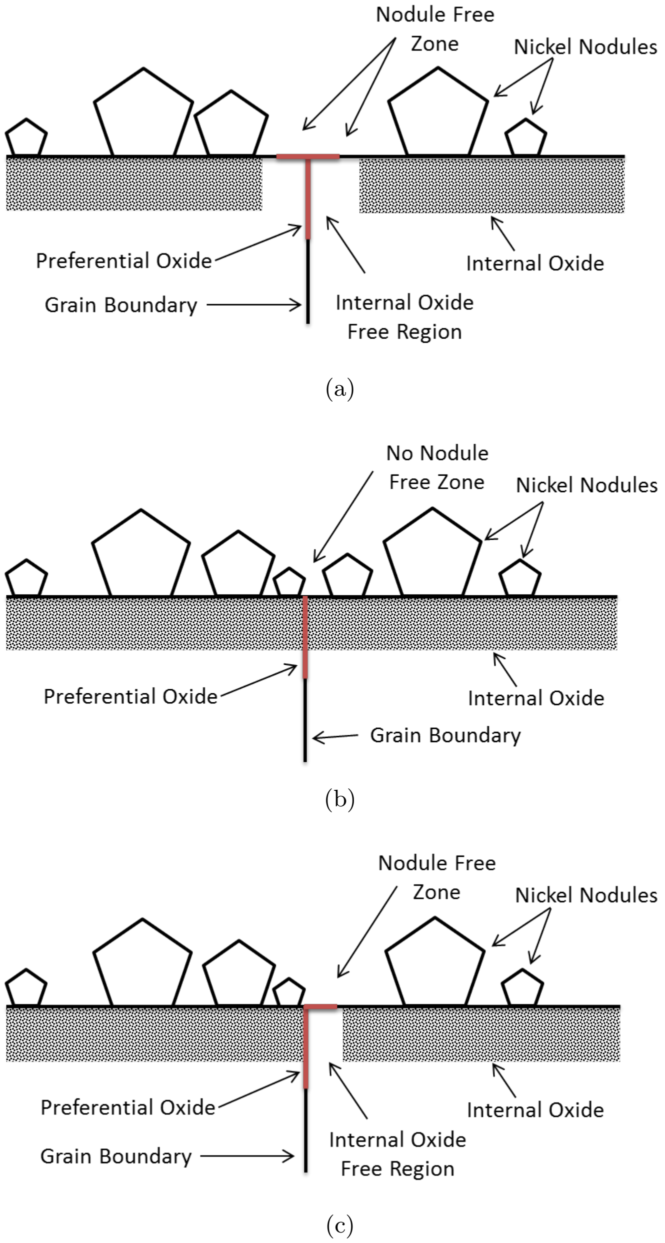
Nodule Free Zone
Nickel Nodules
Preferential Oxide
Grain Boundary
Internal Oxide Free Region
Internal Oxide
(a)
No Nodule Free Zone
Nickel Nodules
Preferential Oxide
Internal Oxide
Grain Boundary
(b)
Nodule Free Zone
Nickel Nodules
Preferential Oxide
Grain Boundary
Internal Oxide Free Region
Internal Oxide
(c)

Figure 11.1 – Schematic of the NFZ (a), NNFZ (b) and HH (c) boundary types, including the internal oxidation associated with the grain boundary surface oxide.

The three grain boundary morphologies are defined as:

- Nodule Free Zone (NFZ): The metallic nickel nodules formed on the surface are not present in the vicinity of the grain boundary. The region under the nodule free zone is devoid of internal oxide particles and a continuous oxide film is observed on the surface above the grain boundary, this is interpreted to prevent the inward transport of oxygen thus the lack of internal oxide particles.

- No Nodule Free Zone (NNFZ): The metallic nickel nodules are present up to the grain boundary on both sides of the grain boundary. Internal oxide particles are also observed to be present up to the grain boundary and little to no film oxide is observed at the surface. TEM analysis of a NNFZ boundary (one sample) indicated that grain boundary migration had occurred at depth greater than the internal oxide (Figure 8.45).

- Half and Half (HH): Metallic nickel nodules are present up to the grain boundary on one side whist a NFZ is present on the other side. As with the NFZ and NNFZ, the internal oxide is only present under the nickel nodules and a continuous film oxide is observed at the surface in the region of the NFZ. In all observed TEM samples (four boundaries) the migration was observed to occur in the region free of internal oxide. Additional evidence of the migration was observed in multiple FIB cross-sections (i.e. Figure 8.27), where an unusual kink in the grain boundary was observed in the vicinity of the preferential oxide which was characteristic of the grain boundary migration (Figure 8.44).

11.1 Internal Oxidation

11.1.1 Oxygen Diffusivity

The internal oxidation of alloy 600 was observed at both 500°C and 400°C, but was not observed at 350°C. The effect of strain was demonstrated by the different penetration characteristics observed between CW and AR forms of WF675. The IO in the as-received material exhibited an oxide which was in the form of interconnected particles of non-uniform thickness. The regions observed with the greatest penetration were formed by fine particles, whilst the shallower penetrations were coarser and less densely packed relative to the maximum penetrations (Figure 8.20). The cold-worked samples exhibited an IO of uniform thickness and oxide particle size on all the observed oxidised grain.

It is suggested that the observed difference in internal oxidation depth is a result of the difference in microstructure, specifically the hot worked structure in the as-forged material which produces local differences in the dislocation densities opposed to the cold worked material which is of uniform density. The variable dislocation density produces local variations in the oxygen diffusivity and thus produces an internal oxide of variable thicknesses whilst the cold worked material by contrast produces oxide penetrations of uniform thickness. The changes in oxide particle sizes in the IO layer (i.e. Figure 8.49(a)) are suggested to be a result of the different diffusivities and not the cause of the variable penetrations (previous work has indicated that different morphologies of oxide particles can act to enhance or hinder the inward transport of oxygen due to an increased density of incoherent boundaries acting as a short circuit and large oxides acting as a physical barrier to the transport of oxygen [64, 67, 170]).

Based on the observed maximums of IO at 500°C shown in Table 8.1, the oxygen diffusivity has been calculated. The calculations are based on equation 2.3 using the oxygen solubility (N_O^s) from Park et al. [171] (equation 11.1); the results are given in Table 11.1. The consistency between the oxygen diffusivity in the AR and CW forms of WF675 is attributed to the use of the maximum values, not the average values. Within the forged alloy there are regions of high strain, these will produce penetrations which are comparable to that of the cold worked material. The key difference between the materials is the uniform penetration observed in the CW, contrasted to the sporadic penetration depths in the AR.

$$N_O^s = 8.3\exp^{-55\mathrm{kJ}/RT} \tag{11.1}$$

Table 11.1 – Oxygen Diffusion rates in WF675 at 400°C and 500°C.

Temperature (°C)	Duration (h)	Oxygen Diffusion Rate m^2s^{-1}	
		AR	CW
500	66	2.31×10^{-21}	2.14×10^{-21}
500	500	1.79×10^{-20}	1.21×10^{-20}
400	500	-	1.49×10^{-22}

At 400°C, the TEM results show that the IO appeared to follow what is speculated to be dislocations and does not form discrete spherical particles as expected by Wagner's model of IO. The presence of an oxide film and the non-spherical IO at 400°C leads to questioning of the validity of using Wagner's equation, as the criteria from which it was derived are not met. However the resulting value calculated at 400°C of the oxygen diffusivity ($1.49\times10^{-22}m^2s^{-1}$ in the CW material) is consistent with the previous higher temperature work [171].

The order of magnitude difference in the calculated oxygen diffusion rates in

WF675 at 500°C for the two test durations is believed to be a result of two accelerating factors. The oxygen transport along the incoherent interface of the oxide/matrix and the compressive strain produced in the matrix by the volume change associated with the formation of the oxides. Both these factors would produce an increase in the oxygen diffusivity after a critical time, the initial stages of internal oxidation are not accelerated by either of these mechanisms and thus the shorter duration test has a reduced diffusion coefficient as the percentage of time spent at the reduced diffusion rate is greater.

Given the close pack nature of the oxide particles relative to high temperature work in literature [172] and the mechanisms available for stress relief (discussed in 11.1.2), it is implied that the dominant factor for the apparent acceleration is the presence of a short circuit diffusion path at the incoherent oxide/matrix interface. Given the nature of the IO the chance of a blocking effect by which the presence of large internal oxides act to physically prevent the inward transport of oxygen is considered low.

The oxygen diffusivity values calculated from 500°C and 400°C are consistent with the majority of the data given in Figure 3.19 and significantly less than that predicted for the IO mechanism of PWSCC. However a number of factors can be considered to accommodate the difference between the predicted and experimental results. Primarily the calculated oxygen diffusivity is a bulk value, whilst PWSCC is a grain boundary phenomenon and thus grain boundary diffusivity (which would be significantly greater than that of the bulk) is a more relevant value. The data used is obtained from an atmospheric (low pressure) exposure system when PWSCC occurs at high pressure. The effect of these factors can be seen when looking at the preferential oxidation of a grain boundary. In addition to this there was no load applied to the sample, the presence of an applied load has been shown to change the oxide penetration rate [111, 172].

11.1.2 Formation of Nickel Nodules

The formation of the nickel nodules only occurs when internal oxidation is developed in the alloy, evidence that the formed nickel nodules are a result of a stress relief mechanism. Stress is generated as a result of the volume change created by the formation of the oxide, see equation 2.5 in section 2.2.

The volume expansion which occurs in Alloy 600 can be calculated from equation 11.2. This differs to that of equation 2.5 where it was assumed that the molar volume of the alloy was equal to that of nickel, thus did not change during the oxidation. It should be noted that despite being modified (Appendix G), the presence of iron is still not fully accounted for. The equation used to calculated the volume change as a result of internal oxidation is

$$\Delta V = (1 - N_{Cr}^{0})V_{Ni} + 0.5N_{Cr}^{0}V_{Cr_2O_3} - V_{alloy} \tag{11.2}$$

where ΔV is the volume change as a result of 1 mole of the Alloy 600 being internally oxidised, N_{Cr}^{0} is the molar fraction of chromium in the alloy, V_{Ni} molar volume of nickel, $V_{Cr_2O_3}$ is the molar volume of Cr_2O_3 and V_{alloy} is the molar volume of the alloy. For these calculations $V_{Ni} = 6.67\ cm^3$, $V_{Cr_2O_3} = 29.1\ cm^3$ and $V_{alloy} = 6.76\ cm^3$ [64,173].

This yields an expansion of 19% per mol of Alloy 600 which is internally oxidised, thus generating significant compressive stress within the sample. The stress can be relieved by the rejection of the nickel to the surface or the physical sliding of grains to accommodate the expansion. Grain boundary sliding was not observed (step changes in height on the surface at grains) and is not considered as a viable mechanism for stress relief due to the low temperatures.

The rejection of nickel can occur by a number of mechanisms, the fact that nodules are formed opposed to a film implies that the outward diffusion of nickel is a result of a localised phenomenon (diffusion along slip bands or pipe diffusion by dislocations), not bulk diffusion. Two previously proposed mechanisms to account for this type of rejection are pipe diffusion and extrusion. The extrusion of nickel is not considered to be a viable mechanism for the formation of the nodules as if this was the case it would be expected that trapped particles of Cr_2O_3 would be observed by the FIB-SEM cross-sectioning within the nodules.

As such it is deduced that the formation of the nickel nodules is a result of the pipe diffusion of nickel to the surface to relieve the stress generated by the IO. This is supported by the formation of nodules along twin boundaries, as in Figure 8.14. The un-oxidised twin boundaries act as a channel for the outward diffusion of nickel, whilst the oxide on the grain boundaries inhibits the outward diffusion. The variable penetrations of IO observed in the AR material also explains the observed difference in densities of nickel nodule at the surface on different grains, which can also be seen in Figure 8.14.

11.2 Grain Boundary Preferential Oxides

The value of K_{oxide} can be seen as comparable to the diffusion rate calculated by Scott [168]. The data for both steam and water are illustrated in (Figure 11.2) and values given in Table 11.2.

The calculated values of K_{oxide} are seen to be significantly less than what was cal-

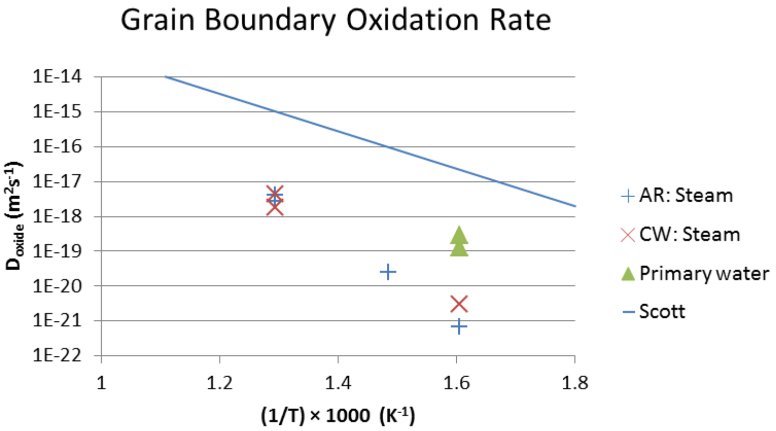

Figure 11.2 – The calculated preferential oxidation rates as a function of temperature, the values predicted to account for IO as a PWSCC mechanism is given for comparison [168].

Table 11.2 – The calculated preferential oxidation rates as a function of temperature for AR-WF675 and 15%CW-WF675.

Temperature (°C)	Duration (h)	$K_{oxide}\ m^2 s^{-1}$	
		AR	CW
500	66	4.07×10^{-18}	4.49×10^{-18}
500	500	2.67×10^{-18}	1.74×10^{-18}
400	500	1.23×10^{-20}	2.50×10^{-20}
350	500	6.94×10^{-22}	2.78×10^{-21}
350 (autoclave)	500	1.48×10^{-19}	3.55×10^{-19}

culated by Scott et al [168]. However, it should be noted that initial results from an on-going study has shown that there appears to be an effect of residual stress on the oxidation rate [111]. Also, there is a two orders of magnitude difference in K_{oxide} (10^{-21} in low pressure steam and 10^{-19} for high pressure water) between tests in low pressure steam and high pressure water at 350°C.

The oxidation rate combines the effect of oxygen diffusivity, chromium diffusivity and the reaction kinetics to produce a single variable. On the assumption that the preferential oxide is responsible for PWSCC, this rate will give an indication of a material susceptibility to PWSCC. In the case of oxygen being the rate limiting step, this value can be considered to reflect the oxygen diffusivity, for chromium availability being the rate limiting step it represents the chromium diffusivity. A more realistic view is that initially the availability of oxygen limits the reaction rate, however, as the preferential oxide develops a short circuit diffusion path is created, the creation of which consumes the available chromium, thus transferring the rate limiting step from oxygen availability to chromium availability.

Although cold-worked specimens were more susceptible than the as-received WF675 specimens to PWSCC, the maximum observed oxide penetration depths were similar (Table 8.2) between the materials. However, it was noted that the as-received samples showed considerable variability in depth of oxidation in contrast to the relatively uniform depth of oxidation observed in the cold worked samples. It is suggested that the hot worked microstructure (mixed recrystallized and recovered) present in the as-received forged structure is responsible for the variation.

The activation energy measured for K_{Oxide} (221 kJ.mol^{-1} and 171 kJ.mol^{-1} for AR and CW WF675 respectively) is consistent with that observed for the initiation of PWSCC, lending support to the belief that the preferential oxidation of grain boundaries is responsible for the initiation of PWSCC. The value is at the top end of the range found for that of propagation (the consensus is that the value for propagation is in the region of 130 kJ.mol^{-1}); however the presence of a crack and resulting strain localisation at the crack tip may act to lower the activation energy.

The chromium depletion profiles observed adjacent to the grain boundary preferential oxides were unusual as they did not appear to follow a pattern expected from a diffusion controlled process (section 8.4.5). They varied between samples with the only constant being a strong asymmetry, in all cases the depletion could be seen to expand at points beyond the depth of the preferential oxide. The explanation put forward for the unusual chromium profiles is not that they are a result of chromium diffusion to the grain boundary to form the oxide as often suggested, but that of grain boundary migration. This is supported by the fact that the chromium depleted zone is accompanied by depletion in iron and less obviously in aluminium and titanium all of the same profile.

The continuous oxide on the grain boundary; is postulated to prevent the transport of nickel to the surface as no nodules of nickel are observed to form at the surface along the grain boundaries and enhance the inward transport of oxygen. The result of which is that the nickel is transported into the grain and/or along the grain boundary. The nickel rejection and corresponding volume change will induce a substantial localised strain into the material. Both the induced strain and compositional change are possible causes of the grain boundary migration.

The profile of the grain boundary oxide (NFZ, NNFZ or HH) is linked to the surface oxide morphology. In all cases, the nodule free zone is accompanied by a region free of internal oxides and a film oxide at the surface. In the cases of the HH boundaries, the nodule free zone was observed to coincide with the grain boundary migration, whilst in the NNFZ boundaries the migration occurred below the IO layer. The occurrence of HH boundaries was uncommon in the solution annealed alloy. The suspected cause of the different surface oxides is the strain localisation/mismatch at the boundary.

The presence of a titanium and aluminium oxide in advance of the chromium oxide is significant but not unexpected. This might have a role in the intergranular oxide penetration by providing an incoherent path for accelerated oxygen transport. However this feature was only observed in the exposures conducted at 500°C, lower temperature tests had titanium and aluminium present within the chromium oxide, but not observed in advance.

The presence of these oxides in advance of the chromium oxides may provide an explanation for the oxides deviating from the grain boundary. It is possible that the small oxide is not sufficient to prevent the grain boundary from migrating; as such a fast transport path for oxygen is left on the original grain boundary after migration occurs, this would subsequently oxidise to form the chromium oxide.

11.3 Oxidation of Carbides

The preferential oxidation of carbides in both steam and autoclave testing was observed. The oxidised carbides observed extended beyond the IO layer, but no IO was observed beyond the preferentially oxidised carbide. Furthermore, in the case of the internal oxides, the oxide formed changes from discontinuous to continuous in the presence of the carbides (Figure 8.31, 8.32(a)). The initial interpretation of this result is that the carbides appear to be responsible for an increase in the oxidation rate in the internal oxides and not to hinder the oxidation of grain boundaries.

The accelerated oxidation may be attributed to the incoherent boundary at the carbide/matrix interface resulting in enhanced oxygen diffusivity and/or the carbide acting as a chromium source. The latter case would support the suggestion that the limiting condition in the oxidation is the availability of chromium, not oxygen [174]. However, the observations of a material comparable to the matrix (typically of a few nm but up to 400 nm) separating the oxide from the carbide (Figure 8.31 and Figure 8.33) supports the incoherent interface as the cause of the carbide oxidation. It should be noted that the separation was not observed in all cases (Figure 8.30) and that the carbide does not necessarily oxidise in this scenario, but facilitates the oxidation of its surroundings.

The rapid oxidation (faster than the surrounding material) of the carbides initially appears to be in contrast with the formulated hypothesis chromium carbides are beneficial to PWSCC because they act as oxygen traps [40]. However, extended oxidation exposures would be required (exposures in which the observed preferential oxidation exceeds the size of the largest carbides) to get a true assessment of the carbide influence on oxidation, as they may accelerate oxidation in the vicinity of the carbide, but prevent additional penetrations beyond the carbide. The oxygen trap theory is supported by the observations that: The carbides form a preferential oxide in the internally oxidised zone, the continuous preferential oxide implies a greater consumption of oxygen. The carbides oxidised beyond the internally oxidised zone are not observed to accelerate the internal oxidation as a result.

11.4 The Effect of Surface Finish

The surface finish of the samples had a dramatic effect on the oxide formation, both in steam and in water. The oxides formed in autoclave testing have been reported in the literature to be a Cr oxide film with Ni-Fe-Cr spinel oxides formed on top [37], this is the same as the oxide formed in the present work on the P600 surface. However, the use of a surface representative of the bulk (OPS) in the same test produced a crystallographic oxide which was dependant on the crystal orientation of the matrix and had no spinels. The rotation in the oxide at a twin in Figure 9.1(a) illustrates the crystallographic nature of the oxide. The formation of a spinel free oxide has previously been obtained by the use of titanium autoclaves [175]. The previous work suggested that the spinels are a result of the cation solubility (predominately Fe cations) in simulated primary water reducing during cooling, hence precipitating out and forming deposits. The cations are present in the primary water as a result of the stainless steel components used in the construction of the autoclave, thus are not present in autoclaves constructed of titanium. The production of a spinel free surface suggests that an initiation site is required to form a deposition. However, the nature of the observed spinels does support the previous assumptions that they are deposited not grown as the FIB cross-sectioning indicated that they formed on top of the chromium oxide.

As with the autoclave test, the steam testing showed a dramatic change in the oxide morphology. The formation of the Ni nodules in the 500°C steam was concluded to be the result of the outward diffusion of Ni, as a result of Ni rejection and stress build up associated with the formation of an internal/preferential oxidation. The P600 surface was observed to form a passive oxide film; this is attributed to the deformed layer producing enhanced diffusivities. The enhanced outward chromium diffusivity produces the outer oxide layer which supresses the inward diffusion of oxygen and hence prevent IO. The lack of IO means that no nickel rejection will occur and hence the observed nodule free surface.

The preferential oxidation observed on the P600 surface in both steam and water is suppressed relative to the OPS surface. In the high temperature steam tests, the formation of preferential oxide is completely suppressed by an external oxide whilst in the lower temperature water the deformed layer is seen to oxidise. The oxidation of the deformed layer in the autoclave follows the fine grain structure; the formed oxide is thick relative to the preferential oxide observed on grain boundaries and not linked to the presence of a grain boundary below the deformed layer. As such the fine grained structure is effectively obscuring the grain boundary (it prevents the grain boundary being observed as a fast transport path as the entire deformed layer has accelerated transport, thus the grain boundary will not oxidise preferentially), once the fine grained structure has been oxidised it is suggested that the oxidation will transfer to the following bulk grain boundaries in the matrix. However this implies that the fine grained deformed layer is delaying the onset of PWSCC.

CHAPTER

TWELVE

COMMENTS ON THE IMPLICATIONS FOR SCC STUDIES

The work presented in this thesis has investigated a number of factors which not only lend themselves to the understanding of PWSCC, but also to the test methodology which is used in these investigations. The use of hydrogenated steam is not a conventional medium but has been shown to replicate the effect of PWSCC, with some limitations attached. The effect of surface finish is something which has in the previous work not had sufficient attention (surface finishes are often defined but not discussed or put into context of PWSCC).

12.1 The Validity of Steam as an Environment for PWSCC Studies

The use of low pressure hydrogenated steam as a proxy to the primary circuit of a PWR has been shown to be a valid environment, with a number of limitations. The data generated in this study have shown that SCC in the hydrogenated steam environment is consistent with PWSCC with respect to the fracture morphology and potential dependency. These aspects of SCC in steam are similar to that reported in high pressure autoclave tests at lower temperatures and thus supports the use of low pressure steam as an alternative test method.

The lack of cation solubility in the steam produces an oxide which differs to that reported in the literature. However both 500°C steam and 350°C autoclave tests produce a chromium rich oxide when in reducing conditions relative to the Ni/NiO transition point. The lack of spinels forming in the steam tests is concluded to be a result of the low, near zero cation solubility of the steam. The lower pressure of the steam produces a reduced kinetics of the oxidation, as illustrated by the three orders of magnitude difference K_{Oxide} between the test conditions. Given the similarities between the oxides formed in the two environments (chromium rich) it is suggested that the key difference between the systems is the kinetics of the reactions, not a fundamental change in the oxide formation.

The reduced kinetics of steam due to the low pressure was countered by an increased test temperature, but there are limits to how much acceleration can be achieved. The limitations of valid test temperatures are when the microstructure of the alloy will be altered by the test and when any form of conventional IO occurs. The first point at which the microstructure of the alloy is altered is in the region of $\approx 525°C$, at this point carbides can precipitate and/or grow [176].

Tests where IO occurs should be used with caution for SCC studies as the stress generated by the volume change could affect the results, however this temperature is dependent on the surface finish. The stress generation is more probable to have a significant effect on SCC tests relative to oxidation studies. The limiting factor in temperature for oxidation studies is when the grain boundary oxide changes from a continuous preferential oxide to the formation of discrete particles of oxide, it is suggested that at this point the nature of the cracking will not be representative of PWSCC. An alternative method to countering the reduced kinetics would be the use of supercritical water or a pressurised hydrogenated steam system.

12.2 The Effect of Surface Finish

The strain-free surface obtained by OPS polishing was significantly more susceptible to SCC, despite the deformed layer and rough surface being expected to be detrimental to SCC initiation. The result agrees with results by Scenini et al. at 400°C in high pressure steam [74]. The enhanced susceptibility (accelerated initiation) of a strain free surface to SCC can be described by the observed preferential oxides and the deformed layer. The deformed layer will increase the diffusivity (due to the greater density of grain boundaries and increased dislocations density from the localised cold work) of both oxygen and chromium in the alloy, but the increased outward diffusivity of chromium promotes the external oxide formation which inhibiting the inward diffusion of oxygen and hence delaying the initiation of SCC cracking. This transition between external and internal intergranular oxide as a result of surface finish was observed in both the steam and autoclave testing.

The effect of the deformed layer can be considered to offset PWSCC initiation. This simplest method to account for such an effect when modelling PWSCC would be by the introduction of an effective exposure time ($t_{effective}$) as opposed to the true exposure time ($t_{exposure}$). This could take the form of

$$t_{effective} = t_{exposure} - t_{deformed} \tag{12.1}$$

were $t_{deformed}$ is the time associated with the oxidation of the deformed layer and is assumed to occur in preference to the grain boundary oxidation. It may also account for part of the variable initiation times observed in laboratory tests.

It can reasonably be assumed that the finish on plant components is substantially worse than those used in PWSCC tests. This fact cannot however be taken to imply a reduced susceptibility to PWSCC. The deformed layer in plant components is of such a size that it should be considered as a cold worked form of the material with its own cracking properties, not a surface local, deformed layer. Recent work by Vailant et al. has shown that a large cold worked layer is detrimental to PWSCC and could only be considered beneficial in a limited number of situations (i.e. at applied loads less or slightly higher than the bulk yield stress, the superficial cold worked layer still has a compressive stresses resulting from the mechanical deformation, in this case, the effective stress at the surface does not resulting in yielding, thus the load at the surface does not exceed the threshold load for PWSCC) [121].

The point at which a surface deformed layer transitions to be considered as a cold worked material at the surface (a cold-worked layer) with independent cracking properties is not well defined, but can be seen as important to SCC studies. A local deformed layer (≈2 µm in the current work) has been shown to be beneficial for PWSCC as a result of modified oxidation properties, but a large cold worked layer (≈2 mm) at the surface is detrimental to PWSCC [121]. To clarify the two scenarios, a deformed layer should be defined as one which is local to the surface and only affects the oxidation properties of the material, a cold worked layer is one which is of sufficient size to sustain propagation of a PWSCC crack, thus has independent cracking properties. From this definition it can be said that a deformed layer is beneficial to PWSCC whilst a cold worked layer is detrimental.

The effect of sample preparation can be seen on the reference samples supplied, the samples supplied as reference to PWSCC were observed to have a significant deformed layer which would have altered the initiation time and thus the test results. It is recommended that SCC results should only be compared to those of like surface finishes or when work has been done to account for the differences which result from the deformed layer.

Part V

Conclusion

CHAPTER

THIRTEEN

CONCLUSIONS

In this study, the possibility of using low pressure hydrogenated steam to simulate primary water reactor (PWR) conditions has been examined. The oxides formed on alloy 600 (heat WF675, in the as received condition and 15% cold worked in tension) between 350°C and 500°C in low pressure steam have been characterised and compared to oxide that formed in high pressure water in autoclave tests at 350°C. The comparison shows that the oxidation behaviours are similar but not identical.

PWSCC tests on 19% cold rolled WF675 has demonstrated the effect of surface finish and the implications it can have on PWSCC tests. The work has shown that tests regarding PWSCC, especially initiation should be carried out on a sample which has a surface representative of a bulk and a correction factor for the effect of a deformed layer should be introduced to account for the delay in the initiation it causes.

The main points covered in this study are:

- SCC of 19% cold rolled WF675 in hydrogenated steam exhibited a similar potential dependency to that observed in lower temperature autoclave PWSCC tests.

- The surfaces mechanically-prepared to 600 grit were less susceptible to SCC compared to a 60 nm OPS surface with no deformed layer.

- Internal oxidation, both classical and preferential grain boundary oxidation was observed in specimens exposed at 500°C and 400°C. Conversely, only preferential intergranular oxidation was detected in specimens tested in the autoclave and steam at 350°C.

- The bulk oxygen diffusivity was calculated from the internal oxidation after 500 h exposures. At 500°C the oxygen diffusivty was determined to be

1.79×10^{-20} m^2s^{-1} for AR-WF675 and 1.21×10^{-20} m^2s^{-1} for 15%CW-WF675, the oxygen diffusivity at 400°C in 15%CW-WF675 was calculated to be 1.49×10^{-22} m^2s^{-1}.

- The oxygen diffusivities calculated from internal oxidation as a result of shorter duration exposures (66 h) at 500°C were found to be lower than the values calculated in 500 h exposures (2.31×10^{-21} m^2s^{-1} for AR-WF675 and 2.14×10^{-21} m^2s^{-1} for 15%CW-WF675). This is attributed to oxygen transport along the incoherent interface of the oxide/matrix and the compressive strain produced in the matrix by the volume change associated with the formation of the internal oxides.

- Grain boundary oxygen diffusivities were not calculated as previous work has shown that a preferential oxide acts as a fast transport path for oxygen [158]. A preferential oxidation rate constant is calculated as a more relevant parameter for PWSCC; this combines the oxygen and chromium diffusivity with the oxidation kinetics into a single parameter.

- The preferential oxidation rate K_{oxide} in hydrogenated steam with a hydrogen to steam ratio of 20 have been determined to be

  $$K_{oxide} = A \exp^{\frac{-Q}{RT}}$$

  with $A = 2.27 \times 10^{-3}$ m^2s^{-1} and $Q = 221$ kJ.mol^{-1} for AR-WF675 and $A = 5.04 \times 10^{-7}$ m^2s^{-1} and $Q = 171$ kJ.mol^{-1} for 15% cold worked WF675. These values are consistent with the activation energy of PWSCC initiation.

- Preferential oxidation rates were compared to the diffusivity of oxygen that Scott predicted for his PWSCC. The measured values were not consistent with Scott's prediction, but the results from high pressure autoclave tests were closer than results obtained at atmospheric pressure. All tests were carried out with no applied load which may provide an explanation for the discrepancy.

- The preferential intergranular oxidation observed in the steam-exposed specimens occurred at a low rate compared to that in specimens exposed in pressurised autoclaves at the same temperature.

- Carbides appeared to accelerate both internal and preferential intergranular oxidation and this finding was discussed in terms of chromium availability and the carbide/matrix incoherent interface accelerating the inward transport of oxygen. The incoherent interface was identified to be the probable cause due to the presence of matrix like material between the carbide and the oxide, implying the oxidation of the matrix and not the carbide.

- The observation that the oxidation around the carbides did not extend beyond the depth of the carbide and into the matrix, supports the idea that the carbides act as oxygen traps.
- Asymmetric Ni-enrichment associated with the intergranular oxide was detected, it is suggested that the enrichment of nickel and depletion of chromium is a result of grain boundary migration and not the chromium diffusivity.
- Nodules of nickel formed at the surface are attributed to nickel rejection caused by the volume expansion associated with internal oxidation.
- The preferential oxidation is postulated to enhance oxygen diffusivity at the grain boundary while hindering the outward diffusion of nickel. This prevents the rejection of nickel at the grain boundary to reliave the stress generated by the oxidation as a result of the volume expansion.

CHAPTER
FOURTEEN

FUTURE WORK

Throughout the study it is inevitable that ideas are generated which are beyond the remit of the current work, yet would provide useful areas of studies for future work, this details some of the areas believed to be of most interest.

First and foremost of this is the further examination of the effect of surface finish on oxidation, SCC and corrosion fatigue. The current results have been interpreted as an effect of the deformed layer producing enhanced local diffusivity at the surface and as such change the corrosion behaviours. If this is the case the effect should occur on Alloy 600 when exposed to other corrosive environments and on different materials when tested with variable surface finishes. With regard to the nuclear industry work of a similar nature on stainless steels, Alloy 690 and Alloy 800 would be of interest when tested in environments comparable to; primary water, secondary side water and advanced gas cooled reactor environments (high pressure CO_2).

With regard to the modelling of PWSCC the identification of an offset time for PWSCC based on a deformed layer should be considered a priority. This could be achieved by the production of a set of samples with a range of deformed layers at the surface. Exposure of this set, with samples pulled periodically to be cross-sectioned would allow the identification of the time at which intergranular penetration initiate. This data could then be used to retrospectively apply a corrected time to previous PWSCC results where the surface finish is known, both for in-service and laboratory samples.

The PhD set out with the focus of examining the oxygen and chromium diffusivity in WF675, however the outcome was that of a preferential oxidation rate and the suggestion that the chromium depletion is a result of grain boundary migration, coupled with the validation of hydrogenated steam as a viable environment for PWSCC. The grain boundary migration rate could be examined by using a large grained material with a low carbide density. Cross-sectioning a long boundary (≈ 100 µm) near to one end prior to oxidation, then cross-sectioning the same boundary several microns away from the previous cross-section after oxidation would allow the movement to be visualised, repeating the process could lead to the velocity and magnitude of the migration being implied.

The material used predominately in this PhD was a forging and as such had a complex strain path; the use of a solution annealed material provided an un-stressed reference. It is suggested that stress accelerates oxidation. Inducing stress into the solution annealed material and subsequently characterising the local stresses at grain boundaries prior to oxidation by the micro-hole drilling technique, currently being developed for FIB. This would allow for the quantification of the effect of local stress on the preferential oxidation of a grain boundary. Additionally applying the method after oxidation to determine the change in stress would allow the effect of volume change due to oxidation to be explored. The limitations of this test is that a large grain material is required and that the assumption that the stress along a single grain boundary is constant; hence a solution annealed material is most suitable.

Part VI

Appendix

APPENDIX

A

CONVERTING R TO CC/KG OF HYDROGEN

For comparison of steam tests to autoclave tests, the test parameter R can be converted to an equivalent cc/kg of hydrogen at a given temperature. Similar calculations based on the Nernst equation to derive this relationship can be found in appendix D of [13].

The partial pressure of oxygen in steam can be calculated from the reaction (A.1).

$$H_2O \rightleftharpoons H_2 + \frac{1}{2}O \tag{A.1}$$

The Gibbs free energy associated with this reaction is given by:

$$\Delta G_{H_2O} = \Delta G^0_{H_2O} - RT\ln\left[\frac{p[H_2]p[O_2]^{\frac{1}{2}}}{p[H_2O]}\right] \tag{A.2}$$

where ΔG_{H_2O} is the Gibbs free energy of the reaction, $\Delta G^0_{H_2O}$ is the Gibbs free energy of formation, R is the universal gas constant, T is the absolute temperature and p is the partial pressure.

Assuming the system is at equilibrium ($\Delta G_{H_2O} = 0$), it rearranges to give the oxygen partial pressure to be:

$$pO_2 = \left(\frac{pH_2O}{pH_2}\right)^2 \exp\left[\frac{2\Delta G^0_{H_2O}}{RT}\right] \tag{A.3}$$

In the case when the partial pressure is equal to that of the Ni/NiO transition point it becomes

$$pO_{2_{Ni/NiO}} = \left(\frac{pH_2O}{pH_{2_{Ni/NiO}}}\right)^2 \exp\left[\frac{2\Delta G^0_{H_2O}}{RT}\right] \tag{A.4}$$

The definition of R is

$$R_{test} = \frac{pO2_{Ni/NiO}}{pO_2} \tag{A.5}$$

Substituting A.3 and A.4 into A.5 results in

$$R = \frac{pO2_{Ni/NiO}}{pO_2} = \left[\frac{pH_2}{pH2_{Ni/NiO}}\right]^2 \tag{A.6}$$

The partial pressure of the hydrogen can be seen as equivalent to the cc/kg of hydrogen, when looking at the ratios

$$R = \left[\frac{cc/kg\ H_2}{cc/kg\ H_2\ at\ Ni/NiO\ Boundary}\right]^2 \tag{A.7}$$

Andresen et al have measured $PH2_{Ni/NiO}$ as a function of temperature to be [177]

$$cc/kg\ H_2\ at\ Ni/NiO\ Boundary = 10^{0.0111T(^{\circ}\mathrm{C})-2.59} \tag{A.8}$$

Thus the R values used in this report can converted by A.7 into cc/kg of hydrogen equivalent at 325°C, as summarised in Table A.1.

Table A.1 – Table converting steam test parameter R to equivalent cc/kg of hydrogen at 325°C.

R	H_2 (cc/kg)
0.1	3
1.5	12
8	28
20	45
70	84

APPENDIX

B

HYDROGENATED STEAM FLOW CALIBRATION CURVES

Rig 1

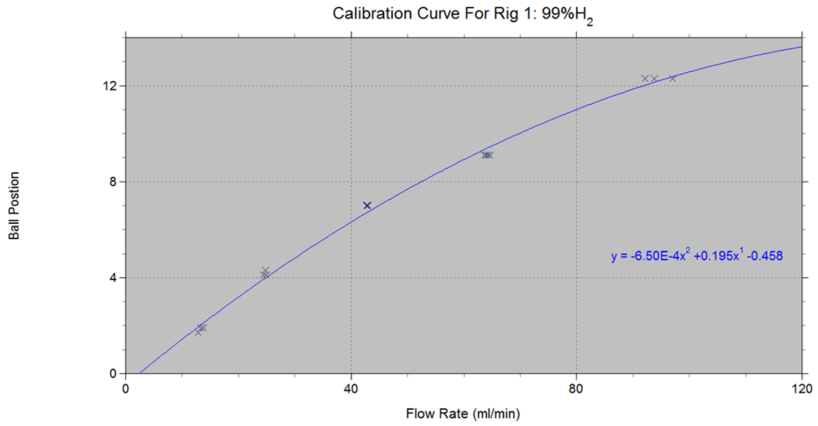

Figure B.1 – Calibration curve obtain for Rig 1 using pure hydrogen.

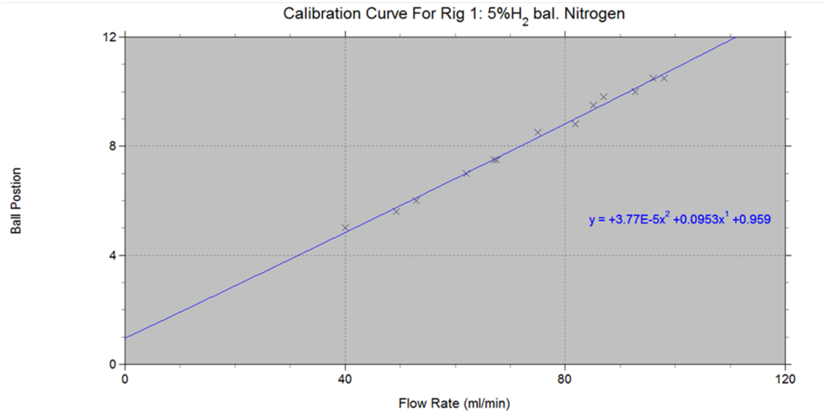

Figure B.2 – Calibration curve obtain for Rig 1 using 5%hydrogen bal. nitrogen.

Rig 2

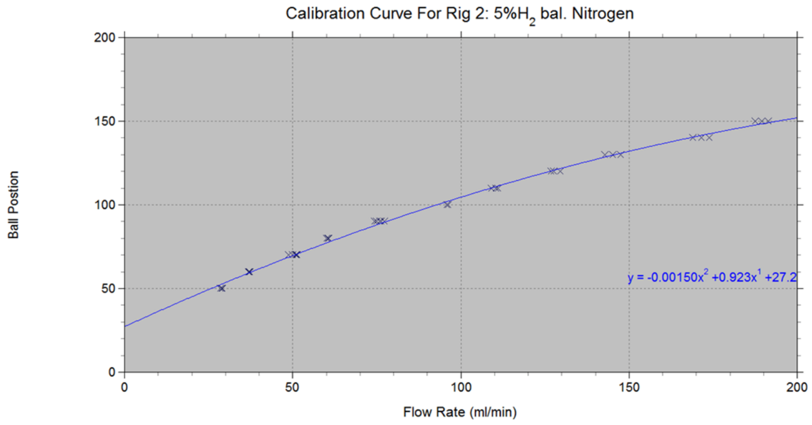

Figure B.3 – Calibration curve obtain for Rig 2 using 5%hydrogen bal. nitrogen.

APPENDIX

C

RIG 1 OPERATING PROCEDURE

The operation of the hydrogenated steam oxidation system is relatively straight forward; however care must be taken due to the nature of the system. The basic operation of the system is as follows:

Starting conditions and checks:

- All power to the system is turned off.
- Valve for water inlet into the pre-heater should be shut.
- Fill the water supply and remove any air locks in the system up to the inlet valve.
- Ensure the gas bottle has required gas and pressure. Before starting ensure the gas bottle is shut.

Test set up:

- Place samples in reaction vessel with the surface of interest face up and seal the system.
- Set a low flow rate of the gas (hydrogen or hydrogen nitrogen mix) and ensure that the flow on the outlet bubbler is consistent with the inlet flow, if not check the system for leaks and fix.
- Increase the gas flow rate and purge the system with a minimum of ten flushes.
- Turn on all heating controls and heat the system (pre-heater, furnace and pipe heating).

  Pre-heater is 150°C.

  Pipe heating is heating tape, which is calibrated to be approximately 110°C.

Furness temperature is the test temperature.

- Once system is heated and stable at the required temperature, set the gas flow to the test flow rate, turn on the water pump and open the water inlet valve.
- Monitor the system for the next hour to ensure no leaks develop, gas flow is constant and the temperature remains.
- During the test constantly monitor water and gas supply, refill water and replace gas cylinder as required.

Shutdown:

- Shut off the water inlet valve and turn off the pump.
- Increase the gas flow rate to a maximum.
- Turn of all heating and allow the system to cool.
- When temperature is less than 35°C turn the gas off and remove samples.

Emergency shutdown Procedure:

- Shut gas bottle, turn all power off.

APPENDIX D

RIG 2 OPERATING PROCEDURE

As with rig 1, the operation of the system is relatively straight forward; but has an increased complexity due to the tensile tester and the seals and cooling associated with it. The basic operation of the system is as follows:

Starting conditions and checks:

- All power is turned off, except for the tensile tester and control computer which are on.
- Valve for water inlet into the pre-heater should be shut.
- Fill the water supply and remove any air locks in the system up to the inlet valve.
- Ensure the gas bottle has required gas and pressure. Before starting ensure the gas bottle is shut.
- All O-ring seals on the system have been replaced (this is required after/before every test).

Test set up:

- Measure exact sample geometries and load the sample into the tensile tester, care must be taken not to bend the sample when loading and to avoid the heating coil in the reaction vessel. The top pin for attaching the pull rod should not be installed and room to allow for expansion during the heating given.
- Seal the system and attach the cooling.
- Set a low flow rate of the gas (hydrogen or hydrogen nitrogen mix) and ensure that the flow on the outlet bubbler is consistent with the inlet flow, if not check the system for leaks and fix.

- Turn on the chillier and ensure it is working, check temperature and flow (air locks and leaks are possible from the reattachment).
- Increase the gas flow rate and purge the system with a minimum of ten flushes.
- Turn on all heating controls and heat the system (pre-heater, furnace and pipe heating).

  Pre-heater is 150°C.

  Pipe heating is heating tape, which is calibrated to be approximately 200°C.

  Furness temperature is the test temperature.
- Once system is heated and stable at the required temperature, set the gas flow to the test flow rate, turn on the water pump and open the water inlet valve.
- Monitor the system for the next hour to ensure no leaks develop, gas flow is constant and the temperature remains.
- Install the top pull rod pin and load the sample (normal load ramp rate of 100 newton's per minute is used); caution the pull rod will be hot.
- During the test constantly monitor water and gas supply, refill water and replace gas cylinder as required.

Shutdown:

- If sample has not failed, end test program and remove top pull road pin (this will prevent the sample been destroyed by the contractions during the cooling)
- Shut off the water inlet valve and turn off the pump.
- Increase the gas flow rate to a maximum.
- Turn of all heating and allow the system to cool.
- When temperature is less than 35°C turn of the chillier and the gas, remove sample.

Emergency shut down procedure:

- Shut gas bottle, turn all power off.

APPENDIX

E

500 H, 500°C, AS-RECEIVED WF675 3D IMAGE

CD with a set of 200 images taken from FIB sequential slice and view for a 500°C test conducted at R=20 for 500 h on As-Received WF675

APPENDIX

F

500 H, 500°C, COLD WORKED WF675 3D IMAGE

CD with a set of 280 images taken from FIB sequential slice and view for a 500°C test conducted at R=20 for 500 h cold worked WF675.

APPENDIX

G

CALCULATIONS OF THE VOLUME CHANGE ASSOCIATED WITH INTERNAL OXIDATION

The volume change (ΔV) of the material due to oxidation can be calculated by

$$\Delta V = V_{after} - V_{before} \tag{G.1}$$

where V_{before} is the molar volume before oxidation and V_{after} is the total volume after oxidation. In the case of alloy 600 oxidising to form a Cr_2O_3

$$V_{before} = V_{alloy600} \tag{G.2}$$

$$V_{after} = V_{oxide} + V_{bulk} \tag{G.3}$$

where $V_{alloy600}$ is the molar volume of alloy 600, V_{oxide} is the molar volume of the formed chromium oxide and V_{bulk} is the molar volume of the bulk material left after oxidation.

Assuming the oxidation of 1 mol of alloy 600, with sufficient oxygen to consume all chromium to produce Cr_2O_3, implies that the volume of the oxide is half the mol fraction of chromium in the alloy times the molar volume of the oxide (half as two chromium per oxide)

$$V_{oxide} = 0.5 N_{Cr}^{0} V_{Cr_2O_3} \tag{G.4}$$

where N_{Cr}^{0} is the molar fraction of chromium in the alloy and $V_{Cr_2O_3}$ is the molar volume of Cr_2O_3.

The removal of all the chromium implies that the volume of the bulk material is that of the formed nickel-iron material, not alloy 600. Given that chromium has the lowest density of the three main components of the alloy implies that the resulting nickel-iron bulk alloy will have an increased density and reduced molar volume. Assuming the resulting alloy has a molar volume equal to that of nickel 200 (pure nickel) implies that the bulk volume

$$V_{bulk} = (1 - N_{Cr}^0)V_{Ni200} \tag{G.5}$$

where V_{Ni200} is the molar volume of nickel 200. Combining the above results in the volume change

$$\Delta V = (1 - N_{Cr}^0)V_{Ni} + 0.5N_{Cr}^0 V_{Cr_2O_3} - V_{alloy} \tag{G.6}$$

BIBLIOGRAPHY

[1] World Nuclear Association. WNA Pocket Guide. In *Nuclear Power Reactor Characteristics*. WNA, 2012.

[2] International Atomic Energy Agency. Annual reference data series no.2. In *Nuclear Power Reactors in the World*. IAEA, 2012.

[3] J Massoud. Metallurgy. In *Materials Reliability and Degradation Management Issues and Associated Tools for Nuclear Power Plants*, 2010.

[4] Special metals website. Alloy 600 Technical Bulletin. `http://www.specialmetals.com/documents/Inconel%20alloy%20600%20%28Sept%202008%29.pdf`. Visited on the 10th January 2011.

[5] J Davis. *Nickel, cobalt, and their alloys*. ASM International, 2000.

[6] P. M. Scott and P. Combrade. On the mechanism of stress corrosion crack initiation and growth in alloy 600 exposed to PWR primary water. In *Eleventh international conference on environmental degradation of materials in nuclear power systems – water reactors*, Stevenson, Washington, August 2003.

[7] R. W. Staehle and J. A. Gorman. Quantitative assessment of submodes of stress corrosion cracking on the secondary side of steam generator tubing in pressurized water reactors: part 1. *Corrosion*, 59(11):931–994, November 2003.

[8] H. Coriou, L. Grall, Y. Legall, and S. Vettier. Stress corrosion cracking of Inconel in high temperature water. In *Third Colloquium of Metallurgy*, page 161, Saclay, 1960. North Holland.

[9] H. R. Copson and S. W. Dean. Effect of contaminants on resistance to stress corrosion cracking of Ni–Cr alloy 600 in pressurized water. *Corrosion*, 21:1–8, 1965.

[10] T. Couvant. Vitesses de propagation par corrosion sous contrainte dans l'alliage 600 laminé exposé au milieu primaire des REP. Technical report, EDF, 2000.

[11] F. Léonard. *Study of Stress Corrosion Cracking of Alloy 600 in High Temperature High Pressure water*. PhD thesis, University of Manchester, 2010.

[12] N. Lorho. *SCC susceptibility in Alloy 600 with different strain histories*. PhD thesis, University of Manchester, 2013.

[13] F. Scenini. *The effect of surface preparation on the oxidation and SCC behaviour of alloy 600 and 690 in hydrogenated steam.* PhD thesis, The University of Manchester, 2006.

[14] F. Scenini, R. C. Newman, R. A. Cottis, and R. J. Jacko. Alloy oxidation studies related to PWSCC. In *Twelfth international conference on environmental degradation of materials in nuclear power systems – water reactors*, Salt Lake City, Utah, August 2005. TMS (The Minerals, Metals & Materials Society).

[15] S. J. Patel. A century of discoveries, inventors, and new nickel alloys. *Journal of the Minerals, Metals and Materials Society*, 58(9):18–20, 2006.

[16] G. P. Airey. Microstructural aspects of the thermal treatment of Inconel alloy 600. *Metallography*, 13(1):21–41, February 1980.

[17] Y.S. Sato, P. Arkom, H. Kokawa, T.W. Nelson, and R.J. Steel. Effect of microstructure on properties of friction stir welded inconel alloy 600. *Materials Science and Engineering: A*, 477(1-2):250 – 258, 2007. 3rd International Conference on Spray Deposition and Melt Atomization (SDMA 2006) and the 6th International Conference on Spray Forming (ICSF VI).

[18] Sandmeyer steel company website. Alloy 600 Technical Bulletin. `http://www.sandmeyersteel.com/images/Alloy-600-Spec-Sheet.pdf`. Visited on the 31th January 2011.

[19] HPAlloys website. `http://www.hpalloy.com/alloys/descriptions/INCONEL600.html`. Visited on the 12th May 2009.

[20] P. M. Scott and C. Benhamou. An overview of recent observations and interpretations of IGSCC in nickel base alloys in PWR primary water. In *Tenth International Conference on Environmental Degradation of Materials in Nuclear Power Systems – Water Reactors*, Lake Tahoe, Nevada, August 2001. TMS (The Minerals, Metals & Materials Society).

[21] P. M. Scott. An overview of materials degradation by stress corrosion in PWRs. In *EUROCORR 2004*, Nice, France, September 2004.

[22] W. K. Soppet O. K. Chopra and W. J. Shack. Effects of alloy chemistry, cold work, and water chemistry on corrosion fatigue and stress corrosion cracking of nickel alloys and welds. Technical report, Argonne National Laboratory, 2001.

[23] W. Bamford and J. Hall. Cracking of alloy 600 nozzles and welds in PWRs: review of cracking events and repair service experience. In *Twelfth International Conference on Environmental Degradation of Materials in Nuclear Power Systems – Water Reactors*, Salt Lake City, Utah, August 2005. TMS (The Minerals, Metals & Materials Society).

[24] *ASM Handbook Volume 2: Properties and Selection: Nonferrous Alloys and Special-Purpose Materials.* ASM International, 1990.

[25] Special metals website. Alloy 690 Technical Bulletin. `http://www.specialmetals.com/documents/Inconel%20alloy%20600%20%28Sept%202008%29.pdf`. Visited on the 10th January 2011.

[26] R. G. Ballinger. Light water reactors: materials of construction and their performance. In *International Conference on Plant Materials Degradation - Application to the Stress Corrosion Cracking of Ni-base Alloys*, EDF R&D centre of Les Renardières, Moret–Sur–Loing, France, November 2008.

[27] A. Aguilar, J. L. Albarran, H. F. Lopez, and L. Martinez. Microstructural response on the cracking resistance of alloy 600. *Materials Letters*, 61(1):274–277, 2007.

[28] G. S. Was and K. Lian. Role of carbides in stress corrosion cracking resistance of alloy 600 and controlled–purity Ni–16% Cr–9% Fe in primary water at 360 °C. *Corrosion*, 54(9):675–688, September 1998.

[29] M. Thuvander and K. Stiller. Evolution of grain boundary chemistry in a Ni–17Cr–9Fe model alloy. *Materials Science and Engineering A*, 250(1):93–98, July 1998.

[30] K. Fruzzetti. Primary system dose reduction through chemistry: Problem and approach. In *Material Degradation Course for Utility Engineers (MAI)*, 2010.

[31] *ASM Handbook Volume 2: Alloy Phase Diagrams.* ASM International, 1990.

[32] H. L. Lukas and P. Agraval. Chromium–Iron–Nickel. In G. Effenberg and S. Ilyenko, editors, *Iron systems: phase diagrams, crystallographic and thermodynamic data*, Iron systems. Springer, Berlin, 2008.

[33] P. L. Andresen and M. M. Morra. Stress corrosion cracking of stainless steels and nickel alloys in high-temperature water. *Corrosion*, 64(1):15–29, January 2008.

[34] J. M. Park, W. S. Ryu, and Y. H. Kang. DSC study on carbide precipitation reaction in Inconel 600. *Journal of Nuclear Materials*, 209(3):221–225, May 1994.

[35] S. Chevalier. *Shreir's Corrosion. 1.07 Mechanisms and Kinetics of Oxidation.* Oxford, 2010.

[36] C. Wagner. Theoretical analysis of the diffusion processes determining the oxidation rates of alloys. *Elektrochem*, 99:369, 1952.

[37] P. Combrade, P. M. Scott, M. Foucault, E. Andrieu, and P. Marcus. Oxidation of Ni base alloys in PWR water: oxide layers and associated damage to the base metal. In *Twelfth International Conference on Environmental Degradation of Materials in Nuclear Power Systems – Water Reactors*, Salt Lake City, Utah, August 2005. TMS (The Minerals, Metals & Materials Society).

[38] F. Delabrouille, L. Legras, F. Vaillant, P. Scott, B. Viguier, and E. Andrieu. Effect of the chromium content and strain on the corrosion of nickel based alloys in primary water of pressurized water reactors. In *Twelfth International Conference on Environmental Degradation of Materials in Nuclear Power Systems – Water Reactors*, Salt Lake City, Utah, August 2005. TMS (The Minerals, Metals & Materials Society).

[39] F. Delabrouille. *Caractérisation par MET de fissures de corrosion sous contrainte d'alliages á base de nickel : influence de la teneur en chrome et de la chimie du milieu.* PhD thesis, Institut national polytechnique de Toulouse, November 2004.

[40] J. Panter, B. Viguier, J.–M. Cloué, M. Foucault, P. Combrade, and E. Andrieu. Influence of oxide films on primary water stress corrosion cracking initiation of alloy 600. *Journal of Nuclear Materials*, 348(1-2):213–221, 2006.

[41] A. Machet. *Etude des premiers stades d'oxydation d'alliages inoxydables dans l'eau à haute température.* PhD thesis, Université Pierre et Marie Curie – Paris VI, 2004.

[42] P. Combrade and P. Scott. The role of surface films on alloy 600 corrosion in pressurised water reactors. In T. Magnin, editor, *Corrosion-Deformation Interactions CDI '96: (EFC 21).* CDI '96 in conjunction with EUROCORR '96, Maney Publishing, 1997.

[43] A. Machet, A. Galtayries, P. Marcus, P. Combrade, P. Jolivet, and P. Scott. XPS study of oxides formed on nickel-base alloys in high-temperature and high-pressure water. *Surface and Interface Analysis*, 34(1):197–200, 2002.

[44] T. Terachi, N. Totsuka, T. Yamada, T. Nakagawa, H. Deguchi, M. Horiuchi, and M. Oshitani. Influence of dissolved hydrogen on structure of oxide film on alloy 600 formed in primary water of pressurized water reactor. *Journal of Nuclear Science and Technology (Japan)*, 7:509–516, 2003.

[45] F. Carrette, L. Guinard, and B. Pieraggi. Kinetics of corrosion products release from nickel-base alloys corroding in primary water conditions: a new modelling of release. In *Ninth International Conference on Water Chemistry of Nuclear Reactors Systems*, SFEN Avignon, 2002.

[46] A. Machet, A. Galtayries, S. Zanna, L. Klein, V. Maurice, P. Jolivet, M. Foucault, P. Combrade, P. Scott, and P. Marcus. XPS and STM study of the growth and structure of passive films in high temperature water on a nickel-base alloy. *Electrochimica Acta*, 49(22-23):3957–3964, September 2004.

[47] R. C. Newman, T. S. Gendron, and P. M. Scott. Internal oxidation and embrittlement of alloy 600. In F. P. Ford, S. M. Bruemmer, and G. S. Was, editors, *Ninth International Symposium on Environmental Degradation of Materials in Nuclear Power Systems – Water Reactors*, pages 79–93, Newport Beach, California, August 1999. TMS (The Minerals, Metals & Materials Society).

[48] L. Thomas, B. R. Johnson, J. S. Vetrano, and S. M. Bruemmer. Microstructural and microchemical characterization of primary-side cracks in an alloy 600 nozzle head penetration and its alloy 182 j-weld from the david–besse reactor vessel. In *Twelfth International Conference on Environmental Degradation of Materials in Nuclear Power Systems – Water Reactors*, Salt Lake City, Utah, August 2005. TMS (The Minerals, Metals & Materials Society).

[49] P. Laghoutaris, J. Chêne, C. Guerre, O. Raquet, M. Sennour, R. Molins, F. Vaillant, and P. Scott. Contribution to understanding of stress corrosion

cracking of alloy 600 in PWR primary water. *Energy Materials: Materials Science and Engineering for Energy Systems*, 3:119–125, June 2008.

[50] C. Guerre, P. Laghoutaris, J. Chene, L. Marchetti, R. Molins, C. Duhamel, and M. Sennour. Stress corrosion cracking of alloy 600 in PWR primary water : Influence of chromium, hydrogen and oxygen diffusion. In *Fifteenth International Conference on Environmental Degradation of Materials in Nuclear Power Systems-Water Reactors*, Cheyenne Mountain, Colorado Springs, 2011.

[51] L. Legras, F. Delabrouille, F. Vaillant, and J.M. Boursier. ATEM & SEM study of the oxides developed in scc cracks and at the surface of nickel based alloys exposed in primary water. In *Thirteenth International Conference on Environmental Degradation of Materials in Nuclear Power Systems Whistler, British Columbia August 19 - 23, 2007*, 2007.

[52] P. Gupta, T. Dutta, S. Mal, and J. Narayan. Controlled p-type to n-type conductivity transformation in nio thin films by ultraviolet-laser irradiation. *Journal of Applied Physics*, 111, 2012.

[53] A. Loucif, J.-P. Petit, Y. Wouters, and P. Combrade. Effect of dissolved hydrogen, surface conditions and composition on the electronic properties of the oxide films formed on nickel-base alloys in PWR primary water. In *Fifteenth International Conference on Enviromental Degradation of Materials in Nuclear Power Plants - Water Reactors*, Cheyenne Mountain, Colorado Spring, 2011.

[54] R. Molaei, R. Bayati, and J. Narayan. Crystallographic characteristics and p-type to n-type transition in epitaxial nio thin film. *Crystal Growth & Design*, 13:5459–5465, 2013.

[55] T. Dutta, P. Gupta, A. Gupta, , and J. Narayan. Effect of li doping in nio thin films on its transparent and conducting properties and its application in heteroepitaxial p-n junctions. *Journal of Applied Physics*, 108, 2010.

[56] R.A Rapp. The transition from internal to external oxidation and the formation of interruption bands in silver-indium alloys. *Acta Metallurgica*, 9:730–741, 1961.

[57] B. Gleeson. *Shreir's Corrosion. 1.09 Thermodynamics and Theory of External and Internal Oxidation of Alloys.* Oxford, 2010.

[58] C. Wagner. Types of reactions in the oxidation of alloys. *Elektrochem*, 63:772–782, 1959.

[59] Carl Wagner. Reaktionstypen bei der oxydation von legierungen. *Elektrochem*, 63:772–782, 1959.

[60] L. Bradley, G.C. Wood, and F.H. Stott. The effects of stress on the internal oxidation of Ni-Cr and Ni-Al alloys. *Materials Science Forum Vols. 251-254*, pages 341–348, 1997.

[61] L. D. Petheh, B. Mathur, and A. B. Biswas. Transition from internal to external oxidation in indium-silver alloys. *Canadian Journal of Chemistry*, 46:1187–1196, 1968.

[62] W. Schwartzkopf. Beitrag zur inneren oxydation von nickel-legierungen. *Elektrochem*, 63:830, 1959.

[63] T. Onishi, S. Nakakubo, and M. Takeda. Calculations of internal oxidation rate equations and boundary conditions between internal and external oxidation in silicon containing steels. *Materials Transactions,*, 51:482–487, 2010.

[64] G. C. Wood, F. H. Stott, D. P. Whittle, Y. Shida, and B. D. Bastow. The high–temperature internal oxidation and intergranular oxidation of nickel–chromium alloys. *Corrosion Science*, 23(1):9–25, 1983.

[65] Y. Shida, G. C. Wood, F. H. Stott, D. P. Whittle, and B. D. Bastow. Intergranular oxidation and internal void formation in Ni–40 % Cr alloys. *Corrosion Science*, 21(8):581–597, 1981.

[66] J.S. Wolf, J.W. Weeton, J.C. Freche, United States. National Aeronautics, and Space Administration. *NASA TN D-2813*. NASA technical note. National Aeronautics and Space Administration, 1965.

[67] F. H. Stott, Y. Shida, D. P. Whittle, G. C. Wood, and B. D. Bastoww. The morphological and structural development ot internal oxides in nickel-aluminum alloys at high temperatures. *Oxidation of Metals*, 18:127–146, 1982.

[68] S. Guruswamy, S. M. Park, J. P. Hirth, and R. A. Rapp. Internal oxidation of Ag-In alloys: Stress relief and the influence of imposed strain. *Oxidation of Metals*, 26:77–100, 1985.

[69] J.R. Mackert, R D; Fairhurst, and C Wagner. High-temperature behavior of a pd–ag alloy for porcelain. *Journal of Dental Research*, 62:1229–1235, 1983.

[70] B. M. Capell. *Intergranular stress corrosion cracking and selective internal oxidation of Ni-Cr-Fe alloys in hydrogenated steam.* PhD thesis, The University of Michigan, 2005.

[71] B. Capell, L. Fournier, and G. Was. Intergranular cracking behavior of Ni–16Cr–9Fe–C alloys in hydrogenated steam. In *Tenth International Conference on Environmental Degradation of Materials in Nuclear Power Systems – Water Reactors*, Lake Tahoe, Nevada, August 2001. TMS (The Minerals, Metals & Materials Society).

[72] Y. Otoguro, M. Sakakibara, T. Saito, H. Ito, and Y. Inoue. Oxidation behaviour of austenitic heat-resisting steels in a high temperature and high pressure steam environment. *Transactions ISIJ*, 28:761–768, 1988.

[73] G. Sui, J. M. Titchmarsh, G. B. Heys, and J. Congleton. Stress corrosion cracking of alloy 600 and alloy 690 in hydrogen/steam at 380°C. *Corrosion Science*, 39(3):565–587, March 1997.

[74] F. Scenini, R. C. Newman, R. A. Cottis, and R. J. Jacko. Effects of surface preparation on intergranular stress corrosion cracking of alloy 600 in hydrogenated steam. *Corrosion*, 64(11):824–835, November 2008.

[75] T. S. Gendron, S. J. Bushby, R. D. Cleland, and R. C. Newman. Oxidation embrittlement of alloy 600 in hydrogenated steam at 400 °C. In T. Magnin, editor, *Corrosion-Deformation Interactions CDI '96: (EFC 21).* CDI '96 in conjunction with EUROCORR '96, Maney Publishing, 1997.

[76] J. Ferguson and H. Lopez. Oxidation products of Inconel alloys 600 and 690 in pressurized water reactor environments and their role in intergranular stress corrosion cracking. *Metallurgical and Materials Transactions A*, 37(8):2471–2479, 2006.

[77] G. Economy, R. J. Jacko, and F. W. Pement. IGSCC behavior of alloy 600 steam generator tubing in water or steam tests above 360°C. *Corrosion*, 43(12):727–734, December 1987.

[78] F. Scenini, R. C. Newman, R. A. Cottis, and R. J. Jacko. Dependance of PWSCC of alloy 600 on its oxidation behavior. In *NACE International Corrosion 2007*, Nashville, Tennessee, U.S.A., March 2007.

[79] W. J. Quadakkers and J. Zurek. *Shreir's Corrosion. 1.17 Oxidation in Steam and Steam/Hydrogen Environments.* Oxford, 2010.

[80] G. A. Young, W. W. Wilkening, D. S. Morton, E. Richey, and N. Lewis. The mechanism and modeling of intergranular stress corrosion cracking of nickel-chromium-iron alloys exposed to high purity water. In *Twelfth International Conference on Environmental Degradation of Materials in Nuclear Power Systems – Water Reactors*, Salt Lake City, Utah, August 2005. TMS (The Minerals, Metals & Materials Society).

[81] P. L. Surman and J. E. Castle. Gas phase transport in the oxidation of fe and steel. *Corrosion Science*, 9(10):771 – 777, 1969.

[82] Neil Birks, Gerald Heler, and Frederick Pettit. *Introduction to the high temperature oxidation of metals.* Cambridge University Press, 2nd edition, 2006.

[83] M. Montgomery and A. Karlsson. Survey of oxidation in steamside conditions. *VGB Kraftwerkstechnik*, 75:235–240, 1995.

[84] A Fry, S Osgerb, and M. Wright. Oxidation of alloys in steam environments - a review, in principles of steam oxidation. 2002. Technical report, NPL Report, 2002.

[85] P Scott and F. Vaillant. History of corrosion and mechanical degradation in operating plants: Plant affected areas and actions. In *Materials Reliability and Degradation Management Issues and Associated Tools for Nuclear Power Plants*, 2010.

[86] P. M. Scott and F. Vaillant. Corrosion in LWRs. In *International Conference on Plant Materials Degradation - Application to the Stress Corrosion Cracking of Ni Base Alloys*, EDF R&D centre of Les Renardières, Moret Sur Loing, France, November 2008.

[87] M. Bachet. Fundamentals of PWR water chemistry. In *Materials Reliability and Degradation Management Issues and Associated Tools for Nuclear Power Plants*, 2010.

[88] F. Vaillant, J. D. Mithieux, O. Bouvier, D. Vancon, G. Zacharie, Y. Brechet, and F. Louchet. influence of chromium content and microstructure on creep and PWSCC resistance on nickel based alloys. In *Ninth International Conference on Environmental Degradation of Materials in Nuclear Power Systems – Water Reactors*, 1999.

[89] H. Coriou, L. Grall, P. Olivier, and S. Vettier. Influence of carbon and nickel content on stress corrosion cracking of austenitic stainless alloys in pure or chlorinated water at 350°C. In *Conference of Fundamental Aspects of Stress Corrosion Cracking and Hydrogen Embrittlement of Iron Base Alloys*, page 235, Tokyo, Japan, 1969. The Iron and Steel Institute of Japan.

[90] T. Yonezawa and K. Onimura. Effect of chemical compositions and microstructure on the stress corrosion cracking resistance of nickel-based alloys in high-temperature water. In *International Conference on Evaluation of Materials Performance in Severe Environments, EVALMAT'89*, page 235, Tokyo, Japan, 1989. The Iron and Steel Institute of Japan.

[91] G. S. Was, J. K. Sung, and T. M. Angeliu. Effects of grain boundary chemistry on the intergranular cracking behavior of Ni–16Cr–9Fe in high–temperature water. *Metallurgical Transactions A*, 23:3343–3359, 1992.

[92] F. Vaillant, J.M. Boursier, Y. Rouillon, O. Raquet, M. Helie, P. Scott, and M. Foucault. Assessment of PWSCC resistance of Alloy 690. In *EPRI Workshop Alloy 600*, Santa Ana Pueblo (NM), 2005.

[93] J. M. Boursier, D. Desjardins, and F. Vaillant. The influence of the strain-rate on the stress corrosion cracking of alloy 600 in high temperature primary water. *Corrosion Science*, 37(3):493–508, March 1995.

[94] G. L. Webb and M. G. Burke'. Stress corrosion cracking behavior of ally 600 in high: Temperature water. In *The Seventh International Symposium on Environmental Degradation of Materials in Nuclear Power Systems: Water Reactors*, 1995.

[95] F. Vaillant, J.M. Boursier, and C Amzallag. Le corrosion sous contrainte des allages de nickel dans l'eau á haute température. Technical report, EDF R&D, 2005.

[96] S. M. Bruemmer and G. S. Was. Microstructural and microchemical mechanisms controlling intergranular stress corrosion cracking in light-water-reactor systems. *Journal of Nuclear Materials*, 216:348–363, October 1994.

[97] B. Alexandreanu, B. Capell, and G. S. Was. Combined effect of special grain boundaries and grain boundary carbides on IGSCC of Ni–16Cr–9Fe–xC alloys. *Materials Science and Engineering A*, 300(1-2):94–104, February 2001.

[98] V. Y. Gertsman and S. M. Bruemmer. Study of grain boundary character along intergranular stress corrosion crack paths in austenitic alloys. *Acta Materialia*, 49(9):1589–1598, May 2001.

[99] J.A. Gorman and E.S. Hunt. Critical factors assessment for u-bend and transition cracking,. In *Workshop on Primary-Side Stress Corrosion Cracking of PWR Steam Generator Tubing*, 1985.

[100] F. Vaillant and P. Moulart. Evaluation en laboratoire des vitesses de propagation par corrosion sous contrainte en milieu primaire de matériaux massifs en alliage 600. Technical Report HT-29/02/002/A, EDF R&D, January 2002.

[101] R. W. Staehle and J. A. Gorman. Quantitative assessment of submodes of stress corrosion cracking on the secondary side of steam generator tubing in pressurized water reactors: part 2. *Corrosion*, 60(1):5–63, January 2004.

[102] R. B. Rebak and Z. Szklarska–Smialowska. The mechanism of stress corrosion cracking of alloy 600 in high temperature water. *Corrosion Science*, 38(6):971–988, June 1996.

[103] D. S. Morton, R. A. Etien, J. B. Eager, N. Lewis, and E. Richey. SCC initiation testing of nickel-based alloys in high temperature water. In *Workshop on detection, avoidance, mechanisms, modeling and prediction of SCC initiation in water-cooled nuclear reactor plants*, Beaune, France, September 2009.

[104] D. Van Rooyen T. S. Bulischeck. Stress corrosion cracking of alloy 600 using the constant strain rate test. *Corrosion*, 37:597–607, 1981.

[105] T. Terachi, T. Yamada, T. Miyamoto, and K. Arioka. *scc* growth behaviors of austenitic stainless steels in simulated PWR primary water. *Journal of Nuclear Materials*, 426:59 – 70, 2012.

[106] Z. Szklarska-Smialowska, Z. Xia, and R. R. Valbuena. Mechanism of crack growth in alloy 600 in high-temperature deaerated water. *Corrosion*, 56(9):676–681, September 1994.

[107] J. Hou, Q.J. Peng, Z.P. Lu, T. Shoji, J.Q. Wang, E.-H. Han, and W. Ke. Effects of cold working degrees on grain boundary characters and strain concentration at grain boundaries in alloy 600. *Corrosion Science*, 53(3):1137 – 1142, 2011.

[108] S. Yamazaki, Z. Lu, Y. Ito, Y. Takeda, and T. Shoji. The effect of prior deformation on stress corrosion cracking growth rates of alloy 600 materials in a simulated pressurized water reactor primary water. *Corrosion Science*, 50(3):835–846, March 2008.

[109] D. Féron, E. Herms, and B. Tanguy. Behavior of stainless steels in pressurized water reactor primary circuits. *Journal of Nuclear Materials*, 427:364–377, 2012.

[110] J. Lindsay, F. Scenini, X. Zhou, G. Bertali, R.A. Cottis, M.G. Burke, F. Carrette, and F. Vaillant. Characterisation of stress corrosion cracking and internal oxidation of alloy 600 in high temperature hydrogenated steam. In *Sixteenth International Conference on Environmental Degradation of Materials in Nuclear Power Systems – Water Reactors*, Ashville, North Carolina, 2013.

[111] G. Bertali, F. Scenini, J. Lindsay, B. Winiarski, X. Zhong, and M. G. Burke. Oxidation studies of alloy 600 in low pressure hydrogenated steam. In *Sixteenth International Conference on Environmental Degradation of Materials in Nuclear Power Systems – Water Reactors*, 2013.

[112] S. Lozano-Perez, K. Kruska, I. Iyengar, T. Terachi, and T. Yamada. The role of cold work and applied stress on surface oxidation of 304 stainless steel. *Corrosion Science*, 56:78–85, 2012.

[113] W. C. Moshier and C. M. Brown. Effect of cold work and processing orientation on stress corrosion cracking behavior of Alloy 600. *Corrosion*, 56(3):307–320, March 2000.

[114] J.H. Schmitt, E.L. Shen, and J.L. Raphanel. A parameter for measuring the magnitude of a change of strain path: Validation and comparison with experiments on low carbon steel. *International Journal of Plasticity*, 10:535–551, 1994.

[115] T. Couvant, F. Vaillant, J. M. Boursier, and D. Delafosse. Effect of strain-path on stress corrosion cracking of AISI 304L stainless steel in PWR primary environment at 360°C. In *EUROCORR 2004*, Nice, France, September 2004.

[116] T. Couvant, L. Legras, A. Herbelin, A. Musienko, Q. Vertenelle, G. Ilevbare, D. Delafosse, G. Cailletaud, and J. Hickling. Development of understanding of the interaction between localized deformation and SCC of austenitic stainless steels exposed to primary PWR environment. In *EUROCORR 2008*, Edinbourgh, Scotland, September 2008.

[117] T. Couvant, N. Huin, T. Ghys, and G. Ilevbare. Strain localization effect on PWSCC susceptibility of Ni-base alloys. Technical Report H-B60-2009-02587-EN, EDF R&D, 2009.

[118] I. Karaman, H. Sehitoglu, H.J. Maier, and Y.I. Chumlyakov. Competing mechanisms and modeling of deformation in austenitic stainless steel single crystals with and without nitrogen. *Acta Materialia*, 49:3919–3933, 2001.

[119] L Tribouilloy, F Vaillant, J-M Olive, M Puigalli, L Legras, T Couvant, J-M Boursier, Y Rouillon, and C Amzallag. Stress corrosion cracking on cold-worked austenitic stainless steels in pwr environment. In *Thirteenth International Conference on Environmental Degradation of Materials in Nuclear Power Systems – Water Reactors*, 2007.

[120] T. Couvant. Vitesses de propagation par corrosion sous contrainte dans l'alliage 600 laminé exposé au milieu primaire des REP. Technical Report H-T29-2007-02119-FR, EDF R&D, 2007.

[121] F Vaillant, C Leseigneur, P Le-Delliou, T Couvant, S Miloudi, and Y Thebault. Laboratory stress corrosion cracking propagation in a superficial cold-worked layer in sg divider plates in alloy 600. In *Fifteenth International Conference on Enviromental Degradation of Materials in Nuclear Power Plants - Water Reactors*, Cheyenne Mountain, Colorado Spring, 2011.

[122] V. N. Shah, D. B. Lowenstein, A. P. L. Turner, S. R. Ward, J. A. Gorman, P. E. MacDonald, and G. H. Weidenhamer. Assessment of primary water stress corrosion cracking of PWR steam generator tubes. *Nuclear Engineering and Design*, 134(2-3):199–215, May 1992.

[123] G. Economy, R. J. Jacko, and J. A. Begley. Influence of hydrogen partial pressure on the IGSCC behavior of alloy 600 tubing in 360°C water or 400°C steam. In *NACE International Corrosion 1987*, Houston, Texas, U.S.A., March 1987.

[124] E. Richey, D. S. Morton, and M. K. Schurman. SCC initiation testing of nickel-based alloys using in-situ monitored uniaxial tensile specimens. In *Twelfth International Conference on Environmental Degradation of Materials in Nuclear Power Systems – Water Reactors*, Salt Lake City, Utah, August 2005. TMS (The Minerals, Metals & Materials Society).

[125] P. M. Scott and M. Le Calvar. On the role of oxygen in stress corrosion cracking as a function of temperature. In T. Magnin, editor, *Corrosion-Deformation Interactions CDI '96: (EFC 21)*, pages 384–393. CDI '96 in conjunction with EUROCORR '96, Maney Publishing, 1997.

[126] D. S. Morton, S. A. Attanasio, E. Richey, and G. A. Young. In search of the true temperature and stress intensity factor dependencies for PWSCC. In *Twelfth International Conference on Environmental Degradation of Materials in Nuclear Power Systems – Water Reactors*, Salt Lake City, Utah, August 2005. TMS (The Minerals, Metals & Materials Society).

[127] R. J. Jacko and R. E. Gold. Crack growth rates in primary side materials in elevated pH PWR water. In *Twelfth International Conference on Environmental Degradation of Materials in Nuclear Power Systems – Water Reactors*, Salt Lake City, Utah, August 2005. TMS (The Minerals, Metals & Materials Society).

[128] D. S. Morton, S. A. Attanasio, and G. A. Young. Primary water SCC understanding and characterization through fundamental testing in the vicinity of the nickel/nickel oxide phase transition. In *Tenth International Conference on Environmental Degradation of Materials in Nuclear Power Systems – Water Reactors*, Lake Tahoe, Nevada, August 2001. TMS (The Minerals, Metals & Materials Society).

[129] R. J. Jacko and R. E. Gold. Crack initiation in alloy 600 SG tubing in elevated pH PWR primary water. In *Twelfth International Conference on Environmental Degradation of Materials in Nuclear Power Systems – Water Reactors*, Salt Lake City, Utah, August 2005. TMS (The Minerals, Metals & Materials Society).

[130] C. H. Shen and P. G. Shewmon. A mechanism for hydrogen-induced intergranular stress corrosion cracking in alloy 600. *Metallurgical Transactions A*, 21:1261–1271, 1990.

[131] R. Rios. *Etude des mécanismes de corrosion sous contrainte de l'Alliage 600 dans l'eau a haute température.* PhD thesis, Université des Sciences et Techniques de Lille, 1993.

[132] K. Norring, B. Rosboreg, J. Engstrom, and J. Svenson. Influence of LiOH and H_2 on primary side IGSCC of alloy 600 steam generator tubes. In *International symposium of Fontevraud II*, page 234, Paris, France, 1990.

[133] C. Soustelle, M. Foucault, and P. Combrade. PWSCC of Alloy 600: a parametric study of the surface film effects. In F. P. Ford, S. M. Bruemmer, and G. S. Was, editors, *Ninth International Conference on Environmental Degradation of Materials in Nuclear Power Systems – Water Reactors*, pages 105–114, Newport Beach, California, August 1999. TMS (The Minerals, Metals & Materials Society).

[134] T. B. Cassagne, P. Combrade, M. A. Foucault, and A. Gelpi. The influence of mechanical and environmental parameters on the crack growth behaviour of alloy 600 in PWR primary water. In *Twelfth Scandinavian Corrosion Congress & EUROCORR'92*, pages 55–67, Espoo, Finland, May 1992.

[135] P. Abadie. *Fissuration par corrosion sous contrainte de l'Alliage 600 dans l'eau a haute température : contribution d'une approche phénoménologique a la compréhension des mécanismes.* PhD thesis, Ecole des Mines de Saint-Etienne, 1998.

[136] D. Caron. *Influence de l'hydrogene sur la vitesse de propagation des fissures de corrosion sous contrainte dans l'alliage 600 en milieu primaire des réacteurs nucléaires à eau sous pression.* PhD thesis, Ecole de matériaux de Lyon, 2000.

[137] T. Cassange, D. Caron, J. Daret, A. Mazille, and G. Turluer. Stress corrosion crack growth rate measurments in alloy 600 and 182 in primary water loops under constant load. In *Ninth Environmental Degradation of Materials in Nuclear Power Systems - Water Reactor*, Amelia Island, 1997.

[138] H. K. Birnbaum, I. M. Robertson, P. Sofronis, and D. Teter. Mechanisms of hydrogen related fracture - a review. In T. Magnin, editor, *Corrosion-Deformation Interactions CDI '96: (EFC 21).* CDI '96 in conjunction with EUROCORR '96, Maney Publishing, 1997.

[139] K. Sieradski and R. C. Newman. Brittle behaviour of ductile metals during stress corrosion cracking. *Philosophical Magazine A*, 51:95, 1985.

[140] S. P. Lynch. Environmentally assisted cracking: Overview of evidence for an adsorption-induced localised-slip process. *Acta Metallurgica*, 36(10):2639–2661, October 1988.

[141] D. A. Jones. Localized surface plasticity during stress corrosion cracking. *Corrosion*, 52(5):356–362, May 1996.

[142] N. J. Petch. The lowering of fracture-stress due to surface adsorption. *Phil. Mag*, 1:331, 1956.

[143] A. R. Troiano. The role of hydrogen and other interstitials in the mechanical behaviour of metals. *Trans. ASM*, 52:54, 1960.

[144] C. A. Zapffe and C. E. Sims. Hydrogen embrittlement, internal stress and defects in steels. *Transactions of the Metallurgical Society, American Institute of Mining, Metallurgical and Petroleum Engineers*, 145:225–227, 1940.

[145] C. A. Zapffe. Neumann bands and the planar pressure theory of hydrogen embrittlement. *J. I. S. I.*, 154,:123, 1946.

[146] T. M. Angeliu and G. S. Was. Creep and intergranular cracking of Ni-Cr-Fe-C in 360°C argon. *Metallurgical and Materials Transactions A*, 25:1169–1183, 1990.

[147] G. S. Was, D. J. Paraventi, and J. L. Hertzberg. Mechanisms of environmentally-enhanced deformation and intergranular cracking of Ni-16Cr-9Fe alloys. In T. Magnin, editor, *Corrosion-Deformation Interactions CDI '96: (EFC 21)*. CDI '96 in conjunction with EUROCORR '96, Maney Publishing, 1997.

[148] R. W. Staehle and J. A. Gorman. Quantitative assessment of submodes of stress corrosion cracking on the secondary side of steam generator tubing in pressurized water reactors: part 3. *Corrosion*, 60(2):115–180, January 2004.

[149] T. Magnin, R. Chieragatti, and R. Oltra. Mechanism of brittle fracture in a ductile 316 alloy during stress corrosion. *Acta Metallurgica et Materialia*, 38(7):1313–1319, July 1990.

[150] F. Foct, O. de Bouvier, and T. Magnin. Stress corrosion cracking mechanisms of alloy 600 polycrystals and single crystals in primary water — Influence of hydrogen. *Metallurgical and Materials Transactions A*, 31(8):2025–2036, 2000.

[151] H. L. Logan. Film-rupture mechanism of stress corrosion. *Journal of Research of the National Bureau of Standards*, 48(2):99–105, February 1952.

[152] F. P. Ford. 3 mechanisms of environmentally-assisted cracking. *International Journal of Pressure Vessels and Piping*, 40(5):343–362, 1989.

[153] J Kwonb. Evaluation of mechanical and environmental parameters affecting primary water stress corrosion cracking of nickel-based alloys. In *Proceedings of the 12th International Conference on Environmental Degradation of Materials in Nuclear Power System: Water Reactors*, 2005.

[154] F. P. Ford. Quantitative prediction of environmentally assisted cracking. *Corrosion*, 52(5):375–395, April 1996.

[155] D. L. Douglass. A critique of internal oxidation in alloys during the post-wagner era. *Oxidation of Metals*, 44:81–111, 1995.

[156] P. Scott, P. Combrade, and F. Vaillant. Selective oxidation at grain boundaries and internal oxidation. In *International Conference on Plant Materials Degradation - Application to the Stress Corrosion Cracking of Ni-base Alloys*, EDF R&D centre of Les Renardières, Moret–Sur–Loing, France, November 2008.

[157] R. W. Staehle and Z. Fang. Comments on a proposed mechanism of internal oxidation for alloy 600 as applied to low potential SCC. In F. P. Ford, S. M. Bruemmer, and G. S. Was, editors, *Ninth International Conference on Environmental Degradation of Materials in Nuclear Power Systems – Water Reactors*, pages 69–78, Newport Beach, California, August 1999. TMS (The Minerals, Metals & Materials Society).

[158] P. Laghoutaris, C. Guerre, J. Chene, C. Duhamel, R. Molins, I. De Curiere, F. Vaillant, and P.Scott. Contribution to model stress corrosion cracking of Alloy 600 in PWR primary water. In *Workshop on detection, avoidance, mechanisms, modeling and prediction of SCC initiation in water-cooled nuclear reactor plants*, Beaune, France, September 2009.

[159] H. Comert and J. N. Pratt. The standard molar gibbs free energy of formation of NiO from high-temperture e.m.f. measurments. *J. Chem. Thermodynamics*, 16:1145–1148, 1984.

[160] A. Werner, B. Skilbred, and H. Field. Mena 3100: Scanning electron microscopy (sem). Lecture Slides, 2009.

[161] James Carr. Private communication, 2013.

[162] The Electron Microscopy group, part of the Department of Material Science and Metallurgy, University of Cambridge, UK. High Angle Annular Dark Field (HAADF) STEM Tomography. `http://http://www-hrem.msm.cam.ac.uk/research/CETP/STEM_Tomo.html`. Visited on the 10th January 2013.

[163] Australian Microscopy and Microanalysis Research Faclity. `http://www.ammrf.org.au/myscope/tem/introduction/`. Visited on the 13th June 2013.

[164] L. E. Thomas and S. M. Bruemmer. High-resolution characterization of intergranular attack and stress corrosion cracking of alloy 600 in high-temperature primary water. *Corrosion*, 56(6):572–587, June 2000.

[165] F. Leonard, F. Di Gioacchino, R. Cottis, F. Vaillant, J. Quinta da Fonseca, F. Carrette, and G. Ilevbare. The role of lattice curvature on the SCC susceptibility of alloy 600. In *Fifteenth International Conference on Enviromental Degradation of Materials in Nuclear Power Plants - Water Reactors*, Cheyenne Mountain, Colorado Spring, 2011.

[166] D.J. Dyson and K.W. Andrews. Carbide M_7C_3 and its formation in alloy steels. *Journal of the Iron & Steel Institute*, 207:208–219, 1969.

[167] Y.S. Lim, J.H Suh, J.S Kim, and H. Kuk. Microscopic investigation of sensitized Ni-base alloy 600 after laser surface melting. *Metallurgical and Materials Transactions A*, 28:1223–1231, 1997.

[168] P. Scott and M. Le Calvar. Some possible mechanisms of intergranular stress corrosion cracking of alloy 600 in PWR primary water. In *Fourteenth International Conference on Environmental Degradation of Materials in Nuclear Power Systems – Water Reactors*, pages 657–667, San Diego, California, August 1993. TMS (The Minerals, Metals & Materials Society).

[169] F. Carrette, M. C. Lafont, G. Chatainier, L. Guinard, and B. Pieraggi. Analysis and tem examination of corrosion scales grown on alloy 690 exposed to pressurized water at 325°C. *Surface and Interface Analysisis*, 34:135–138, 2002.

[170] Y. Shida, F. H. Stott, B. D. Bastoww, and D. P. Whittle. Development of preferential intergranular oxides in nickel-aluminum alloys at high temperatures. *Oxidation of Metals*, 18:93–113, 1982.

[171] J.W Park and C.J. Altstetter. The diffusion and solubility of oxygen in solid nickel. *Metallurgical Transactions A*, 18:43–50, 1987.

[172] S. Guruswamy, S. M. Park, J. P. Hirth, and R. A. Rapp. Internal oxidation of Ag-In alloys: Stress relief and the influence of imposed strain. *Oxidation of Metals,*, 26, 1986.

[173] Chemical Abstracts Service. CAS database entry 00-033-0945.

[174] C. Guerre, O. Raquet, L. Duisabeau, and G. Turluer. Effect of cyclic loadings on the stress corrosion crack growth rate in Alloy 600 in PWR primary water. In *EUROCORR 2004*, Nice, France, September 2004.

[175] K. Kruska, P. Chou, O. Calonne, L. Fournier, and S. Lozano-Perez. Atom-probe tomography of surface and grain boundary oxides in alloy 600 and alloy 690 exposed to simulated pwr primary water. In *Sixteenth International Conference on Environmental Degradation of Materials in Nuclear Power Systems – Water Reactors*, Ashville, North Carolina, 2013.

[176] G. S. Was and R. M. Kruger. A thermodynamic and kinetic basis for understanding chromium depletion in Ni-Cr-Fe alloys. *Acta Metallurgica*, 33(5):841–854, May 1985.

[177] P. L. Andresen, J. Hickling, A. Ahluwalia, and J. Wilson. Effect of dissolved H_2 on SCC of Ni aloys and weld metals. In *NACE International Corrosion 2009*, Atlanta, Georgia, U.S.A., March 2009.